Understanding and Controlling the Microstructure of Organic Semiconductors

Belinda Boehm

A thesis submitted in fulfilment of the requirements for
the degree of Doctor of Philosophy

March 2022

THE UNIVERSITY
of ADELAIDE

Department of Chemistry, School of Physical Sciences
The University of Adelaide
Australia

Supervisors:
A/Prof David M. Huang
A/Prof Tak W. Kee

Contents

List of Figures

List of Tables

List of Abbreviations

A	alkyl
AA	all-atom
AdResS	Adaptive Resolution Simulation
BHJ	bulk heterojunction
bTh	bithiophene
CB	chlorobenzene
CED	cohesive energy density
CF	chloroform
CG	coarse-grained
CN	1-chloronaphthalene
CV	collective variable
DCB	*o*-dichlorobenzene
EO	ethylene oxide
FET	field-effect transistor
GB	Gay-Berne
HI	hydrodynamic interactions
IBI	iterative Boltzmann inversion
LC	liquid crystal
LCD	liquid crystal display
LJ	Lennard Jones
MC	Monte Carlo
MD	molecular dynamics
MEH-PPV	poly(2-methoxy-5-(2'-ethylhexyloxy)-1,4-phenylenevinylene)
MSD	mean squared displacement
P(NDI2OD-T2)	poly[N,N'-bis(2-octyldodecyl)naphthalene-1,4,5,8-bis(dicarboximide)-2,6-diyl]-alt-5,5'-(2,2'-bithiophene)
NDI	naphthalene diimide
OFET	organic field-effect transistor

OLED	organic light-emitting diode
OPES	on-the-fly probability enhanced sampling
OPLS	optimised potentials for liquid simulations
OPV	organic photovoltaic
OSC	organic semiconductor
OTS	octadecyltrichlorosilane
P3HT	poly(3-hexyl thiophene)
PMF	potential of mean force
PNIPAM	poly(N-isopropylacrylamide)
PPPM	particle–particle particle–mesh
RDF	radial distribution function
R_g	radius of gyration
RMS	root-mean squared
SAM	self-assembled monolayer
SAXS	small-angle X-ray scattering
SEC	size-exclusion chromatography
Th	thiophene
TOL	toluene
T_{sub}	substrate temperature
vdW	van der Waals
WCA	Weeks-Chandler Anderson
XY	xylene

Abstract

With applications ranging from lightweight and flexible photovoltaics and electronics to energy-efficient lighting, organic semiconductors (OSCs) are an important class of molecules for many emerging technologies. However, commercial uptake is currently low and their performance typically poorer than other semiconducting materials. OSC devices are often fabricated using solution-processing methods, and while this allows for cheap production and is the source of many of their novel applications, difficulty in predicting both the behaviour in solution, and the ordering of particles at interfaces once deposited, means that progress towards improving device performance is slow. Progress is further impeded by a lack of understanding of the general physical principles that control both the solution-phase and interfacial morphology. This means that innovation in the OSC field often proceeds via laborious experimental trial-and-error approaches. The work presented in this thesis provides some general rules for controlling both interfacial and solution-phase morphology of OSCs. These rules lead to simple design principles that are expected to be useful for choosing appropriate conditions and chemical structures for achieving high-performance devices. Additionally, the performance of existing metrics of polymer solubility is examined in terms of how accurately the solution-phase morphology of OSCs is able to be predicted under conditions where specific interactions – such as between solvent and backbone, or side-chains and backbone – may be important.

Computational simulation methods, whether highly specific all-atom simulations, or those using more general coarse-grained models, are useful for obtaining molecular-scale understanding of the processes that occur both in solution and at interfaces. Using a general coarse-grained model, parameterised to approximate a broad range of typical OSC structures, a number of molecular and system properties that play a key role in controlling interfacial orientation of isotropic fluids of disk-shaped anisotropic particles were able to be determined. The orientation at both solid and vapour interfaces of these OSC-like particles over a wide range of temperatures was found to follow universal scaling with a simple free energy

metric, calculated as the free energy difference between two fully-aligned extremes. Based on these results, a set of guidelines for choosing molecular properties and processing conditions in order to achieve a target orientation at either the solid or vapour interface has been proposed.

Turning to the solution-phase behaviour, a coarse-grained model of OSC polymer P(NDI2OD-T2), also known as N2200, was developed. Using this model, the aggregation properties in solvents of varying quality have been examined, and kinetic processes found to be important for accurately predicting the final aggregate structure. In poor solvents, the stability of aggregates consisting of partially overlapping chains led to the build up of extended rod-like aggregates, rather than the conventionally predicted collapse of single-chains. Whether a single-chain or multi-chain aggregation pathway is followed was found to depend on the backbone flexibility, polymer concentration, and chain length. Based on this observation, a simple theory was developed relating the chain length to the concentration at which single-chain folding and multi-chain aggregation are expected to occur at the same rate. Good agreement was found between the theory and simulation results. It is therefore apparent that concentration and chain-length, which are simple parameters to tune experimentally, have a significant, yet predictable, effect on the morphology of OSC polymer aggregates in solution.

Finally, reported discrepancies between experimental techniques for measuring the aggregation properties of OSCs were examined. Simple theories of mixing, such as Flory-Huggins theory, are commonly used to understand the solution-phase aggregation of OSC polymers from molecular simulations. Through a series of all-atom simulations of OSC polymer P(NDI2OD-T2) this theory was found to fail, under certain circumstances, to fully describe the solution-phase aggregation of these types of molecules. Though generally accurate, the simple theory does not capture specific interactions, which appear to be important for capturing the correct aggregation behaviour of P(NDI2OD-T2). The substitution of the commonly-used alkyl side-chains of P(NDI2OD-T2) for an ethylene oxide derivative, for example, leads to a more disordered aggregate structure in some solvents due strong side-chain backbone interactions. Likewise, strong solvent–backbone interactions between P(NDI2OD-T2) and 1-chloronaphthalene may lead to a previously unreported solvent-separated aggregate structure which may explain experimental discrepancies.

Declaration

I certify that this work contains no material which has been accepted for the award of any other degree or diploma in my name in any university or other tertiary institution and, to the best of my knowledge and belief, contains no material previously published or written by another person, except where due reference has been made in the text. In addition, I certify that no part of this work will, in the future, be used in a submission in my name for any other degree or diploma in any university or other tertiary institution without the prior approval of the University of Adelaide and where applicable, any partner institution responsible for the joint award of this degree.

I give consent to this copy of my thesis, when deposited in the University Library, being made available for loan and photocopying, subject to the provisions of the Copyright Act 1968.

I also give permission for the digital version of my thesis to be made available on the web, via the University's digital research repository, the Library Search and also through web search engines, unless permission has been granted by the University to restrict access for a period of time.

I acknowledge the support I have received for my research through the provision of an Australian Government Research Training Program Scholarship.

Belinda Boehm
March 2022

Acknowledgements

There are many people whose presence in my life over the past five (or longer) years has, either directly or indirectly, led me to the stage of being able to present this completed, and hopefully interesting, thesis. Without these people, the document you read today would not exist in its current form, if at all, and they all deserve much more thanks than a simple written acknowledgement.

Firstly, to my supervisor, David Huang. Your guidance and support over the course of my PhD, and my M.Phil before that, has been invaluable. You have taught me not just the relevant theory, but also how to write, how to research, and how to approach problems in a way that I am sure will stand me in good stead wherever the future takes me. Thank you for your patience through my *many* mistakes, and for the time you take to help not just me, but all your students. It does not go unnoticed.

To all of the Huang-Kee research group, both past and present. It has been a joy to share this journey, and office, with you. Thank you to Alex Begbie, Alex Stuart, Andrew Tarzia, Holly Baldock, Jess De La Perelle, Marltan Wilson, Ozgur Cekmer, Patrick Tapping, and Rohan Hudson for coming along for the ride – you have all made this experience so much more bearable! Special thanks to Huong Nguyen for sharing delicious sweets with me, and for chats about research, computers, and life. I will miss you very much.

Outside of academia, a number of friends have helped to keep me sane, and to keep my brain functioning with a multitude of board games. To Thomas, Alysha, Sam, Erin, Crowy, Jodie, Danni, and Katie (come back please!) – life would be very lonely and much less fun without you all. Likewise to Simon, Ella, Nuske, and Alex. And, finally, to Mark and Helen. From our beginnings as undergrad lab partners, we have come a long way together and I wouldn't be here without you two. Special shout out to Mark, who, in between bouts of destroying zealots in Gloomhaven, found the time to proofread sections of this thesis.

It would be remiss of me to not thank my family, who have provided so much love and support over the past couple years, and indeed through my whole life.

Thank you to Wayne and Jenine for the countless meals and board games we have shared over the last almost-ten years. To my brother Martin (who must also get special thanks for proofreading sections of this thesis), for your encouragement and advice for entering life outside of academia. And, of course, to my parents. I would not have made it here without your love, support, and guidance. You can all stop asking when I'm going to be finished now.

Finally, to Jonathan. You have walked every step of this PhD journey alongside me and I legitimately don't think I would have made it to the end without you. You have encouraged me through so many tears, and we have celebrated all the little wins together. We can finally open that bottle of wine now – I think we deserve it! Thank you.

Dedication

For my family –
Mum, Dad, Martin, and Jono.
And Barbados.

1

Introduction

"Some do. Some teach. The rest look it up."

— Archivist, *Magic: the gathering*

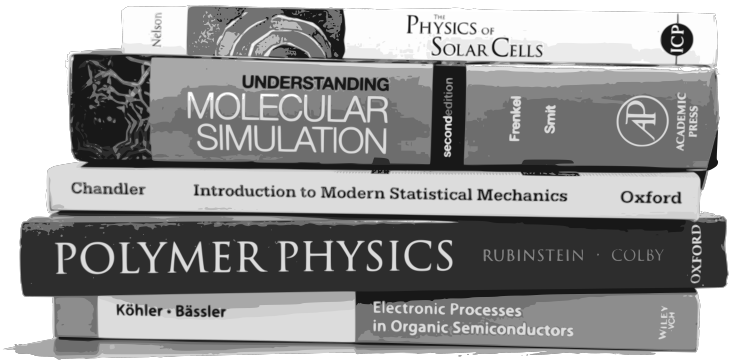

Some of the content for this chapter is taken directly from the following publication:

> Boehm, B. J.; Nguyen, H. T. L.; Huang, D. M. The Interplay of Interfaces, Supramolecular Assembly, and Electronics in Organic Semiconductors. *J. Phys: Condens. Matter* **2019**, *31*, 423001.

Chapter 1

AUTHORSHIP STATEMENTS

Principal author (candidate): Belinda J. Boehm
Contribution: 60%
Literature search, writing, and drafting of the majority of the paper. This paper constitutes a literature review I conducted during the period of my Higher Degree by Research candidature and is not subject to any obligations or contractual agreements with a third party that would constrain its inclusion in this thesis. I am the primary author of this paper.

Signature: Date: 22/02/2022

Co-author contributions

By signing the Statement of Authorship, each author certifies that:

1. the candidate's stated contribution to the publication is accurate (as detailed above);
2. permission is granted for the candidate to include the publication in the thesis; and
3. the sum of all co-author contributions is equal to 100% less the candidate's stated contribution

Co-Author: Huong T. L. Nguyen
Contribution: 15%
Literature search and summary of parts of this paper related to coarse-graining methods for anisotropic particles. Assisted in revision of the manuscript.

Signature: Date: 23/02/2022

Co-Author: David M. Huang
Contribution: 25%
Wrote sections related to continuum methods (not included in this thesis). Assisted with literature search and summary, and revision of the manuscript. Acted as corresponding author.

Signature: Date: 22/02/2022

1.1 ORGANIC SEMICONDUCTORS

From origins as a scientific curiosity in the late 1800s, semiconductors have come to pervade every aspect of our technologically focused lives, so much so that it has become difficult, if not impossible, to imagine life without them. Most conventional electronic devices employ inorganic silicon semiconductors, which are relatively efficient, and well suited to applications such as roof-top solar, personal (and larger) computers, and lighting applications. Rather than being fabricated from silicon, organic semiconductors (OSCs) are predominantly made of carbon and present a number of advantages over their inorganic counterparts. However, while these materials, which range from small molecules to polymers, are now the basis of a lucrative industry in electronic displays, many promising applications, such as photovoltaics, remain largely untapped.

1.1.1 APPLICATIONS AND LIMITATIONS

The semiconducting properties of OSCs come from the molecule's conjugated backbone; that is the alternating single and double bonds that extend across the entire molecule. This conjugated backbone allows OSCs to transport electrons efficiently, and absorb and emit visible light. While these charge transport properties do not make OSCs unique from conventional inorganic semiconductors, their organic nature means that they can be readily processed from solution, allowing for cheap and energy efficient device fabrication. As only thin films are required to create functional devices, these materials are amenable to processes such as printing onto flexible substrates.[2,3] This has the ability to decrease production costs, and to lead to novel applications in lightweight and flexible electronics.[4,5]

Despite these advantages and potentially useful applications, the uptake of OSCs has been relatively slow, and device efficiencies remain lower than for inorganic equivalents. One of the largest impediments towards faster progress is the difficulty of predicting behaviour – either in solution or the liquid phase – from the chemical structure of the constituent molecules. This is related to the interactions between OSC molecules: unlike in inorganic materials, intermolecular interactions in OSCs are typically weak non-covalent forces, giving behaviour that is much more variable and challenging to predict. Thus, a fundamental understanding of the physical principles that drive processes such as solution-phase aggregation, or molecular alignment at interfaces, would be useful in moving towards the rational design of high performing OSCs for commercialisable applications.

1.1.2 STRUCTURES: SMALL MOLECULES AND POLYMERS

As the only common feature required for functional OSCs is a conjugated backbone, and possibly a degree of solubility in common organic solvents, there are a wide variety of molecular structures that have been employed effectively. These molecules can be broadly classified into small, discrete molecules, and polymers. Whether small molecule or polymeric, most OSCs consist of a conjugated, often fused ring, system, which has low solubility in the typically-aromatic common organic solvents. Alkyl side-chains are therefore often employed to increase solubility. The chemical structures of molecules and functional groups relevant to this work are shown in Fig. 1.1.

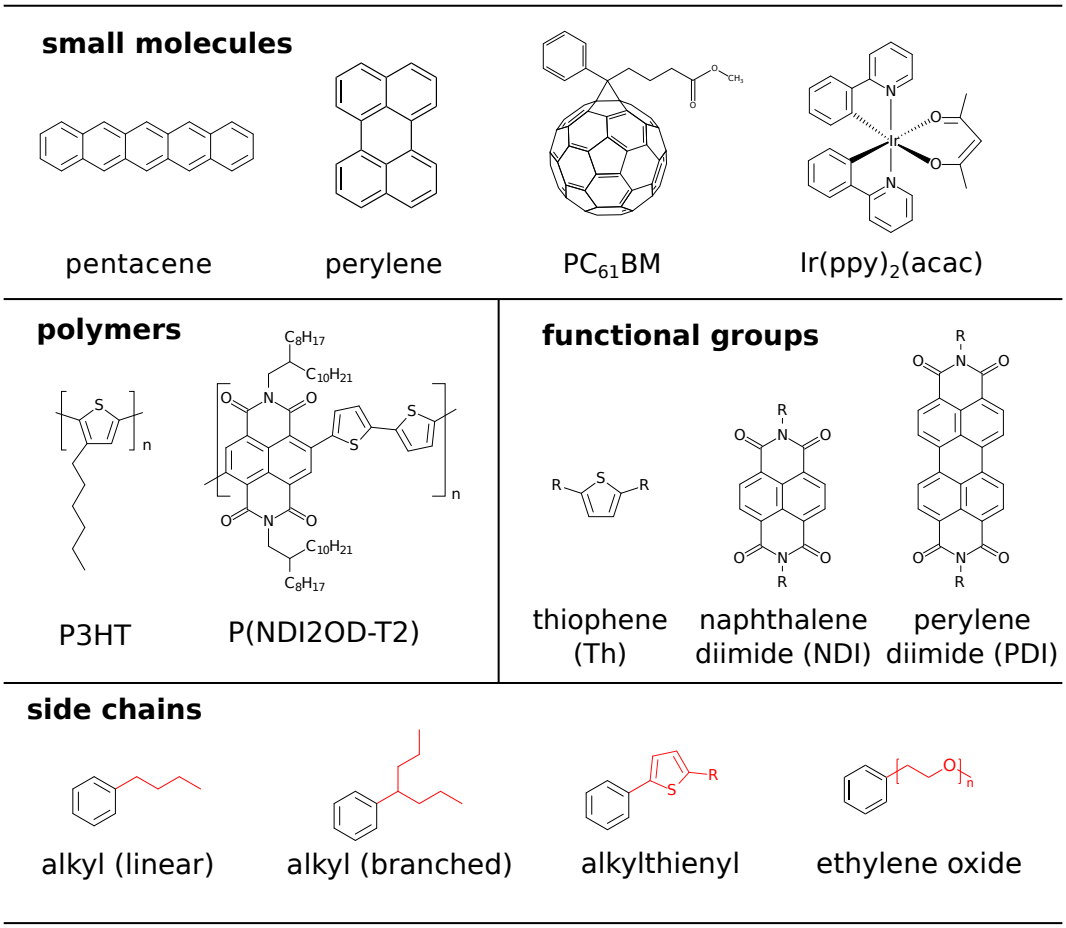

Fig. 1.1 Chemical structures of a number of molecules and functional groups relevant to this work. Ellipsoidal particles based on perylene are studied in Chapter 3, and P(NDI2OD-T2) is studied in depth in Chapters 4 and 5.

As OSCs generally feature a planar, conjugated backbone, they are able to form ordered, π-stacked structures with good orbital overlap. This results in an efficient charge transport pathway perpendicular to the plane of the conjugated backbone.

Nevertheless, charge transport in the π-stacking direction is on the order to 10–100× slower than along the polymer backbone.[6] The alkyl side-chains that many OSCs feature in order to improve solubility are insulating in nature, meaning charge transport through these side-chains is negligible.

1.1.3 Importance and control of microstructure

Although a variety of device architectures are used, the active layer of OSC-based devices can be simply considered as a thin film of OSC material (on the order of 100s of nm thick), interfacing with either a solid dielectric, another semiconducting material, or a vapour phase (Fig. 1.2). As charge-transport rates depend on the alignment and arrangement of OSCs (the microstructure), the behaviour of molecules both in the bulk and at any interfaces is important for improving device performance. At interfaces, many examples, both experimental (e.g. refs 7–10) and computational (e.g. refs 11–15), of semiconducting molecules displaying preferential alignment can be found in the literature, but few general rules for predicting interfacial orientation from chemical structure or processing conditions appear to exist. Many factors have been implicated in control of interfacial orientation, including, among others, molecular shape,[14,16–18] the presence, length, and composition of side chains,[8–10,19] backbone planarity,[20] temperature,[14,15,17] and solvent choice.[14,20,21] Understanding the reasons behind these factors is important for the rational design of high performing organic semiconductors.

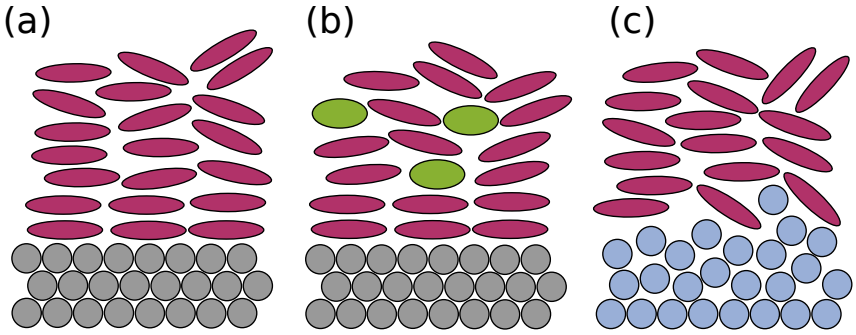

Fig. 1.2 Schematic of general OSC interfaces: (a) semiconductor-dielectric interface for organic field-effect transistors (OFETs); (b) semiconductor host-guest mixture on a substrate for organic light-emitting diodes (OLEDs); and (c) bulk-heterojunction electron donor-acceptor interface for organic photovoltaics (OPVs). Image from ref 1.

While the interface alignment can be used to template the bulk thin film behaviour, the bulk microstructure can also be influenced by modifying the backbone, side-chains, or solvent. Depending on the choice of molecular and system properties, the thin-film microstructure can range from amorphous, to predominantly disor-

dered with small regions of crystallinity, to fully crystalline.[22–25] While it was long assumed that high crystallinity was necessary for high performance, more recent work has shown that small crystalline regions connected via long tie-chains are sufficient for good charge transport properties.[24,26] Although it remains difficult to predict, especially for polymers, the thin-film microstructure has been shown to depend on a number of factors, ranging from polymer molecular weight,[27–30] to side-chain composition and length,[9,31–33] backbone planarity,[34] chemical structure,[32,35–38] and processing conditions.[21,22,25,39–44] Of particular importance, and also influenced by, among others, these same properties, is the solution-phase behaviour of OSCs. Given that most OSC-based devices are fabricated using solution-processing methods, and that correlations have been reported between solution-phase behaviour, thin film microstructure, and device performance,[25] controlling the solution-phase behaviour is likely to be an effective means towards improving device performance. In the following sections we examine in more detail the properties that affect the behaviour at interfaces (Section 1.2) and in solution (Section 1.3).

1.2 CONTROLLING INTERFACE ORIENTATION

The interesting optoelectronic properties of OSCs arise from significant delocalisation of π electrons due to extended conjugation (alternation of single and double or triple bonds) in the molecular structure, as illustrated in Fig. 1.1. Accordingly, OSC molecules generally consist of highly anisotropic rigid subunits such as fused aromatic rings. This molecular shape anisotropy has consequences for the interfacial supramolecular assembly of OSCs, and optoelectronic processes, as detailed in this and the following sections.

The presence of an interface between a system of anisotropic particles with another phase (e.g. a gas, solid, liquid) breaks the translational symmetry of the system and can induce orientational ordering at the interface, even when the bulk phase is isotropic. For a collection of biaxially anisotropic particles, in which each particle has three inequivalent principal axes, the possible preferred orientations with respect to the interface can be classified into three extremes – end-on, face-on, or edge-on (Fig. 1.3) – with the actual orientation for a specific system possibly being intermediate between these extremes. For conjugated molecules such as OSCs, variations in the preferred orientation will change the orientation of the π-stacking direction with respect to the interface, which has implications for exciton and charge dynamics.

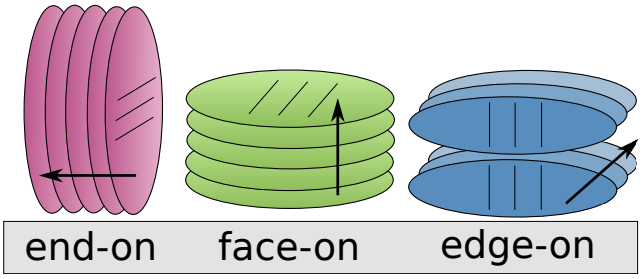

Fig. 1.3 Classification of orientations of a collection of biaxially anisotropic particles with respect to a surface. Arrows indicate the direction of the shortest molecular axis, which is generally the π-stacking direction in organic semiconductors. The surface is shown in grey. Image from ref 1.

1.2.1 Role of interfaces and supramolecular assembly

It has long been known that molecular anisotropy at interfaces is important for enhancing charge transport and device performance, with Sirringhaus et al.[45] reporting significantly higher field-effect transistor (FET) mobility with edge-on orientations of poly(3-hexyl thiophene) (P3HT) than face-on orientations of the same molecule over 20 years ago.[45] Since then, many studies of have found similar correlations between orientation and device performance for OLED,[46–49] OPV,[7–9] and OFET[25,50,51] devices. In general, in-plane alignment of the transition dipole moment of emitter molecules with respect to the substrate gives better optical properties in OLEDs,[46] a face-on alignment at donor–acceptor interfaces appears to be generally preferred for good performance in bulk heterojunction (BHJ) OPVs,[7–9] and edge-on alignment is found in most high-performance OFETs,[45,52] although face-on structures may still give good mobility in some cases.[53,54] It is therefore important that alignment at these interfaces can be controlled. In the work presented in Chapter 3, we are primarily concerned with the orientation at the interface with a solid substrate or vapour phase, which are of particular importance for the performance of OFETs.

In organic transistors, charge transport occurs in an OSC material that has been deposited onto the surface of a dielectric, with transport restricted to an accumulation layer within a few nm of the semiconductor–dielectric interface.[55–58] The microstructure at this interface therefore has a significant effect on the charge-carrier mobility, which is the key performance metric of OFETs, and also plays an important role in OLEDs and OPVs. Indeed, a linear correlation between molecular tilt angle at the interface and OFET saturation mobility has recently been shown.[25] Additionally, a number of studies have shown that, although semicrystalline semiconductors show similar charge mobilities on different dielectric surfaces, the mobility of amorphous semiconductors depends strongly on the properties of the dielectric.[54,59–62] Thus,

understanding the structures at the interface, which can differ significantly from that in the bulk,[27,63] is important for improving device performance. The many studies on bulk morphology are, therefore, not necessarily relevant for correlating electronic processes and morphology in these devices.

The orientational order (edge-on or face-on) and, for polymers, the direction of the backbone with respect to the source and drain electrodes play a significant role in organic transistor performance. An edge-on alignment to the dielectric surface, where the π-stacking direction is parallel to the substrate, is expected to enhance charge mobility. This is due to the much higher mobility of charge carriers in the π-stacking direction, related to the substantial overlap of the π-orbitals, than through the insulating aliphatic chains (Fig. 1.4), which would occur in a face-on orientation.[64] For polymers, a backbone direction parallel to the charge-transport direction (i.e. between source and drain electrodes) will give the fastest charge transport, as charge carriers can move along the backbone (Fig. 1.4);[64] however, this will be a function of chain length as shorter polymer chains will require more interchain hops along this direction.[64] On the other hand, small molecules give the greatest performance when the π-stacking direction is the same direction as charge transport, as this facilitates hopping between adjacent small molecules in the desired direction.[65] Indeed, when methods that induce order in certain directions are used for the generation of films, highly anisotropic charge transport has been observed.[66,67]

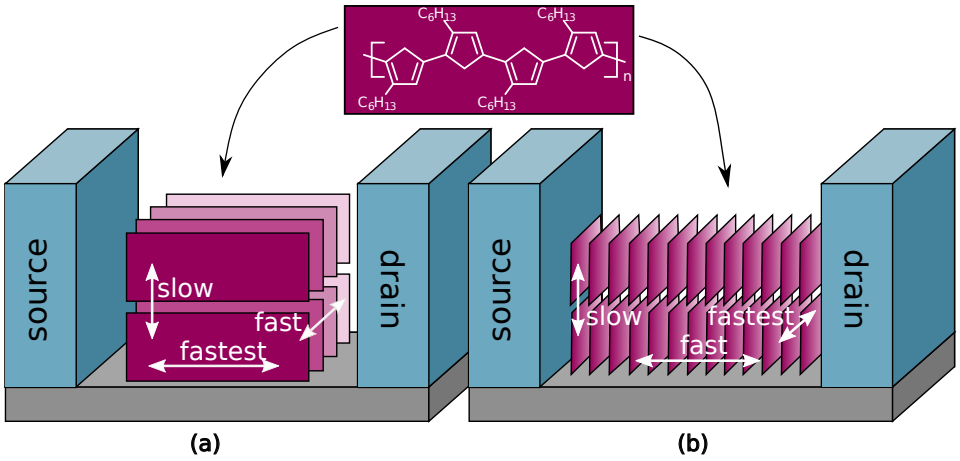

Fig. 1.4 Architecture of a bottom-gate bottom-contact OFET at the dielectric interface. Polymers are shown in an edge-on conformation with backbone either (a) parallel or (b) perpendicular to the required charge transport direction. Charge transport is fastest along the polymer backbone, slower, but still fast, in the π-stacking direction, and slowest along the lamellar stacking direction. Image from ref 1.

A number of factors have been shown to influence edge-on versus face-on orien-

tation with respect to the dielectric interface, ranging from the molecular weight (for polymers),[26,27,68] to the side chain[16,51] and backbone[16,20] structure, the substrate composition,[11,16,52,67,69,70] deposition technique,[64,66,71,72] and the solubility of the material.[16,20,21,25,27,67,73]

1.2.2 THEORETICAL BACKGROUND

Orientational ordering of anisotropic particles at interfaces has long been studied, particularly in the domain of liquid crystals,[74] in which experimental, theoretical, and computational studies on this topic have been extensively reviewed.[75–78] Most of this work has focused on the equilibrium behaviour of single-component fluids of uniaxial mesogens, in which each molecule has one inequivalent and two equivalent principal axes. Thus, the full complexity of OSC systems, which often comprise multi-component blends of biaxial molecules whose microstructure is formed under non-equilibrium conditions, cannot be fully understood based on these studies. Nevertheless, this extensive body of work provides a basic conceptual framework for understanding interfacial alignment of OSCs.

One general finding of studies of liquid crystals is that the direction of interfacial alignment is non-universal,[77,79] and depends on the details of the intermolecular interactions, such as the competition between anisotropic repulsive and attractive interactions.[80] Nevertheless, some general trends can be gleaned from theoretical and computational studies of model liquid crystal interfaces.

Most theoretical and computational studies have focused on either the liquid–vapour interface or the nematic–isotropic interface between coexisting nematic and isotropic liquid phases of a single-component fluid. For purely repulsive intermolecular interactions, orientational ordering is governed by excluded-volume entropic effects, which result in perpendicular alignment of prolate molecules at the free (vapour-like) interface.[79,80] Note that although purely repulsive particles do not have coexisting liquid and vapour phases, a liquid-vapour-like interface can be stabilised by an external field acting perpendicular to the plane of the interface. On the other hand, for molecules with both (short-range) repulsive interactions and (longer-range) attractive interactions, various alignments are obtained depending on the anisotropy of the molecular shape and interaction strength. Most molecular simulations of liquid crystals with attractive interactions have used the Gay-Berne (GB) potential,[77,81] which is a general anisotropic potential energy function that depends on the relative position and orientation of pairs of ellipsoidal molecules. For a uniaxial molecule, the molecular shape anisotropy in the GB potential is characterised by the parameter κ, which is the ratio of the molecule length to breadth, while the interaction strength anisotropy is characterised by the parameter κ', which is the ratio of the attractive well depth for side-to-side versus end-to-

end interactions. For both prolate[82–84] and oblate spheroids[84] over a range of temperatures and κ and κ' values, alignment at the vapour interface has been shown to be controlled by the κ/κ' ratio, with $\kappa/\kappa' > 1$ yielding planar (parallel) alignment and $\kappa/\kappa' < 1$ giving perpendicular alignment. This behaviour was rationalised based on the relative energies of different cleavage planes of close-packed ordered arrays of molecules. This essentially amounts to the exposed interface being the one with the lowest interfacial tension, and suggests that interfacial ordering is energetically rather than entropically controlled by the parameters chosen in these systems.

Compared with the vapour interface, orientational ordering of a liquid crystal at a solid interface is complicated by the influence of the interaction with the solid. Thus, theoretical and computational studies of this situation have been more limited and a general theoretical understanding is lacking.[76] For purely repulsive hard-core interactions between prolate molecules and with a solid surface, entropic excluded-volume effects favour planar alignment with the surface,[85] opposite to the perpendicular alignment found for similar molecules at the vapour interface.[80] Similarly, semiflexible polymers, which in a sense can be considered highly anisotropic prolate molecules, confined by a repulsive solid surface tend to align parallel to it.[86] For molecules with both repulsive and attractive interactions with each other and with the solid substrate, the interfacial ordering depends on the details of the substrate–molecule interaction strength and anisotropy.[87] For example, planar anchoring is observed for strong coupling between model GB ellipsoidal particles and a solid substrate at which the substrate–molecule interactions favour this alignment. These effects are summarised in Fig. 1.5.

The behaviour of anisotropic particles at the interface with another fluid is also important, with these interfaces being found, for example, in BHJ OPVs. Fluid–fluid interfaces, will not, however, be examined in this work, so we refer the interested reader to our recent review,[1] and to theoretical studies on this type on interface[88,89] for more details.

1.2.3 Towards general principles for controlling interfacial orientation

As noted in the previous section, the orientation of semiconductors with respect to their interfaces is an important property for improving performance in a variety of organic-electronic device types. This is important in organic transistors as described above, but also in BHJ organic solar cells and OLEDs. Many factors have been shown to influence the interfacial orientation of OSCs, ranging from material properties (that is the properties of the molecules themselves, either semiconductor or substrate and solvent), to the processing conditions for device fabrication. As they are not relevant to this work, we will not discuss in detail properties such as elemental composition[7,10,90] and side-chains,[8,9,16,19] nor polymer-

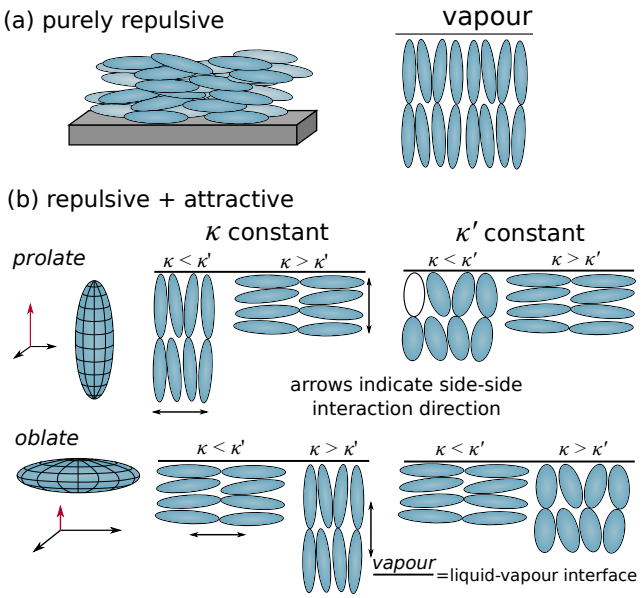

Fig. 1.5 (a) Orientation of (left) hard rods at the interface with a solid substrate, or (right) a vapour. An ellipsoid with purely repulsive interactions has been shown to have a preference for parallel alignment at the solid interface, and perpendicular at the vapour. Note, again, that a system of purely repulsive particles does not have a coexisting liquid-vapour interface, but this kind of interface can be stabilised by an external field acting perpendicular to the plane of the interface. (b) Orientation of an ellipsoid, having both attractive and repulsive interactions, at the interface with its vapour. For an ellipsoid at the vapour interface, increasing the side–side interaction strength (decreasing κ', left) or increasing aspect ratio (increasing κ, right) gives a parallel orientation for both prolate (top) and oblate (bottom) ellipsoids. The red arrow indicates the axis that defines orientation. The direction perpendicular to this defines the side–side direction. Image adapted from ref 1.

specific factors[10,27,30,68,91–96] or processing conditions[10,12,14,15,17,48,66,97–104] and non-equilibrium methods,[64,66,72,105–112] though they are undoubtedly important. For a more thorough breakdown of the different properties that affect interfacial orientation, we refer the reader to ref 1, and to the review of Osaka et al.[10] for more detail of OSC polymers. We will, however, examine the effect of shape and interaction anisotropy as these are of relevance to subsequent chapters.

1.2.3.1 Shape anisotropy

As explained in Section 1.2.2, hard prolate particles with purely repulsive interactions preferentially align perpendicular to a free (vapour-like) interface,[79,80] and parallel to a solid interface[85] due to excluded-volume entropic effects (Fig. 1.5). This type of behaviour has been observed experimentally in a number of real systems for a range of molecules of different shapes and lengths. Studies of vapour deposition, in which molecules were deposited from the gas phase onto a solid substrate, have

shown that rods of various lengths prefer to orient perpendicularly to the vapour interface following deposition.[14,17,100,102] The orientation preferences described are not unexpected, having been shown to be the preferred orientation for purely repulsive prolate particles. Given that the influence of attractive interactions is expected to effect orientational preference,[83,84] it is interesting to note that all of the molecules studied exhibited the same alignment behaviour. Coarse-grained molecular simulations of particles parameterised just to reproduce molecular shape have shown similar trends to both experimental and all-atom simulations,[15,17] indicating that molecular shape is an important parameter for determining orientation at the vapour interface. In addition, longer molecules have been shown, through computational studies, to show stronger orientational anisotropy than their shorter counterparts,[14,17] again pointing to a strong dependence of interfacial orientation on shape anisotropy.

1.2.3.2 Intermolecular interactions

As discussed in Section 1.2.2, changes to non-bonded (attractive) intermolecular interactions for fixed molecular-shape anisotropy can lead to dramatic changes to surface anchoring (e.g. from planar to perpendicular). Thus, these interactions are expected to strongly influence molecular orientation at OSC interfaces. Strong attraction between the face of an OSC and a solid or another molecule would give a face-on orientation, whereas if the interactions between the face of the conjugated molecule and the substrate were unfavourable, or the interactions of the substrate with the molecules edges stronger, an edge-on orientation would be preferred. This is consistent with reports from molecular simulation of a semiconducting polymer at different solid interfaces where low substrate–semiconductor interaction strength gives edge-on oriented polymers and high interaction strength gives face-on.[11] In addition to influencing the orientation at the interface, the strength of the attractive interactions can also influence the distance from the interface to which the orientational order is maintained, with stronger van der Waals (vdW) interactions between substrate and semiconductor having been shown to give a thicker oriented interface.[14]

In the OSC field, intermolecular interactions at interfaces are often characterised in terms of surface energy. Correlations between substrate surface energy and interfacial alignment have recently been observed for semiconducting polymer films, with lower surface energy associated with a more edge-on interfacial orientation than a higher energy surface.[113] This is consistent with favourable interactions between the polymer alkyl side-chains with the similar side-chains of a low-energy self-assembled monolayer (SAM)-treated surface, which is maximised in the edge-on orientation. Similar behaviour has also been observed in simulation studies of a

semiconducting oligomer in solution at various interfaces: if interaction between the π-conjugated plane (face) of the molecule was more energetically favourable than the interactions of the same plane with the interface (either gas phase or solid), the edge-on configuration was preferred, and vice versa.[11]

1.2.4 SUMMARY

From the preceding discussion, it should be clear that, although there are many factors which have been shown to influence interfacial anisotropy of OSCs, many of them have not yet been systematically studied. Although some interesting trends are starting to emerge, further study is required if general principles for controlling molecular alignment at semiconductor interfaces are desired. The orientation of uniaxial repulsive particles at the vapour interface, and to a lesser extent solid and fluid interfaces, is fairly well understood, however the role of attractive interactions, which are important for real materials, and the balance between repulsive and attractive interactions, is less clear. A better understanding of these interactions may enhance our understanding of the preferential alignment observed in relation to modifications such as aggregation, and backbone structure.

Although many OSCs can form liquid crystalline phases, the behaviour of particles in a solution, which is the most relevant phase for OSC-device fabrication, will not necessarily be captured by general theories of these anisotropic phases. Additionally, interaction parameters in the past have not typically been chosen to represent OSCs, and although many of the parameterisations may fall within the range reasonable for these types of molecules, there is no guarantee that OSCs will behave in a manner consistent with previous studies. The work presented in Chapter 3 addresses a number of these issues by looking at the behaviour of isotropic liquids of disk-like particles with shape and interactions chosen to be representative of a wide range or OSC small molecules at both the solid and vapour interface.

1.3 CONTROLLING SOLUTION-PHASE STRUCTURE

As solution processing methods are common in the production of organic-electronic devices, solvent is a simple parameter to tune, and is known to have a significant effect on polymer conformation. It has been proposed that high mobility in polymeric semiconductors can be achieved using poor solvents that induce a greater degree of pre-aggregation (aggregation in solution prior to deposition on the substrate), as these can give enhanced liquid-crystalline ordering,[21] which is generally associated with more regular alignment. Even for non-liquid-crystalline materials, the forma-

tion of large aggregates has been observed to give rise to edge-on orientations at the substrate interface.[16,66] The larger the aggregate, the greater the effect and the stronger the preference for edge-on structures.[66]

Given the correlations between solution-phase behaviour and thin-film microstructure, both in the bulk and at interfaces,[16,22,25,38,66,114] it is important to understand how the molecular properties and solvent affect the solution-phase behaviour/structure, particularly for polymers. As device performance is related to the active layer morphology,[25,26,38,45,53,62,115–118] simple methods for tuning this morphology, such as the choice of solvent or concentration, are valuable for enhancing the efficiency of OSC-based devices. Indeed, the solution-phase structure of semiconducting polymers has been directly correlated to thin-film structure, and performance.[6,25] Tuning of this microstructure through changing the solvent quality has been shown to affect the optoelectronic properties of OSC-based materials.[114,119,120]

1.3.1 Effect of molecular properties on solution-phase structure

For OSC polymers, the relationship between properties such as backbone planarity and molecular weight, and device performance, has been well studied. For example, increasing the planarity of the backbone has been shown to enhance charge transport along the backbone, effectively increasing the conjugation length.[34] Molecular weight has also been shown to influence crystallinity, with higher molecular weight chains of OSC polymer P3HT decreasing the crystallinity.[28] In fact, many polymers appear to have an optimal molecular weight for achieving peak device performance. In some cases, intermediate molecular weights have been found to give the best performance,[28,29,121] attributed to the presence of chains sufficiently long to bridge the crystalline regions in a disordered aggregate structure[6,24] without the disordered regions becoming too large and separated.[28] However, it has also been shown that, for OSC polymer P(NDI2OD-T2), performance increases with decreasing molecular weight, with the lowest molecular weight polymers giving the greatest performance.[27] This was proposed to be due to less aggregation of the shorter chains, which enhances the liquid-crystalline order of the solution and is translated into a more ordered morphology.[27] The dependence of polymer microstructure on molecular weight therefore appears to be highly system specific.

In addition to molecular weight and backbone planarity, modification of the side-chains can also influence microstructure for OSC polymers, and accordingly the charge mobility.[32,118,122–124] Tuning the side-chain length and placement,[118,122–124] or replacing bulky branched chains with linear ones,[31,32,118,124–126] can change polymer packing, potentially leading to more ordered domains. Alternatively, different functional groups can be incoporated into the sidechains, which may

enhance the interactions between polymer chains, also influencing the packing of these molecules.[8,9,32,126]

1.3.2 IMPORTANCE OF SOLVENT

For all polymers, whether OSC or not, the behaviour in solution can generally be explained in terms of the relative strength of the interactions between polymer and solvent. In good solvents, in which the strength of the polymer–polymer attractive interactions are weaker than the polymer–solvent attractions, polymers are expected to form extended coil structures. At the other end of the spectrum, in poor solvents, in which the polymer–polymer or solvent–solvent attractive interactions are stronger than the polymer–solvent, more compact, globular, structures are expected. This will be discussed in more detail in Chapter 2.3.

A simple predictor for polymer solubility is the Flory-Huggins interaction parameter, which, based on the relative strength of the solvent–solvent, solvent–polymer, and polymer–polymer attractive interactions, predicts the solvent quality, ranging from good to poor, for a particular solvent–polymer pair.[127] This theory, which is described in detail in Chapter 2, has been successfully applied to OSC polymers in the past,[128–130] predicting aggregation behaviour consistent with experiment. However, recent studies of OSC polymer P(NDI2OD-T2) have shown the formation of rod-like aggregates, with sizes up to an order of magnitude larger than a fully extended single chain, in poor solvents, which are not predicted by any existing theories.[25] We propose that this behaviour is due to the stability of partially overlapping chains in poor solvents, which leads to the build-up of extended aggregates in a brick-works like fashion. This kind of aggregation, which gives a kinetically trapped aggregate rather than the fully-overlapping thermodynamic minimum, has not been previously reported, and will be discussed in detail in Chapter 4.

Related to the effect of flexibility and solvent quality, a number of studies have looked at the behaviour of general semiflexible polymers in solution, developing phase diagrams for single-,[131–133] and multi-chain[134] aggregation. With the exception of the recent work of Cohen et al. [132] these studies have employed bead-spring type models with spherical sites, which cannot capture the typical π-stacking behaviour of OSCs. Despite this, they provide useful insights into how semiflexible polymers aggregate, both as a single chain and with other chains. Single-chains show a variety of stable knot phases, hairpins, and extended rod-like or ideal-chain structures.[131–133] The preferred structure has been shown to depend on the backbone flexibility and solvent quality (or, equivalently, temperature) with more compact/folded structures being preferred at higher flexibilities and lower solvent qualities (lower temperatures). For multichain aggregates, a similar relationship

was observed between solvent quality (or temperature), backbone flexibility, and the structure of the aggregate.[134]

The single-chain behaviour of semiflexible polymers – a class of polymers encompassing many OSCs as well as important biological molecules such as DNA – has been well studied by simulation[131–133,135–139] and theory.[140–144] A number of studies have examined the effect of backbone flexibility and interaction strength (equivalent to solvent quality and temperature),[131–133,139,140] or just the backbone flexibility,[135,143] on the folded structure, the kinetics of the folding process,[133,137,138] or the effect of properties such as charge,[136] shape of monomer units,[139] or chain length[144] on the final collapsed structure. The effect of stiffness,[138] chain length,[138,141] and interaction strength[142] on the folding kinetics, and the mechanism of folding[144] have also been examined.

Although the single-chain behaviour of semiflexible polymers appears to be generally well understood, how this translates to the behaviour of multi-chain systems, in which the systems are far from the infinite dilution of an equivalent single-chain system, is not as well studied. The effect of backbone stiffness and interaction strength on the equilibrium aggregate structure of generic semiflexible polymers has been previously studied,[134] showing a variety of different multi-chain aggregate structures, ranging from compact globules at high flexibility, to licorice-like twisted rods for stiffer chains. However, it should be emphasised that this model used spherical beads, which do not capture the π-stacking interactions that characterise the aggregation of OSCs. Nor did it address how non-equilibrium processes may affect the aggregation pathway. Both of these factors are examined in the work in Chapter 4. Nevertheless, multi-chain aggregation is expected to be a possible pathway for OSC polymers in solution, with the preference for no aggregation, single-chain folding, or multi-chain aggregation expected to be related to the solvent quality (or, equivalently, strength of intermolecular interactions), backbone flexibility, and polymer concentration in solution. In Chapter 4, we have proposed some novel relationships between backbone flexibility, chain length, polymer concentration, and the relative degree of single-chain and multi-chain aggregation, which provide a powerful means of tuning aggregate structure.

1.4 SIMULATION OF ORGANIC SEMICONDUCTORS

The work presented in the following chapters uses molecular simulation to examine the behaviour of OSCs under different conditions, both in solution and in the liquid phase at interfaces.

At interfaces, as the microstructure in OSC devices is known to be important for device performance, being able to characterise this microstructure and its rela-

tionship to electronic processes would facilitate the design of higher performing devices. Although possible, it is often experimentally challenging to characterise these interfaces as they are generally buried within the device.[115,145] Additionally, it is difficult, if not impossible, to extract molecular-level detail from experimental data of OSC films due to their significant disorder. With the ability to directly simulate and visualise these interfaces on an atomic scale, computer simulations are an attractive method for uncovering the intricacies of structure and assembly mechanisms of OSCs at interfaces. Since most of the computer-simulation techniques discussed in this section and their general use to study OSC morphology have been comprehensively reviewed previously,[146–148] the techniques themselves will only briefly be described here, with the focus being on applications that clarify the role of interface anisotropy or solution-phase behaviour. Techniques that are relevant to the work in subsequent chapters will be discussed in more detail in Chapter 2.

In terms of solution-phase behaviour, experimental characterisation is more straightforward than at interfaces. However, while experimental techniques can give good detail of monomers, it is often difficult to understand, from the measurable end result, what processes or interactions are important for achieving the observed behaviour. Molecular level detail of the solution-phase polymer structure – whether the structure of an aggregate or a free chain – also cannot be obtained from experiments. It therefore becomes difficult to generalise these results to other molecules, leading to an absence of general understanding of why different molecular properties result in different microstructures. Techniques such as molecular dynamics (MD), a classical simulation technique (see Chapter 2.1 for details) are particularly useful for examining solution-phase behaviour as they can directly show, albeit on a much shorter timescale, the behaviour of all OSC and solvent molecules (or a subset of these particles) in the system. This can provide insights into the specific interactions that may be important for the equilibrium behaviour, which are generally not obtainable through even high resolution experimental techniques.

A distinction should be made here between atomistic (all-atom (AA)) and coarse-grained (CG) particle-based simulations. In AA simulations, which are used in the work in Chapter 5, every atom is treated explicitly, whereas CG models, such as those used in Chapters 3 and 4, group atoms together into a single interaction site. This grouping decreases the degrees of freedom of the system at the expense of atomic resolution with the goal of reducing computational expense. The application of both methods to the study of OSC behaviour will be discussed in the following sections, and details on the specifics of the techniques in Chapter 2.

We also briefly note that lattice-based models are an interesting alternative to the off-lattice models that are used in this work, and have been used in the past to model amyloid aggregation and protein folding (e.g. refs 149, 150), processes

which are likely to share many characteristics with the aggregation and folding of OSC polymers. However, aggregates formed by OSC polymers are typically highly anisotropic, with aggregation predominantly occurring in the π-stacking direction. For this kind of aggregation to be modelled effectively with a lattice-based model, the orientation of the lattice sites would need to be included, resulting in a model that is likely just as complicated as an off-lattice model, with the additional disadvantage of potentially predisposing the system to forming particular types of aggregates. For these reasons, only off-lattice methods will be considered further in this work.

As an intermediate between lattice methods and continuous MD, discontinuous MD, in which the inter-particle interactions are represented by square-well potentials, is another interesting alternative to the off-lattice, continuous MD simulations used in this work. This model, whilst still being an off-lattice method, can lead to significant speed-up relative to continuous MD as particle positions and velocities only need to be calculated when discontinuities in the potential are reached (e.g. when particles collide), and has been used successfully in the past to predict peptide aggregation (e.g. refs 151, 152). However, these methods are not widely implemented, and may be difficult to parameterise for OSC molecules, limiting their use. Additionally, the continuous LJ potentials used in this work are no more complex than discontinuous square-well potentials, both being characterised by a single length scale and a single energy scale. There is, therefore, little to be gained in terms of the speedup that may be expected if using a simpler potential.

1.4.1 ALL-ATOM SIMULATIONS

The use of AA MD simulation to study the physical structure and assembly at OSC interfaces is becoming more common as computational power increases. In particular, the process of vapour deposition has been extensively studied by MD for a variety of substrates and small molecules[13–15,49,97,153–157] (Fig. 1.6). While these simulations generally agree well with experimentally observed phenomena, such as the dependence of orientation on substrate temperature (T_{sub}), they also provide further insight into the mechanisms of the process with a level of detail that is difficult, if not impossible, to obtain from experimental techniques.

As for solution-phase behaviour, Jackson et al. [24] have used AA simulations to study a wide variety of OSC polymers in order to determine how aggregation occurs in solution. They observed a number of different conformational classes over a variety of conjugated polymers, with the final aggregate structure dependent on properties such as backbone linearity and dihedral distributions.[24] This work predominantly used implicit solvent calculations, in which the polymer was modelled atomistically and the solvent treated as a background dielectric. This greatly

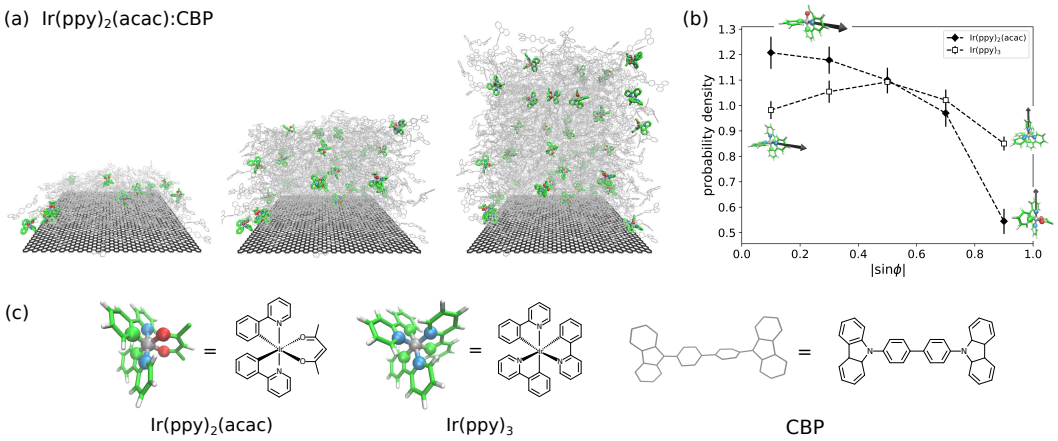

Fig. 1.6 (a) Snapshots of a simulation of vapour deposition of a host–emitter OLED system onto a graphene substrate (black, thick line representation).[49] The host is CBP (grey lines) and the emitter is $Ir(ppy)_2(acac)$ (green). Hydrogens are omitted for clarity. (b) Transition dipole moment (TDM) orientation for $Ir(ppy)_2(acac)$ (filled diamonds) and $Ir(ppy)_3$ (unfilled squares) from deposition simulations.[49] A value of $|\sin\phi|$ of 0 corresponds to horizontal alignment of the transition dipole moment and 1 to vertical, as shown in the overlaid structures. The TDMs for both molecules are assumed to lie along the Ir–N bonds. In the structures, only one TDM is shown for clarity as a black arrow. (c) Chemical structures of $Ir(ppy)_2(acac)$, $Ir(ppy)_3$, and CPB. For the iridium complexes: green = carbon, blue = nitrogen, red = oxygen, grey = iridium, white = hydrogen. The molecules in (a) are coloured accordingly. Image from ref 1.

enhances the efficiency of the calculations, especially when the property of interest is the equilibrium aggregate structure, but will not necessarily accurately capture the folding dynamics. In order to study the equilibrium aggregate structure, they also biased the system towards folding to avoid the kinetic traps of other aggregate structures, noting that other enhanced sampling methods would also be useful in this regard.[24]

Flory-Huggins parameters, which are a simple predictor for the solubility of molecules in a two-component mixture, can be readily calculated from AA MD simulation if a number of assumptions are made. The first of these is Flory-Huggins theory is based on a lattice model in which the size of the lattice sites for both components of the mixture are equal, which is not the case for most polymer–solvent mixtures. As OSCs are generally much larger than solvent molecules, and MD is inherently an off-lattice model, this is a significant assumption, particularly when polymers are considered, as has been done in the past.[128–130] Nevertheless, the relative values of the calculated Flory-Huggins parameters, comparing different solvents for the same polymer, are generally qualitatively consistent with the relative solubility measured from experiments.[128–130] This simple predictor can therefore give interesting insight into the effect of solvent choice on polymer behaviour. As

typically only the per-site interaction energies in pure polymer, solvent, and a mixture (where polymers are not aggregating) are required, relatively short simulations of small systems can be used, as these per-site quantities are not expected to vary significantly with system size. The use of smaller systems means that these kinds of simulations are much more accessible to AA methods, whilst still giving predictions that have been shown to be generally applicable to the behaviour of much larger systems.[130]

1.4.1.1 Challenges for all-atom simulations

Although simulations of up to 100 million atoms (for 100 ns),[158] or up to the millisecond timescale for smaller systems using specialised hardware,[159] are possible, typical simulations can only study a couple million atoms on the nanosecond (or microsecond at best) timescale. This means that slower processes occurring on longer timescales are not able to be explicitly studied. This is particularly relevant when considering the scale of structural variations at interfaces, which generally involve large systems whose assembly occurs over long time periods, which can be infeasible to simulate atomistically. AA simulations of polymers have also generally been limited to chain lengths of 10s of monomers, which is often 1–2 orders of magnitude smaller than those studied experimentally in OSC systems, limiting the ability to realistically capture polymer microstructure using such models.

In order to deal with the problems of size and time scale, while still maintaining atomistic detail, a number of approaches may be taken, potentially at a cost to quantitative accuracy. Simulating at higher concentrations than used in experiments,[160] artificially freezing the motion of particles that are not deemed to be relevant for the processes of interest,[155,156] or modelling processes that are expected to display faster dynamics but similar equilibrium behaviour to the process of interest[12] have all been attempted in the past.

Simulation of solution-phase behaviour, particularly of polymers, is hindered by the system size, which must include both solvent and solute molecules. Polymers for OSC applications are often prepared in relatively dilute solutions (on the order of 0.1–10 g/L) meaning the vast majority of the simulated system will be occupied by solvent molecules. This effect is exacerbated as polymer length increases, as the cubic simulation box should have dimensions on the order of twice the length of the polymer chain in order to prevent both the polymer interacting with itself, and regions of solvent whose behaviour is influenced by the polymer from overlapping (see Chapter 2.1.1.6 for details on finite size effects). As polymer chains are often 10s to 100s of nanometers long, using explicit solvent AA models and realistic polymer chain lengths results in simulation boxes that are unfeasibly large. Because of this, there remain few examples of AA simulation of the solution-phase behaviour of

OSC polymers. Where AA simulations have been attempted, they have used a single chain,[128–130] multiple shorter chains,[24,130,161] or treated the solvent implicitly as a background dielectric rather than individual molecules.[24] With the exception of the work by Jackson et al. [24] and Reid et al. [161], these studies focused predominantly on calculating Flory-Huggins parameters, so required only short simulations (on the order of 5–10 ns) in order to calculate the energy of the system under conditions in which polymers were not aggregating. Though some analysis of the single-chain structure was attempted in ref 129, it is unclear whether these short simulations were sufficiently long to accurately obtain the equilibrium behaviour.

Structural evolution under conditions where aggregation can occur is expected to take place on much larger timescales than those required for calculating the energetics of unaggregated chains as required for the calculation of Flory-Huggins parameters. Studies of a single polymer chain in water have shown that for a relatively short chain (30 monomers) of flexible non-semiconducting polymer poly(N-isopropylacrylamide) (PNIPAM), the time taken to reach an equilibrium conformation is on the order of 600–700 ns, with more than 300 ns required post-equilibrium to sufficiently sample the equilibrium ensemble.[162] This adds challenges when considering processes such as single- or multi-chain aggregation as these long timescales are not achievable for all but the smallest systems. Furthermore, if one considers that the solution-phase, and eventual thin-film, structure and performance may depend on the polymer molecular weight,[27] which can range from 10s to 100s of monomers and is well beyond the size of systems that are feasible to simulate with AA models, it becomes clear that AA simulations are not ideal for obtaining an accurate understanding of polymer aggregation properties. Even for small molecules, studying processes that occur in solution, such as solvent evaporation for the formation of thin-films, require compromises to be made. Concentrations orders of magnitude higher than would be used experimentally have been used in the past[163,164] in order to reach the timescales required for the processes of interest. Even then, these large-scale simulations are still incredibly expensive.

When the equilibrium behaviour, rather than non-equilibrium processes or kinetics, that are of interest, a number of enhanced sampling methods can be used to circumvent some of the challenges associated with AA simulation. These methods apply various biasing techniques to promote sampling of regions of importance, and will be discussed in more detail in Chapter 2.1.5. These kind of methods have been used previously to determine, for example, the aggregation and folding mechanism of OSC polymers.[161]

1.4.2 COARSE-GRAINED SIMULATIONS

While AA simulations provide details of specific interactions at interfaces, and give an atomic understanding of the processes occurring at these interfaces, they are often limited by the size of the system and timescales of the processes of interest. A common way to address these problems is to use CG molecular simulations, in which the number of degrees of freedom in the system is greatly reduced by approximating a collection of atoms as a single interacting site, increasing the simulation efficiency. The coarse-graining process is described in detail in Chapter 2.1.2.2. It is especially important that larger length scales than are feasible atomistically to be reached when one considers, for example, the molecular weight dependence of interface morphology of polymer semiconductors[26,27,68,165] or the domain sizes in BHJs which are typically on the order of around 10 nm.[166] In contrast to AA simulations, CG simulations have been shown to be able to reach appropriate length scales with enough accuracy to model aggregation of conjugated polymer chains in solution[167] and phase separation in conjugated polymer BHJs[94,168,169] (see Fig. 1.7).

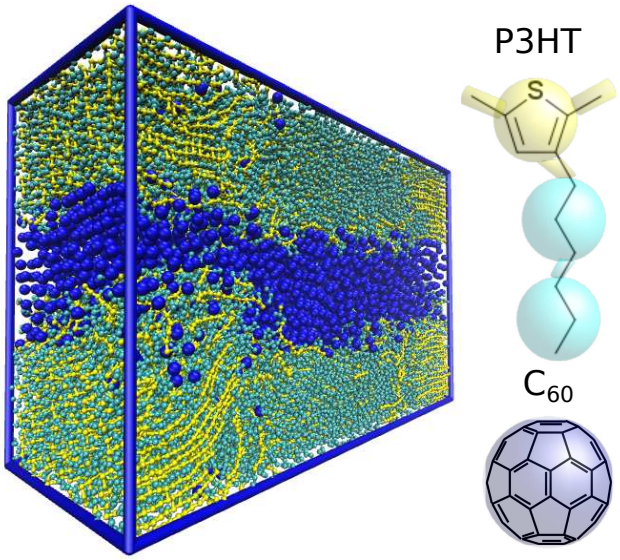

Fig. 1.7 BHJ P3HT:C_{60} donor–acceptor interface from CG MD simulation.[168] Image from ref 1.

Background of coarse-grained MD simulations. The process of coarse-graining is summarised schematically in Fig. 1.8. Groups of atoms expected to have correlated motion are grouped into larger sites whose interactions are parametrised to (hopefully) capture the behaviour of the real AA system. The total potential energy of the system is then calculated as a sum of bonded and non-bonded interactions between CG sites. Two general approaches have been used to parameterise CG interactions:

the top-down approach, in which interactions are chosen to reproduce experimental thermodynamic data,[169] or the bottom-up approach, in which the interactions are tuned to reproduce the physical and thermodynamic properties of an AA model.[170] A number of systematic bottom-up CG methods have been developed, with the goal being to achieve thermodynamic consistency between the CG and AA models, e.g. by matching forces[171] or structural distribution functions,[172] or by minimising the relative entropy[173] between the two models. Readers are referred to ref 170 for a comprehensive review of coarse-graining methods.

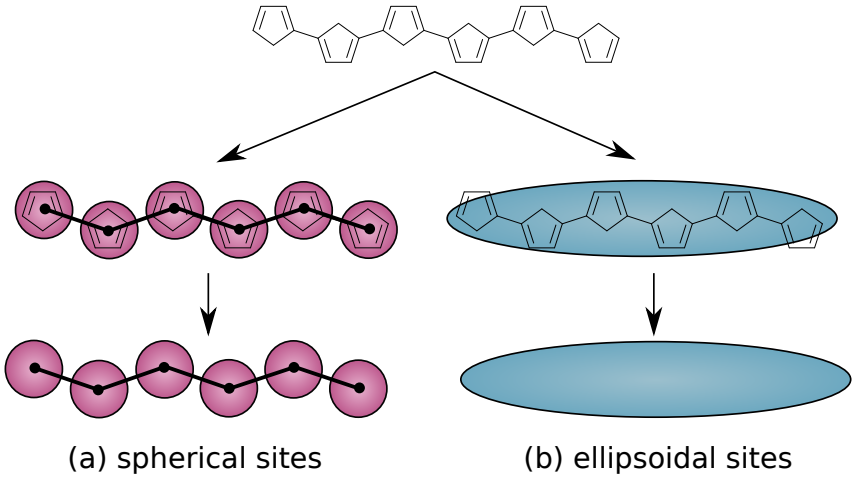

Fig. 1.8 An example of coarse graining of small conjugated molecule sexithiophene into (a) six spherical sites, or (b) a single ellipsoidal site. The spherical model represents each thiophene unit as a sphere connected by their centers of mass (black lines to black dots), while the ellipsoidal model is a representation of how this molecule could be coarse-grained into a single anisotropic particle. Image from ref 1.

Spherical vs anisotropic sites and potentials. To date, CG models have predominantly employed spherical sites for the calculation of non-bonded pair interactions. Although these models have been able to reproduce experimental anisotropic behaviour when the overall molecule (an accumulation of isotropic CG sites) is anisotropic (Fig. 1.7),[15,17,96,98,167] many OSCs consist of large planar subunits with very rigid backbones, so representing them as a collection of spheres may not be accurate or efficient. This is especially problematic when considering properties such as the π-stacking distance, which is known to be important for device performance. An alternative is to use anisotropic – either ellipsoidal[174,175] or disc-shaped[176] – particles. As these sites now have a quantifiable orientation, anisotropic non-bonded potentials are required to model the inter-site interactions as a function not only of distance, but also of orientation. Although these anisotropic interactions are slower to calculate than isotropic ones, a reduction in the number of sites (Fig. 1.8)

for a given level of accuracy can compensate for this. Interpretation of simulation results of an anisotropic model with fewer degrees of freedom and parameters is also potentially simpler. A number of anisotropic non-bonded potentials exist that account for both the distance and orientation dependence of the potential energy when considering ellipsoidal sites. Most commonly used are the GB,[81,177] and RE-squared[178–180] potentials, which are effective for ellipsoidal particles. Further details can be found in the literature.[178–181]

The work presented in Chapter 3 uses anisotropic disk-like particles represented by the GB potential to model molecules representative of many OSC small molecules relatively accurately. In Chapter 4, a spherical site model of P(NDI2OD-T2) is used, where the rigid backbone is modelled as a collection of spheres. This results in an overall anisotropic shaped backbone which is able to capture, with reasonable accuracy, the anisotropic nature of OSC aggregation, which occurs almost exclusively in the π-stacking direction. This gives a level of detail beyond what has been obtainable from spherical models that have been used in the past to study semiflexible polymer aggregation, leading to results that are much more applicable to OSCs.

Study of physical structure and assembly. CG MD models can give valuable insights into mechanistic details of microstructure and assembly processes in OSC devices that cannot be easily studied experimentally and may be computationally inaccessible to AA models. CG models have only been applied in the last decade or so to studying OSC structure and so, compared with AA simulations, CG simulations of OSC interfaces remain quite limited, focusing predominantly on the microstructure and formation of BHJ donor–acceptor interfaces.[168,169,175,182–187] Examples of studying solution-phase behaviour using CG models are, however, more common than their AA counterparts.

Coarse-graining is particularly useful for the study of solution-phase behaviour as, in addition to reducing the number of OSC atoms, the OSC–solvent interactions can be accounted for implicitly and incorporated into the OSC CG interactions. This means that a system that would contain upwards of 100,000 atoms in an AA representation can be reduced to a CG system of less than 10,000 sites, allowing for the simulation of longer polymer chains for longer times. An additional benefit is the generalisability, and easy tuning of interaction parameters, meaning results can be related to a class of molecules, rather than being system specific, and different system parameters can be systematically studied.

In this way, a number of studies have examined the single-chain behaviour of generic semiflexible polymers, finding a relationship between backbone flexibility, solvent quality (or equivalently, temperature) and single-chain conformation.[131–133]

Due to the general nature of the model, these results should be relevant to many OSC polymers. Likewise, multi-chain aggregation of generic polymers with variable stiffness and temperature has also been studied, showing a variety of phases that depend on the nature of system.[134]

As an alternative to general coarse-grained models, systematically coarse-grained models, which are parameterised to be an accurate representation of the matching AA system, are also useful for understanding both the single and multi-chain aggregation behaviour of OSCs.[167] Schwarz et al. [167] studied the aggregation behaviour of OSC polymer P3HT using a systematically parameterised CG model, reaching timescales of up to 5 μs and observing the formation of large aggregates and behaviour consistent with experiments. An even coarser model, where multiple OSC monomers are incorporated into a single CG site, has been systematically parameterised for MEH-PPV and proved useful for capturing the effect of solvent (modelled implicitly using Langevin dynamics) on the single chain behaviour of this polymer.[174] Although not exactly OSCs, the self assembly of π-conjugated peptides has also been studied through CG simulations in a manner that is directly applicable to the study of OSCs polymers such as P(NDI2OD-T2).[188]

Challenges for coarse-grained simulation of organic semiconductors. As with AA MD simulations, CG simulations are not without their challenges. In particular, the loss of molecular detail can be problematic as details about specific interactions, which may be important for understanding device properties, may be lost in the CGing procedure. It is therefore important that the desire for efficiency (fewer sites) be balanced with the need for accuracy. For good predictions, the model must be able to capture important intra- and intermolecular rearrangements which may necessitate a greater number of sites in order to prevent information loss.[189,190]

Another desirable feature of a CG model, which is not necessarily easy to achieve, is transferability to thermodynamic conditions beyond which it was parameterised. To this end, a model that is able to capture the molecular rearrangements that occur at changing temperatures is important.[189] Generally, this can be achieved by using a greater number of CG sites, or using anisotropic sites which better retain the relevant degrees of freedom of planar molecules.[176]

Additionally, despite their increase in accessible time scale relative to atomistic MD, CG models are still unable to achieve the time scales relevant to processes such as solvent-based film deposition. Although as computing power increases these time scales should begin to become more accessible, alternative methods, such as continuum methods, which will not be discussed in detail here (see ref 1), or hybrid approaches using CG semiconductors and a continuum or implicit solvent will likely be necessary to realistically model such processes. However, care must

be taken to account for hydrodynamic interactions (particularly for polymers)[191] and the concentration dependence of the CG interactions when solvent degrees of freedom are integrated out.

1.5 PROJECT OUTLINE

In the following chapters, molecular simulation techniques are used to examine the behaviour of a variety of OSC molecules at interfaces (Chapter 3) and in solution (Chapters 4 and 5).

In Chapter 3 we have identified a universal predictor for the orientation of ellipsoids with parameters typical of OSC small molecules, ranging from benzene, to perylene, and porphine, at both solid and vapour interfaces. This work extends the studies discussed in Section 1.2.2 for purely repulsive particles at interfaces, to systems that are much more representative of OSCs. The effect of temperature, shape and interaction anisotropy, substrate type, and density, were examined to understand the significance of these factors for controlling orientation. These general results can be related to the behaviour of actual OSC molecules, and some broad guidelines for tuning alignment at these interfaces are provided.

In Chapter 4 we have developed an AA model for high preforming OSC polymer P(NDI2OD-T2), which was used to systematically parameterise a CG model. This CG model was used to study the solution-phase behaviour of P(NDI2OD-T2) with chain lengths on the order of those used experimentally. Using this model, we were able to explain the experimentally observed formation of large rod-like aggregates in poor solvent,[25] leading to an improved understanding of the effect of the relative rates of single-chain folding and multi-chain aggregation, and the associated dependence on chain-length, flexibility, concentration, and solvent quality, on the single- or multi-chain structures expected in solution. The relative rates of these processes have not been previously examined, though appear to have a significant impact on the solution-phase behaviour of OSC polymers, hinting at the ability to use polymer concentration in solution to influence the aggregate structure. While the work in this chapter used a model parameterised to represent P(NDI2OD-T2), these results are not specific to a single polymer, but are generalisable to other semiflexible polymers.

The importance of specific interactions, either polymer–solvent or side-chain–solvent, is examined in Chapter 5 using the AA model of P(NDI2OD-T2) parameterised in Chapter 4, and that of an analogous molecule with different side-chains (ethylene oxide-based rather than alkyl). The effect of these different side-chains on the solution-phase structure of the two P(NDI2OD-T2) analogues was examined in terms of the relative solubilities of the polymer components (backbone or side-chain) in various solvents commonly studied experimentally,[22,25] quantified using

Flory-Huggins theory. Though it generally gave good agreement with the relative experimental solubility as calculated by UV-vis spectroscopy for both polymers, Flory-Huggins theory could neither fully explain some of the stranger aggregation properties of P(NDI2OD-T2) that have been anecdotally observed, nor the significant differences in the shape of the UV-vis absorption spectra for the two polymers. As Flory-Huggins parameters calculated from MD simulations have been recently proposed to be a good indicator of the relative extent of solution-phase aggregation,[130] this work provides an important reminder that simple models for solubility, though often sufficient, do not necessarily capture the full picture, especially when specific interactions (e.g. between side-chain and backbone) may be significant. Examining the structures of the polymer aggregates in more detail provided insight into the solution-phase, and aggregate, behaviour of these polymers with implications for choice of side-chains and solvent structure on device microstructure.

2

Computational Methods

"With all due respect John, I am the head of IT, and I have it on good authority that if you type 'Google' into Google, you can break the internet."

— Jen, *The IT Crowd*

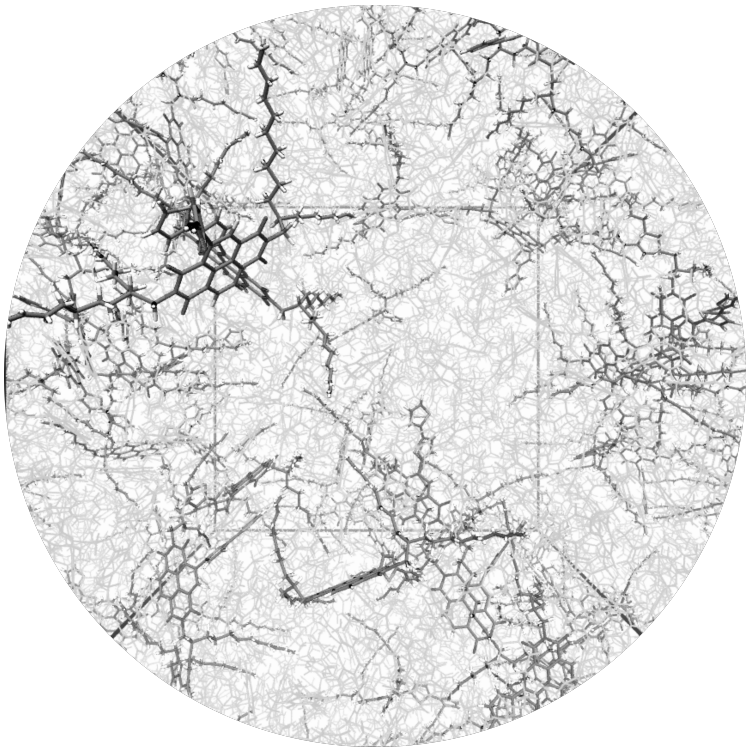

2.1 MOLECULAR DYNAMICS

As with many areas of chemistry, there are a number of different methods for studying the behaviour organic semiconductor (OSC) molecules both in solution and at interfaces, with the choice depending on the resolution and timescale required. Experimental techniques, such as UV-visible spectroscopy or microscopy, can give insights into properties such as the degree of aggregation, the size and orientation of aggregates, or the surface morphology. Although useful, these techniques are generally low in resolution, giving details only on the average/bulk properties of the system. While experimental techniques exist that have atomic resolution (e.g. x-ray crystallography), these generally rely on the material being crystalline. Even in the solid state, this is not necessarily the case for OSCs, with their generally disordered structures hindering atom-level experimental analysis. For these disordered structures, or for molecules in solution, if atomic/molecular scale detail is desired, for example to understand how specific molecular interactions relate to experimental trends, computational methods are therefore required.

Giving the highest resolution, quantum calculations can prove useful for understanding electronic processes, but are limited to small molecules and cannot easily include the effect of solvent or other surrounding molecules. For understanding the morphology and dynamics of OSCs in the solution- or liquid-phase, the electronic processes that are accessible via quantum calculations become less important, and these properties can effectively be explained by the nuclear motion. Particle motion can then be treated using classical molecular dynamics (MD) simulation techniques. In this work we differentiate between all-atom (AA) and coarse-grained (CG) methods, which again allow for different levels of resolution and accessible timescales. AA simulations involve explicit simulation of all atoms in the system and can reach up to the microsecond scale for 10s of millions of atoms,[192] although systems of this size are challenging to simulate and smaller systems are generally more common. To reach larger timescales, or to study properties more generally, CG simulations can be useful. These simulations combine multiple atoms into a single site, and generally integrate out the solvent (instead accounting for it implicitly), greatly increasing simulation efficiency.

Despite differences in simulation techniques (e.g. AA versus CG), and the plethora of MD simulation software packages available, the general algorithm for running an MD simulation remains the same with the forces acting on each particle computed according to Newton's equations of motion

$$\boldsymbol{F}_i(\boldsymbol{r}) = m\frac{\mathrm{d}^2\boldsymbol{r}}{\mathrm{d}t^2} \tag{2.1}$$

These forces are practically computed from the initial position and velocity distribu-

tion, and the interactions between all N particles, $U(\boldsymbol{r}^N)$, as specified by the chosen force-field as

$$\boldsymbol{F}_i(\boldsymbol{r}) = -\nabla_i U(\boldsymbol{r}^N) \tag{2.2}$$

where $\boldsymbol{F}_i(\boldsymbol{r})$ is the force acting on particle i, and $\boldsymbol{r}^N$ is the configuration of the N-particle system. Under constant number of particle, volume, and energy (NVE) conditions, the particle positions are then updated by integrating eqn (2.2) and the process iterated as required, typically with a timestep of 1–2 fs for AA simulations, or much larger (and strongly dependent on the degree of coarse-graining) in the CG case. In all the following simulations, the velocity Verlet[193,194] algorithm was used to numerically integrate the equations of motion.

As it is generally beneficial to study systems as close to experimental conditions as possible, temperature and pressure control are also important factors in MD simulation. To maintain constant temperature, additional dynamical variables can be coupled to the particle velocities in order to maintain a velocity distribution consistent with the desired temperature. In this work we have used a Nosé-Hoover thermostat[195,196] for temperature control in AA simulations. To model the background implicit solvent in CG simulations, a Langevin thermostat[197] was used. This will be described in more detail in Section 2.1.4. Where required, pressure control was implemented using a Nosé-Hoover barostat,[198] which couples the box volume to additional dynamical variables, such that the size of the box fluctuates in order to maintain a constant pressure in the system.

2.1.1 computing interparticle forces

In order to accurately model the dynamics of the system of interest, the molecular mechanics force-field, which define the interactions between various atom types, as well as the bonded parameters, is perhaps the most important choice for a successful simulation. Although the parameters may be different between CG and AA models, the principles remain the same. In both cases, the total potential energy, $U(\boldsymbol{r}^N)$, of the system is a sum of the total bonded, $U_{\text{bonded}}(\boldsymbol{r}^N)$, and non-bonded, $U_{\text{non-bonded}}(\boldsymbol{r}^N)$, interactions:

$$U(\boldsymbol{r}^N) = \sum U_{\text{bonded}}(\boldsymbol{r}^N) + \sum U_{\text{non-bonded}}(\boldsymbol{r}^N) \tag{2.3}$$

The bonded interactions can be divided into bond, angle, dihedral, and improper potentials, and the short and long-ranged non-bonded interactions. The non-bonded interactions are generally (and in this work) assumed to be the sum of pair interactions. For a system of N particles:

$$U(\boldsymbol{r}^N) = \underbrace{U_{\text{bond}} + U_{\text{angle}} + U_{\text{dihed}} + U_{\text{improp}}}_{\text{bonded}} + \underbrace{U_{\text{coul}} + U_{\text{vdw}}}_{\text{non-bonded}} \tag{2.4}$$

where

$$U_{\text{bond}} = \sum_{i \in \text{bonds}} U_{\text{bond},i} \tag{2.5}$$

$$U_{\text{angle}} = \sum_{i \in \text{angles}} U_{\text{angle},i} \tag{2.6}$$

$$U_{\text{dihed}} = \sum_{i \in \text{diheds}} U_{\text{dihed},i} \tag{2.7}$$

$$U_{\text{improp}} = \sum_{i \in \text{improps}} U_{\text{improp},i} \tag{2.8}$$

are the bond, angle, dihedral and improper potentials respectively, and

$$U_{\text{coul}} = \sum_{i,j \in \text{pairs}} U_{\text{coul},ij} \tag{2.9}$$

$$U_{\text{vdw}} = \sum_{i,j \in \text{pairs}} U_{\text{vdw},ij} \tag{2.10}$$

the Coulombic and van der Waals (vdW) components of the non-bonded energy, calculated over the configuration of the whole system. Each of these terms will be discussed in more detail in the subsequent sections although it should be noted that actual computation of the Coulombic interactions is somewhat more complicated than represented in the idealised case of eqn (2.9). The means by which this energy is more practically evaluated is discussed in more detail in Section 2.1.1.5.

2.1.1.1 Bonded interaction potentials

Bond potentials U_{bond} are typically treated as a harmonic potential with bond stretching coefficient $k_{b,i}$ for bond i, and separation between two bonded particles l_i with equilibrium bond length $l_{0,i}$:

$$U_{\text{bond},i}(l_i) = k_{b,i}(l_i - l_{0,i})^2 \tag{2.11}$$

Angles are generally treated similarly as harmonic oscillators with bending coefficient $k_{a,i}$ and angle defined by three particles θ_i with equilibrium angle $\theta_{0,i}$ for bond angle i:

$$U_{\text{angle},i}(\theta_i) = k_{a,i}(\theta_i - \theta_{0,i})^2 \tag{2.12}$$

Two different dihedral potentials are used in the AA simulations in this work: the OPLS style dihedral $U^{\text{OPLS}}_{\text{dihed}}(\phi_i)$

$$\begin{aligned} U^{\text{OPLS}}_{\text{dihed}}(\phi_i) = \frac{1}{2}K_1\left[1 + \cos(\phi_i)\right] + \frac{1}{2}K_2\left[1 - \cos(2\phi_i)\right] \\ + \frac{1}{2}K_3\left[1 + \cos(3\phi_i)\right] + \frac{1}{2}K_4\left[1 - \cos(4\phi_i)\right] \end{aligned} \tag{2.13}$$

with parameters $K_{n,i}$ for dihedral angle ϕ_i, and an alternative form

$$U^{\mathrm{m/h}}_{\mathrm{dihed}}(\phi_i) = \sum_{n=0}^{m} K_n \cos^{n-1}(\phi_i) \tag{2.14}$$

where $m = 4$ or 8. The case where $m = 4$ is implemented in LAMMPS as the multi/harmonic dihedral, and is equivalent to the OPLS style dihedral defined in eqn (2.13). Improper torsions are modelled with a cosine potential (implemented in LAMMPS as the cvff improper style):

$$U_{\mathrm{improp},i}(\psi_i) = K\left[1 + d\cos(n\psi_i)\right] \tag{2.15}$$

where $d = 1$ or -1, K is an energy parameter, and n an integer.

2.1.1.2 Isotropic non-bonded interaction potentials

Non-bonded interactions can be divided into short-ranged (vdW) and longer-ranged (electrostatic/coulombic) interactions. For isotropic (spherical/point) particles, such as those used in the AA and some of the CG simulations in this work, the Lennard Jones (LJ) potential, $U_{\mathrm{LJ}}(r_{ij})$, is used to capture the short range repulsive and longer-ranged attractive interactions between two particles separated by distance r_{ij}:

$$U_{\mathrm{vdw},ij}(r_{ij}) = U_{\mathrm{LJ}}(r_{ij}) = 4\epsilon_{ij}\left[\left(\frac{\sigma_{ij}}{r_{ij}}\right)^{12} - \left(\frac{\sigma_{ij}}{r_{ij}}\right)^{6}\right] \tag{2.16}$$

where σ_{ij} determines the length scale of the interaction, and ϵ_{ij} the energy scale.

2.1.1.3 Anisotropic non-bonded interaction potentials

Alternate potentials exist to model vdW interactions for anisotropic (e.g. ellipsoidal) particles. Commonly used potentials include the Gay-Berne (GB),[81,177,199] RE^2,[178] and S-function expansion.[176,200] In this work, we use the GB potential to model the behaviour of OSC-like ellipsoids (Chapter 3). This potential is an generalisation of the LJ potential (eqn (2.16)) to aspherical particles.

The GB potential is an anisotropic, shifted LJ potential which is defined by ellipsoid shapes and relative interaction energies. The potential depends on both distance and orientation, with the relative position of the two particles i and j described by the vector $\boldsymbol{r}_{ij} = \boldsymbol{r}_i - \boldsymbol{r}_j$ for two particles positioned at $\boldsymbol{r}_i$ and $\boldsymbol{r}_j$, respectively. The orientation of the particles is defined by the rotation matrices $\boldsymbol{A}_i$ and $\boldsymbol{A}_j$, which transform the orientations of the two particles from the lab frame to the body frame. Each particle has shape and interaction anisotropy, with the shape anisotropy described by the diagonal shape matrix $\boldsymbol{S}_i = \mathrm{diag}(\sigma_{\mathrm{a}i}, \sigma_{\mathrm{b}i}, \sigma_{\mathrm{c}i})/2$, where $\sigma_{\mathrm{a}i}$, $\sigma_{\mathrm{b}i}$, and $\sigma_{\mathrm{c}i}$ are the particle's principal diameters. The interaction anisotropy is similarly described by $\boldsymbol{E}_i = \mathrm{diag}(\epsilon_{\mathrm{a}i}, \epsilon_{\mathrm{b}i}, \epsilon_{\mathrm{c}i})$, for interaction well depths along the

principal axes ϵ_{ai}, ϵ_{bi}, and ϵ_{ci}. The interaction potential between these two particles is then given as

$$u_{\mathrm{GB}}\left(\boldsymbol{r}_{ij},\boldsymbol{A}_i,\boldsymbol{A}_j\right)=u_{\mathrm{r}}\left(\boldsymbol{r}_{ij},\boldsymbol{A}_i,\boldsymbol{A}_j\right)\eta\left(\boldsymbol{A}_i,\boldsymbol{A}_j\right)\chi\left(\boldsymbol{r}_{ij},\boldsymbol{A}_i,\boldsymbol{A}_j\right), \tag{2.17}$$

where the first term describes the distance dependence of the potential, and the others account for the effects of particle shape and interaction anisotropy.

The first term, u_{r}, is a shifted LJ potential that describes the distance dependence of the GB interaction:

$$u_{\mathrm{r}}(\boldsymbol{r}_{ij},\boldsymbol{A}_i,\boldsymbol{A}_j)=4\epsilon_{ij}\left[\left(\frac{\sigma_{ij}}{h_{ij}+\sigma_{ij}}\right)^{12}-\left(\frac{\sigma_{ij}}{h_{ij}+\sigma_{ij}}\right)^{6}\right]. \tag{2.18}$$

It differs from eqn (2.16) only in the interparticle distance: r_{ij} in the LJ potential is replaced by the distance of closest approach h_{ij}, which can be approximated as[178]

$$h_{ij}\left(\boldsymbol{r}_{ij},\boldsymbol{A}_i,\boldsymbol{A}_j\right)=r_{ij}-\left(\frac{1}{2}\hat{\boldsymbol{r}}_{ij}^{\mathrm{T}}\boldsymbol{G}_{ij}^{-1}\hat{\boldsymbol{r}}_{ij}\right)^{-1/2}, \tag{2.19}$$

where $r_{ij}=\left|\boldsymbol{r}_{ij}\right|$, $\hat{\boldsymbol{r}}_{ij}=\boldsymbol{r}_{ij}/r_{ij}$, and

$$\boldsymbol{G}_{ij}=\boldsymbol{A}_i^{\mathrm{T}}\boldsymbol{S}_i^2\boldsymbol{A}_i+\boldsymbol{A}_j^{\mathrm{T}}\boldsymbol{S}_j^2\boldsymbol{A}_j. \tag{2.20}$$

The position and orientation dependence of the interaction strength is described by the other terms in eqn (2.17), η and χ. They are given by

$$\eta\left(\boldsymbol{A}_i,\boldsymbol{A}_j\right)=\left[\frac{2\bar{\sigma}_i\bar{\sigma}_j}{\det\left(\boldsymbol{G}_{ij}\right)}\right]^{\nu/2} \tag{2.21}$$

and

$$\chi\left(\boldsymbol{r}_{ij},\boldsymbol{A}_i,\boldsymbol{A}_j\right)=\left(2\hat{\boldsymbol{r}}_{ij}^{\mathrm{T}}\boldsymbol{B}_{ij}^{-1}\hat{\boldsymbol{r}}_{ij}\right)^{\mu}, \tag{2.22}$$

where

$$\bar{\sigma}_i=\left(\sigma_{ai}\sigma_{bi}+\sigma_{ci}^2\right)\left(\sigma_{ai}\sigma_{bi}\right)^{1/2}, \tag{2.23}$$

$$\boldsymbol{B}_{ij}=\boldsymbol{A}_i^{\mathrm{T}}\boldsymbol{E}_i^{-1/\mu}\boldsymbol{A}_i+\boldsymbol{A}_j^{\mathrm{T}}\boldsymbol{E}_j^{-1/\mu}\boldsymbol{A}_j, \tag{2.24}$$

and ν and μ are parameters that tune the shape of the potential.

2.1.1.4 Long-range electrostatics

Where particles are charged, electrostatic interactions between two particles with charges q_i and q_j separated by distance r_{ij} are computed as

$$U_{\mathrm{coul},ij}(r_{ij})=\frac{q_iq_j}{4\pi\epsilon_0\epsilon_{\mathrm{r}}r_{ij}} \tag{2.25}$$

where ϵ_0 is the vacuum permittivity, and ϵ_{r} the dielectric constant of the medium. In all the work presented here where charged particles are used, a value of $\epsilon_{\mathrm{r}}=1$ was used.

2.1.1.5 Dealing with long-ranged interactions

The computation of forces in eqn (2.2) relies on calculating the non-bonded interactions in eqn (2.4) between all pairs of particles in the system. This computation can therefore be a significant source of efficiency loss in a molecular simulation, scaling as N^2 for total number of particles in the system N and making study of all but the smallest systems infeasible. To counteract this, interactions beyond a certain cutoff distance, r_c, are generally assumed to be negligible, and the interactions between particles separated by more than this distance are not computed. VdW interactions decay rapidly with distance, so the truncation of the interactions beyond a sufficiently large cutoff (generally on the order of 10–15 Å, and specific to the force-field used) does not introduce significant error to the calculated forces. It does, however, introduce a small discontinuity in the energy, which is equal to $U_{\mathrm{LJ}}(r_{ij})$ for distances shorter than the cutoff r_c, and 0 beyond. This discontinuity may result in unphysical behaviour but can be treated in a number of ways. In this work, the energy is shifted up by a constant such that $U_{\mathrm{LJ}} = 0$ at r_c.

Although the short-ranged interactions do not suffer significantly from the truncation of the interactions at r_c, electrostatics decay over a much longer range so cannot so simply be neglected. A number of algorithms exist to efficiently calculate the long-range electrostatic interactions. In the work in the following chapters, the particle–particle particle–mesh (PPPM) method is used.[201] Ewald summation methods, such as PPPM, split the electrostatic potential due to a charged particle into a short-range component and a long-range component, with the long range component calculated in Fourier space. In PPPM, the particles are mapped to a grid, the potential calculated using Fourier methods to solve Poisson's equation, and the resulting electric field mapped back to the particles.

2.1.1.6 Finite-size effects and periodic boundary conditions

One of the potential limitations to MD simulation is the inaccessibility of experimental-sized systems: even a single drop of water contains on the order of 10^{21} molecules, significantly higher than the range typically accessible to MD of around one million atoms. If it is assumed that the bulk experimental system is relatively homogeneous, then a smaller system, containing just enough molecules to observe the behaviour of interest, can be used to approximate a much larger system. However, small systems are susceptible to finite-size effects, where the presence of boundaries introduces artefacts into the system properties. This can be overcome by assuming a periodic system, in which the simulation box is replicated in the x, y, and/or z dimensions, effectively creating an infinite system. In order to increase efficiency, only the forces between the closest periodic images of a molecule are computed (Fig. 2.1). The box should be large enough that a molecule does not interact with periodic images of

itself.

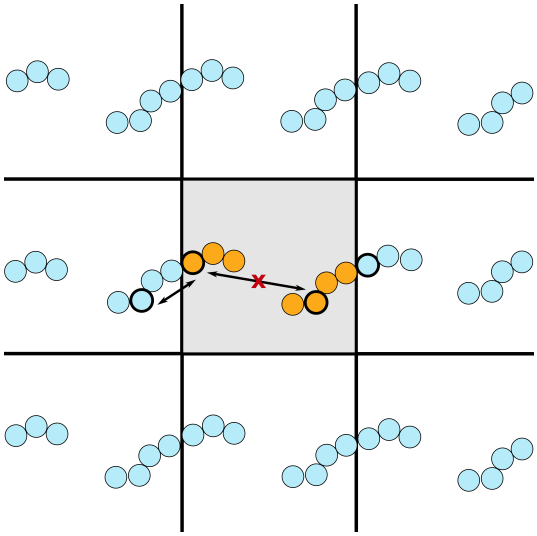

Fig. 2.1 Illustration of periodic boundary conditions in two dimensions. The central grey box represents the simulation cell, where the molecule extending over the boundary interacts with its periodic images. Interactions are only computed between a molecule and its closest periodic images; those further apart, such as the those indicated by the arrow with cross, are not computed.

2.1.2 FORCE-FIELD PARAMETERISATION

Although parameters for many different atom types are available, particularly for small organic molecules, the somewhat different nature of OSCs, most notably their semiflexibility, means that models must be specifically parameterised for the molecules of interest in order to obtain accurate behaviour. Details of how these models can be parameterised are given in more detail below for both AA (Section 2.1.2.1) and CG (Section 2.1.2.2) systems.

2.1.2.1 Parameterisation of all-atom force fields

In AA simulations, every atom is treated explicitly in order to realistically model a specific real-life system. It is therefore important that the interactions, both bonded and non-bonded, between the atoms are reasonably representative of the system of interest. A number of general force fields exist that provide parameters for a wide variety of atom types, and are generally specific to different applications. The optimised potentials for liquid simulations (OPLS) force-field,[202] for example, which is used extensively in this work, was developed to accurately model the behaviour of liquids of generally organic molecules. While these parameters are generally transferable between similar systems, the extended conjugation and relative stiffness of OSC backbones means that additional parameterisation is required in order to

accurately model the molecules of interest here. In this work, we have followed a previously published method,[203] which follows the parameterisation of the OPLS force-field, in order to develop parameters for the high performing OSC polymer P(NDI2OD-T2). The parameterisation procedure, which involves explicit calculation of the atomic point-charges, geometry optimisation to obtain equilibrium bond lengths and angles, and a series of constrained optimisations to calculate a number of key dihedral and bond potentials, is described fully in Chapter 4.

Note that the OPLS force field has been shown to give aggregation properties of OSCs that are consistent with experiments for a wide variety of OSC polymers,[24] and the parameters are, as such, expected to be transferable to other OSC molecules such as those studied in this work.

2.1.2.2 Parameterisation of coarse-grained force-fields

Compared to AA force-fields, described above, which are parameterised to capture the behaviour of individual atoms, CG force-fields generally focus on capturing the mesoscale properties of a system. Some are parameterised to match properties of AA, or alternatively experimental, systems, while others focus on accurately mapping the AA forces to the force acting on a CG site. In all cases, the CG model reduces the number of degrees of freedom in a system by combining multiple atoms into a single site, and often only implicitly accounting for the effect of solvent molecules. Depending on the target result, a number of different methods can be applied to the development of CG models of OSCs. These differ in the structural or thermodynamic properties they attempt to match between AA and CG model. The iterative Boltzmann inversion (IBI) method for example, which is the method used in this work, aims to match structural properties between the AA and CG models by iteratively updating the interaction potentials between CG sites until the probability distributions of non-bonded pair distances, bond lengths, bond angles, dihedrals, and improper torsions converge to the AA target.[172] This method has been previously implemented for studies of OSC polymer P3HT with good success,[41,167,204] and will be discussed in more detail below. Other methods, which will not be discussed in detail here, include force-matching, in which the total force acting on a CG site is matched to the average sum of the forces acting on the particles in the AA model that make up the site in equivalent system configurations,[171,205–207] and relative entropy, where the relative entropy between the CG and AA systems is minimised.[173] An in depth review of CG methods can be found in ref 170.

The IBI method used in the following chapters aims to reproduce the behaviour of an AA system by matching its structural properties; for the non-bonded interactions this is generally the radial distribution function (RDF), though the method is useful for parameterising both bonded and non-bonded interactions. In all cases,

the same iterative procedure is followed. An initial target distribution is generated from the mapping of the AA model to CG sites. This distribution may be, for example, the bond-length distribution for a bond connecting two CG sites, or the RDF – that is the probability of finding a particle at position r relative to the particle of interest – for calculating the non-bonded pair interactions. An initial guess at the potential, $U_0(x)$, where x is the property of interest (e.g pair separation, bond length, etc.), is made, typically the Boltzmann inversion ($-k_{\mathrm{B}}T\ln(P(x))$) of the target distribution $P(x)$, and the CG model simulated using that potential. This can be done using the exact potential (such as by using a tabulated potential in LAMMPS) or by fitting it to an analytical form (such as an LJ potential for the non-bonded interactions, or the harmonic form for a bond potential). The use of an analytical potential generally enhances simulation efficiency, but may result in a slight loss of accuracy. In this work, we fit non-bonded potentials to an LJ potential, bonds and angles to a harmonic or quartic-style potential, dihedrals to the potential described in eqn (2.14) (with $m = 4$), and impropers to the cosine form of eqn (2.15) (see Chapter 4 for full details). The CG distribution is measured and compared to the target distribution. If they match within acceptable error then the process is complete. If not, the potential is updated according to

$$U_{n+1}(x) = U_n(x) + a_n \ln\left(\frac{P_n(x)}{P_{\mathrm{target}}(x)}\right) \tag{2.26}$$

where $U_n(x)$ is the potential for iteration n of the procedure as a function of the variable x , $0 \leq a_n \leq 1$ is a scaling factor that controls how much the potential is changed from the previous iteration, $P_{\mathrm{target}}(x)$ the target distribution of the property being parameterised, and $P_n(x)$ the CG distribution from iteration n. The process is then repeated. For the non-bonded interactions, $P(x)$ is $g(r_{ij})$, the RDF, while for the bonded interactions $P(x)$ is $P_{\mathrm{bond}}(l_i)/l_i^2$, $P_{\mathrm{angle}}(\theta_i)/\sin(\theta_i)$, $P_{\mathrm{dihed}}(\phi_i)$, and $P_{\mathrm{improp}}(\psi_i)$ for the bond, angle, dihedral, and improper distributions, respectively. The entire IBI process is illustrated in Fig. 2.2.

In this work, the IBI method is used for the parameterisation of high-performing OSC polymer P(NDI2OD-T2) into a simplified CG model with atoms whose motions are expected to be correlated grouped into spherical sites. In general, we group each conjugated ring into a single site, and three alkyl carbons into a side-chain site (Fig. 2.3).

2.1.3 anisotropic-site coarse-grained models

The model described above for P(NDI2OD-T2) uses spherical CG sites, though, due to the number of sites, the overall monomer is anisotropic. The naphthalene diimide (NDI) backbone, for example, is made up of four spherical sites, which

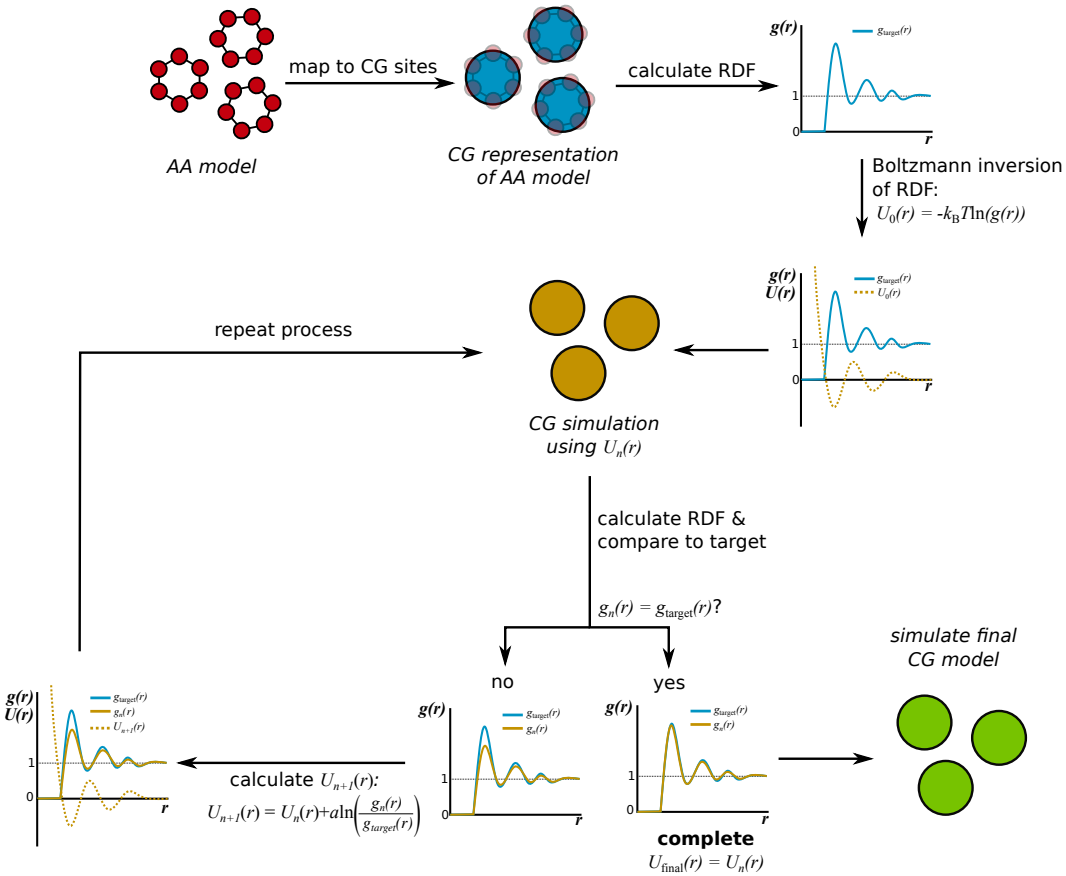

Fig. 2.2 Illustration of the IBI process, from AA model to CG parameters. The process is illustrated for parameterisation of non-bonded interactions using the RDF but is equally applicable to bonded interactions. Typically, as has been done in this work, the potential U_i will be fit to an analytical function for simulation.

to a good approximation, represent the planar structure of the group. While this approximation is reasonable and should give behaviour consistent with the AA model, a better representation of this group may be as a single anisotropic site, such as a disk or oblate ellipsoid (Fig 2.4). Having fewer sites may increase the simulation efficiency (although the additional rotational degrees of freedom of a finite-sized aspherical particle will come with an additional computational cost), and also increase the generality of a model, giving results that may be more applicable to a wide variety of structures. In Chapter 3 we employ an anisotropic-site CG model, in which an entire OSC-like molecule is simulated as a single oblate GB ellipsoid (see Section 2.1.1.3 for details of the GB potential), to study the behaviour of condensed-phase systems at interfaces.

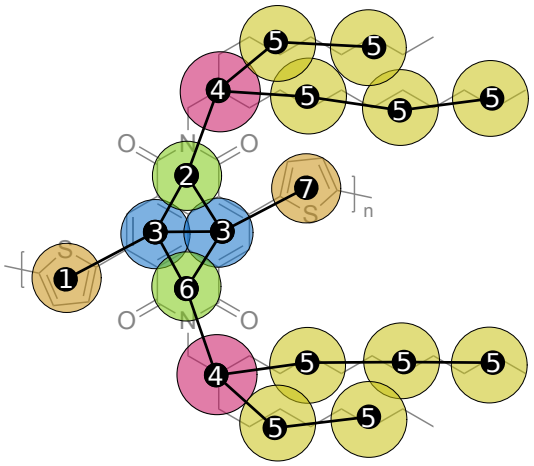

Fig. 2.3 The definition of the CG model of OSC polymer P(NDI2OD-T2) used in Section 4. Relatively rigid groups, such as the individual aromatic rings of the backbone, are coarse-grained into a single spherical CG site. CG sites of the same type are coloured the same.

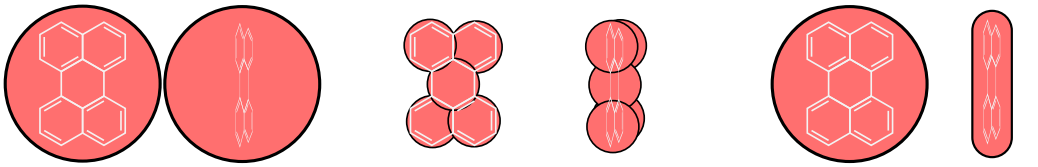

(a) single spherical site **(b)** multiple spherical sites **(c)** single ellipsoidal site

Fig. 2.4 Comparison of three different options for coarse-graining OSC small-molecule perylene. (a) a single spherical site, (b) multiple spherical sites, or (c) a single ellipsoidal site. Side-on and front-on views are shown in all cases. The work in Chapter 4 uses a CG model with multiple spherical sites, and in Chapter 3 a single ellipsoidal site, to represent an OSC molecule.

2.1.4 Implicit solvent simulations: Langevin dynamics

Aside from the significant reduction in the solute degrees of freedom, and the ability to incorporate fast molecular motions (e.g. the C–H bond stretch) into a single rigid site allowing for the use of a larger timestep, one of the main sources of increased efficiency in CG simulations of solution phase processes is the ability to coarse-grain out the solvent. Instead of being explicitly simulated, the effect of solvent is accounted for implicitly through the solute non-bonded interactions. As the RDF includes features related to the solvent behaviour, the IBI procedure used for coarse-graining, which matches the CG and AA RDFs, results in a non-bonded pair potential which includes, approximately, the effect of solvent without the need for it to be explicitly present. This greatly reduces the number of particles needed to be simulated, significantly enhancing the feasible size and length scales for simulation.

While the non-bonded interactions with the solvent are accounted for implicitly

through the pair potential, the dynamic effects, such as the influence of collisions with solvent molecules on the diffusion of the solute, and longer ranged hydrodynamic interactions, are not captured by this. The frictional drag on the solute moving through solvent, as well as the random collisions of solute and solvent molecules, can be incorporated through the use of Langevin dynamics. The use of a Langevin thermostat[197] gives the total force, $\boldsymbol{F}_{\mathrm{L}}$, on each particle with mass m_i and position $\boldsymbol{r}$ at time t, $\boldsymbol{F}_{\mathrm{L}} = m_i\ddot{\boldsymbol{r}}$, as

$$\boldsymbol{F}_{\mathrm{L}}(t) = m_i\ddot{\boldsymbol{r}}_i(t) = \boldsymbol{f}_i(t) - m_i\gamma\dot{\boldsymbol{r}}_i(t) + \zeta_i(t). \tag{2.27}$$

Here, $\boldsymbol{f}_i(t)$ is the force acting on particle i due to the interparticle potential, and $m_i\gamma\dot{\boldsymbol{r}}_i(t)$ the frictional drag in a solvent with friction coefficient γ. $\zeta_i(t)$ is the force due to random collisions with the solvent, which satisfies $\langle\zeta_i(t)\rangle = 0$ and $\langle\zeta_i(t)\zeta_j(t')\rangle = 2\gamma k_{\mathrm{B}}Tm_i\delta_{ij}\delta(t-t')$, where δ_{ij} is the Kronecker delta and $\delta(t-t')$ is the Dirac delta function for time separation $t-t'$.

While Langevin dynamics is an effective method for including the effect of solvent collisions and viscosity implicitly in the calculation, it does not account for hydrodynamics, which may be important for the behaviour of OSC polymers in solution. Although we do not include hydrodynamic interactions in this work due to the increased computational complexity, a number of algorithms, such as the use of a Lattice-Boltzmann fluid,[208] do exist to enable their inclusion and would provide an interesting extension on much of the work conducted in Chapter 4. This method uses a lattice-based representation of a fluid, which interacts with solvated molecules to mimic the effect of a background solvent without much of the additional computational complexity and cost. It could therefore be applied to more accurately capture the effect of hydrodynamic interactions on polymer diffusion as studied in Chapter 4.

2.1.5 Enhanced sampling methods

Although MD simulation does provide a means to study the dynamics and time evolution of systems, it is often only the final equilibrium state, or the features of the free energy landscape separating states of importance, that is of interest. Often, significant free-energy barriers separate important states, meaning these states, which may require a rare event to reach, are inaccessible to non-biased MD simulations on achievable timescales. It is often, therefore, useful to map the free energy pathway between different states of a system to provide insights into how likely a specific state is to occur in a realistic system, or what the most likely pathway towards the equilibrium state may be. A number of methods for calculating free energy profiles, or potentials of mean force (PMFs), exist, by which certain system collective variables (CVs) can be biased to fully explore the relevant areas of the

free energy landscape. In Chapters 4 and 5 we use on-the-fly probability enhanced sampling (OPES),[209] a variation on metadynamics,[210] in which small repulsive gaussians are added over the course of the simulation to bias the system away from visiting regions it has previously visited, to examine the aggregation behaviour of P(NDI2OD-T2).

At convergence, the OPES method samples a target probability distribution, $P_{\text{bias}}(s)$, of the CVs of interest, s, which differs from the equilibrium Boltzmann distribution, $P(s)$. This target distribution is, in the well-tempered case, related to the equilibrium distribution as $P_{\text{bias}}(s) \propto P(s)^{1/\xi}$, where free energy barriers on the target free energy surface are reduced by a factor of $\xi > 1$ (where ξ is known as the bias factor) relative to the unbiased surface, and is obtained by adding the bias

$$V(s) = k_{\text{B}}T \ln\left(\frac{P_{\text{bias}}(s)}{P(s)}\right). \tag{2.28}$$

Due to the relationship between $P_{\text{bias}}(s)$ and $P(s)$, the bias, $V(s)$, can be determined from an estimate of $P(s)$, which is constructed by biasing the system away from regions of the free energy landscape that it has already visited by regularly depositing gaussians, then reweighting to obtain an estimate of the unbiased probability, from which the free energy can be estimated.[209] An estimate of the unbiased distribution, $\hat{P}(s,t)$, can be obtained using kernel density estimation as

$$\langle \hat{P}(s,t) \rangle = \frac{\sum_{t'=0}^{t} w(t') K(s - s(t'), \sigma_{\text{K}})}{\sum_{t'=0}^{t} w(t')} \tag{2.29}$$

where $w(t')$ is the weight at time t' given by $w(t') = \exp(V(s,t')/k_{\text{B}}T)$, and $K(s - s(t'), \sigma_{\text{K}})$ are kernels (Gaussians in this work), centered at $s(t)$ with bandwidth (related to the width of the Gaussian kernels) σ_{K}, summed over all times between t' and t.[211,212]

2.2 DESCRIBING THE BEHAVIOUR OF ANISOTROPIC PARTICLES

In Chapter 3 we examine the behaviour of a condensed-phased systems of anisotropic particles. While a system of spherical particles can be fully described by the center-of-mass position of the particles, quantified through, for example, the RDF, anisotropic particles also have orientational degrees-of-freedom that can introduce changes in phase behaviour beyond that which is possible for spherical molecules. The most extreme effect of the additional orientational degrees-of-freedom manifest as liquid crystal (LC) phases, in which the bulk fluid has either positional, or positional and orientational order (see Fig. 2.5) whilst still maintaining the faster dynamics of a liquid system.

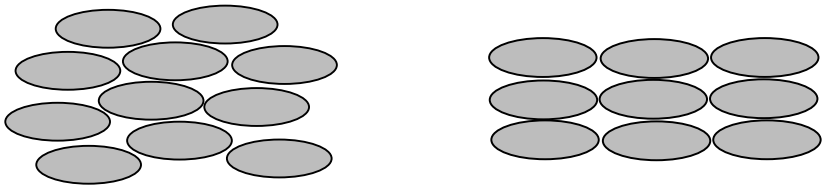

(a) nematic **(b)** smectic

Fig. 2.5 Comparison of the nematic and smectic liquid crystalline phases. In the nematic phase, anisotropic particles have orientational order, while the smectic phase shows both positional and orientational ordering.

In the work presented in Chapter 3 we predominantly considered systems in which the bulk fluid remained isotropic rather than adopting these LC phases, but symmetry breaking induced by the interfaces resulted in a degree of orientation ordering at these interfaces. We describe this orientation through the P_2 order parameter, here defined as:

$$s(z) = \langle P_2 \cos(\theta) \rangle_z = \frac{3\langle \cos^2(\theta) \rangle_z - 1}{2} \tag{2.30}$$

where θ is the angle between the unique axis of a uniaxial ellipsoid, calculated as a function of z, the distance from the substrate. This parameter adopts a value of 1 when the unique axis is perpendicular to the z axis, and -0.5 when it is parallel (Fig. 2.6). If the fluid is isotropic, $s(z) = 0$.

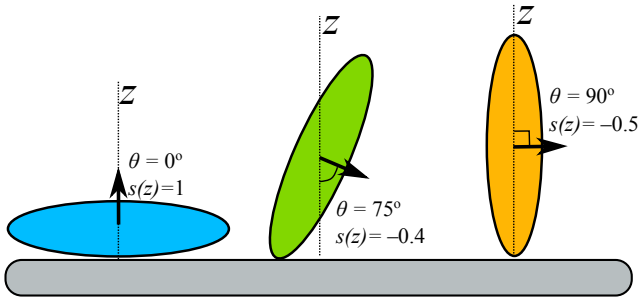

Fig. 2.6 Definition of the orientational order parameter $s(z)$, described in eqn (2.30), for a uniaxial oblate ellipsoid. The arrow indicates the unique axis. The angle between this ellipsoid axis and the z axis can be used to define the alignment of a collection of these particles.

2.3 ANALYSIS OF POLYMER SOLUTIONS

In Chapters 4 and 5, we examine the effect of solvent quality and side-chain structure on polymer chain conformation in the context of semiconducting polymer P(NDI2OD-T2). Broadly, Chapter 4 looks at the types and structures of aggregates

formed by P(NDI2OD-T2) under different conditions, while in Chapter 5 the effect of solvent quality on aggregation properties of P(NDI2OD-T2) is discussed in the context of the Flory-Huggins theory of polymer mixing.

2.3.1 POLYMER MIXING: FLORY-HUGGINS THEORY

A rough understanding of the solution-phase behaviour of polymers can be obtained by classifying solvents into three general classes: good, theta, and poor. In a good solvent, polymer–solvent attractive interactions are sufficiently strong (or polymer–polymer and solvent–solvent attractive interactions sufficiently weak) that no aggregation of the polymer is observed. An extended chain conformation is therefore expected, where the polymer will neither interact strongly with other polymers in solution, nor collapse into a globule. In contrast, in a poor solvent, polymer–polymer or solvent–solvent attractive interactions are strong relative to the polymer–solvent attractive interactions. This results in aggregation of polymer chains, or folding of individual chains into compact structures, though the specifics of the behaviour will depend on both the solvent quality and the backbone properties. In a theta solvent, the polymer will act as an ideal chain for which there is neither an energetic penalty nor a reward for aggregation.[127]

Flory-Huggins theory[213,214] is a theory for predicting mixing of two-component systems (e.g. polymer in solvent) and quantifies the solvent quality based on the relative solvent–solvent, solvent–polymer, and polymer–polymer interactions. It has successfully been used to predict the solubility of OSCs in the past.[128–130] Flory-Huggins theory approximates a binary mixture (here between species A and B) as a lattice site model for which the energy of mixing can be written in terms of pair interactions between adjacent lattice sites. The Flory-Huggins interaction parameter, χ_{FH}, can be defined from these interactions, and describes the difference between the unlike and like interaction energies per lattice site relative to the thermal energy $k_{\mathrm{B}}T$. See ref 127 for details.

The method we use here for calculating χ_{FH} from MD simulations was inspired by that of Caddeo et al. [129] who calculated the Flory-Huggins parameter from the cohesive energy density (CED) of a pure polymer, pure solvent, and mixed system. The CED is related to the energy required to go from a condensed to vapour phase of a specific system per unit volume, so is a measure of the total intermolecular non-bonded interactions within the system. In the work of Caddeo et al. [129] the CED was estimated from the total non-bonded potential energy in the condensed phase simulations. As MD force-fields artificially partition the bonded (particularly the dihedrals) and non-bonded interactions, we have extended this definition to include the bonded interactions, which may also change significantly on mixing, by using the total potential energy (that is the total bonded + non-bonded energy per

unit volume) rather than the CED. χ_{FH} is then calculated as

$$\chi_{FH} = \frac{U_{mix}}{N\phi_p\phi_s k_B T} \tag{2.31}$$

where U_{mix} is the change in total potential energy (bonded + non-bonded interactions) on mixing, N is the number of lattice sites in the mixture, and ϕ_p and ϕ_s are the volume fractions of polymer and solvent in the mixture respectively. The mixing energy U_{mix} in eqn (2.31) is related to the total potential energy per solvent molecule in the mixture U_m, the pure solvent U_s, and the pure polymer U_p systems as

$$U_{mix} = U_m - N_s U_s - N_p U_p \tag{2.32}$$

where the pure solvent system contains N_s solvent molecules, the pure polymer system N_p monomers, and the mixture N_s and N_p solvent molecules and monomers, respectively. The resulting value of χ_{FH} will then be a measure of the solvent quality: a good solvent is expected to have a negative value of χ_{FH} while a poor solvent is expected to have positive χ_{FH}.

2.3.2 Chain conformations

A number of measures of polymer chain conformation are used in this work to understand the effect of solvent quality and backbone flexibility on aggregate structure (Chapter 4). Here we describe a number of important properties that are relevant to this work in more detail.

2.3.2.1 Radius of gyration

The radius of gyration, R_g, describes how extended or compact a single chain, or aggregate, is. It is defined as the root mean squared distance between a point on the polymer chain and the polymer's center-of-mass:

$$R_g^2 = \frac{1}{N}\sum_{i=1}^{N} |\boldsymbol{R}_i - \boldsymbol{R}_{COM}|^2 \tag{2.33}$$

where $\boldsymbol{R}_i$ is the position of monomer i, and $\boldsymbol{R}_{COM}$ the center-of-mass of the polymer chain of length N.[127] A more compact conformation of a polymer will have a smaller radius of gyration, while an extended structure will have a larger R_g.

2.3.2.2 End-to-end distance and contour length

The end-to-end vector is, unsurprisingly, the vector connecting the monomers at the two ends of the polymers. The mean-squared end-to-end distance, R_{ee}, can be defined from this vector as

$$\langle R_{ee}^2 \rangle = \langle |\boldsymbol{R}_N - \boldsymbol{R}_1|^2 \rangle \tag{2.34}$$

where $\boldsymbol{R}_N - \boldsymbol{R}_1$ is the distance between the end monomers (monomers 1 and N positioned at $\boldsymbol{R}_1$ and $\boldsymbol{R}_N$ respectively for chain length N) averaged over all chain conformations. Like the radius of gyration, it can be used as a measure of how extended or collapsed a polymer chain is: a folded polymer structure will have a smaller end-to-end distance than a fully extended chain.

Related to this property is the contour length, R_{max}, which is the total length of the polymer chain if fully extended.

2.3.2.3 *Persistence length and Kuhn length*

The persistence length and Kuhn length are related measures of the stiffness of the polymer backbone. The ideal chain described by the previous parameters can equivalently be described as a freely jointed chain where the polymer is divided into equal segments that give the same $\langle R_{\text{ee}} \rangle$ and R_{max} as the ideal chain (Fig. 2.7). The size of this segment is the Kuhn length, b, which can be defined as

$$b = \frac{\left\langle R_{\text{ee}}^2 \right\rangle}{R_{\text{max}}} \tag{2.35}$$

for mean-square end-to-end distance R_{ee}, and contour length R_{max}. For the worm-like chain model, the persistence length l_{p} is simply related to the Kuhn length b as $l_{\text{p}} = b/2$.

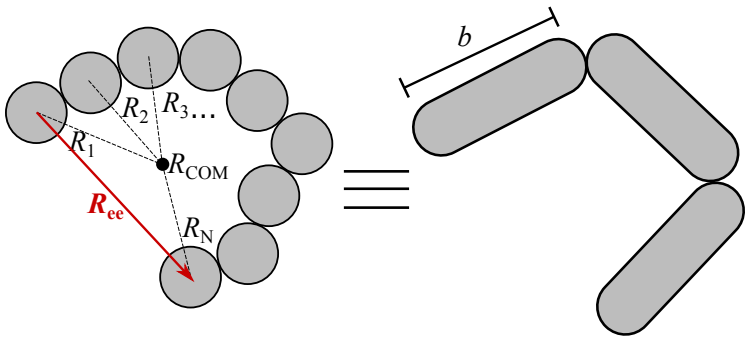

Fig. 2.7 Description of some important properties for describing polymer conformation. Each grey circle represents a single monomer of an ideal chain. The black dashed lines highlight the distances used for the calculation of the radius of gyration. The red line shows the end-to-end distance R_{ee}^2. The structure on the right is the equivalent freely jointed chain, described by the same $\langle R_{\text{ee}} \rangle$, and R_{max} as the ideal chain model.

3

A simple predictor of interface orientation of fluids of disk-like anisotropic particles and its implications for organic semiconductors

"Entropy shakes its angry fist at you for being clever enough to organize the world."

— Brandon Sanderson, *Alcatraz versus the knights of Crystallia.*

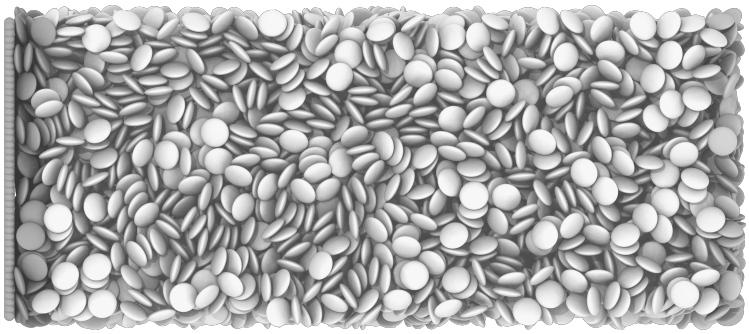

Published

This work has appeared in the following publication:

Boehm, B. J.; Huang, D. M. A Simple Predictor of Interface Orientation of Fluids of Disk-like Anisotropic Particles and Its Implications for Organic Semiconductors. *Soft Matter* **2022**, *18*, 1843–1857.

AUTHORSHIP STATEMENTS

Principal author (candidate): Belinda J. Boehm
Contribution: 85%
Designed coarse-grained model and carried out simulations and analysis. Construction of figures. Conception, writing, and drafting of manuscript. This paper reports on original research I conducted during the period of my Higher Degree by Research candidature and is not subject to any obligations of contractual agreements with a third party that would constrain its inclusion in this thesis. I am the primary author of this paper.

Signature: Date: 22/02/2022

Co-author contributions

By signing the Statement of Authorship, each author certifies that:

1. the candidate's stated contribution to the publication is accurate (as detailed above);
2. permission is granted for the candidate to include the publication in the thesis; and
3. the sum of all co-author contributions is equal to 100% less the candidate's stated contribution

Co-Author: David M. Huang
Contribution: 15%
Conceived project, supervised the model development, simulations, interpretation of results, and the conception and revision of manuscript. Acted as corresponding author.

Signature: Date: 22/02/2022

Abstract

From classical molecular dynamics simulations, we identify a simple and general predictor of molecular orientation at solid and vapour interfaces of isotropic fluids of disk-like anisotropic particles based on their shape and interaction anisotropy. For a wide variety of inter-particle interactions, temperatures, and substrate types within the range of typical organic semiconductors and their processing conditions, we find remarkable universal scaling of the orientation at the interface with the free energy calculated from pair interactions between close-packed nearest neighbours and an empirically derived universal relationship between the entropy and the shape anisotropy and bulk volume fraction of the fluid particles. The face-on orientation of fluid particles at the solid interface is generally predicted to be the equilibrium structure, although the alignment can be controlled by tuning the particle shape and substrate type, while changing the strength of fluid–fluid interactions is likely to play a less effective role. At the vapour interface, only the side-on structure is predicted, and conditions for which the face-on structure may be preferred, such as low temperature, low interaction anisotropy, or low shape anisotropy, are likely to result in little orientation preference (due to the low anisotropy) or be associated with a phase transition to an anisotropic bulk phase for systems with interactions in the range of typical organic semiconductors. Based on these results, we propose a set of guidelines for the rational design and processing of organic semiconductors to achieve a target orientation at a solid or vapour interface.

3.1 INTRODUCTION

Anisotropic molecules, whose shape deviates significantly from spherical, are hugely important in many technologies. In many cases, such molecules can form orientationally ordered liquid-crystal phases that can be controlled by temperature or concentration, and are the basis of a multi-billion dollar display industry, with an extensive history dating back to the late nineteenth century.[216] Additionally, organic molecules with extended π-conjugation, many of which form liquid-crystal phases, have been shown to display interesting opto-electronic properties, and devices based on these organic semiconductors (OSCs) are growing in importance as their performance improves.[217,218]

As important electronic processes often happen in the vicinity of interfaces,[56–58,219] controlling the alignment of molecules at these interfaces is important for optimising the performances of OSC-based devices and liquid crystal displays (LCDs). Due to the anisotropic shape of these molecules, symmetry breaking at both solid and vapour interfaces often leads to a preferred orientation,[74] even when the bulk phase is isotropic. This interface alignment has broad implications for device performance.

For a uniaxial molecule (in which two of the principal axes are equivalent), alignment can vary between the extremes of the non-equivalent molecular axis aligned parallel (planar anchoring; side-on orientation for an oblate ellipsoid) or perpendicular (homeotropic anchoring; face-on orientation for an oblate ellipsoid) to the interface (Fig. 3.1). For biaxial molecules (in which all three principal axes are different), three alignment extremes are possible: face-on, end-on, and side-on.

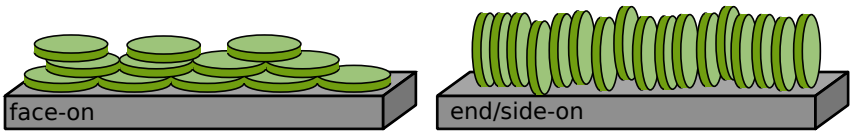

Fig. 3.1 Face-on versus end/side-on alignment at an interface for disk-shaped particles. Interface orientation of rod-like particles can be similarly defined by the angle of their long axis with respect to the interface. For uniaxial particles, end-on and side-on orientations are equivalent.

In OSCs in particular, orientation at the solid and vapour interface is important for improving the performance of a variety of devices, with different functionalities requiring different alignments. In organic field-effect transistors (OFETs), for example, charge mobility is greater when molecules are aligned side-on at the solid dielectric interface, as charge transport can occur in the π-stacking direction rather than having to proceed through the often insulating side-chains.[20,25,45,50,51,64] Conversely, in organic photovoltaics (OPVs), the face-on orientation at the electron donor–acceptor bulk heterojunction (BHJ) interface is favoured as it reduces charge

recombination by allowing efficient charge transport away from the interface, while also ensuring better charge generation by increasing donor–acceptor orbital overlap.[7–9,220,221] More specifically, charge separation at the donor–acceptor interface has been shown to be favoured by a displaced planar (slip-stacked) molecular arrangement rather than a perfectly stacked (cofacial) arrangement because it leads to weakly bound charge-transfer states that can readily separate but are less susceptible to recombination.[222] Organic light-emitting diode (OLED) performance also depends on the orientation of the emitter's transition dipole moment with respect to the substrate, with planar alignment preferred.[46–49] The design of molecules for these devices should therefore focus not only on the electronic properties of the individual molecule, but also on how the molecules align at important interfaces in the device in order to maximise performance.

Although the importance of controlling interface orientation in OSC devices is generally well understood, and there is no shortage of experimental[7–10] or computational[11–15,164] examples of preferential alignment of anisotropic molecules at interfaces, there remain few general rules for predicting alignment at either the solid or vapour interface from the chemical structure of OSC molecules. We have recently extensively reviewed the subject in the context of OSCs,[1] and despite a number of factors being implicated in controlling molecular orientation, in many cases an understanding of the general physical principles that dictate this behaviour was lacking, especially at the solid interface.

There is an extensive history of simulations of liquid crystals using simple computational models (see ref 223 for a review), which have been used to provide a basic understanding of the behaviour of these anisotropic molecules. A smaller subset of these studies have examined the interplay of repulsive and attractive interactions in controlling the interfacial orientation. At a free interface (such as that with a vapour phase), the orientation of anisotropic particles has been studied at various levels, ranging from mean field theories,[80] to particle-based molecular dynamics (MD),[82] and Monte Carlo (MC)[84,224] simulations. It has been found that switching between the face-on and side-on orientation at this interface can be achieved by tuning the anisotropy of the attractive interactions. In the absence of attractive interactions, the long axis of an anisotropic molecule has been predicted to align perpendicular to the interface due to excluded-volume entropic effects.[80] MD simulations of the Gay-Berne (GB) fluid have indicated a dependence of the orientation at the vapour interface of nematic fluids on the ratio of the shape anisotropy to the interaction anisotropy of the particles.[82,84] Fluids that are isotropic in the bulk have also been shown to display preferential alignment at a vapour interface.[224]

In contrast, at the solid interface, free volume is maximised in the face-on

orientation, for which the long molecular axis is parallel to the interface.[85] Density functional theory calculations of hard platelets,[225,226] and theoretical calculations of hard spherocylinders[227] and spheroplatelets[228] at hard impenetrable walls show a preference for alignment with the short axis of the molecule perpendicular to the wall due to entropic effects and minimisation of the surface tension. The inclusion of attractive interactions between fluid particles has been predicted to introduce a temperature dependence to interface orientation, with systems at high temperatures showing the same alignment as the purely repulsive systems due to the dominance of entropy, and a transition to the opposite alignment at lower temperatures as energetic effects become more significant.[87,229] Many computational studies of specific systems have shown similar dependences on temperature and interaction anisotropy.[230–235] In general, the orientation at the solid interface depends on both the strength and anisotropy of the fluid–substrate interactions,[87] and the strength of the fluid–fluid interactions.[236] A number of experimental studies report control of orientation at this interface for specific small molecules,[221,230,232,237–241] and the strength of the interactions with the substrate has been shown to directly influence the orientation, again for a specific set of interaction parameters.[231]

An interesting illustration of the contrasting behaviour of hard particles at solid and vapour interfaces is the case of a penetrable wall, from which a particle's centre-of-mass is repelled but which the rest of the molecule can penetrate to varying degrees.[242,243] As the wall interacts isotropically with the centre-of-mass of the anisotropic particle, a highly penetrable wall is qualitatively similar to a free interface, whereas a impenetrable wall represents a solid interface. MC and density functional theory calculations of these interfaces show a transition between face-on alignment at an impenetrable surface and side-on alignment at a fully penetrable wall,[242,243] consistent with previous theoretical predictions at solid and vapour interfaces, respectively, due to excluded-volume entropic effects.[80,229]

Although a number of general rules that appear to be relatively predictive for determining the orientation of anisotropic particles at both solid and vapour interfaces exist, and many specific examples of orientation control can be found in the literature, a more detailed understanding of how molecular shape and interactions control the orientation in general, and the ability to predict orientation based on combined energetic and entropic contributions using a simple analytical expression, is lacking. In this work, we investigate a series of disk-shaped OSC-like systems using equilibrium coarse-grained MD simulations of GB particles between solid and vapour-like interfaces. These simulations allow for systematic tuning of the strength of the interactions, shape of the anisotropic molecule, and its interactions with the substrate, to gain an understanding of how the interplay of these features influences the orientation at both the solid and vapour interfaces. The use of GB

particles, which have a simple ellipsoidal shape, means that these results should be generally applicable to a wide range of molecules, whether OSCs or not, that share similar shapes and interactions, rather than specific to a single type or class of chemical structure.

We focus our work here on systems that are isotropic in the bulk in order to isolate the effects of the interfaces, to remove the additional complications associated with alignment of additional layers, and to broadly understand what happens under experimental conditions in which a thin film of anisotropic molecules is annealed from the melt, deposited from solution, or subjected to high operating temperatures. It is important to note, however, that device fabrication from an isotropic liquid phase is uncommon, and not expected to be possible at room temperature. The behaviour of isotropic liquids is therefore more applicable to post-processing of thin-film devices, which may involve treatment with high temperatures, than to the deposition process. Though studying only simple single-component systems, this work also presents an initial step towards understanding the behaviour of components of mixtures (such as solution-phase OSCs) at various interfaces, which has significant importance for the fabrication of OSC devices. Generalisation to interfaces with bulk fluids that are anisotropic is possible. We also focus on simulations of equilibrium fluid structure.

The paper is organised as follows. We first describe the simulation and analysis methods in Section 3.2. We then show that molecular orientation of anisotropic fluid particles with both repulsive and attractive interactions at the solid and vapour interface of an isotropic fluid cannot generally be predicted using a previously proposed metric, and propose a semi-empirical mean-field estimate of the free-energy difference between the perfectly face-on and side-on orientations as an alternative. We use simulations of purely repulsive particles confined between a solid and vapour interface to obtain quasi-universal relationships for the scaling of the entropic component of the free energy with the shape anisotropy and bulk density of the fluid particles (Section 3.3.1). Combining this estimate of the entropy with an estimate of the energetic component of the free energy from nearest-neighbour pair interactions (Section 3.3.2), we show that this free energy parameter accurately predicts molecular orientation at the solid (Section 3.3.3.1) and vapour (Section 3.3.3.2) interfaces. In Section 3.3.4 we generalise these results into a number of practical design principles for OSCs, with the goal of providing guidelines towards rational design of OSC interfaces.

3.2 METHODS

The orientation of a fluid of anisotropic particles at both solid (impenetrable) and vapour-like (penetrable) interfaces was studied using classical molecular dynamics (MD) simulations. A range of uniaxial oblate Gay-Berne (GB) ellipsoids, representative of typical small OSC molecules, were studied to elucidate the general effects of shape and interaction anisotropy. These simple models greatly increase computational efficiency compared with all-atom simulations, allowing a wide variety of parameters and conditions to be examined. Simulations were carried out using LAMMPS (version 3 March 2020),[181,244] and visualisation and analysis of simulation trajectories were conducted using OVITO.[245]

The GB potential[81] is an anisotropic form of the widely used Lennard Jones (LJ) pair potential, and captures the short-ranged excluded-volume repulsion and longer ranged van der Waals attraction between uncharged anisotropic molecules. The potential is characterised by parameters σ and ϵ that define the length and energy scales of the potential, respectively, parameters ν and μ that tune the shape of the potential, and, for uniaxial particles, the short and long principal diameters, σ_F and σ_S, and dimensionless relative well depths, ϵ_F and ϵ_S, along the corresponding axes (the subscripts "F" and "S" denote "face" and "side", respectively). The anisotropy of the uniaxial particles is described by the shape anisotropy parameter $\kappa = \sigma_\mathrm{F}/\sigma_\mathrm{S}$ and the interaction anisotropy parameter $\kappa' = \epsilon_\mathrm{S}/\epsilon_\mathrm{F}$. A full description of the GB potential and parameters is given in the SI, Section S3.1.

In all simulations, we have used $\nu = 1$ and $\mu = 2$, as is common for the GB potential, in line with its original parameterisation[81] and previous parameterisations of OSC systems,[199] and and have set $\epsilon_\mathrm{S} = 1$ and $\sigma_\mathrm{F} = 1.03\sigma$. A non-bonded interaction cutoff of $3\sigma_\mathrm{S}$ was used for all systems. In order to match experimentally relevant systems, published GB parameters for biaxial models of several simple OSCs[199] were used as a starting point to define the interactions in the systems studied here. The relationship between σ_F and σ was taken from the published perylene model, with a similar relationship found for a range of other simple OSC systems.[199] To obtain a simpler uniaxial representation of each molecule, for which the end–end and side–side interactions and dimensions are equivalent, the published biaxial principal-diameter and well-depth parameters for end–end and side–side interactions were averaged. This typically resulted in changes to these parameters of less than 10 and 20%, respectively, from their original published values. The resulting shape and interaction anisotropies of several small organic molecules are given in Table 3.1 and inform the values of κ and κ' explored.

We have used LJ reduced units throughout this work, with energies, lengths, temperatures, pressures, and times given in units of ϵ, σ, ϵ/k_B, ϵ/σ^3, and $\tau \equiv \sqrt{m_0\sigma^2/\epsilon}$,

Table 3.1 Shape anisotropy parameter κ and interaction anisotropy parameter κ' for uniaxial models of some typical OSCs and benzene based on published parameters for biaxial models.[199] The side–side parameters used to calculate the anisotropies in each uniaxial model were obtained as the average of the side–side and end–end parameters in the biaxial model, as described in the main text.

molecule	κ	κ'
porphine	0.28	0.159
pyrene	0.34	0.164
perylene	0.36	0.190
benzene	0.47	0.270

where m_0 is the unit of mass and k_B is the Boltzmann constant. We note that setting $\epsilon = 1.8$ kcal/mol and $\sigma = 3.2$ Å gives behaviour consistent with the experimental behaviour of perylene, i.e. a density of 1.1 g/cm^3 at 560 K and 1 atm for a system with κ and κ' approximately those of perylene in Table 3.1,[199] and so the parameter range studied should be representative of the behaviour of a variety of OSCs given this choice of ϵ and σ.

To mimic the scaling of molecular mass with molecular size typical of OSCs, the particle mass m was scaled in proportion to the particle volume $v_f = \pi\sigma_F\sigma_S^2/6$ (calculated as the volume for an ellipsoid with principal diameters σ_F, σ_S, and σ_S) to give a constant mass density within the particle. Although approximate, this behaviour is reasonably representative of real systems, for which the mass density within the particle generally varies between 1.4 and 1.7 g/mol/Å^3 when the particle volume is calculated from published biaxial GB parameters[199] (SI Table S3.3). To facilitate comparison between systems with different sized particles, we have analysed results in terms of the volume fraction, ϕ, rather than the number density, ρ_b, in the bulk fluid. The two are related as $\phi = \rho_b v_f$.

To encompass the region of parameter space in Table 3.1 for typical OSCs, values of κ of 0.30, 0.35, 0.40, 0.45, and 0.50, and κ' of 0.15, 0.20, 0.25, and 0.30 were used. Additional κ' values of 0.50 and 0.70 were examined for certain systems to access points with $\kappa' > \kappa$, as interfacial behaviour has previously been predicted to exhibit a transition around $\kappa/\kappa' = 1$ in some circumstances.[84] Several systems with $\kappa' = 1.2$ were also studied to examine the behaviour when side–side interactions are stronger than face–face ones. While side–side interactions that are stronger than the face–face ones are not typical of OSCs-like molecules, they can potentially be accessed through, for example, functionalisation of the aromatic core and may present an interesting means of tuning interfacial orientation. The systems with $\kappa' > 1$ in this work had weaker face–face interactions than the systems with $\kappa' < 1$ in order to maintain an isotropic bulk fluid as the side–side interactions were increased,

meaning face–face interactions were weaker than would be the case for a typical OSC. As the alignment at both solid and vapour interfaces is expected to depend on temperature, due to competition between excluded-volume entropic effects and attractive intermolecular interactions,[229] several temperatures between 0.56 and $0.84\epsilon/k_B$ were studied, corresponding to a temperature range of 507–761 K for the representative OSC systems described above, encompassing a range of temperatures where the OSCs-type molecules that are represented by these GB parameters are liquid. A full list of the specific systems studied is given in the SI, Table S3.6.

Simulations were conducted with the fluid confined in the z direction between two fixed interfaces parallel to the (x, y)-plane, as illustrated in Fig. 3.2a: a particle-based solid surface at the bottom and a perfectly flat wall at the top that interacts with the center of each fluid particle with a repulsive harmonic potential,

$$u_w(z) = \begin{cases} \epsilon_w (z - z_w)^2, & z > z_w, \\ 0, & \text{otherwise}, \end{cases} \tag{3.1}$$

where z_w is the wall position, ϵ_w describes the strength of the wall–particle interaction, and z is the vertical position of the centre of the fluid particle. This repulsive wall was implemented at the top surface of the fluid to maintain an approximately constant average fluid density between systems with particles of the same shape and to prevent evaporation. Similar to a vapour interface, this wall constrained only the vertical position of the centre of a fluid particle and placed no constraints on the position of the particle surface defined by the repulsive part of the GB potential. We will refer to this vapour-like interface as the "vapour interface" in what follows, and note that it is comparable to the penetrable walls used in previous studies of interface ordering of anisotropic particles.[242,243] In contrast, no part of a fluid particle could penetrate the solid surface.

The solid substrate was modelled as a single layer of either atomistic graphene or silicon, positioned with atoms centred at $z = 0$. It has been suggested experimentally that these substrates interact strongly (graphene) or weakly (silicon) with OSCs and may give rise to face-on and side-on orientations, respectively, of the common OSC polymer poly(3-hexyl thiophene) (P3HT).[237] Parameters (non-bonded interactions and bond length) for graphene were taken from the OPLS-AA force field[202] for aromatic carbons ($\epsilon_{ij} = 0.039\epsilon$, $\sigma_{ij} = 1.11\sigma$, bond length = 0.44σ, for $\epsilon = 1.8$ kcal/mol and $\sigma = 3.2$ Å) and atoms positioned in the hexagonal lattice of graphene with separation taken from the OPLS-AA force field as the bond length for aromatic carbons.[202] OPLS parameters were also used for silicon[246] ($\epsilon_{ij} = 0.056\epsilon$, $\sigma_{ij} = 1.70\sigma$) and atoms positioned to give the fcc(001) plane of silicon's diamond cubic lattice (lattice spacing of 1.69σ).[247] Although ϵ_{ij} is larger for silicon, the larger lattice spacing means that the overall attraction of a single GB fluid particle to the substrate is

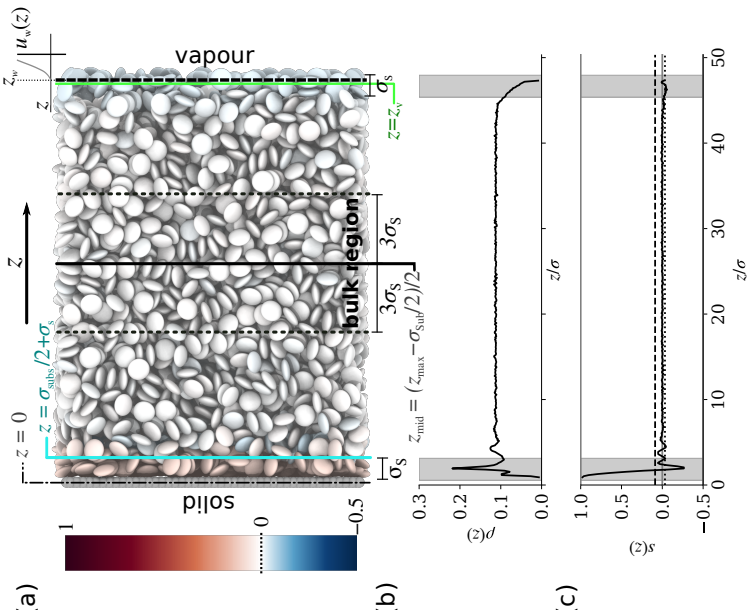

Fig. 3.2 (a) Example of the system setup, with Gay-Berne (GB) fluid particles confined between two surfaces: the impenetrable solid surface consisted of a single layer of Lennard Jones (LJ) particles, centered at $z = 0$ (black dash-dot line), while a repulsive harmonic potential acted on the centre of each fluid particle at the penetrable vapour-like interface (dashed black line) to prevent evaporation. The plot at the top right is representative of the form of this potential. The bulk region was defined as being within $\pm 3\sigma_S$ of the z coordinate of the centre of the box (z_{mid}, black solid line). z_{max} is the maximum z coordinate of any particle during the simulation, σ_{sub} the diameter of a substrate particle, and dotted black lines indicate the bounds of the bulk region. This region was sufficiently far from both interfaces that, except for a couple of the systems that formed anisotropic phases, the fluid had uniform density here. The position of the vapour interface, z_v (green line), was defined as the z-coordinate where the average density was equal to half the average bulk value. The average molecular orientation at the vapour interface, s_{vap}, was calculated as the average of $s(z)$ from eqn (3.2) over particles whose centres were at z coordinates within $z_v \pm \sigma_S/2$ (region indicated in figure). The average molecular orientation at the solid interface, s_{sub}, was calculated by averaging $s(z)$ over fluid particles whose centres were within σ_S of the surface of the substrate (i.e. at $z < \sigma_{sub}/2 + \sigma_S$, cyan line). These definitions selected, to a good approximation, the particles within the first fluid layer at either interface. Particles are coloured by the orientational order parameter $s(z)$ (which is −0.5 and +1, respectively, for fully side-on and face-on orientations), averaged over the entire simulation of this system ($\kappa = 0.4$, $\kappa' = 0.2$, $T^* \equiv k_B T/\epsilon = 0.73$, substrate = graphene). The particles in the two interfacial regions are coloured by the average order parameter calculated over all particles within this region, while all other particles are coloured according to the value of $s(z)$ corresponding to their z coordinate shown in (c). (b) Fluid density $\rho(z)$ and (c) orientational order parameter $s(z)$ profiles calculated over the entire simulation of this system. The shaded areas correspond to the interfacial fluid regions at the solid or vapour interface. Dashed and dotted horizontal lines in (c) correspond to the values of s_{sub} and s_{vap} respectively. Additional $\rho(z)$ and $s(z)$ profiles can be found in the SI, Section S3.5.

weaker for silicon than graphene. An additional substrate with the same structure as graphene but with interactions that were twice as strong ($\epsilon_{ij} = 0.078\epsilon$, $\sigma_{ij} = 1.11\sigma$) was also examined, which we will call the "strong" substrate. The structures of these substrates are shown in the SI, Fig. S3.1. The mixing rules for combining GB parameters of two dissimilar particles,[199] defined by eqns (3.10)–(3.15) of the SI, were used to model the fluid–substrate interactions so as to maintain the correct shape dependence of the interactions. The interaction range σ in eqn (3.9) of the SI was replaced by the arithmetic mean, $(\sigma + \sigma_{ij})/2$, of the fluid and substrate interaction ranges for the fluid–substrate interactions. The substrate parameters, and the influence of the type of substrate on the orientation at both interfaces are given in full in the SI (Table S3.4, Fig. S3.2).

To give comparable steepness for the repulsive potential at the vapour interface to the interaction with the solid substrate, the value of ϵ_w was determined by fitting eqn (3.1) to the repulsive part of the potential energy versus z of a single fluid particle representative of perylene ($\kappa = 0.36$, $\kappa' = 0.19$) interacting with the solid substrate in the face-on orientation for the region where the potential energy was $< 2k_BT$ at $T = 0.62\epsilon/k_B$. This gave a value of $\epsilon_w = 17.8\epsilon$ for the graphene substrate and $\epsilon_w = 8.9\epsilon$ for the silicon substrate. The same values for each substrate were used for both the attractive and repulsive surfaces, and the graphene value also used for the "strong" substrate, as the strength of the wall potential did not significantly affect the behaviour at the vapour interface (SI Fig. S3.2).

All simulations were conducted at constant volume and temperature with the positions of the substrate particles fixed. Each system consisted of 6000 fluid particles and 4680 (graphene) or 800 (silicon) substrate particles. The simulation timestep was 0.012 τ, which corresponds to 5 fs if the unit of mass m_0 is taken to be the molecular mass of perylene. Temperature was controlled with a Nosé-Hoover thermostat[195,196] and set to values of 0.56, 0.62, 0.73, or $0.84\epsilon/k_B$. Most systems were constrained to a constant overall volume fraction ϕ_{av} (that is, the volume fraction calculated from the number density of all particles between $z = \sigma_{sub}/2$, the surface of the substrate, and $z = z_w$, the position of the harmonic wall) of 0.39, corresponding to a real density on the order of 1.1 g/cm^3 if $\epsilon = 1.8$ kcal/mol and $\sigma = 3.2$ Å. The z coordinate of the harmonic wall, chosen to achieve the desired overall volume fraction for the different values of κ, are given in the SI Table S3.1. Additional systems were examined at lower (0.28) and higher (0.49) ϕ_{av} values to determine the dependence (if any) of interfacial orientation on the system density. The pressure in each system was measured as the normal force per unit area acting on the solid substrate. The average pressure at equilibrium was generally $< 200\epsilon/\sigma^3$, but was up to $1200\epsilon/\sigma^3$ for $\phi_{av} = 0.49$.

To initialise the simulations, fluid particles were packed with random positions

and orientations into a large box (periodic in x, y, and z, with x and y dimensions 10× the target values and z dimension equal to the target value). For systems to be simulated with the graphene substrate, the target x and y dimensions were 34.48σ and 34.125σ, respectively, to enable periodic packing of the substrate particles; for the silicon substrate, the final dimensions were $x = y = 33.94\sigma$ for the same reason. The size in the z dimension was used to control the volume fraction of fluid particles and so depended on fluid particle size; the values for various systems can be found in the SI Table S3.1. A soft potential $U_{\text{soft}}(r) = A\left[1 + \cos\left(\frac{\pi r}{r_c}\right)\right]$ for $r < r_c$, where r_c is is a cutoff distance and A an energy pre-factor that varies the "hardness" of the potential, was applied to remove particle overlaps ($r_c = 5\sigma$, A increased linearly from 0 to 16.7ϵ over 20,000 timesteps). Interactions were changed from the soft potential to the GB potential, and the box dimensions shrunk linearly over 50,000 timesteps at a higher temperature of $T = 0.88\epsilon/k_B$ to give the final dimensions outlined above. To initialise the system in an isotropic phase, the fluid particles were then allowed to equilibrate in the bulk system at $T = 0.88\epsilon/k_B$ for another 50,000 time steps. The periodic boundary conditions in the z direction were then removed, and the box extended in the z direction to give a region of vacuum above the bulk fluid. The solid substrate was introduced below the fluid, and the harmonic wall at the vapour interface was positioned at the z coordinate required to give the desired overall volume fraction (SI Table S3.1). The energy of the system was then minimised to remove any overlaps between fluid and interfaces. The system was simulated for a further 510,000 timesteps at the specified temperature, with the equilibration and correlation time for the orientation of the top and bottom fluid layers determined using pymbar's timeseries module,[248,249] which estimates the equilibration time as the time that maximises the number of uncorrelated samples (see ref. 250 for details). Only the data after the equilibration time was used for further analysis. Although a number of systems were simulated that were anisotropic in the bulk (typically for the most anisotropic shapes and interactions; see SI Table S3.6 for a list of systems that formed anisotropic bulk phases), the slow dynamics in these systems did not allow equilibrium properties to be measured reliably over the time scales that were simulated. Results are therefore only reported in the main paper for systems with an isotropic bulk fluid phase.

3.2.1 purely repulsive particle simulations

As their interactions have, to a good approximation, no energetic component, purely repulsive particles were used to determine the contribution of entropy to molecular alignment at the solid and vapour interfaces. For these purely repulsive particles, the shape parameters described above (with $\kappa = 0.30, 0.35, 0.40, 0.45, 0.50$) were used, and κ' was fixed at 0.2 ($\epsilon_S = 1$, $\epsilon_F = 5$). The GB potential was cut-off and

shifted to 0 at the minimum for each orientation to obtain a purely repulsive potential,[251] analogous to the Weeks–Chandler–Andersen (WCA) truncation of the LJ potential.[252] Likewise, a cut-off and shifted form of the fluid–substrate interactions, using the mixing rules for combining GB parameters of two dissimilar particles[199] discussed previously, was used for the interactions with the solid substrate. These simulations were conducted at $T = 0.62\epsilon/k_B$ at overall volume fractions between 0.1 and 0.5 using either the silicon or graphene substrate. Although these systems are expected to be athermal, simulations were also carried out for the silicon substrate at $T = 0.8\epsilon/k_B$ to verify this fact. A full list of the systems studied is given in SI Table S3.5. Data for the different substrates and temperatures were combined to determine the scaling of interface orientation with system parameters (see SI, Section S3.4).

3.3 RESULTS AND DISCUSSION

We have examined the orientation of anisotropic particles with both attractive and repulsive interactions at solid and vapour interfaces. The average molecular orientation as a function of the coordinate, z, perpendicular to the interface was quantified by the orientational order parameter

$$s(z) = \langle P_2(\cos\theta)\rangle_z = \frac{3\left\langle \cos^2\theta \right\rangle_z - 1}{2}, \tag{3.2}$$

where θ is the angle between the short (unique) particle axis and the z axis, and the average $\langle\cdots\rangle_z$ is over all fluid particles whose centres were in the histogram bin centred at position z. A value of 1 indicates fully face-on alignment, and $-\frac{1}{2}$ indicates fully side-on. For isotropic orientations, $s(z) = 0$. Throughout this work, the terms face-on and side-on will be used to describe any orientation that is either *predominantly* face-on ($s(z) > 0$) or side-on ($s(z) < 0$), not just the fully aligned extremes. Representative density and orientation profiles are shown in Fig. 3.2, and selected additional profiles are given in the SI, Section S3.5.

For a bulk nematic GB fluid, the orientation at the vapour interface has previously been shown to scale with the ratio of the shape and interaction anisotropy parameters, κ/κ', with a face-on orientation observed for $\kappa/\kappa' < 1$, and an side-on orientation otherwise.[84] For the systems studied in this work, in which the bulk phase is isotropic rather than nematic and in which solid interfaces are also considered, Fig. 3.3 shows that κ/κ' is not a good predictor of orientation at either the solid or vapour interface. At the vapour interface, the orientation does not appear to depend on κ/κ' for $\kappa/\kappa' > 1$, although there seems to be a transition to very marginally face-on orientations at $\kappa/\kappa' < 1$, as predicted previously for bulk nematic

fluids.[84] The systems that display a slightly face-on orientation are those with the most isotropic interactions studied here ($\kappa' = 0.7$), resulting in very slight orientation preference, while those with the more face-on orientation are where side–side interactions are stronger than face–face ($\kappa' = 1.2$). Stronger alignment could be achieved by decreasing κ' (increasing interaction anisotropy), but the corresponding increase in the shape anisotropy κ required to maintain $\kappa/\kappa' < 1$, coupled with the more anisotropic interactions, would likely result in systems that are anisotropic in the bulk. At the solid interface, there is a weak trend towards a more face-on orientation as κ/κ' decreases within each set of substrate/temperature conditions, but there is a strong dependence on temperature and $\kappa/\kappa' = 1$ does not correspond to the transition from side-on to face-on orientation. This dependence on temperature points to a significant entropic contribution, which is only accounted for implicitly in the κ/κ' parameter through the shape anisotropy κ.

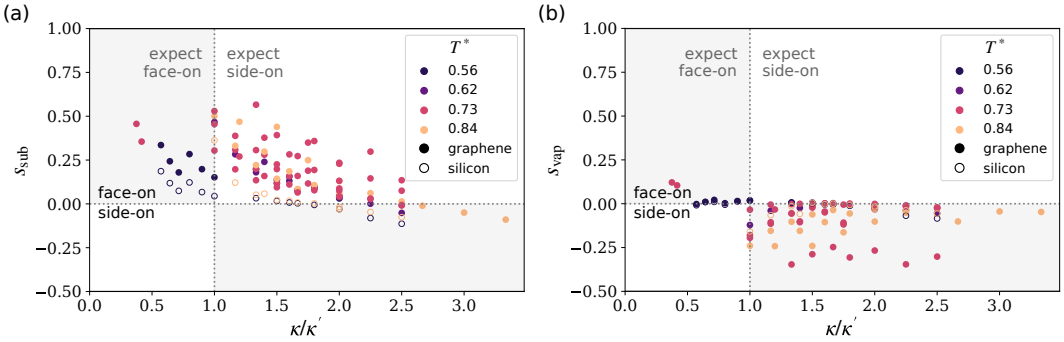

Fig. 3.3 Interface orientational order parameter, s, versus shape-anisotropy:interaction-anisotropy ratio, κ/κ', at the (a) solid and (b) vapour interfaces for graphene-structure (graphene or "strong"; filled symbols) and silicon (unfilled symbols) substrates and various reduced temperatures, $T^* \equiv k_B T/\epsilon$.

Thus, we have considered an alternative metric for predicting the orientation at both solid and vapour interfaces based on an estimate of the free-energy difference between the perfectly face-on ($\theta = 0$) and side-on ($\theta = \pi/2$) orientations, which explicitly accounts for the roles of temperature and fluid–substrate interactions. The overall free energy includes an entropic term, $\Delta\bar{S}$, described in Section 3.3.1 and calculated based on the shape anisotropy, κ, and bulk volume fraction, ϕ, of the system, and an energetic term, $\Delta\bar{U}$, described in Section 3.3.2 and based on the interactions between nearest-neighbour particles. The free energy difference per interface particle between perfectly face-on and side-on orientations is calculated as

$$\Delta\bar{F} = \Delta\bar{U} - T\Delta\bar{S}. \tag{3.3}$$

where overbars indicate per-particle quantities. A predominantly face-on orientation is predicted for $\Delta\bar{F} < 0$, and side-on for $\Delta\bar{F} > 0$, with the degree of interface

alignment expected to increase as the magnitude of $\Delta\bar{F}$ increases.

3.3.1 ENTROPIC COMPONENT

Although a number of theories exist to quantify the entropy difference between face-on and side-on interface configurations,[80,85,227–229] a simple, accurate, analytical expression for the entropy as a function of system parameters is lacking, and a nematic bulk phase is often assumed.[85] Instead, we have taken a semi-empirical approach, in which the entropy difference is measured in a comparatively small number of MD simulations of purely repulsive particles, to obtain a universal scaling relationship at the solid and vapour interfaces.

Due to the absence of attractive interactions, any alignment of the purely repulsive particles at the solid or vapour interfaces can, to a good approximation, be attributed entirely to entropy. The Helmholtz free energy difference between two states of a system can be calculated as $\Delta F = \Delta U - T\Delta S$, which in the absence of an energetic contribution ($\Delta U = 0$) gives $\Delta F = -T\Delta S$. The entropy difference per interface particle between states of a system in the NVT ensemble with perfectly face-on and side-on orientations at an interface can then be estimated as

$$\Delta\bar{S} = -\frac{\Delta\bar{F}}{T} = k_{\mathrm{B}} \ln\left(\frac{P_{\mathrm{F}}}{P_{\mathrm{S}}}\right), \tag{3.4}$$

where P_{F} and P_{S} are the probabilities of finding a fluid particle in the solid or vapour interfacial region (defined in Fig. 3.2) in the perfectly face-on ($\cos(\theta) = 1$) and side-on ($\cos(\theta) = 0$) orientations, respectively. The orientational probability distribution $P(\cos(\theta))$ versus $\cos(\theta)$ was approximated as a normalised histogram of observations of the value of $\cos(\theta)$ for fluid particles found in the interfacial region during the simulation, using evenly spaced histogram bins of width $\Delta\cos(\theta) = 0.04$ between $\cos(\theta) = 0$ and $\cos(\theta) = 1$. P_{S} and P_{F} were taken as the histogram values of the first (probability of $0 \leq \cos(\theta) \leq \Delta\cos(\theta)$) and last (probability of $1 - \Delta\cos(\theta) < \cos(\theta) \leq 1$) histogram bins, respectively. It was verified that the histogram bin size was sufficiently small and the number of histogram counts sufficiently large that further decreasing it had little effect on the calculated entropy difference. Examples of the distribution of $\cos(\theta)$ in the interfacial regions are given in the SI, Fig S3.6.

The orientation at the solid interface was found always to be predominantly face-on, while a predominantly side-on orientation was exclusively found at the vapour interface (Fig. 3.4). In both cases, the degree of alignment was found to depend systematically on the volume fraction of the bulk fluid and the shape anisotropy of the fluid particles, with higher densities and shape anisotropies giving a greater degree of alignment. It has previously been predicted that a variety of hard anisotropic particles align with their long axis parallel to a solid substrate,[85,225–228]

as this alignment maximises the free volume and hence is the entropically favoured orientation.[85,228] The opposite argument can be applied at the vapour interface, where the particles are able to extend over the interface, increasing the free volume when their long axis is perpendicular to the interface.[80] Studies of hard ellipsoids at penetrable walls also show this behaviour.[242,243] Thus, for oblate particles, a face-on orientation at the solid interface and a side-on orientation at the vapour interfaces are predicted to be entropically favoured, which is qualitatively consistent with the results presented here.

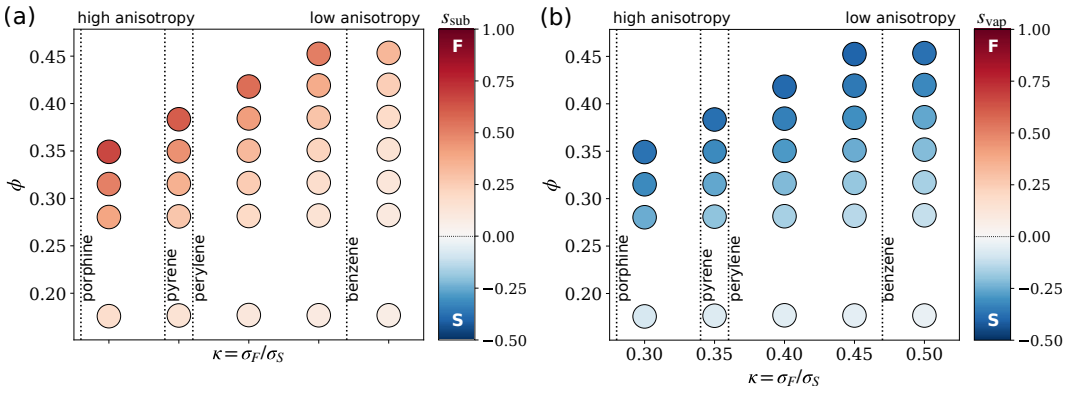

Fig. 3.4 Orientational order parameter of purely repulsive fluid particles at (a) a purely repulsive graphene-like substrate and (b) the vapour interface as a function of shape anisotropy and bulk fluid volume fraction at $T = 0.62\epsilon/k_B$. The colour of each point indicates the value of the order parameter at each interface. The shape anisotropy of various OSCs is indicated for reference. The labels 'F' and 'S' in the colour bar indicate face-on and side-on orientations, respectively. The orientational order parameter value for this and the other substrates and temperatures can be found in the SI, Table S3.5. (The missing points at low κ and high ϕ formed anisotropic bulk phases and could not be equilibrated on the simulation time scale, and so are not included.)

Based on expectations from free-volume arguments[85] that the entropy difference between face-on and side-on interface configurations of purely repulsive particles is controlled by the fluid density (or volume fraction) and molecular shape anisotropy, with the entropy difference increasing with increasing density and shape anisotropy (decreasing κ for oblate particles), we have fit the entropy difference at each interface for all systems to a power law with a positive exponent for ϕ and a negative one for κ. The entropy difference was found to have a quasi-universal power-law dependence on ϕ/κ at the solid interface and on $\phi/\kappa^{1/2}$ at the vapour interface, where ϕ is the bulk fluid volume fraction and κ is the shape anisotropy, as shown in Fig. 3.5, although there is some scatter in the data, particularly for the solid interface. The

scaling relationships that best fit the data in Fig. 3.5 were

$$\Delta\bar{S}_{\text{sub}} = 2.84k_{\text{B}}\left(\frac{\phi}{\kappa}\right)^{2.61} \tag{3.5}$$

at the solid interface and

$$\Delta\bar{S}_{\text{vap}} = -26.29k_{\text{B}}\left(\frac{\phi}{\kappa^{1/2}}\right)^{3.55} \tag{3.6}$$

at the vapour, where a negative value favours a predominantly side-on orientation and positive favours face-on. Note that these empirical relationships were obtained for GB parameters $\nu = 1$ and $\mu = 2$ and may not be valid for repulsive GB potentials with other ν and μ values.

While the scaling at the vapour interface with $\phi/\kappa^{1/2}$ is the same for both substrates, the relationship between the entropy difference and ϕ/κ for the silicon substrate is not as straightforward as that for the graphene substrate (Fig. 3.5a). Due to the spacing of the substrate particles (SI Fig. S3.1), the fluid–substrate potential has more significant lateral corrugations at the silicon interface compared with graphene. This induces a greater dependence of the potential on the in-plane (x, y) coordinates compared to graphene, which is much closer to an "ideal" planar solid surface for which the potential depends only on the z coordinate. Despite the additional variability, the overall scaling behaviour follows the same trend at both substrates, and the fit to all the data was used.

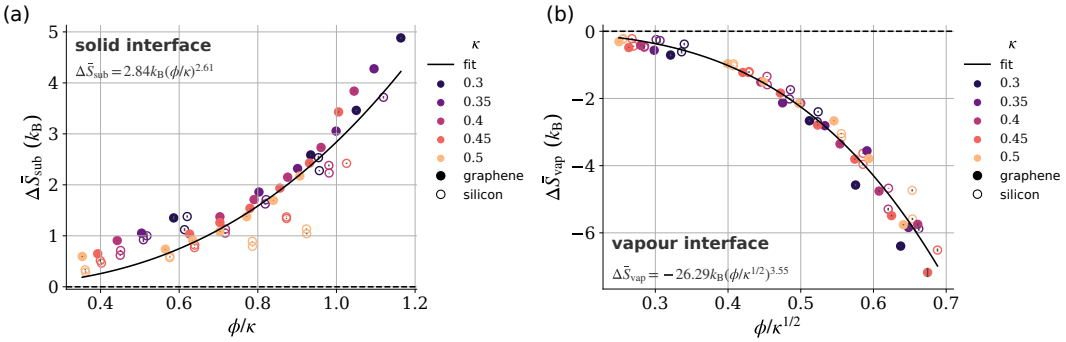

Fig. 3.5 Entropy difference per particle between face-on and side-on orientations as a function of ϕ/κ^n at the (a) solid ($n = 1$) and (b) vapour ($n = 1/2$) interfaces, where ϕ is the bulk volume fraction and κ is the shape anisotropy of the fluid particles. The data here includes all sets of conditions for graphene- (filled symbols) and silicon-like (unfilled symbols) repulsive substrate at $T = 0.62$ or $0.84\epsilon/k_{\text{B}}$. The temperature does not significantly affect the scaling (SI Fig. S3.3). Plots comparing the differences for different temperatures and substrate types are given in the SI, Section S3.4.

Overall, if entropy is the only contributing factor and the system is isotropic in the bulk region, the orientation preference at the solid interface is expected to be

face-on, and side-on at the vapour interface, consistent with previously published theories and calculations.[80,82,84,85,224–229,242,243] Increasing the effect of entropy, such as by using higher temperatures, more anisotropic particles, or higher pressures (to increase density), could be used to enhance this alignment if desired at either interface.

3.3.2 energetic component

The alignment of particles with attractive interactions at the solid interface is complicated by attractive interactions of the fluid with the substrate and within the fluid itself. Qualitatively, the face-on orientation should be energetically favoured when the face–substrate interactions are strong (although this will also depend on the relative strength of the fluid face–face, side–side, and side–substrate interactions), and the side-on orientation should be energetically favoured when the fluid particle's face–face interactions are stronger than both their side–side and face–substrate interactions. Assuming that the fluid is isotropic everywhere except for the layer adjacent to the interface, and that a fully face-on particle interacts with six nearest neighbours through side–side interactions (hcp packing) while a side-on particle has two face–face interactions and two side–side interactions (cubic packing with inequivalent lattice spacing) with its nearest neighbours (as found in simulations in which the interface layer was close to fully aligned, as shown in SI Fig. S3.7), the difference in energy per interfacial fluid particle between a completely face-on orientated interfacial fluid layer and a completely side-on oriented one can be estimated to be

$$\begin{aligned}\Delta\bar{U} &= \bar{U}_{\mathrm{F}} - \bar{U}_{\mathrm{S}} \\ &= \left[\bar{U}_{\mathrm{Fs}} + 6\bar{U}_{\mathrm{Sf}}/2\right] - \left[\bar{U}_{\mathrm{Ss}} + \left(2\bar{U}_{\mathrm{Sf}} + 2\bar{U}_{\mathrm{Ff}}\right)/2\right] \\ &= \bar{U}_{\mathrm{Fs}} - \bar{U}_{\mathrm{Ss}} + 2\bar{U}_{\mathrm{Sf}} - \bar{U}_{\mathrm{Ff}},\end{aligned} \tag{3.7}$$

where $\bar{U}_{\mathrm{F}}$ ($\bar{U}_{\mathrm{S}}$) is the interaction energy of a particle in the face-on (side-on) orientation with its nearest neighbours in the interfacial layer and with the substrate. (Note that the nearest-neighbour fluid interactions are halved in these equations because each such interaction contributes to the energy of two interfacial fluid particles.) $\bar{U}_{ij}$ is the interaction energy in the face-on/face–face orientation (for i = F) or side-on/side–side orientation (for i = S) with the substrate (for j = s) or another fluid particle (for j = f). For fluid–fluid interactions, the interaction energy in either the face–face or side–side orientation was taken as the minimum of the GB pair potential in the specified orientation. $\bar{U}_{\mathrm{Fs}}$ and $\bar{U}_{\mathrm{Ss}}$ were calculated as the minimum in the interaction between a single GB ellipsoid and the substrate in the face–face and side–side orientations, respectively. As a particle-based substrate was

used in this work rather than being perfectly flat, the energy minimum was averaged over 100 random positions on the substrate. Eqn (3.7) also applies for the energy difference per fluid particle at the vapour interface, but with the fluid–substrate interactions set to zero, i.e. $\bar{U}_{\mathrm{Fs}} = \bar{U}_{\mathrm{Ss}} = 0$.

Although the consideration of only nearest-neighbour interactions in the calculation of the interfacial energy difference is a major simplification, it accounts for the most significant inter-particle interactions due to the rapid decay of interaction strength with inter-particle separation; for example, next-nearest-neighbour interactions are only a few percent of the nearest-neighbour interactions in the face–face orientation for the systems studied. Thus, even though a more complex description of interfacial energetics that includes more inter-particle interactions may be more quantitatively accurate, it is not expected to qualitatively affect our findings.

3.3.3 Predicting alignment at solid and vapour interfaces

To predict the behaviour at both the solid and vapour interfaces, we have used the free energy described in eqn (3.3), with the entropic component determined from the bulk volume fraction and shape anisotropy of each system as described by eqns (3.5) and (3.6) for the solid and vapour interfaces, respectively, and with the energetic component determined from the nearest-neighbour interactions in the interfacial layer as described by eqn (3.7).

3.3.3.1 Solid interface

The average molecular orientation at the solid substrate, measured by the orientation order parameter s_{sub}, shows excellent universal scaling with the free energy difference defined by eqn (3.3) for the entire range of systems studied, covering temperatures from 0.56 to $0.84\epsilon/k_{\mathrm{B}}$, bulk volume fractions from 0.29 to 0.50, strongly and weakly interacting substrates, and shape and interaction anisotropies corresponding to molecules as varied as benzene, perylene, and porphine (Fig. 3.6a; see SI Table S3.6 for a full list of systems). Interestingly, although systems with a predominantly side-on orientation at the solid interface are observed, they are relatively rare, being obtained in less than 15% of cases. These side-on systems generally correspond to situations for which the fluid particles have low shape anisotropy (high κ), the system is at low temperature, and to a lesser extent the fluid particles have high interaction anisotropy (low κ'). The rarity of the side-on orientation points to a dominant entropic contribution in most systems studied.

On separating the free energy into its energetic (Fig. 3.6b) and entropic (Fig. 3.6c) components, the reason for the preference for the face-on orientation at this interface becomes clear. Over the range of parameters studied, the energetic component varies from favouring the side-on orientation by values typically in the range of

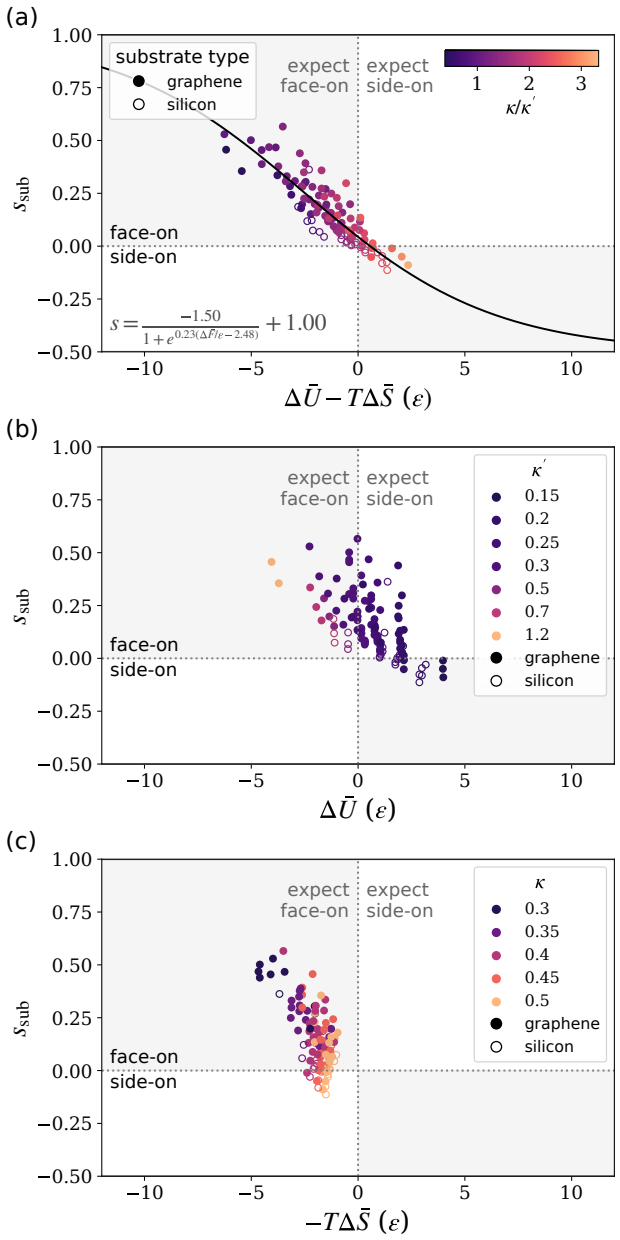

Fig. 3.6 Orientational order parameter s_{sub} at the solid interface as a function of (a) overall, (b) energetic, and (c) entropic components of the interfacial free energy difference. A least-squares best fit to a logistic function, constrained to go to −0.5 and 1 at high and low $\Delta\bar{U} - T\Delta\bar{S}$ respectively, is shown in (a). The energetic component is coloured by the interaction anisotropy parameter, the entropy component by the shape anisotropy parameter, and the overall free energy by the ratio of the two parameters. Filled symbols correspond to the graphene-structure substrate (graphene or "strong") and unfilled symbols to the silicon substrate. Shaded grey regions highlight where the points should fall if obeying the predicted scaling with the free energy or free energy component.

approximately 2ϵ, to the face-on orientation by a similar amount. Over the same range of parameters, the entropic component of the free energy always favours the face-on orientation by between 1 and 5ϵ, increasing in magnitude as the shape becomes more anisotropic. The combined result of these effects is an orientation that is only side-on under conditions where the entropic contribution is lowest (low temperature, low shape anisotropy) or the energetic contribution highest (highly anisotropic interactions). Although highly anisotropic interactions shift the energetic term significantly towards favouring the side-on orientation, high temperatures would be required in many cases to maintain an isotropic bulk fluid, which would increase the mangitude of the entropic term in the opposing direction, giving little change to the overall free energy. This separation of the free energy into its components also highlights that neither the energy nor the entropy is sufficient to completely explain the observed interface orientation, again emphasising the importance of both contributions for accurately predicting the orientation.

When examining the effect of the substrate on the interface orientation, a slight dependence of the scaling of orientation with free energy difference is observed, with the observed orientation at the silicon substrate generally being shifted towards side-on relative to systems at the graphene–structured substrate (with either regular or strong interactions) for the same free energy difference (SI Fig. S3.2). As described previously in the context of the purely repulsive systems, this slight substrate dependence is likely due to the looser packing of substrate particles in the silicon substrate compared with the graphene substrate. This increases the dependence of the fluid–substrate potential on the in-plane coordinates of the fluid particle at the silicon substrate, which behaves as a slighly penetrable surface, relative to the graphene substrate, which is much closer to an "ideal" smooth impenetrable solid substrate. No dependence of the scaling relationship on the strength of the fluid–substrate interactions was observed, however, with the results at the graphene and "strong" (same particle arrangement but double the interaction strength) substrates showing the same behaviour. This result indicates that patterning of the substrate may be an effective method to favour a more side-on alignment, as has been previously observed,[253] although further study would be required to fully understand this behaviour.

Although it appears difficult to significantly influence the interfacial orientation by tuning fluid–fluid interaction strength within the realm of reasonable OSC parameters while the bulk fluid remains in an isotropic liquid phase, the energetic component of the free energy difference does have a strong dependence on the strength of the fluid–substrate interactions. Switching from a strongly (e.g. graphite) to weakly (e.g. silica) interacting substrate has been shown experimentally[221,230,232,237–241] and computationally[231] to influence the orientation at the

solid interface for a range of OSCs. Fig. 3.7 highlights the relative importance of the fluid–substrate interactions: the difference in energy on switching from a strongly to weakly interacting substrate (e.g. graphene to silicon) is comparable to changing the interaction anisotropy from values close to those representative of benzene to perylene (a significant structural change), and is sufficient to switch the free energy from favouring face-on to side-on orientation in some cases.

Although increasing the strength of the substrate–fluid interactions will increase both the side–substrate and face–substrate interaction strength, which make equal and opposite contributions to the energetic component of the interface free energy different in eqn (3.7), the face–substrate interactions are expected to dominate for most cases studied in this work due to two factors. First, the stronger face–face interaction compared with side–side interaction ($\kappa' < 1$) typical of OSCs leads to the strength of face–substrate interactions increasing more rapidly than that of side–substrate interactions when the substrate–substrate interaction strength is increased isotropically, given the mixing rules for fluid–substrate interactions. Second, for oblate ($\kappa < 1$) particle shapes typical of OSCs (all the systems studied in this work), a face-on particle interacts with more substrate particles than a side-on particle, and so the strength of the interaction of a fluid particle with the whole substrate increases more rapidly for face-on particles than for side-on particles when the substrate–substrate interaction strength is increased isotropically, even if the fluid particles have no interaction anisotropy ($\kappa' = 1$). Overall, while changing the fluid–fluid or fluid–substrate interactions are both plausible ways of influencing the energy, large structural changes would likely be required chemically to significantly change the fluid–fluid interaction anisotropy, which will likely also change the shape anisotropy and bulk phase behaviour of the fluid. It should generally be much simpler to change the nature of the solid substrate.

The fluid particles studied here are representative of small OSC molecules such as perylene that do not have any side-chains, but many OSCs feature alkyl side-chains designed to enhance their solubility. The different chemical nature of the backbone and side-chain (one being a conjugated π-system, the other an alkyl chain) means that changing the substrate to favour interactions with either one or the other should enhance either the face-on (strong backbone–substrate interactions) or side-on (strong side-chain–substrate interactions) orientations at the substrate interface. Although we do not consider any molecules with side-chains here, the impact of side-chains can be approximated in the coarse-grained modelling framework used in this work by considering their effect on the overall fluid–substrate interactions: a substrate that is more strongly attracted to the side-chains (particle side) will energetically favour the side-on orientation. This behaviour has been observed experimentally, for example though treatment of a substrate with a self-assembled

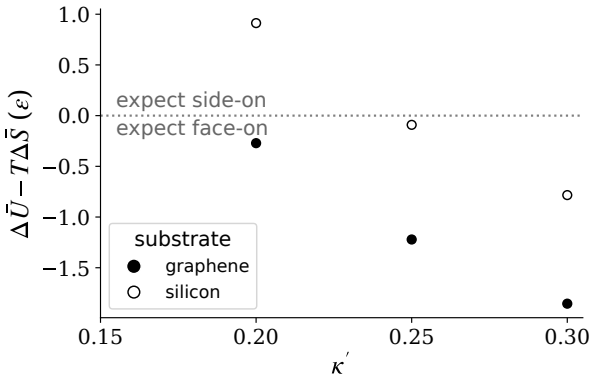

Fig. 3.7 Interface free energy difference as a function of interaction anisotropy parameter κ' at $T = 0.62\epsilon/k_B$ for graphene (filled symbols) and silicon (unfilled symbols) substrates.

monolayer of octadecyltrichlorosilane (OTS).[254]

3.3.3.2 Vapour interface

In contrast to alignment at the solid interface, which depends on the fluid–fluid *and* fluid–substrate interactions, the energetic driver for orientation at the vapour interface is simply expected to be related to the relative strength of the interactions for a face-on and side-on fluid particle with other fluid particles in the interfacial layer. Face–face interactions are maximised in the side-on orientation, so increasing the strength of these interactions is expected to promote the side-on orientation. Compared with the solid interface, the vapour interface does not show as clear universal scaling of the molecular orientation with the interface free energy parameter in eqn (3.3), but a strong trend with the free energy is still observed (Fig. 3.8a). Where $\kappa' < 1$, the orientation at this interface converges towards isotropic at the vapour interface as the free energy approaches zero, and becomes more aligned as the free energy magnitude increases. At high values of κ' (low interaction anisotropy), the energetic component (Fig. 3.8b) shifts towards very slightly favouring a face-on orientation, qualitatively consistent with previous predictions of ordering of bulk nematic fluids at the free interface.[84]

Several systems were also examined with $\kappa' > 1$, corresponding to stronger side–side than face–face interactions, as it is expected to promote the face-on orientation at the vapour interface. Even with reduced face–face interaction strength, bringing them outside the range of typical OSCs, most of these systems did not remain isotropic in the bulk. The two that did were the least anisotropic in shape and are the face-on outliers at $\Delta\bar{U} - T\Delta\bar{S} \approx 2\epsilon$ in Fig. 3.8a. While this result shows that it is possible to achieve a slight face-on orientation at the vapour interface for anisotropic

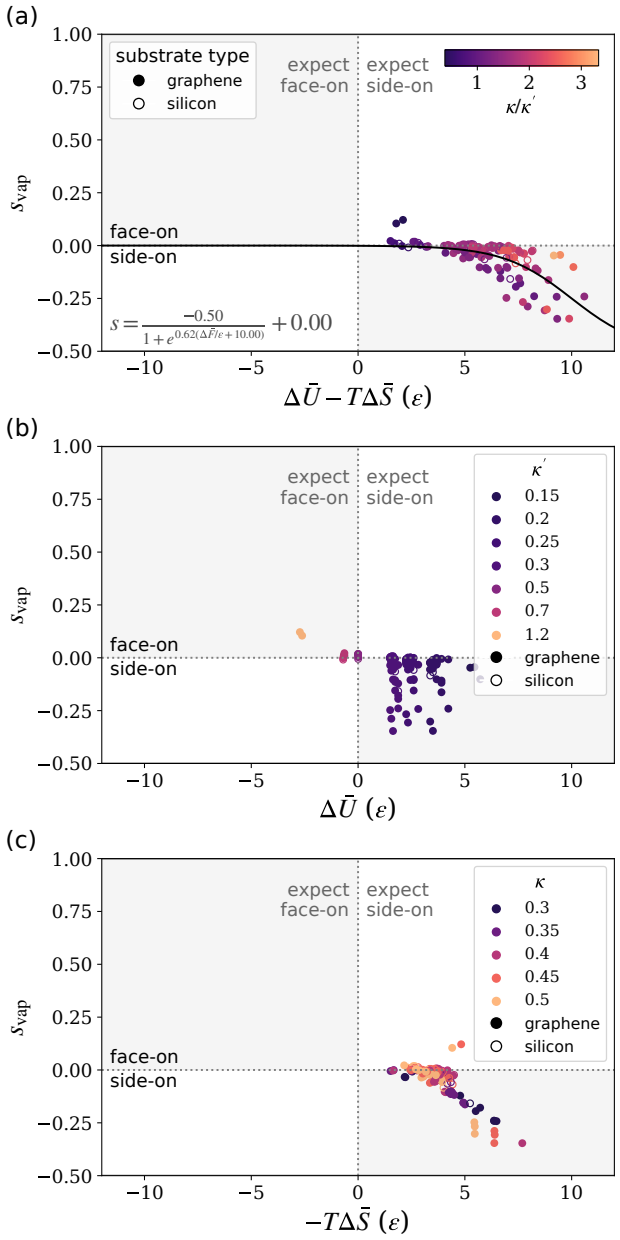

Fig. 3.8 Orientational order parameter s_{vap} at the vapour interface as a function of the (a) overall, (b) energetic, and (c) entropic components of the interfacial free energy difference. A least-squares best fit to a logistic function, constrained to go to −0.5 and 0 at high and low $\Delta\bar{U} - T\Delta\bar{S}$ respectively is shown in (a). The energetic component is coloured by the interaction anisotropy parameter, the entropy component by the shape anisotropy parameter, and the overall free energy by the ratio of the two parameters. Filled symbols correspond to simulations with the graphene-structure substrate (graphene or "strong") and unfilled symbols to the silicon substrate. Shaded grey regions highlight where the points should fall if obeying the predicted scaling with the free energy or free energy component.

particles while still maintaining an isotropic bulk phase, these points do not fall in the region where the simple free-energy predictor presented here predicts a face-on orientation.

The deviation from universal scaling at the vapour interface is likely due to several factors. Firstly, for a number of the systems, particularly those at high density, the pressure, measured as the normal force on the substrate, was relatively high – up to $1200\epsilon/\sigma^3$ in some cases. Examining the dependence of the relationship between s_{vap} and the free energy on system pressure (SI, Fig. S3.9b) shows more extreme side-on orientation (lower values of s_{vap}) at higher pressures for the same value of the free energy. While the orientation at the solid interface also shows a slight pressure dependence (SI, Fig. S3.9a), the effect at the vapour interface is more pronounced. As the vapour interface is constrained by a repulsive harmonic wall, interacting with the centers of each fluid particle, high pressures correspond to a strong interaction between the fluid particles and this wall, artificially suppressing fluctuations and in some cases (e.g. SI, Fig. S3.5a) resulting in a density enhancement relative to the bulk and oscillations in the density profile that are not representative of a true vapour interface.

Secondly, as the energetic component of the interfacial free energy in eqn (3.7) is calculated assuming an idealised packing structure for a fully face-on and side-on interfacial layer, variations in the packing structure at the interface reduce the accuracy of the estimated free energy. The positions of fluid particles are less strongly constrained by the vapour interface than the solid substrate, and the side-on packing that predominates at the vapour interface appears to be less robust to disorder than the face-on packing that predominates at the solid interface, due to the tendency of nearest neighbours to be displaced parallel or angled slightly with respect to one another. Weaker ordering at the vapour interface results in molecular packings that deviate from the idealised structures, as shown in the SI in Fig. S3.8. Similarly, the calculation of the energetic component of the free energy based solely on the fully face-on and fully side-on configurations means that the predictability of the model is likely to be poorer for systems with interfacial orientation that is closer to isotropic.

Despite these complications, the results indicate that it is difficult to obtain a face-on orientation under equilibrium conditions of isotropic bulk GB fluids for parameters representative of OSCs. For the systems studied here, the interaction energy favours the face-on orientation when the interaction strength is the most isotropic ($\kappa' = 0.7$) of the values studied (Fig. 3.8b), though only marginally, and more significantly when κ' is increased to > 1. In all cases, however, the entropic term (Fig. 3.8c) is sufficiently large that the overall free energy still predicts the side-on orientation. While significantly lowering the temperature would help to

transition to the face-on orientation by reducing the entropic contribution, this is likely to result in a transition to a liquid-crystal or crystalline bulk phase. On the other hand, reducing the entropic component by reducing the shape anisotropy is likely to lead to a more isotropic interface orientation.

It has previously been shown that the orientation of similar GB particles at a nematic–vapour interface can be easily switched between face-on for $\kappa/\kappa' < 1$ to side-on $\kappa/\kappa' > 1$,[84] whereas only a very slight preference for the face-on orientation was observed if $\kappa/\kappa' < 1$ for the isotropic-bulk systems studied here (Fig. 3.3b). The greater propensity for a nematic bulk fluid to give the face-on orientation at the vapour interface compared with an isotropic bulk fluid can be understood qualitatively in terms of differences between the interfacial energy of the face-on relative to the side-on orientation in the two cases. For the isotropic fluid, this energy is described by eqn (3.7), whereas for the nematic fluid, interactions with the adjacent anisotropic fluid layer must also be taken into account. Assuming that, compared with the isotropic fluid, each fluid particle in the interfacial layer of the nematic fluid interacts with an additional particle of the same orientation in the next fluid layer, the face-on orientation is predicted to be more energetically stabilised relative to the side-on orientation in the nematic fluid than in the isotropic fluid for the systems studied here with $\kappa' < 1$ and in ref 84, for which the face–face interactions were always stronger than the side–side ones ($\kappa' < 1$).

3.3.4 Guidelines for controlling OSC interface orientation

In all manner of OSC-based devices, orientation at interfaces has been correlated with device performance.[7–9,20,25,45–51,64,220] Reliably controlling the orientation at these interfaces is therefore an important step towards designing high-performing molecules for commercial applications. Based on the results presented in the previous sections, we propose several general guidelines, which are supported by empirical evidence, for how the molecular structure, interface, and processing conditions may be tuned to shift towards the desired alignment at these interfaces.

Increased shape anisotropy promotes a face-on orientation at the solid interface, and side-on at the vapour. A number of experimental studies have shown that backbone planarisation (induced by fluorination of the backbone,[7,90,255] or extending the conjugation of the backbone, such as by adding aromatic components between the backbone and side-chains,[8] both of which can be associated with an increase in shape anisotropy) results in a more face-on orientation at the donor–acceptor interface in OPVs. It should be noted that both of these chemical modifications will also influence the energetics, so an interplay between changes in interaction strength and shape will control the orientation at the interfaces.

Stronger fluid face–face (or weaker side–side) interactions promote side-on orientation at both interfaces. Enhancing the hydrogen-bonding capabilities of a small molecule in the side–side direction has recently been shown to promote a more face-on orientation at a solid substrate,[256] consistent with the predictions of our model. However, other methods to tune the interaction anisotropy, such as introducing longer/bulkier side-chains that may block the face of the molecule or deplanarising the backbone, also change the shape anisotropy, which may have the opposite effect on interface orientation.

Increasing the interaction strength of a solid substrate promotes the face-on orientation at the solid interface. There are many published examples of substrates that interact more strongly with the semiconductor shifting the orientation towards face-on,[221,230–232,238–241] consistent with the behaviour observed here for different substrates. Choosing a substrate that interacts favourably with either OSC backbone or side-chains may therefore be an effective means of tuning the orientation at this interface.

Processing conditions that favour entropy promote face-on orientation at the solid interface, and side-on at the vapour. In cases where the equilibrium orientation is face-on at the solid interface (which appear to be many), processes such as melt annealing may allow the equilibrium orientation to be obtained, even if deposited through a non-equilibrium method in the opposite orientation.[237,257] However, when considering high temperatures, care should be taken to ensure that the orientation remains in the entropically favoured orientation as the system is cooled down, which can be achieved by rapid quenching, as the degree of alignment will be a function of temperature.

Conditions for which the bulk fluid is anisotropic, or side–side interactions are stronger than face–face ones, can give the face-on orientation at the vapour interface. From our predictions based on the behaviour of a bulk isotropic fluid, the face-on orientation at the vapour interface is difficult to achieve, although it could be obtained by systems with stronger side–side than face–face interactions (e.g. by chemical functionalisation of the aromatic core of the OSC). The interface orientation of liquid crystal fluids has previously been shown to be much more variable.[84] Under appropriate conditions, many OSCs form liquid-crystal phases, meaning the predictions of ref 84 based on the shape and interaction anisotropy can be applied to tune the orientation at the vapour interface.

Non-equilibrium processing can result in different behaviour than that predicted here. The above guidelines were proposed based on equilibrium behaviour, but could be

circumvented using non-equilibrium methods to potentially reach the more difficult to obtain orientations (face-on at the vapour interface, side-on at the solid interface). Many common device processing techniques, such as vapour deposition (see refs 258 and 259 for extensive reviews of this method and how processing temperature can influence the orientation), spin coating, or blade coating, are non-equilibrium in nature and so will not necessarily result in the equilibrium structures predicted in this work.

3.4 CONCLUSIONS

Through the use of classical simulations of oblate ellipsoidal fluid particles, this work provides a general analysis of how particle shape and interaction anisotropy influence the equilibrium orientation of a wide variety of isotropic liquids at interfaces with both a solid and vapour-like phase. For a range of parameters spanning a subset of OSC space, different substrate types, and different thermodynamic conditions, we find remarkable universal scaling of interface orientation with a simple interfacial free energy parameter based on nearest-neighbour pair interactions and the interfacial entropy of purely repulsive particles of the same shape. Based on these results, we propose several practical methods for achieving the desired orientation at both interfaces, which we hope provide a pathway towards the rational design of high performing OSC-based devices.

At the interface with a solid, the entropically favoured orientation is face-on, consistent with previous theories based on excluded volume entropic effects. Even when attractions are introduced, the orientation is largely influenced by the entropy and can be tuned by modifying the shape anisotropy. The side-on orientation is more difficult to obtain, but can be achieved most simply by using a substrate that interacts weakly with the face of the fluid particle (or strongly with its side).

The entropically favoured orientation at the vapour interface is side-on, in contrast to the alignment at the solid substrate, but again can be rationalised through excluded-volume entropic effects. Importantly, in all cases studied here, the orientation at the vapour interface of a fluid that is isotropic in the bulk is predicted, and generally observed, to be side-on. Conditions for which the face-on orientation is favoured appear to be difficult to achieve for an isotropic bulk liquid phase for interactions typical of OSCs, but can be obtained if the system has a bulk liquid-crystal phase. Tuning of molecular shape and interaction parameters can result in a shift towards a more isotropic interfacial layer.

Many open questions remain in this area, such as how side-chains, biaxiality, degree of polymerisation, multiple fluid components, or non-equilibrium processes such as pre-aggregation of molecules in solution during solvent evaporation, influ-

ence the orientation, but we hope that this work provides a useful starting point for understanding some simple methods for how interfacial orientation can be systematically tuned. Additionally, although this work focuses on oblate ellipsoidal particles, representative of molecules such as perylene, similar arguments should be applicable to prolate molecules such as pentacene. Further studies that account for interactions with the surrounding layers may allow this analysis to be extended to the non-isotropic systems that may be more typical of certain OSC molecules.

Supporting Information

S3.1 SIMULATION PARAMETERS FOR ORGANIC-SEMICONDUCTOR-LIKE OBLATE ELLIPSOIDS

All simulations used the LAMMPS[244] implementation of the GB potential,[181] which is a generalisation of the original uniaxial GB potential[81] to dissimilar biaxial ellipsoidal particles.[199] In this potential, the anisotropy of the shape of a particle i is defined in terms of the particle's principal diameters, $\sigma_{\mathrm{a}i}$, $\sigma_{\mathrm{b}i}$, and $\sigma_{\mathrm{c}i}$, by the diagonal shape matrix, $\boldsymbol{S}_i = \mathrm{diag}(\sigma_{\mathrm{a}i}, \sigma_{\mathrm{b}i}, \sigma_{\mathrm{c}i})/2$, while the anisotropy of its interactions is defined in terms of the relative well depths, $\epsilon_{\mathrm{a}i}$, $\epsilon_{\mathrm{b}i}$, and $\epsilon_{\mathrm{c}i}$, along the corresponding axes by the diagonal interaction matrix, $\boldsymbol{E}_i = \mathrm{diag}(\epsilon_{\mathrm{a}i}, \epsilon_{\mathrm{b}i}, \epsilon_{\mathrm{c}i})$. For the uniaxial oblate ellipsoidal particles studied in this work, $\sigma_{\mathrm{a}i} = \sigma_{\mathrm{c}i} \equiv \sigma_{\mathrm{S}}$, $\sigma_{\mathrm{b}i} \equiv \sigma_{\mathrm{F}}$, $\epsilon_{\mathrm{a}i} = \epsilon_{\mathrm{c}i} \equiv \epsilon_{\mathrm{S}}$, and $\epsilon_{\mathrm{b}i} \equiv \epsilon_{\mathrm{F}}$, where the subscripts "S" and "F" indicate diameters or well depths in the side–side and face–face directions, respectively.

The interaction potential between two particles, i and j, is

$$u_{\mathrm{GB}}\left(\boldsymbol{r}_{ij}, \boldsymbol{A}_i, \boldsymbol{A}_j\right) = u_{\mathrm{r}}\left(\boldsymbol{r}_{ij}, \boldsymbol{A}_i, \boldsymbol{A}_j\right) \eta\left(\boldsymbol{A}_i, \boldsymbol{A}_j\right) \chi\left(\boldsymbol{r}_{ij}, \boldsymbol{A}_i, \boldsymbol{A}_j\right), \tag{3.8}$$

where $\boldsymbol{r}_{ij} = \boldsymbol{r}_i - \boldsymbol{r}_j$ is the vector between the particle centres at positions $\boldsymbol{r}_i$ and $\boldsymbol{r}_j$, respectively, and $\boldsymbol{A}_i$ and $\boldsymbol{A}_j$ are rotation matrices transforming the orientations of the two particles from the lab frame to the body frame. The first factor, u_{r}, in eqn (3.8) controls the distance dependence of the interaction and takes the form of a shifted LJ potential,

$$u_{\mathrm{r}}\left(\boldsymbol{r}_{ij}, \boldsymbol{A}_i, \boldsymbol{A}_j\right) = 4\epsilon \left[\left(\frac{\sigma}{h_{ij} + \sigma} \right)^{12} - \left(\frac{\sigma}{h_{ij} + \sigma} \right)^{6} \right], \tag{3.9}$$

where σ and ϵ define the length and energy scales of the potential, respectively, and h_{ij} is the distance of closest approach of the particles, approximated as[178]

$$h_{ij}\left(\boldsymbol{r}_{ij}, \boldsymbol{A}_i, \boldsymbol{A}_j\right) = r_{ij} - \left(\frac{1}{2} \hat{\boldsymbol{r}}_{ij}^{\mathrm{T}} \boldsymbol{G}_{ij}^{-1} \hat{\boldsymbol{r}}_{ij} \right)^{-1/2}, \tag{3.10}$$

where $r_{ij} = \left|\boldsymbol{r}_{ij}\right|$, $\hat{\boldsymbol{r}}_{ij} = \boldsymbol{r}_{ij}/r_{ij}$, and

$$\boldsymbol{G}_{ij} = \boldsymbol{A}_i^{\mathrm{T}} \boldsymbol{S}_i^2 \boldsymbol{A}_i + \boldsymbol{A}_j^{\mathrm{T}} \boldsymbol{S}_j^2 \boldsymbol{A}_j. \tag{3.11}$$

The other two factors, η and χ, in eqn (3.8) control the position and orientation dependence of the interaction strength, and are given by

$$\eta\left(\boldsymbol{A}_i, \boldsymbol{A}_j\right) = \left[\frac{2\bar{\sigma}_i\bar{\sigma}_j}{\det\left(\boldsymbol{G}_{ij}\right)}\right]^{\nu/2} \tag{3.12}$$

and

$$\chi\left(\boldsymbol{r}_{ij}, \boldsymbol{A}_i, \boldsymbol{A}_j\right) = \left(2\hat{\boldsymbol{r}}_{ij}^{\mathrm{T}}\boldsymbol{B}_{ij}^{-1}\hat{\boldsymbol{r}}_{ij}\right)^{\mu}, \tag{3.13}$$

where

$$\bar{\sigma}_i = \left(\sigma_{\mathrm{a}i}\sigma_{\mathrm{b}i} + \sigma_{\mathrm{c}i}^2\right)\left(\sigma_{\mathrm{a}i}\sigma_{\mathrm{b}i}\right)^{1/2}, \tag{3.14}$$

$$\boldsymbol{B}_{ij} = \boldsymbol{A}_i^{\mathrm{T}}\boldsymbol{E}_i^{-1/\mu}\boldsymbol{A}_i + \boldsymbol{A}_j^{\mathrm{T}}\boldsymbol{E}_j^{-1/\mu}\boldsymbol{A}_j, \tag{3.15}$$

and ν and μ are parameters that tune the shape of the potential.

The anisotropy of the GB potential for uniaxial particles can be fully described in terms of two parameters: the shape anisotropy parameter $\kappa = \sigma_{\mathrm{F}}/\sigma_{\mathrm{S}}$ and the interaction anisotropy parameter $\kappa' = \epsilon_{\mathrm{S}}/\epsilon_{\mathrm{F}}$. Parameters used to simulate a range of values of κ and κ' typical of common OSCs are given in Tables S3.1 and S3.2, respectively. The parameter range studied is reasonably representative of OSC systems for an energy scale of $\epsilon = 1$ kcal/mol and length scale of $\sigma = 3.2\,\text{Å}$ (bulk density approx $1.1\,\mathrm{g\,cm^{-3}}$ at 560 K and 1 atm for $\kappa = 0.36$, $\kappa' = 0.19$, which is representative of perylene). For all simulations the values of ν and μ previously used to model typical OSCs with the biaxial GB potential were used ($\nu = 1$ and $\mu = 2$).[199]

Particle masses were chosen to maintain the same mass density of a single particle with volume $\frac{\pi\sigma_{\mathrm{S}}^2\sigma_{\mathrm{F}}}{6}$ as the previously published biaxial GB perylene model with volume $\frac{\pi\sigma_{\mathrm{S}}\sigma_{\mathrm{F}}\sigma_{\mathrm{E}}}{6}$ and mass $252.3\,\mathrm{g\,mol^{-1}}$, where the additional diameter ($i = \mathrm{E}$) corresponds to the third unique principal diameter unique of the biaxial particle (end–end). Table S3.3 shows the variation of this density for the various published biaxial molecules,[199] and shows that, although there is some variability in this parameter across different molecules, for this wide variety of molecules it is relatively constant at between 1.4 and $1.7\,\mathrm{g\,mol^{-1}\,Å^{-3}}$.

OPLS-AA LJ parameters for aromatic carbon[202] or silicon[246] were used to model the solid substrate, with particles placed in the typical arrangements for these surfaces. Substrate particles were treated with the GB potential, with the elements of the shape matrix and interaction matrix all set to the same value ($\sigma_{ai} = \sigma_{bi} = \sigma_{ci} = \sigma_{ij}$, $\epsilon_{ai} = \epsilon_{bi} = \epsilon_{ci} = \epsilon_{ij}/\epsilon$). Fluid–substrate interactions were then calculated using the mixing rules defined by eqns (3.10)–(3.15). For substrate–fluid interactions, σ in eqn S2 was replaced by $(\sigma + \sigma_{ij})/2$. Substrate parameters are summarised in Table S3.4.

Table S3.1 Shape anisotropy parameter $\kappa = \sigma_F/\sigma_S$ given values of the principal diameter in the face–face (σ_F) and side–side (σ_S) directions used in the simulations. The size z_w of the box in the z-dimension required to constrain the overall volume fraction to the target value of ϕ_{av} is also given.

κ	σ_F/σ	σ_S/σ	ϕ_{av}	z_w/σ
			0.28	115.63
0.30	1.03	3.43	0.39	84.06
			0.49	65.94
			0.28	85.00
0.35	1.03	2.94	0.39	61.88
			0.49	48.44
			0.28	65.00
0.40	1.03	2.56	0.39	47.19
			0.49	37.19
			0.28	51.25
0.45	1.03	2.29	0.39	37.50
			0.49	29.38
			0.28	41.56
0.50	1.03	2.06	0.39	30.31
			0.49	23.80

Table S3.2 Interaction anisotropy parameter $\kappa = \epsilon_S/\epsilon_F$ given values of the well depth in the face–face (ϵ_F) and side–side (ϵ_S) orientations.

κ'	ϵ_F	ϵ_S
0.15	6.67	1
0.20	5.00	1
0.25	4.00	1
0.30	3.33	1
0.50	2.00	1
0.70	1.43	1
1.20	1.67	2

Table S3.3 Mass density of various oblate ellipsoidal molecules, given their molecular weight (MW) and principal diameters σ_i from published biaxial GB models.[199]

compound	MW (g/mol)	σ_S	σ_F	σ_E	density (g/mol/Å^3)
porphine	310.35	11.4	3.2	11.4	1.41
benzene	78.11	6.3	3.1	6.5	1.17
perylene	252.30	8.2	3.3	10.4	1.69
pyrene	202.25	8.1	3.2	10.5	1.40
benzoquinone	108.10	6.0	3.2	7.4	1.44
naphthalene	128.17	6.5	3.3	8.2	1.37
anthraquinone	208.00	7.2	3.2	10.5	1.58
tetrazine	82.06	5.3	3.9	6.9	1.14

Table S3.4 LJ parameters for substrate particles from the OPLS-AA force field. Particles were treated as GB particles with $\sigma_{ai} = \sigma_{bi} = \sigma_{ci} = \sigma_{ij}$, and $\epsilon_{ai} = \epsilon_{bi} = \epsilon_{ci} = \epsilon_{ij}/\epsilon$. The substrate labelled "strong" is an artifically strongly interacting substrate with the same structure as graphene and twice the value of ϵ_{ij}.

	ϵ_{sub}/ϵ	σ_{sub}/σ	ϵ_{ij}/ϵ	σ_{ij}/σ
graphene	1	1.11	0.04	1.11
silicon	1	1.25	0.06	1.25
"strong"	1	1.11	0.08	1.11

S3.2 LIST OF SIMULATED SYSTEMS

The tables below list all the systems simulated in this work, as well as their key results. Table S3.5 lists the purely repulsive systems, and Table S3.6 the systems with both attractive and repulsive interactions. In both cases, a number of systems were not isotropic in the bulk and were not included in the plots in the main text. Due to the lower mobility of the particles in these anisotropic-bulk systems, simulation configurations in these systems were not necessarily sampled from the equilibrium distribution for the MD simulation protocol used in this work.

Table S3.5 Complete list of the *purely repulsive* systems studied in this work. Items highlighted in red were anisotropic in the bulk and are not included in the plots in the main text. $T^* = k_B T/\epsilon$ is the reduced temperature, ϕ_{av} is the overall volume fraction to which the system was constrained by the position of the harmonic wall (i.e. the average fluid volume fraction between $z = \sigma_{sub}/2$, the surface of the solid substrate, and z_w, the position of the harmonic wall), and ϕ is the volume fraction of particles in the bulk fluid (calculated based on the number of GB particles with centers-of-mass within $\pm 3\sigma_S$ of the center of the system). The orientational order parameter at the solid (s_{sub}) and vapour (s_{vap}) interfaces, and the corresponding orientations (F = face-on, S = side-on) are given in the final four columns. The systems that gave the much less common side-on orientation at the solid substrate are highlighted in bold.

substrate type	T^*	κ	κ'	ϕ_{av}	ϕ	s_{sub}	orient$_{sub}$	s_{vap}	orient$_{vap}$
silicon	0.62	0.30	0.20	0.18	0.19	0.17	F	−0.06	S
silicon	0.62	0.30	0.20	0.28	0.29	0.37	F	−0.26	S
silicon	0.62	0.30	0.20	0.39	0.39	0.71	F	−0.42	S
silicon	0.62	0.30	0.20	0.46	0.46	−0.45	**S**	−0.46	S
silicon	0.62	0.35	0.20	0.18	0.18	0.13	F	−0.06	S
silicon	0.62	0.35	0.20	0.28	0.29	0.23	F	−0.21	S

Continued on next page

substrate type	T^*	κ	κ'	ϕ_{av}	ϕ	s_{sub}	orient$_{sub}$	s_{vap}	orient$_{vap}$
silicon	0.62	0.35	0.20	0.39	0.39	0.61	F	−0.39	S
silicon	0.62	0.35	0.20	0.46	0.47	0.81	F	−0.45	S
silicon	0.62	0.40	0.20	0.18	0.18	0.10	F	−0.05	S
silicon	0.62	0.40	0.20	0.28	0.29	0.16	F	−0.17	S
silicon	0.62	0.40	0.20	0.39	0.39	0.37	F	−0.35	S
silicon	0.62	0.40	0.20	0.46	0.46	0.65	F	−0.44	S
silicon	0.62	0.45	0.20	0.18	0.18	0.07	F	−0.04	S
silicon	0.62	0.45	0.20	0.28	0.29	0.10	F	−0.14	S
silicon	0.62	0.45	0.20	0.39	0.39	0.19	F	−0.32	S
silicon	0.62	0.45	0.20	0.46	0.46	0.41	F	−0.41	S
silicon	0.62	0.50	0.20	0.18	0.18	0.06	F	−0.04	S
silicon	0.62	0.50	0.20	0.28	0.29	0.07	F	−0.13	S
silicon	0.62	0.50	0.20	0.39	0.39	0.10	F	−0.28	S
silicon	0.62	0.50	0.20	0.46	0.46	0.12	F	−0.38	S
silicon	0.84	0.30	0.20	0.18	0.18	0.15	F	−0.05	S
silicon	0.84	0.30	0.20	0.28	0.29	0.35	F	−0.24	S

Continued on next page

substrate type	T^*	κ	κ'	ϕ_{av}	ϕ	s_{sub}	orient$_{sub}$	s_{vap}	orient$_{vap}$
silicon	0.84	0.30	0.20	0.39	0.39	0.67	F	−0.40	S
silicon	0.84	0.30	0.20	0.46	0.46	0.63	F	−0.45	S
silicon	0.84	0.35	0.20	0.18	0.18	0.13	F	−0.07	S
silicon	0.84	0.35	0.20	0.28	0.29	0.24	F	−0.20	S
silicon	0.84	0.35	0.20	0.39	0.39	0.56	F	−0.38	S
silicon	0.84	0.35	0.20	0.46	0.46	0.66	F	−0.44	S
silicon	0.84	0.40	0.20	0.18	0.18	0.09	F	−0.06	S
silicon	0.84	0.40	0.20	0.28	0.29	0.15	F	−0.16	S
silicon	0.84	0.40	0.20	0.39	0.39	0.33	F	−0.34	S
silicon	0.84	0.40	0.20	0.46	0.46	0.64	F	−0.42	S
silicon	0.84	0.45	0.20	0.18	0.18	0.07	F	−0.05	S
silicon	0.84	0.45	0.20	0.28	0.29	0.11	F	−0.13	S
silicon	0.84	0.45	0.20	0.39	0.39	0.19	F	−0.30	S
silicon	0.84	0.45	0.20	0.46	0.46	0.36	F	−0.39	S
silicon	0.84	0.50	0.20	0.18	0.18	0.05	F	−0.04	S
silicon	0.84	0.50	0.20	0.28	0.29	0.07	F	−0.12	S

Continued on next page

substrate type	T^*	κ	κ'	ϕ_{av}	ϕ	s_{sub}	$orient_{sub}$	s_{vap}	$orient_{vap}$
silicon	0.84	0.50	0.20	0.39	0.39	0.11	F	−0.27	S
silicon	0.84	0.50	0.20	0.46	0.46	0.16	F	−0.36	S
graphene	0.62	0.30	0.20	0.18	0.18	0.18	F	−0.09	S
graphene	0.62	0.30	0.20	0.28	0.28	0.40	F	−0.25	S
graphene	0.62	0.30	0.20	0.32	0.32	0.51	F	−0.32	S
graphene	0.62	0.30	0.20	0.35	0.35	0.67	F	−0.37	S
graphene	0.62	0.30	0.20	0.39	0.39	0.75	F	−0.41	S
graphene	0.62	0.30	0.20	0.42	0.42	0.83	F	−0.43	S
graphene	0.62	0.30	0.20	0.46	0.45	0.75	F	−0.45	S
graphene	0.62	0.30	0.20	0.49	0.50	0.12	F	−0.47	S
graphene	0.62	0.35	0.20	0.18	0.18	0.14	F	−0.07	S
graphene	0.62	0.35	0.20	0.28	0.28	0.28	F	−0.20	S
graphene	0.62	0.35	0.20	0.32	0.32	0.36	F	−0.26	S
graphene	0.62	0.35	0.20	0.35	0.35	0.46	F	−0.32	S
graphene	0.62	0.35	0.20	0.39	0.38	0.61	F	−0.38	S
graphene	0.62	0.35	0.20	0.42	0.42	0.73	F	−0.42	S

Continued on next page

substrate type	T^*	κ	κ'	ϕ_{av}	ϕ	s_{sub}	orient$_{sub}$	s_{vap}	orient$_{vap}$
graphene	0.62	0.35	0.20	0.46	0.46	0.67	F	−0.45	S
graphene	0.62	0.35	0.20	0.49	0.48	−0.40	**S**	−0.46	S
graphene	0.62	0.40	0.20	0.18	0.18	0.12	F	−0.06	S
graphene	0.62	0.40	0.20	0.28	0.28	0.20	F	−0.17	S
graphene	0.62	0.40	0.20	0.32	0.32	0.25	F	−0.22	S
graphene	0.62	0.40	0.20	0.35	0.35	0.32	F	−0.29	S
graphene	0.62	0.40	0.20	0.39	0.38	0.41	F	−0.34	S
graphene	0.62	0.40	0.20	0.42	0.42	0.56	F	−0.39	S
graphene	0.62	0.40	0.20	0.46	0.45	0.69	F	−0.43	S
graphene	0.62	0.40	0.20	0.49	0.49	−0.37	**S**	−0.45	S
graphene	0.62	0.45	0.20	0.18	0.18	0.09	F	−0.05	S
graphene	0.62	0.45	0.20	0.28	0.28	0.15	F	−0.14	S
graphene	0.62	0.45	0.20	0.32	0.32	0.18	F	−0.19	S
graphene	0.62	0.45	0.20	0.35	0.35	0.22	F	−0.25	S
graphene	0.62	0.45	0.20	0.39	0.39	0.29	F	−0.31	S
graphene	0.62	0.45	0.20	0.42	0.42	0.37	F	−0.36	S

Continued on next page

substrate type	T^*	κ	κ'	ϕ_{av}	ϕ	s_{sub}	orient$_{sub}$	s_{vap}	orient$_{vap}$
graphene	0.62	0.45	0.20	0.46	0.45	0.51	F	−0.40	S
graphene	0.62	0.45	0.20	0.49	0.47	0.67	F	−0.45	S
graphene	0.62	0.50	0.20	0.18	0.18	0.07	F	−0.04	S
graphene	0.62	0.50	0.20	0.28	0.28	0.10	F	−0.12	S
graphene	0.62	0.50	0.20	0.32	0.32	0.12	F	−0.17	S
graphene	0.62	0.50	0.20	0.35	0.35	0.15	F	−0.22	S
graphene	0.62	0.50	0.20	0.39	0.39	0.19	F	−0.26	S
graphene	0.62	0.50	0.20	0.42	0.42	0.25	F	−0.32	S
graphene	0.62	0.50	0.20	0.46	0.45	0.33	F	−0.37	S
graphene	0.62	0.50	0.20	0.49	0.49	0.49	F	−0.42	S

Table S3.6 Complete list of the *attractive* systems studied in this work. Items highlighted in red were anisotropic in the bulk and are not included in the plots in the main text. $T^* = k_B T/\epsilon$ is the reduced temperature, ϕ_{av} is the overall volume fraction to which the system was constrained by the position of the harmonic wall (i.e. the average fluid volume fraction between $z = \sigma_{sub}/2$, the surface of the solid substrate, and z_w, the position of the harmonic wall), and ϕ is the volume fraction of particles in the bulk fluid (calculated based on the number of GB particles with centers-of-mass within $\pm 3\sigma_S$ of the center of the system). $P^* = P/(\epsilon/\sigma^3)$ is the reduced pressure, measured as the normal force per unit area acting on the solid substrate. The orientational order parameter at the solid (s_{sub}) and vapour (s_{vap}) interfaces, and the corresponding orientations (F = face-on, S = side-on) are given in the final four columns. The systems that gave the much less common side-on orientation at the solid substrate are highlighted in bold.

substrate type	T^*	κ	κ'	ϕ_{av}	ϕ	P^*	s_{sub}	orient$_{sub}$	s_{vap}	orient$_{vap}$
graphene	0.56	0.40	0.15	0.39	0.53	−3.18	0.07	F	−0.29	S
graphene	0.56	0.40	0.20	0.39	0.53	−9.35	0.32	F	−0.00	S
graphene	0.56	0.40	0.25	0.39	0.44	0.65	0.16	F	−0.00	S
graphene	0.56	0.40	0.30	0.39	0.43	−0.63	0.20	F	0.00	F
graphene	0.56	0.40	0.50	0.39	0.40	51.30	0.28	F	0.01	F

Continued on next page

substrate type	T^*	κ	κ'	ϕ_{av}	ϕ	P^*	s_{sub}	orient$_{sub}$	s_{vap}	orient$_{vap}$
graphene	0.56	0.40	0.70	0.39	0.39	100.99	0.34	F	0.00	F
graphene	**0.56**	**0.45**	**0.15**	**0.39**	**0.53**	**2.40**	**−0.30**	**S**	**−0.13**	**S**
graphene	**0.56**	**0.45**	**0.20**	**0.39**	**0.54**	**4.54**	**−0.44**	**S**	**−0.42**	**S**
graphene	0.56	0.45	0.25	0.39	0.46	−3.85	0.10	F	−0.01	S
graphene	0.56	0.45	0.30	0.39	0.45	2.01	0.14	F	0.01	F
graphene	0.56	0.45	0.50	0.39	0.41	16.24	0.20	F	0.02	F
graphene	0.56	0.45	0.70	0.39	0.40	61.66	0.24	F	0.02	F
graphene	0.56	0.50	0.15	0.39	0.54	−3.42	0.03	F	0.41	F
graphene	**0.56**	**0.50**	**0.20**	**0.39**	**0.56**	**−1.56**	**−0.45**	**S**	**−0.42**	**S**
graphene	0.56	0.50	0.25	0.39	0.48	−1.29	0.03	F	−0.03	S
graphene	0.56	0.50	0.30	0.39	0.47	−5.46	0.08	F	−0.00	S
graphene	0.56	0.50	0.50	0.39	0.43	−2.25	0.15	F	0.02	F
graphene	0.56	0.50	0.70	0.39	0.41	31.89	0.18	F	0.02	F
graphene	**0.62**	**0.30**	**0.15**	**0.39**	**0.53**	**3.25**	**−0.31**	**S**	**0.87**	**F**
graphene	0.62	0.30	0.20	0.39	0.55	10.91	0.79	F	−0.14	S
graphene	0.62	0.30	0.25	0.39	0.36	30.77	0.85	F	−0.05	S

Continued on next page

substrate type	T^*	κ	κ'	ϕ_{av}	ϕ	P^*	s_{sub}	orient$_{sub}$	s_{vap}	orient$_{vap}$
graphene	0.62	0.30	0.30	0.39	0.39	99.24	0.47	F	−0.11	S
graphene	**0.62**	**0.35**	**0.15**	**0.39**	**0.51**	**−4.83**	**−0.14**	**S**	**−0.01**	**S**
graphene	0.62	0.35	0.20	0.39	0.42	1.23	0.13	F	−0.01	S
graphene	0.62	0.35	0.25	0.39	0.40	31.20	0.24	F	−0.02	S
graphene	0.62	0.35	0.30	0.39	0.39	63.98	0.28	F	−0.04	S
graphene	0.62	0.40	0.15	0.39	0.53	1.78	0.32	F	0.13	F
graphene	0.62	0.40	0.20	0.39	0.44	−1.95	0.05	F	−0.03	S
graphene	0.62	0.40	0.25	0.39	0.42	9.10	0.13	F	−0.00	S
graphene	0.62	0.40	0.30	0.39	0.41	25.53	0.18	F	0.01	F
graphene	**0.62**	**0.45**	**0.15**	**0.39**	**0.53**	**−9.52**	**−0.46**	**S**	**0.62**	**F**
graphene	0.62	0.45	0.20	0.39	0.46	4.24	0.00	F	−0.04	S
graphene	0.62	0.45	0.25	0.39	0.44	−1.49	0.09	F	−0.01	S
graphene	0.62	0.45	0.30	0.39	0.43	0.83	0.12	F	0.00	F
graphene	0.62	0.50	0.15	0.39	0.55	−3.38	0.60	F	0.56	F
graphene	**0.62**	**0.50**	**0.20**	**0.39**	**0.47**	**−2.95**	**−0.05**	**S**	**−0.05**	**S**
graphene	0.62	0.50	0.25	0.39	0.46	−0.36	0.04	F	−0.01	S

Continued on next page

substrate type	T^*	κ	κ'	ϕ_{av}	ϕ	P^*	s_{sub}	orient$_{sub}$	s_{vap}	orient$_{vap}$
graphene	0.62	0.50	0.30	0.39	0.45	−2.67	0.07	F	−0.00	S
graphene	**0.73**	**0.30**	**0.15**	**0.39**	**0.48**	**6.45**	**−0.25**	**S**	**0.16**	**F**
graphene	0.73	0.30	0.20	0.39	0.37	51.20	0.21	F	−0.09	S
graphene	0.73	0.30	0.25	0.39	0.38	140.89	0.51	F	−0.18	S
graphene	0.73	0.30	0.30	0.39	0.39	160.90	0.45	F	−0.17	S
graphene	0.73	0.30	1.20	0.39	0.51	10.81	0.86	F	0.55	F
graphene	0.73	0.35	0.15	0.39	0.50	1.55	0.03	F	0.28	F
graphene	0.73	0.35	0.20	0.39	0.39	72.54	0.19	F	−0.12	S
graphene	0.73	0.35	0.25	0.39	0.39	120.80	0.28	F	−0.11	S
graphene	0.73	0.35	0.30	0.39	0.39	152.56	0.31	F	−0.11	S
graphene	0.73	0.35	1.20	0.39	0.49	−1.10	0.83	F	0.42	F
graphene	**0.73**	**0.40**	**0.15**	**0.39**	**0.52**	**0.09**	**−0.05**	**S**	**0.40**	**F**
graphene	0.73	0.40	0.20	0.39	0.40	48.12	0.09	F	−0.03	S
graphene	0.73	0.40	0.25	0.39	0.40	85.89	0.16	F	−0.04	S
graphene	0.73	0.40	0.30	0.39	0.39	124.30	0.20	F	−0.05	S
graphene	0.73	0.40	1.20	0.39	0.44	−8.62	0.66	F	0.14	F

Continued on next page

substrate type	T^*	κ	κ'	ϕ_{av}	ϕ	P^*	s_{sub}	orient$_{sub}$	s_{vap}	orient$_{vap}$
graphene	**0.73**	**0.45**	**0.15**	**0.39**	**0.53**	**10.94**	**−0.46**	**S**	**−0.13**	**S**
graphene	0.73	0.45	0.20	0.39	0.42	1.03	0.03	F	−0.02	S
graphene	0.73	0.45	0.25	0.39	0.41	24.60	0.09	F	−0.01	S
graphene	0.73	0.45	0.30	0.39	0.40	66.25	0.12	F	−0.02	S
graphene	0.73	0.45	1.20	0.39	0.45	−0.60	0.46	F	0.12	F
graphene	**0.73**	**0.50**	**0.15**	**0.39**	**0.54**	**−2.20**	**−0.45**	**S**	**−0.34**	**S**
graphene	**0.73**	**0.50**	**0.20**	**0.39**	**0.44**	**0.58**	**−0.01**	**S**	**−0.03**	**S**
graphene	0.73	0.50	0.25	0.39	0.43	6.87	0.04	F	−0.01	S
graphene	0.73	0.50	0.30	0.39	0.41	28.52	0.07	F	−0.00	S
graphene	0.73	0.50	1.20	0.39	0.47	7.47	0.36	F	0.10	F
graphene	0.84	0.30	0.15	0.39	0.49	32.68	0.10	F	−0.00	S
graphene	0.84	0.30	0.20	0.39	0.39	179.11	0.44	F	−0.23	S
graphene	0.84	0.30	0.25	0.39	0.39	222.26	0.47	F	−0.24	S
graphene	0.84	0.30	0.30	0.39	0.39	268.33	0.50	F	−0.23	S
graphene	0.84	0.35	0.15	0.39	0.41	35.60	0.07	F	−0.03	S
graphene	0.84	0.35	0.20	0.39	0.39	186.33	0.25	F	−0.16	S

Continued on next page

substrate type	T^*	κ	κ'	ϕ_{av}	ϕ	P^*	s_{sub}	orient$_{sub}$	s_{vap}	orient$_{vap}$
graphene	0.84	0.35	0.25	0.39	0.39	230.39	0.30	F	−0.15	S
graphene	0.84	0.35	0.30	0.39	0.39	265.63	0.33	F	−0.15	S
graphene	**0.84**	**0.40**	**0.15**	**0.39**	**0.40**	**67.48**	**−0.01**	**S**	**−0.10**	**S**
graphene	0.84	0.40	0.20	0.39	0.40	144.52	0.13	F	−0.09	S
graphene	0.84	0.40	0.25	0.39	0.39	211.95	0.19	F	−0.09	S
graphene	0.84	0.40	0.30	0.39	0.39	244.84	0.22	F	−0.09	S
graphene	**0.84**	**0.45**	**0.15**	**0.39**	**0.41**	**24.87**	**−0.05**	**S**	**−0.05**	**S**
graphene	0.84	0.45	0.20	0.39	0.40	85.53	0.06	F	−0.05	S
graphene	0.84	0.45	0.25	0.39	0.40	145.06	0.11	F	−0.05	S
graphene	0.84	0.45	0.30	0.39	0.39	185.75	0.14	F	−0.06	S
graphene	**0.84**	**0.50**	**0.15**	**0.39**	**0.43**	**5.58**	**−0.09**	**S**	**−0.05**	**S**
graphene	0.84	0.50	0.20	0.39	0.41	54.45	0.01	F	−0.02	S
graphene	0.84	0.50	0.25	0.39	0.41	102.42	0.06	F	−0.03	S
graphene	0.84	0.50	0.30	0.39	0.40	171.51	0.08	F	−0.03	S
silicon	0.56	0.40	0.15	0.39	0.52	0.55	0.13	F	0.00	F
silicon	0.56	0.40	0.20	0.39	0.53	0.49	0.75	F	0.14	F

Continued on next page

substrate type	T^*	κ	κ'	ϕ_{av}	ϕ	P^*	s_{sub}	$\text{orient}_{\text{sub}}$	s_{vap}	$\text{orient}_{\text{vap}}$
silicon	0.56	0.40	0.25	0.39	0.44	3.06	0.01	F	−0.01	S
silicon	0.56	0.40	0.30	0.39	0.43	7.25	0.03	F	0.01	F
silicon	0.56	0.40	0.50	0.39	0.41	76.82	0.12	F	0.00	F
silicon	0.56	0.40	0.70	0.39	0.40	135.44	0.19	F	0.00	F
silicon	0.56	0.45	0.15	0.39	0.53	0.20	0.27	F	−0.08	S
silicon	**0.56**	**0.45**	**0.20**	**0.39**	**0.48**	**−0.16**	**−0.08**	**S**	**−0.07**	**S**
silicon	**0.56**	**0.45**	**0.25**	**0.39**	**0.46**	**2.08**	**−0.01**	**S**	**−0.02**	**S**
silicon	0.56	0.45	0.30	0.39	0.45	−0.51	0.02	F	0.00	F
silicon	0.56	0.45	0.50	0.39	0.42	38.87	0.07	F	0.02	F
silicon	0.56	0.45	0.70	0.39	0.41	102.01	0.12	F	0.02	F
silicon	0.56	0.50	0.15	0.39	0.54	0.36	0.53	F	0.14	F
silicon	**0.56**	**0.50**	**0.20**	**0.39**	**0.49**	**−1.56**	**−0.11**	**S**	**−0.08**	**S**
silicon	**0.56**	**0.50**	**0.25**	**0.39**	**0.48**	**−2.59**	**−0.03**	**S**	**−0.03**	**S**
silicon	0.56	0.50	0.30	0.39	0.47	0.54	0.00	F	−0.00	S
silicon	0.56	0.50	0.50	0.39	0.44	16.57	0.04	F	0.02	F
silicon	0.56	0.50	0.70	0.39	0.42	71.13	0.07	F	0.01	F

Continued on next page

substrate type	T^*	κ	κ'	ϕ_{av}	ϕ	P^*	s_{sub}	orient$_{sub}$	s_{vap}	orient$_{vap}$
silicon	0.62	0.30	0.15	0.39	0.51	0.92	0.04	F	0.05	F
silicon	**0.62**	**0.30**	**0.20**	**0.39**	**0.52**	**2.32**	**−0.13**	**S**	**0.34**	**F**
silicon	0.62	0.30	0.25	0.39	0.37	46.17	0.11	F	−0.06	S
silicon	0.62	0.30	0.30	0.39	0.40	105.42	0.36	F	−0.15	S
silicon	0.62	0.35	0.15	0.39	0.51	−0.15	0.13	F	−0.37	S
silicon	0.62	0.35	0.20	0.39	0.55	0.67	0.13	F	0.06	F
silicon	0.62	0.35	0.25	0.39	0.41	48.99	0.06	F	−0.06	S
silicon	0.62	0.35	0.30	0.39	0.40	82.29	0.12	F	−0.07	S
silicon	0.62	0.40	0.15	0.39	0.52	−0.53	0.21	F	0.38	F
silicon	**0.62**	**0.40**	**0.20**	**0.39**	**0.44**	**4.26**	**−0.03**	**S**	**−0.03**	**S**
silicon	0.62	0.40	0.25	0.39	0.42	20.01	0.02	F	−0.01	S
silicon	0.62	0.40	0.30	0.39	0.41	44.82	0.05	F	−0.01	S
silicon	0.62	0.45	0.15	0.39	0.53	1.33	0.33	F	0.12	F
silicon	**0.62**	**0.45**	**0.20**	**0.39**	**0.46**	**−0.60**	**−0.05**	**S**	**−0.04**	**S**
silicon	0.62	0.45	0.25	0.39	0.44	3.46	0.00	F	−0.01	S
silicon	0.62	0.45	0.30	0.39	0.43	14.95	0.02	F	0.01	F

Continued on next page

substrate type	T^*	κ	κ'	ϕ_{av}	ϕ	P^*	s_{sub}	orient$_{sub}$	s_{vap}	orient$_{vap}$
silicon	**0.62**	**0.50**	**0.15**	**0.39**	**0.54**	**0.91**	**−0.13**	**S**	**0.66**	**F**
silicon	**0.62**	**0.50**	**0.20**	**0.39**	**0.47**	**2.32**	**−0.08**	**S**	**−0.06**	**S**
silicon	**0.62**	**0.50**	**0.25**	**0.39**	**0.46**	**1.50**	**−0.02**	**S**	**−0.02**	**S**
silicon	0.62	0.50	0.30	0.39	0.45	5.02	0.01	F	−0.00	S
strong	0.73	0.30	0.15	0.39	0.56	3.96	0.37	F	0.20	F
strong	0.73	0.30	0.20	0.39	0.38	53.85	0.88	F	−0.11	S
strong	0.73	0.30	0.25	0.39	0.38	135.93	0.85	F	−0.19	S
strong	0.73	0.30	0.30	0.39	0.39	175.05	0.53	F	−0.19	S
strong	0.73	0.35	0.15	0.39	0.54	−0.16	0.83	F	0.45	F
strong	0.73	0.35	0.20	0.39	0.39	81.81	0.35	F	−0.11	S
strong	0.73	0.35	0.25	0.39	0.39	114.61	0.38	F	−0.10	S
strong	0.73	0.35	0.30	0.39	0.39	154.31	0.39	F	−0.11	S
strong	0.73	0.40	0.15	0.39	0.51	−2.32	0.55	F	−0.17	S
strong	0.73	0.40	0.20	0.39	0.40	30.86	0.23	F	−0.02	S
strong	0.73	0.40	0.25	0.39	0.40	73.55	0.28	F	−0.04	S
strong	0.73	0.40	0.30	0.39	0.39	112.77	0.31	F	−0.05	S

Continued on next page

substrate type	T^*	κ	κ'	ϕ_{av}	ϕ	P^*	s_{sub}	orient$_{sub}$	s_{vap}	orient$_{vap}$
strong	**0.73**	**0.45**	**0.15**	**0.39**	**0.55**	**−1.31**	**−0.45**	**S**	**−0.43**	**S**
strong	0.73	0.45	0.20	0.39	0.42	5.02	0.15	F	−0.01	S
strong	0.73	0.45	0.25	0.39	0.41	24.41	0.19	F	−0.01	S
strong	0.73	0.45	0.30	0.39	0.40	76.86	0.23	F	−0.01	S
strong	**0.73**	**0.50**	**0.15**	**0.39**	**0.55**	**6.90**	**−0.46**	**S**	**−0.40**	**S**
strong	0.73	0.50	0.20	0.39	0.44	6.84	0.07	F	−0.02	S
strong	0.73	0.50	0.25	0.39	0.43	−1.09	0.13	F	−0.01	S
strong	0.73	0.50	0.30	0.39	0.41	14.99	0.16	F	−0.00	S
graphene	**0.73**	**0.30**	**0.15**	**0.28**	**0.46**	**3.89**	**−0.22**	**S**	**−0.24**	**S**
graphene	0.73	0.30	0.20	0.28	0.31	24.03	0.20	F	−0.00	S
graphene	0.73	0.30	0.25	0.28	0.30	35.74	0.27	F	−0.03	S
graphene	0.73	0.30	0.30	0.28	0.30	51.85	0.30	F	−0.03	S
graphene	**0.73**	**0.35**	**0.15**	**0.28**	**0.43**	**−3.31**	**−0.03**	**S**	**−0.26**	**S**
graphene	0.73	0.35	0.20	0.28	0.33	12.28	0.12	F	−0.00	S
graphene	0.73	0.35	0.25	0.28	0.30	24.35	0.16	F	−0.00	S
graphene	0.73	0.35	0.30	0.28	0.29	27.60	0.20	F	−0.00	S

Continued on next page

substrate type	T^*	κ	κ'	ϕ_{av}	ϕ	P^*	s_{sub}	orient$_{sub}$	s_{vap}	orient$_{vap}$
graphene	0.73	0.40	0.15	0.28	0.42	4.15	0.13	F	−0.10	S
graphene	0.73	0.40	0.20	0.28	0.39	5.24	0.08	F	−0.00	S
graphene	0.73	0.40	0.25	0.28	0.36	4.72	0.11	F	−0.00	S
graphene	0.73	0.40	0.30	0.28	0.32	15.13	0.13	F	0.00	F
graphene	0.73	0.45	0.15	0.28	0.37	−5.80	0.68	F	0.58	F
graphene	0.73	0.45	0.20	0.28	0.42	8.69	0.03	F	−0.01	S
graphene	0.73	0.45	0.25	0.28	0.40	5.97	0.08	F	−0.00	S
graphene	0.73	0.45	0.30	0.28	0.38	11.34	0.09	F	−0.00	S
graphene	**0.73**	**0.50**	**0.15**	**0.28**	**0.39**	**1.48**	**−0.09**	**S**	**0.69**	**F**
graphene	**0.73**	**0.50**	**0.20**	**0.28**	**0.44**	**−0.64**	**−0.01**	**S**	**−0.02**	**S**
graphene	0.73	0.50	0.25	0.28	0.42	3.46	0.04	F	−0.01	S
graphene	0.73	0.50	0.30	0.28	0.41	0.10	0.07	F	0.00	F
graphene	**0.73**	**0.30**	**0.15**	**0.49**	**0.50**	**62.01**	**−0.35**	**S**	**−0.36**	**S**
graphene	**0.73**	**0.30**	**0.20**	**0.49**	**0.51**	**109.18**	**−0.07**	**S**	**−0.36**	**S**
graphene	0.73	0.30	0.25	0.49	0.48	181.89	0.15	F	−0.32	S
graphene	0.73	0.30	0.30	0.49	0.52	263.23	0.48	F	−0.28	S

Continued on next page

substrate type	T^*	κ	κ'	ϕ_{av}	ϕ	P^*	s_{sub}	orient$_{sub}$	s_{vap}	orient$_{vap}$
graphene	**0.73**	**0.35**	**0.15**	**0.49**	**0.52**	**43.38**	**−0.46**	**S**	**−0.25**	**S**
graphene	**0.73**	**0.35**	**0.20**	**0.49**	**0.48**	**151.11**	**−0.42**	**S**	**−0.31**	**S**
graphene	0.73	0.35	0.25	0.49	0.51	350.30	0.36	F	−0.24	S
graphene	0.73	0.35	0.30	0.49	0.53	454.14	0.50	F	−0.27	S
graphene	**0.73**	**0.40**	**0.15**	**0.49**	**0.52**	**30.11**	**−0.19**	**S**	**−0.38**	**S**
graphene	**0.73**	**0.40**	**0.20**	**0.49**	**0.48**	**319.78**	**−0.16**	**S**	**−0.40**	**S**
graphene	0.73	0.40	0.25	0.49	0.47	775.73	0.41	F	−0.40	S
graphene	0.73	0.40	0.30	0.49	0.49	952.70	0.57	F	−0.34	S
graphene	**0.73**	**0.45**	**0.15**	**0.49**	**0.55**	**24.49**	**−0.14**	**S**	**−0.23**	**S**
graphene	0.73	0.45	0.20	0.49	0.49	818.67	0.30	F	−0.34	S
graphene	0.73	0.45	0.25	0.49	0.49	953.54	0.36	F	−0.30	S
graphene	0.73	0.45	0.30	0.49	0.49	1053.37	0.39	F	−0.28	S
graphene	**0.73**	**0.50**	**0.15**	**0.49**	**0.52**	**6.56**	**−0.46**	**S**	**−0.44**	**S**
graphene	0.73	0.50	0.20	0.49	0.50	896.87	0.13	F	−0.30	S
graphene	0.73	0.50	0.25	0.49	0.50	1073.39	0.23	F	−0.27	S
graphene	0.73	0.50	0.30	0.49	0.50	1155.16	0.27	F	−0.25	S

S3.3 SUBSTRATE PARAMETERS AND EFFECT ON ALIGNMENT

Two different substrates structures were examined to determine the effect of interaction strength and substrate features on alignment at the solid interface. Interaction parameters for the different substrates can be found in Section S3.1 Table S3.4. The arrangement of particles in the two substrates, shown in Fig. S3.1, was chosen to mimic that of graphene (atom spacing from the OPLS-AA force field for the equilibrium bond length between aromatic carbons[202]), and the fcc(001) plane of silicon's crystal structure (spacing matching silicon's lattice constant)[247] for σ = 3.2 Å.

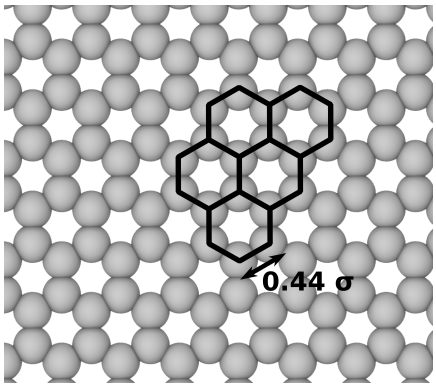

(a) Graphene substrate. Hexagons highlight the positions of the aromatic rings. Distance between all connected carbon atoms is 0.44 σ.

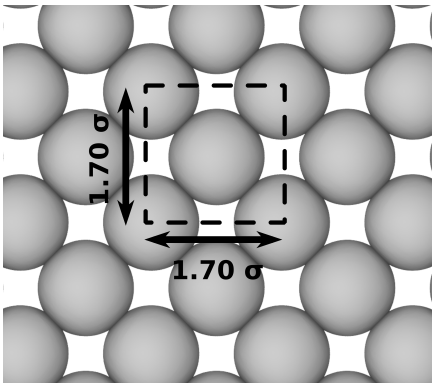

(b) Silicon substrate. Dashed lines indicate the unit cell

Fig. S3.1 Structures of the atomistic substrates used to model the solid substrate.

The dependence of the orientational ordering at the solid and vapour interfaces on the substrate is shown below. At the solid interface, stronger substrate–fluid interactions push the points further left (towards a more face-on orientation) on the phase diagram. The substrate has a negligible effect on the orientation at the vapour interface, as expected. A slight dependence of the alignment at the solid interface on the substrate structure is observed, with the less densely packed silicon substrate giving a slight shift towards the side-on orientation. This can be explained by considering the non-uniform silicon surface as a surface that is slightly penetrable in certain regions, so excluded volume entropic effects are expected to slightly enhance the side-on orientation relative to the face-on for this substrate.

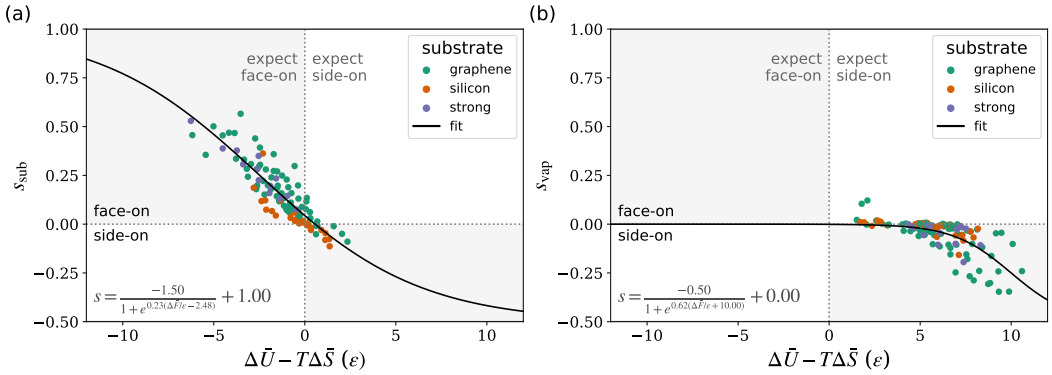

Fig. S3.2 Orientational order parameter at the (a) substrate and (b) vapour interfaces as a function of interfacial free energy difference for different substrate types.

S3.4 DEPENDENCE OF ENTROPY ON SUBSTRATE AND TEMPERATURE

The calculations presented for the entropy difference between the face-on and the side-on alignment at the two interfaces used data from simulations with two different substrates and at different temperatures. The dependence of the entropy scaling on these two factors is shown below (Figs. S3.3, S3.4). In all cases, the entropy does not significantly depend on the simulation conditions, though some variability with the substrate structure, as discussed in the main paper, is observed.

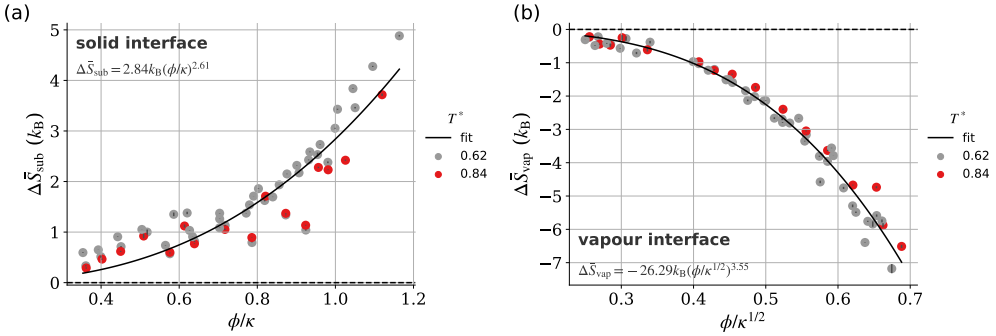

Fig. S3.3 Entropy difference between face-on and side-on orientations per interface particle at the (a) solid and (b) vapour interfaces for different simulation temperatures.

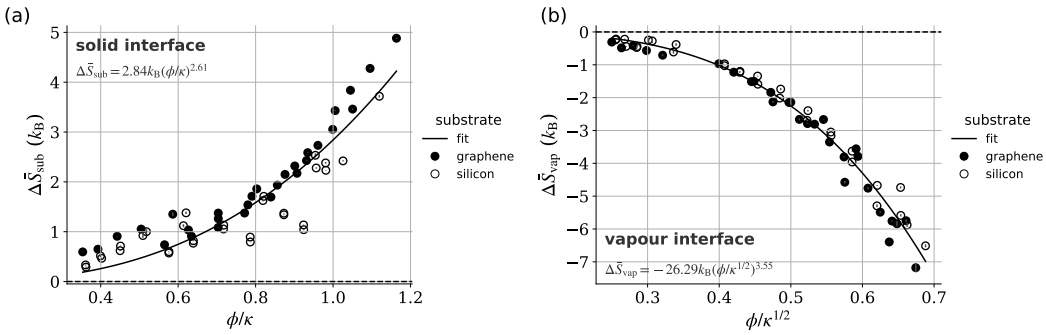

Fig. S3.4 Entropy difference between face-on and side-on orientations per interface particle at the (a) solid and (b) vapour interfaces for different substrate types.

S3.5 SELECTED DENSITY/ORDER PARAMETER PROFILES

The density and orientational order parameter profiles for selected systems is shown. The systems chosen are those that displayed the greatest orientation preference at either interface, and one that is close to isotropic.

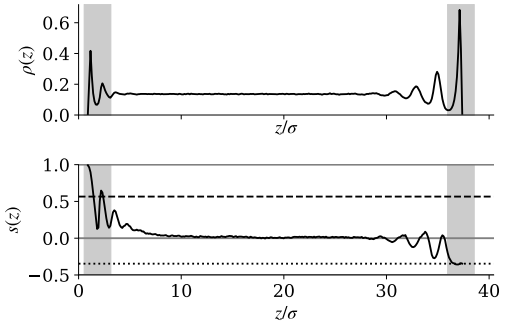

(a) Strongest side-on alignment at vapour interface, and strongest face-on alignment at solid interface: graphene substrate, $\kappa = 0.4$, $\kappa' = 0.3$, $T^* = 0.73$, $\phi_{\text{av}} = 0.49$, $\phi = 0.49$, $P^* = 953$

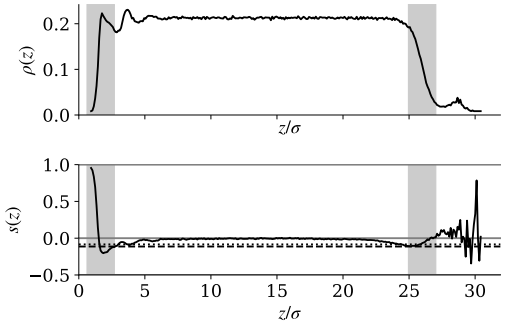

(b) Strongest side-on alignment at solid interface: silicon substrate, $\kappa = 0.5$, $\kappa' = 0.2$, $T^* = 0.56$, $\phi_{\text{av}} = 0.39$, $\phi = 0.49$, $P^* = -1.5$.

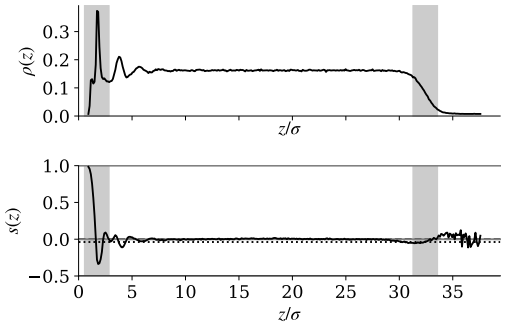

(c) System close to isotropic at both interfaces: graphene substrate $\kappa = 0.45$, $\kappa' = 0.2$, $T^* = 0.62$, $\phi_{\text{av}} = 0.39$, $\phi = 0.46$, $P^* = 4.2$.

Fig. S3.5 Density ($\rho(z)$, top) and orientational order parameter ($s(z)$, bottom) profiles for a selection of systems showing the most extreme of the possible behaviours at each interface. Shaded regions indicate the z coordinates of particles that were considered to be at the solid or vapour interface when calculating s_{sub} and s_{vap}. In all cases, $s(z) \to 1$ as $z \to 0$ since only particles in the face-on orientation can have their centres-of-mass within that distance of the substrate. Hence, the value of s_{sub} is calculated as the average over all particles within the shaded grey regions. Dotted (s_{vap}) and dashed (s_{sub}) lines indicate these interface values. The particles in the solid substrate are centred at at $z = 0$.

S3.6 ORIENTATION DISTRIBUTIONS AT SOLID AND VAPOUR INTERFACES

The orientation distributions at the solid and vapour interfaces for a selection of the systems of purely repulsive particles, used to calculate the entropic component of the free energy, are shown in Fig. S3.6. All distributions below are for the graphene arrangement of substrate particles at $T^* = 0.62$. θ is the angle between the short of the fluid particle and the z-axis (normal to the substrate). $\cos(\theta) = 0$ corresponds to the perfectly side-on orientation, and $\cos(\theta) = 1$ to perfectly face-on.

Note that conditions for which $P(\cos(\theta) = 1)$ was found to be zero (due to the finite simulation duration and very low probability of these configurations) were not used in the determination of the scaling of the face-on/side-on entropy difference with ϕ and κ. These conditions were found to correspond to systems for which the bulk fluid was not isotropic and so were not used in predicting interface orientation in the paper.

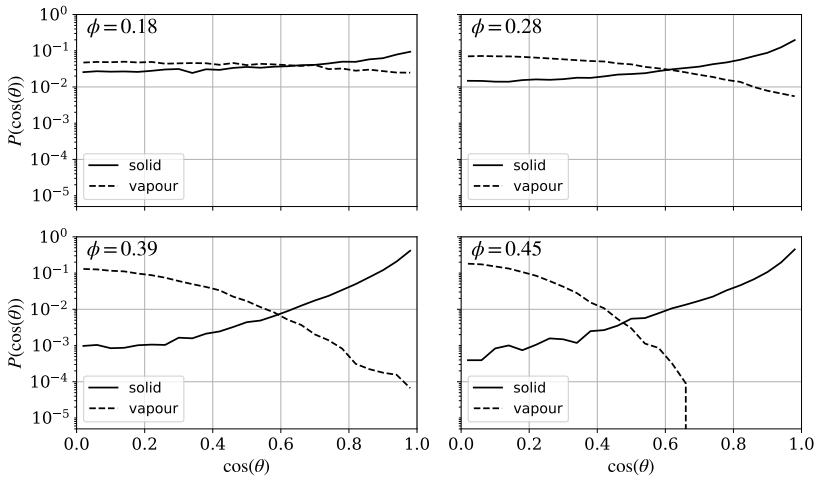

(a) $\kappa = 0.30$

Fig. S3.6 Orientation distributions at the interfaces in simulations of purely repulsive particles. Solid lines are the distributions at the solid interface and dashed lines are those at the vapour interface.

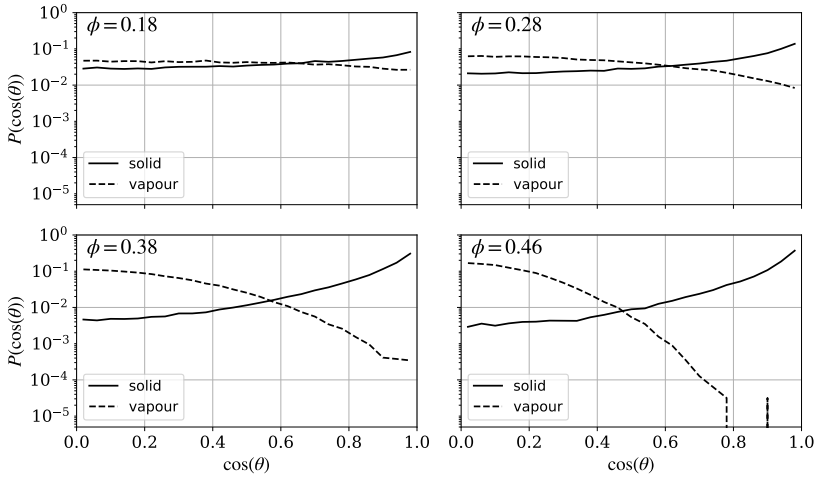

(b) $\kappa = 0.35$

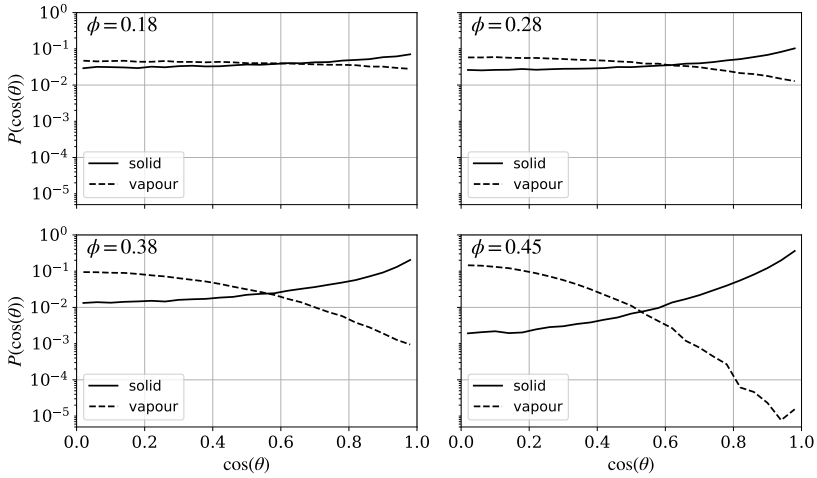

(c) $\kappa = 0.40$

Fig. S3.6 Orientation distributions at the interfaces in simulations of purely repulsive particles. Solid lines are the distributions at the solid interface and dashed lines are those at the vapour interface.

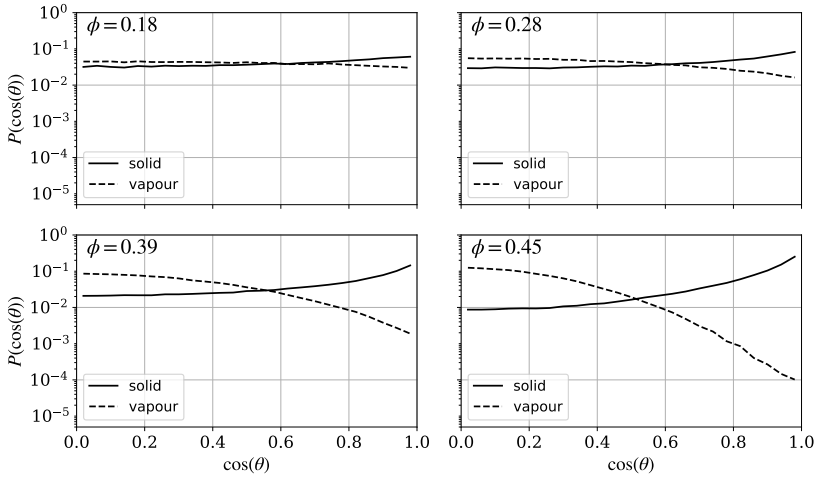

(d) $\kappa = 0.45$

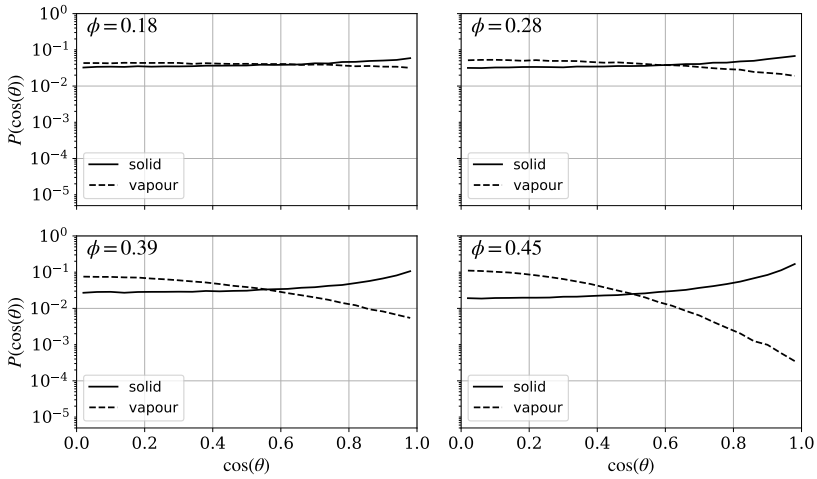

(e) $\kappa = 0.50$

Fig. S3.6 Orientation distributions at the interfaces in simulations of purely repulsive particles. Solid lines are the distributions at the solid interface and dashed lines are those at the vapour interface.

S3.7 PACKING OF CLOSE-PACKED ELLIPSOIDS IN FACE-ON AND SIDE-ON ORIENTATIONS

In order to calculate the interaction energy difference between a fluid particle in the face-on or side-on orientation and its nearest neighbours (main paper, eqn (3.7)), the packing of a layer of fully face-on or fully side-on particles was assumed. Through examination of simulated systems that formed highly aligned layers at either interface (in these cases, the alignment continued into the bulk), it was found that the fluid particles pack in such a way that a face-on particle has six nearest neighbours in the same layer, all in the side–side orientation, while a side-on particle has four nearest neighbours (two face–face, two side–side) in the same layer. It should be noted that the side-on case was somewhat more disordered.

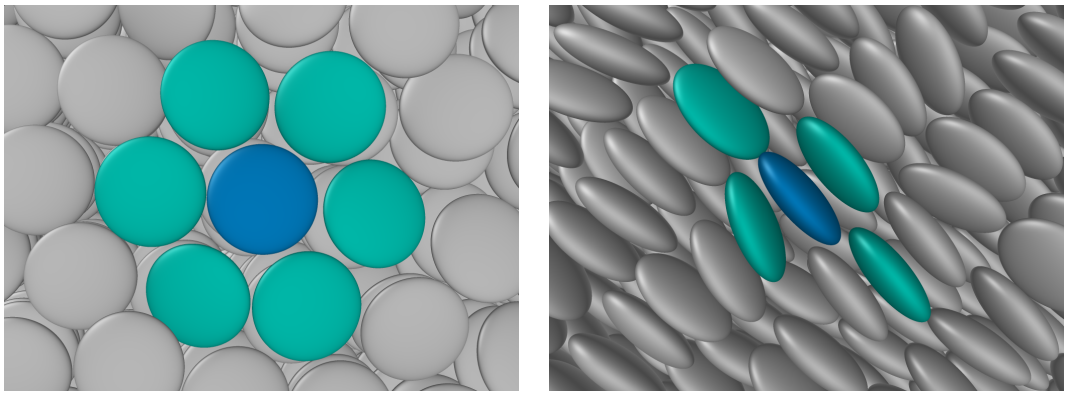

(a) A face-on particle (blue) has 6 nearest neighbours (green) in its closest packing. All six interact in the side–side orientation.

(b) A side-on particle (blue) has four nearest neighbours (green) in the observed packing. Two interact in the face–face and two in the side–side orientations.

Fig. S3.7 Closest packing of fluid particles in the (a) face-on and (b) side-on orientations to an interface.

Comparing this ideal alignment with systems in which the bulk fluid is isotropic, some deviation from this assumed behaviour is observed, with a more disordered interface in these cases, especially for the side-on orientation at the vapour interface.

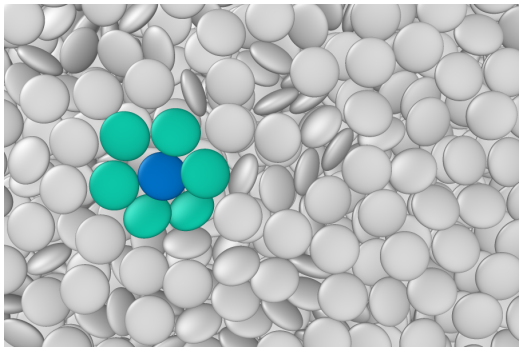

(a) An example of face-on packing at the solid interface in a system in which the bulk fluid is isotropic. Highlighted particles show the assumed packing from Fig. S3.7(a) for face-on particles.

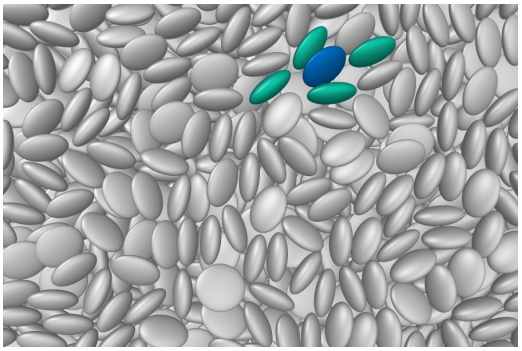

(b) An example of side-on packing at the vapour interface in a system in which the bulk fluid is isotropic. Highlighted particles show the assumed packing from Fig. S3.7(b) for side-on particles.

Fig. S3.8 An example of the actual arrangement of particles in (a) the face-on orientation at the solid substrate, and (b) the side-on orientation at the vapour interface. These snapshots come from the system with the strongest alignment at both interfaces (graphene substrate, $\kappa = 0.4$, $\kappa' = 0.3$, $T^* = 0.73$, $\phi_{\text{av}} = 0.49$). Although some instances of the assumed packing are observed at both interfaces, the particles are generally more disordered, especially in the side-on orientation at the vapour interface.

S3.8 EFFECT OF PRESSURE

In order to maintain a constant, and experimentally relevant (for OSCs), density over the range of parameters and temperatures studied, and to prevent evaporation, the positions of the two walls (repulsive harmonic wall at the vapour interface, and solid wall) were fixed. This resulted in high pressures in some circumstances, with the particles at the vapour interface pushed up against the harmonic wall. Although it does not appear that the pressure influences the orientation at the solid interface significantly (Fig. S3.9a), there is a slight dependence of the orientation at the vapour interface on pressure (Fig. S3.9b).

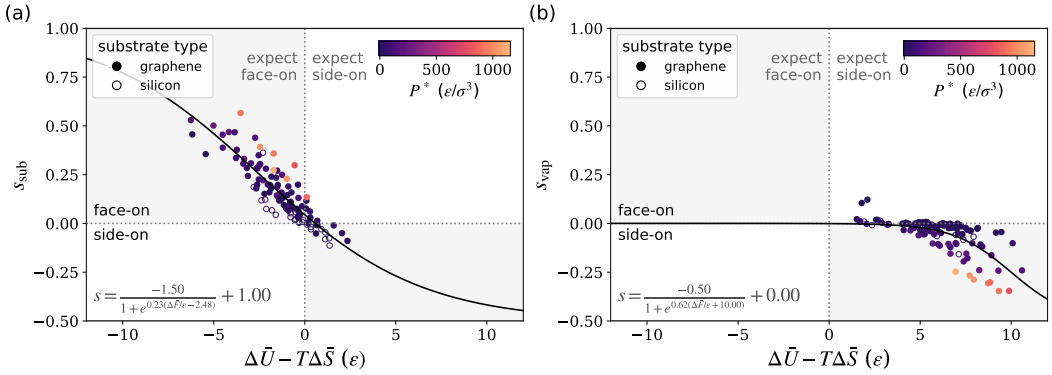

Fig. S3.9 Orientational order parameter at the (a) solid and (b) vapour interfaces as a function of the interface free energy difference, with points colour-coded by the average reduced pressure ($P^* = P/(\epsilon/\sigma^3)$, calculated from the normal force per unit area on the solid substrate). The scaling of the orientation with free energy difference is largely independent of pressure, except at very high pressures.

4

Competing single-chain folding and multi-chain aggregation pathways control solution-phase aggregate morphology of organic semiconducting polymers

"I am so sick of moving like a slug. I want to move like a cheetah. Or a slug driving a remote controlled car. Something more plausible than that, but fast."

— Lesley Knope, *Parks and Recreation*

Unpublished work written in manuscript style

Abstract

Understanding the solution-phase behaviour of organic semiconducting polymers is important for systematically improving the performance of devices based on solution-processed thin films of these molecules. Solvent quality, which is a simple parameter to tune experimentally, is especially important as it can give rise to significantly different polymer chain conformations, with poorer solvents conventionally expected to give more collapsed chains than good solvents, in which polymer chains remain swollen. However, under certain conditions, high-performance organic-semiconducting polymer P(NDI2OD-T2), also known as N2200, has been shown to form extended rod-like aggregates in poor solvents, much larger than a single chain and in contrast to previous studies of this polymer and the conventional understanding of solution-phase polymer behaviour. In this work, we parameterise a coarse-grained model for P(NDI2OD-T2) to reproduce the structure and dynamics of an all-atom explicit solvent model, and use it to study the effect of solvent quality on the solution-phase behaviour of this polymer. We find that in poor solvent conditions, aggregation through only a few monomers gives effectively inseparable chains, leading to the formation of extended structures of partially overlapping chains via non-equilibrium assembly. For better solvents, weaker polymer–polymer interactions allow rearrangement towards the thermodynamic minimum of fully overlapping chains. This behaviour requires that multi-chain aggregation occurs faster than chain folding, which we show is the case for the chain lengths and concentrations shown experimentally to form rod-like aggregates. This kinetically controlled process introduces a dependence of aggregate structure on concentration, chain length, and chain flexibility, which we show is able to reconcile experimental findings and is generalisable to the solution-phase assembly of other semiflexible polymers.

4.1 INTRODUCTION

Organic semiconductors (OSCs) have a number of advantages over conventional silicion-based semiconductors for the fabrication of lightweight, flexible, and low-cost electronic devices. These advantages generally stem from their ability to be processed from solution,[2] with printing processes enabling cheap deposition over large surfaces to generate uniform thin films.[3] Particularly for polymers, the solution-phase morphology, and its relationship with solid-state structure, is often difficult to predict, with the final thin-film structure depending on factors such as the chemical structure,[32,35–38] molecular weight,[27,30] solvent,[21,22,25,39–41] solution concentration,[42,43] and dissolution temperature[44] as well as non-equilibrium processes that occur during or post deposition.[40,105] This multitude of contributing factors means the systematic design of molecules and processing conditions for achieving good performance can be challenging. Indeed, both the importance of pre-aggregation in solution for achieving a desired microstructure,[38,44,260] and the relationship between the morphology of the OSC active layer and device performance,[25,26,38,45,53,62,115–118] have been well studied. In general, for high-performing devices, some degree of order in the deposited film is desired, although it has been shown that a fully crystalline material is not required, and may in fact be disadvantageous,[38] with ordered nanoscale domains connected by long tie-chains sufficient for good charge-carrier mobility.[26]

Understanding the solution-phase aggregation properties is particularly important for improving device performance, as devices are often fabricated using solution-processing methods. The morphology of OSCs in solution has been correlated with thin-film structure, and with device performance.[21,25,30,44] For high-performance OSC polymer P(NDI2OD-T2) (SI Fig. S4.1), also known as N2200, the formation of large rod-like aggregates has been observed experimentally in poor solvents such as toluene and xylene, and has been shown to be associated with increased electron mobility. These aggregates were shown, using small-angle X-ray scattering (SAXS) techniques, to have a radius of gyration (R_g) an order of magnitude larger than the same chains in a good solvent, indicating the formation of extended multi-chain structures that are not predicted by any existing theories.[25] This is in contrast to the behaviour predicted from previous studies of P(NDI2OD-T2) which, based on the lack of dependence on polymer concentration of the spectral shift in poor solvents and analytical centrifugation measurements, suggested that aggregation behaviour in toluene is a single-chain process caused by chain collapse and folding.[22] Notably, these experiments were conducted at a much lower concentration than the SAXS measurements (5 g/L for SAXS in ref 25, up to 1 g/L in ref 22), as well as using significantly longer chains (31 kDa in ref 25, and 118,

181, or 1105 kDa in ref 22), which may explain the reported discrepancy. Indeed, multi-chain aggregation has been observed for other OSC polymers such as MEH-PPV,[261] PffBT4T-2DT, D-DPP3T-EH, and PffBT4T-2OD,[44] with concentration- and molecular-weight-dependent effects observed.

Although the morphology and dynamics of *flexible* polymers is generally well understood,[127] OSC polymers typically have a stiffer, semiflexible backbone which, coupled with the more anisotropic shape and interactions imparted by the conjugated backbone, means that the aggregate structure may deviate from that predicted for flexible chains. Indeed, for both single-[131–133] and multi-chain[134] systems, both the backbone stiffness and solvent quality have been shown to be important for predicting the types of structures formed.

For flexible polymers, the conformation of a single polymer chain in solution is strongly correlated with the solvent quality; that is the relative strength of the polymer–polymer, solvent–solvent, and polymer–solvent interactions. Under good solvent conditions, where polymer–solvent attractions dominate, the chain is expected to be extended, while a more compact, collapsed structure is expected under poor solvent conditions in order to minimise unfavourable interactions with the solvent, or to maximise favourable intramolecular polymer interactions. Metrics such as the radius of gyration are therefore expected to decrease as solvent quality decreases and chains become more compact. When chains are sufficiently flexible, this behaviour has been observed in a number of simulation studies of single chains, with a transition from an extended coil to collapsed globule structure observed with decreasing solvent quality.[131–133] As chain stiffness increases, different structures, such as hairpins or toroids, take the place of disordered globules for poorer solvent qualities, with the exact structure depending on both the solvent quality and chain flexibility.[131–133,135] Other simulation studies have examined the effect of backbone stiffness and attraction on the single-chain behaviour of semiflexible dipolar polymers, observing collapsed globules for flexible chains, and toroids for stiffer ones when attractive interactions are strong.[136]

While a multitude of studies have examined single-chain behaviour using simulations,[131–133,135–139] or theory,[140–144] those examining multi-chain systems, which are more relevant for the behaviour of realistic OSC systems in which chains are rarely so isolated, are less common. As with the single-chain behaviour, the equilibrium structure of multi-chain systems has been shown to depend on the solvent quality and backbone stiffness: for flexible chains in poor solvents, disordered aggregates have been observed, and, as chain stiffness increased, the types of aggregates shift from amorphous to twisted or folded rod-like structures.[134] For a more comprehensive review of the behaviour of semiflexible polymers in dilute solutions, the reader is referred to ref 262.

Although solution-phase molecular simulations of multi-chain systems of OSC polymers are relatively rare, owing to the need for often prohibitively large systems to explicitly account for solvent, especially for long polymer chains, studies examining OSC solubility using all-atom (AA) molecular simulation methods can be found. Some[128–130] have used mean-field solution theories such as Flory-Huggins theory, in which simulations of short oligomers were used to estimate the Flory-Huggins parameter, which is used as a measure of solvent quality and thus the propensity for aggregation. Others[24,161] have examined the aggregation mechanism and effect of solvent and polymer properties, again using short chains or implicit solvent models. While these studies provide valuable insights into some of the many factors affecting the solution-phase morphology, Flory-Huggins theory provides a fairly simple model of the effects of polymer chain length and the relative strength of the solvent–solvent, solvent–polymer, and polymer–polymer interactions on solubility; it does not capture the roles of chain stiffness and conformation and so cannot account for extended aggregates expected for P(NDI2OD-T2). Other simulation studies that have more accurately calculated solubility through free energy perturbation methods,[161] and examined aggregation mechanisms and the effect of various molecular properties on the solution-phase behaviour,[24,161] have not been able to reach experimental chain lengths and have generally considered only the equilibrium behaviour as the timescales relevant to the kinetic processes are generally not accessible to detailed AA models.[162]

In this work we have developed a systematically coarse-grained (CG) model of P(NDI2OD-T2) in order to investigate the reported formation of large extended aggregates in poor solvents.[25] By combining atoms with correlated motion into a single CG site, and accounting implicitly for solvent, the number of degrees of freedom of the system can be greatly reduced. This allows access to polymer length and timescales on the order of those studied experimentally. Similar models have previously been developed for commonly studied OSC polymer P3HT[167,168] and used to accurately predict the experimental solution-phase conformation of this polymer, giving results consistent with the more computationally expensive AA model. In the case of P3HT, multi-chain aggregation was observed in CG simulations but, likely due to the lower concentration and longer chain length or the vastly different chemical structure of P3HT compared with P(NDI2OD-T2), although these aggregates were rod-like in nature, the extreme increase of radius of gyration relative to that of a single chain was not observed.[167]

Our CG model of P(NDI2OD-T2) is used to examine the behaviour of this polymer under conditions corresponding to varying solvent qualities. We initially examine the types of aggregates formed under different solvent conditions (Section 4.3.1), and relate the aggregate structure to the strength of intermolecular

interactions and the persistence of aggregates composed of partially overlapping chains (Section 4.3.2). The kinetics of the competing effects of single-chain folding and multi-chain aggregation, and how these may vary with concentration, molecular weight, and chain flexibility, are also considered (Section 4.3.3).

4.2 METHODS

To examine the solution–phase behaviour of close-to-experimental length polymer chains on the μs timescale, a systematically coarse-grained model of P(NDI2OD-T2), parameterised to reproduce the structural properties of monomers in an AA system, was developed. In the following sections we describe the parametrisation of the AA model and the AA simulations used to parameterise the CG model (Section 4.2.1), the parameterisation procedure for the CG model (Section 4.2.2), and the CG simulations (Section 4.2.3). All simulations were conducted using the LAMMPS software package[244,263–265] and analysis and visualisation using OVITO[245] and VMD.[266]

4.2.1 ALL-ATOM SIMULATIONS

4.2.1.1 Parameterisation of all-atom model

As many OSC polymers such as P(NDI2OD-T2) have a relatively rigid backbone and extended conjugation, their bonded parameters – particular between conjugated units – and charges are not expected to be accurately captured by general purpose force fields.[267] In order to accurately model these systems atomistically, certain parameters must therefore be calculated rather than relying on their pre-existing counterparts in the force field. Here we have based our parameterisation on the OPLS force field[202,268–273] as it has been shown to accurately describe structural and thermodynamic properties of several small-molecule OSCs[274,275] and accurately describes the properties of many organic liquids, which are commonly used as solvents for OSCs. We note that a previous AA model of P(NDI2OD-T2) has been parameterised with the AMBER force field,[129] but, to the best of our knowledge, no OPLS parameters exist for this polymer.

OPLS parameters have been obtained previously for a wide variety of OSC polymers,[24] and we have used the method outlined in that work for this parameterisation of P(NDI2OD-T2). In all cases, the van der Waals (vdW) parameters were taken directly from the OPLS force field for equivalent atom types.[202,268–273] Atomic partial charges were obtained from quantum-chemical calculations as described in the SI Section S4.1. Note that although P(NDI2OD-T2) is typically represented as having a naphthalene diimide (NDI)–bithiophene (bTh) backbone, we have separated the bTh

group into two thiophene (Th) groups and modelled the molecule as Th–NDI–Th, as shown in Fig. 4.1, in order to increase the symmetry of the molecule, allowing for a simpler and more general parameterisation. Within the polymer, the same structure will be obtained, with the only differences being in the structure of the terminal monomers (see SI Fig. S4.1 for a comparison of the two structures).

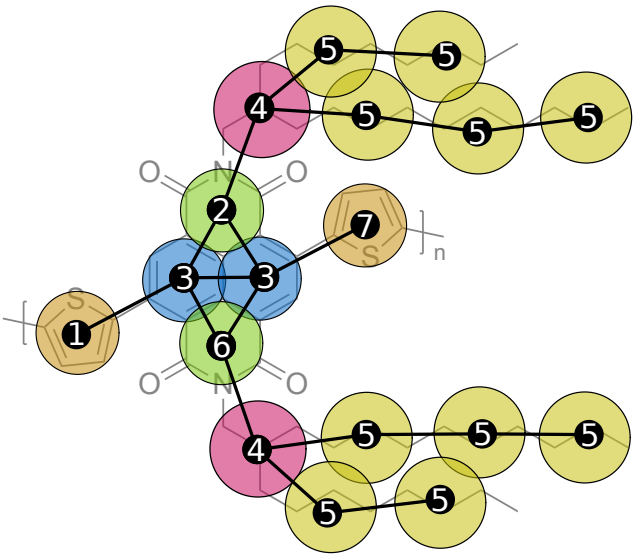

Fig. 4.1 Structure of the AA P(NDI2OD-T2) molecule with the CG model overlaid. CG sites are labelled (1–7) and coloured by their site type. Spherical CG sites are bonded through their centres-of-mass (black lines between black circles). In order to preserve the backbone structure in the AA representation, in which the thiophenes are connected at the 1 and 6 (rather than 1 and 7) carbon positions of the naphthalene group, two different site types for the thiophenes (1 and 7) and imides (2 and 6) are defined. These have the same non-bonded parameters and bond lengths, but different angle potentials in order to achieve a similar geometry to the AA model. Note that the terminal methyl group of one of the side-chains is not included in the coarse-graining in order to reduce the number of site types and facilitate parameterisation.

Most of the bonded parameters for bonds, angles, and dihedrals were taken directly from the OPLS force field for equivalent atom types,[202,268–273] while the equilibrium bond lengths and angles were obtained from the optimised geometry of the monomer (from a quantum-chemical calculation at the B3LYP/6-31+G** level), as has been done previously.[24] The exceptions were the bond stretching potential between NDI and Th groups, and the NDI–Th and Th–Th dihedral potentials. These potentials were parameterised explicitly as they are important for modelling the semiflexibility of the backbone, and expected to depend strongly on the chemical environment, while not being accurately captured by the existing OPLS parameters. These parameters were calculated using a series of constrained geometry optimisations as described in ref 24 and SI Section S4.1. All geometries

were optimised with the side-chains truncated to methyl groups after the tertiary carbon (i.e. R–CH_2–CH–$(CH_3)_2$, where R is the monomer backbone).

For the two explicitly parameterised dihedral potentials we used the functional form

$$U^{\mathrm{m/h}}_{\mathrm{dihed}}(\phi_i)(\phi) = \sum_{n=0}^{m} k_n \cos^n(\phi), \tag{4.1}$$

with $m = 4$ for the Th–Th dihedral, and $m = 8$ for the NDI–Th dihedral, where k_n are fit parameters and ϕ is the dihedral between the 4 atoms of interest. This potential form is equivalent to the more commonly used OPLS-style dihedral (SI eqn (4.17)) when $m = 4$, but more flexible for $m > 4$, with $m = 8$ required to achieve a good fit to the NDI–NDI dihedral potential (see SI Fig. S4.3). The atoms defining these dihedrals are highlighted in the SI Fig. S4.4, and the parameterisation procedure, following the method outlined in ref 24, is given in detail in the SI, Section S4.1.2. The fits of the dihedral potential and a comparison between the behaviour in the final molecular dynamics (MD) system and the values obtained from the quantum calculations are given in the SI Fig. S4.5. All parameters used for the AA simulations in this work are tabulated in Section S4.14 of the SI.

Note that the molecule as parameterised is a free, unaggregated, monomer. It is possible that both extension to a longer polymer chain, or aggregation, may change the electronic properties and hence affect further aggregation properties. The large size of the monomer, coupled with the use of terminal thiophenes for the calculation of the charge distribution as described elsewhere,[24] and the explicit calculation of important torsions from dimers, should lead to reasonable accuracy when extended to longer polymer chains. As for aggregation, recent work has shown that the electrostatic interactions are less important than the vdW interactions for predicting the solution phase aggregation of OSC molecules.[130] Perfectly capturing the conformation dependence of the mesoscale electronic structure of conjugated polymers, which is highly challenging, is therefore not expected to significantly impact the aggregation behaviour, though may be an interesting next step in reaching an even more accurate representation of polymer aggregation.

4.2.1.2 All-atom solution–phase simulation

The non-bonded interactions for the CG model used in this work were parameterised from AA simulations of symmetric P(NDI2OD-T2) monomers in *o*-dichlorobenzene (DCB) at a concentration of approximately 55 g/L (18 monomers, 2937 solvent molecules). Note that this concentration is substantially higher than both the experimental concentrations and those used later in the CG simulations of 5–10 g/L. This higher concentration was used as a system containing multiple monomers is required to get good statistics for the monomer–monomer distributions to be used

in the coarse-graining procedure. Low concentrations would require a prohibitively large number of solvent molecules. The parameters obtained as described above for P(NDI2OD-T2) were used, and parameters from the OPLS-2005 force field[202,268–273] used for the solvent (see SI Section S4.14). DCB was chosen as the solvent based on experimental UV–visible spectroscopy data,[22,25] as it should give little monomer aggregation, guaranteeing a homogeneous system as required by the coarse-graining process.

In all AA simulations in this work, a truncated and shifted Lennard Jones (LJ) potential was used with a cutoff of 11 Å, consistent with the parameterisation of the OPLS force field.[202,273] 1–2 and 1–3 interactions (between particles separated by one and two bonds, respectively) were set to zero, and the 1–4 LJ interactions (between particles separated by three bonds) to 0.5 times their full values, again consistent with the OPLS force field. Electrostatic interactions were calculated using the particle–particle particle–mesh (PPPM) method.[201] Hydrogen-containing bond lengths were constrained to their equilibrium lengths using the SHAKE algorithm,[276] allowing for the use of a timestep of 2 fs.

To initialise the system, the particles were packed, using Packmol,[277] with random positions and orientations into a cubic simulation box at low density (approx. 0.5 g/cm^3, box size of (120 Å)^3 to prevent overlapping particles or interlocking rings. The box was shrunk over 40 ps to higher than the target density (approx. 1.7 g/cm^3, box size (76 Å)^3) at constant energy, then expanded over an additional 20 ps to give approximately the expected experimental solvent density (approx. 1.3 g/cm^3, box size (82.5 Å)^3) as described in ref 278. The energy of the system was then minimised, and velocities assigned from a Maxwell-Boltzmann distribution at a temperature of 300 K. The simulation was then run for 200 ns at constant pressure and temperature, with temperature and pressure controlled using a Nosé-Hoover thermostat (relaxation time scale = 100 fs)[196,279] and barostat (relaxation time scale = 1000 fs),[198] respectively. The equilibration time was determined from the convergence of the monomer–monomer centre-of-mass radial distribution function (RDF) (see SI Fig. S4.7), with the first 50 ns being discarded as the equilibration period.

The bonded parameters were parameterised from simulations of P(NDI2OD-T2) trimers in DCB, so as to include the bonds between monomers. These simulations were set up similarly to the AA simulations, with 8 trimers at the same concentration as the monomer simulations (approx. 55 g/L, 3229 DCB molecules). The same simulation procedure as for the monomer simulations was followed, with initial (low density), intermediate (high density), and final (experimental solvent density) box sizes of (140 Å)^3 (approx. 0.3 g/cm^3), (80 Å)^3 (approx. 1.6 g/cm^3), and (85 Å)^3 (approx. 1.3 g/cm^3) respectively. The system was simulated for 90 ns, again with

the first 50 ns discarded as the equilibration period, based on the convergence of the bonded distributions (SI Fig. S4.8).

4.2.2 coarse-grained model parameterisation

The CG representation of P(NDI2OD-T2) is given in Fig. 4.1. Each aromatic ring was assigned to a single spherical CG site, and the side-chain sites composed of three (site type 5) or four (site type 4) carbon atoms. This mapping groups atoms whose motion is expected to be correlated into the same site. We note that while the entire NDI group is relatively rigid and could theoretically be coarse-grained into a single site, the planar nature of the group means that a large spherical site in this position would not capture important properties such as the π-stacking distance between chains. This issue is especially important when considering that the structure of the final collapsed state of single chains has been shown to depend on the width of the monomers perpendicular to the chain axis,[139] meaning that an accurate representation of the monomer shape is important for obtaining behaviour in the CG model that is consistent with the AA systems. The four-site structure used here for the NDI group captures the anisotropy of the backbone shape and interactions. The use of anisotropic sites would be beneficial, especially for larger, more anisotropic molecules, but these models are currently difficult to parameterise for accurate solution-phase behaviour, and are not likely to offer appreciable speed-up for a molecule such as N2200 for which the backbone can be modelled as a small (here, 6) collection of spheres. The first general, systematic method for coarse-graining condensed phases with anisotropic sites has only recently been developed,[280] so although it has not been used for the work in this thesis, it may provide an interesting extension to this work, particularly for larger polymers for which more significant speed-up and accuracy could be achieved.

Site masses were taken as the sum of the masses of atoms in the AA representation that compose each CG site. Where atoms were shared between sites, such as within the NDI group, the masses were split evenly over the two sites (e.g. the carbon shared between site 2, and both site 3s in the CG representation contributed 1/3 of its mass to each site; see SI table S4.13 for a list of masses).

All CG polymer systems were simulated in implicit solvent using Langevin dynamics[197] to capture the effect of stochastic collisions with solvent molecules and frictional drag. The equations of motion of a particle i with mass m and position $\boldsymbol{r}$ are

$$m_i \ddot{\boldsymbol{r}}_i(t) = \boldsymbol{f}_i(t) - m_i \gamma \dot{\boldsymbol{r}}_i(t) + \zeta_i(t) \tag{4.2}$$

where $\boldsymbol{f}_i(t)$ is the force acting on particle i due to the CG potential and $m_i \gamma \dot{\boldsymbol{r}}_i(t)$ the frictional drag in a solvent with friction coefficient γ. $\zeta_i(t)$ is the force due to

random collisions with the solvent, which satisfies $\langle \zeta_i(t) \rangle = 0$ and $\langle \zeta_i(t)\zeta_j(t') \rangle = 2\gamma k_B T m_i \delta_{ij} \delta(t - t')$. Most CG simulations in this work used a friction coefficient of $\gamma = 0.02$ fs^{-1}, chosen to give a mean squared displacement (MSD) of monomers in the CG model that was consistent with that of the AA model in DCB (SI Fig. S4.6). With this friction coefficient, the maximum timestep that gave stable simulations was 8 fs, which was used for all CG simulations in this work, again unless otherwise stated. A number of simulations were also conducted at lower friction to speed up the dynamics and observe the long time equilibrium behaviour, as well as to examine the effect of viscosity on both single-chain folding, and multi-chain aggregation. These simulations used $\gamma = 0.002$ fs^{-1} (1/10 the as-parameterised friction coefficient) and a timestep of 5 fs. Note that the final equilibrium polymer conformation should be independent of the choice of friction coefficient, with the lower friction coefficient simply allowing the equilibrium conformation to be reached faster. All simulations were carried out at constant number of particles, volume, and temperature (NVT ensemble).

The CG model for P(NDI2OD-T2) was parameterised using the iterative Boltzmann inversion (IBI) method,[172,281] which has been used previously with good success to systematically coarse-grain OSC polymer P3HT in an implicit solvent model,[167] and in polymer–fullerene blends.[168] This method aims to match the local structural distribution functions between equivalent AA and CG systems through an iterative process of updating the interaction potentials of the CG model until the distribution functions of the CG system converge to that of the AA system. We followed the procedure outlined in refs 168 and 167, with the potential for each subsequent iteration, $U_{n+1}(x)$, updated according to

$$U_{n+1}(x) = U_n(x) + a_n \ln\left(\frac{P_n(x)}{P_{\text{target}}(x)}\right) \tag{4.3}$$

where $U_n(x)$ is the potential for iteration n of the procedure as a function of the variable x, $0 \leq a_n \leq 1$ is a scaling factor that controls how much the potential changes between iterations, $P_{\text{target}}(x)$ the target distribution of the property being parameterised (in all cases this is the corresponding distribution in the AA simulation, calculated between the centres-of-mass of the atoms that constitute each CG site), and $P_n(x)$ the CG distribution from iteration n. For the non-bonded interactions, $P(x)$ is the RDF $g(r)$. For the bonded interactions it takes the forms $P_{\text{bond}}(l)/l^2$, $P_{\text{angle}}(\theta)/\sin(\theta)$, $P_{\text{dihed}}(\phi)$, and $P_{\text{improp}}(\psi)$ for the bond, angle, dihedral, and improper distributions, respectively, where l is the bond length, θ the bond angle, and ϕ and ψ proper and improper torsions, respectively. In all cases, the resulting potentials were fit to analytical functions. The definitions of the analytical functions used are given in the SI, Section S4.2.1. Although some accuracy is lost in the fitting to the analytical form, it greatly enhances the computational efficiency over using,

for example, a tabulated potential, while still giving good agreement between the CG and AA distributions (SI Section S4.2.3). In contrast to the AA model, for which the 1–4 interactions were included (albeit at half their full strength), the 1–2, 1–3, and 1–4 interactions were all set to zero in the CG model.

In all cases, systems were initialised by packing the desired monomers/polymers into the simulation box with random position and orientation (in the case of polymers, each chain was a linear arrangement of monomers in which the backbone units were coplanar), and a soft-core potential of the form

$$U_{\text{soft}}(r) = A\left[1 + \cos\frac{\pi r}{r_{\text{c}}}\right],\ r < r_{\text{c}}, \tag{4.4}$$

where r_{c} is a cutoff distance, r the distance between two particles, and A an energy pre-factor that controls the "hardness" of the potential, was applied to remove any overlaps between particles (r_{c} = 6 Å, A increased linearly from 0 to 30 kcal/mol over 5000 fs, timestep = 1 fs).

The fit of an analytical function (SI section S4.2.1) to the Boltzmann inversion of the target distributions was used as an initial guess for all parameters, with the values of ϵ_{ij} in the non-bonded LJ parameters constrained to be initially $0.1 \leq \epsilon_{ij} < 1$ in order to prevent extensive aggregation. The constraints on ϵ_{ij} were removed for the iterative procedure. Bonded interactions were optimised first, through comparison of the target distributions from the AA trimer simulations (8 P(NDI2OD-T2) trimers at approx 55 g/L) described above with distributions from an equivalent CG system of 8 trimers in an (87 Å)^3 box. Note that not every possible bond/angle/dihedral/improper was parameterised or included in the CG model as many are fully defined by other parameters (e.g. the 3–6–3 angle was not parameterised because it is effectively fixed by the 3–6 and 3–3 bonds; see Fig. 4.1 for site definitions). These un-parameterised CG distributions are compared with the AA distributions for the fully parameterised model in the SI Section S4.2.3. The non-bonded parameters were optimised using simulations matched to the AA system of 18 monomers at approx 55 g/L. These CG systems contained 18 monomers in an (84 Å)^3 box. The discrepancy between the CG and AA RDFs at iteration n was quantified as[282]

$$b_n = \sum_{i,j} f_{ij} N_{ij} \tag{4.5}$$

where

$$f_{ij} = \frac{\int_0^{r_b}\left[g_{ij}(r) - g_{ij}^{\text{ref}}(r)\right]^2 \mathrm{d}r}{\int_0^{r_b}\left[g_{ij}^{\text{ref}}(r)\right]^2 \mathrm{d}r} \tag{4.6}$$

where $g_{ij}(r)$ is the CG RDF for site types i and j at iteration n, N_{ij} the number of ij pairs in a monomer, $g_{ij}^{\text{ref}}(r)$ the target AA RDF for each ij pair, and r_b the cutoff

for the non-bonded interactions (here 15 Å, at which point the interaction strength was less than 2% of the strength at the energetic minimum). The variable b_n was found to converge after $n = 12$ iterations, with further iterations not improving the agreement between AA and CG distributions further (see SI Figs. S4.9, S4.10). The parameters from iteration 12 were therefore used for further CG simulations.

Optimising the non-bonded interactions independently of, and after, the bonded interactions as we have done, can potentially perturb the bonded distributions so that they no longer match the corresponding AA distributions. We have verified that this was not the case by comparing the AA bonded distributions to those obtained from a 100 ns simulation of the CG model with the parameterised bonded and non-bonded interactions (SI Section S4.2.3). Good agreement between the AA and CG distributions was still found in all cases. The final bonded and non-bonded parameters are given in the SI Section S4.15.

4.2.2.1 Solvent quality

In order to model a range of solvent conditions, we defined two additional sets of non-bonded CG parameters to approximate solvation in a better solvent and a poorer solvent. The IBI method used in this work relies on the AA reference systems being homogeneous, which makes it especially challenging to parameterise models in poor solvents, in which the equilibrium structure is expected to show extensive polymer aggregation. Instead of explicitly parameterising the model in other solvents, we therefore adopted a simpler approach of scaling the parameters from those parameterised in DCB to give either stronger (representative of a poorer solvent), or weaker (representing a better solvent) interactions. This is similar to the procedure used in ref 167, in which the temperature was scaled to model changing solvent quality. The better solvent parameters (referred to below as the "good" solvent) were obtained by scaling all the non-bonded parameters of the DCB parameterisation to be 20% weaker. Similarly, the poorer solvent parameters (referred to as the "poor" solvent) were obtained by increasing the strength of all non-bonded parameters by 20%. The system with the original parameters, parameterised in DCB, will be referred to as the "intermediate" solvent. It is important to note that some aggregation occurred in the CG simulations with all three of these solvent conditions meaning all were, according to the conventional polymer physics definition, relatively poor solvents. We therefore use the terms "good" and "intermediate" to refer to the better solvents, in which, according to UV–vis spectra of P(NDI2OD-T2) in solvents such as DCB and chlorobenzene, some aggregation is observed without the formation of extended rod-like aggregates.[25] The LJ parameters and curves for these three sets of parameters are given in the SI, Section S4.15.

To confirm that the scaled solvent parameters were reasonable representations

of the behaviour of P(NDI2OD-T2) in a better and poorer solvent, we calculated the free energy as a function of backbone centre-of-mass separation in AA systems of two P(NDI2OD-T2) monomers in DCB, 1-chloronaphthalene (CN) (a better solvent than DCB), and toluene (TOL) (a poorer solvent than DCB, and one of those shown to promote extended rod-like structures experimentally[25]). This free energy was compared with the equivalent free energy calculated for CG monomers with the poor, intermediate, and "good" solvent parameters. Free energies were calculated using on-the-fly probability enhanced sampling (OPES),[209] which, similarly to metadynamics,[210] facilitates the exploration of the entire probability distribution of interest (here that of the centre-of-mass separation) by depositing small repulsive Gaussians (kernels) in collective-variable space over the course of the simulation in order to bias the system against exploring regions it has already visited. Further details on the method can be found in the SI Section S4.3.1. These calculations were carried out using the PLUMED software package, version 2.5.4.[211,212]

All-atom free-energy calculations. For all three solvents, a pair of P(NDI2OD-T2) monomers in the π-stacked configuration, with centre-of-mass (of NDI groups) separation of 3 Å, was placed in the centre of a $(100\ \text{Å})^3$ simulation box, and 1000 solvent molecules packed with random position and orientation around it[277] to give a low density system where solvent molecules do not overlap or interlock. As with the AA simulations described above, the system was shrunk over 40 ps to a higher density (box size $(55\ \text{Å})^3$), then expanded over a further 20 ps to give a $(60.8\ \text{Å})^3$ box. The system was then simulated at constant pressure and temperature for 5 ns to properly solvate the monomers, and to reach the appropriate density. As OPES generally converges faster if it starts near the expected free energy minimum, we placed a harmonic restraining potential of the form

$$U_{\text{w}}(r) = \begin{cases} k_{\text{w}}(r - a_{\text{w}})^2, & r > a_{\text{w}}, \\ 0, & \text{otherwise}, \end{cases} \tag{4.7}$$

on the monomer–monomer centre-of-mass separation r, which acts to keep the separation below a_{w}. Here we set a_{w} to 10 Å and k_{w} to 100 kcal/mol/Å^2 to ensure the monomers stayed close to the expected free energy minimum of the directly π-stacked structure. After 5 ns, this harmonic wall was removed and the OPES simulation begun from the final configuration of this setup procedure. Three collective variables were biased in this procedure: the centre-of-mass separation (where the centre-of-mass was calculated as the centre-of-mass of the NDI group), the angle between the vectors normal to the planes of each NDI group (angle 1), and the angle between this vector of one monomer and the vector connecting the centres-of-mass of the two monomers (angle 2). For this work, we were interested solely in

the free-energy as a function of the monomer separation rather than both separation and orientation, but we note that biasing the angles, which may be expected to be slowly varying collective variables, will aid in achieving faster convergence. The OPES simulation was conducted with a kernel deposition frequency of 5000 timesteps, where kernels were initially of width 0.2 Å for the distance constraint, and 0.06 and 0.12 radians respectively for angles 1 and 2. These initial kernel widths were chosen to be approximately the standard deviation of the unbiased variable at equilibrium. A bias factor, which is used to determine the shape of the target probability distribution,[209] of 10 and an estimated free energy barrier of 30 kcal/mol were used. Additionally, to prevent the monomers becoming too separated and sampling large regions of unimportant (large separation) space, we placed a harmonic wall (eqn (4.7)) at a centre-of-mass separation of 20 Å, again with force constant 100 kcal/mol/Å^2. OPES simulations were then run for approx 1.6 μs in CN, 1.7 μs in DCB, and 1.2 μs in TOL. The reweighting procedure to obtain the unbiased distribution is outlined in the SI, Section S4.3.1.

Coarse-grained free energy calculations. Similar OPES simulations were conducted for the three sets of CG parameters in order to validate the choice of parameters for the "good" and poor solvents, and confirm the agreement between the AA and CG models for the system parameterised in DCB. These simulations were initialised by placing two monomers in the centre of a (60 Å)^3 simulation box (approximately the size of the simulation box for the AA free energy calculations) again in the directly π-stacked configuration, with centre-of-mass separation of 5 Å. A soft-core potential (identical to that used previously) was applied to remove particle overlaps, before switching to the LJ parameters corresponding to the "good", intermediate (DCB), or poor solvents. The energy was minimised, then OPES run for 2 μs with a timestep of 8 fs. As with the AA calculations, the centre-of-mass separation was defined in terms of the centre-of-mass of the NDI groups (site types 2, 3, and 6 in the CG model), and a repulsive harmonic wall (eqn (4.7), k_w = 100 kcal/mol/Å^2) used to keep the monomer centres-of-mass within 20 Å of each other. All of the OPES and reweighting parameters were the same as for the AA equivalent, although in this case, only the separation (not the angles) was biased. Comparing the final free energy curves as a function of centre-of-mass separation showed good agreement between the "good" solvent parameters and CN, the as-parameterised DCB model and its AA equivalent, and the poor solvent parameters and TOL (SI Fig. S4.15). This finding confirms that the poor solvent conditions used here should be a reasonable representation of the conditions that have been experimentally been shown to give extended rod-like aggregates.

4.2.2.2 *Backbone flexibility*

Finally, as the folding of single polymer chains has been shown to depend on backbone stiffness,[131–133] we examined two different backbone stiffnesses: the as-parameterised stiffness (we will refer to this as "regular" stiffness), and a more flexible chain (referred to as "flexible"). The stiffness of each chain was quantified by its Kuhn length, that is the length of freely-jointed segments of the polymer, with more flexible chains having a lower Kuhn length than less flexible equivalents. To model the more flexible chain, the coefficients of the 1(7)–3–3 angles, and 3–7–7–1 dihedral were reduced to 1% of the values of the regular stiffness backbone (see SI Section S4.15 for parameters and plots of these modified potentials), reducing the Kuhn length of the chain by 30–40% in the "good" solvent (SI Fig. S4.16).

4.2.3 COARSE-GRAINED SIMULATIONS

In order to determine the effect of the rates of single-chain folding and multi-chain aggregation, solvent quality, and backbone stiffness on the final aggregate structure, we examined the folding of a number of isolated single chain systems of various molecular weights as a function of backbone stiffness and solvent quality, as well as multi-chain systems representative of the experimental systems studied in ref 25. Averaging of random variables was carried out both within simulations (with most multi-chain simulations consisting of over 100 polymer chains), and over independent simulations.

4.2.3.1 *Single-chain simulation*

Single-chain simulations were conducted for two backbone flexibilities ("regular" and "flexible", described previously), and the two extremes of the solvent qualities studied here ("good" and "poor"). To examine the effect of molecular weight on folding kinetics, we studied three different chain lengths: 10, 20, and 30 monomers, corresponding to $M_n \approx 10$, 20, and 30 kDa, respectively. All systems were set up following the same procedure. First, the single (linear) chain was placed in the centre of the simulation box (side length of 420, 840, and 1260 Å for the 10, 20, and 30 monomer chains, respectively; approximately three times the contour length of the polymer chain). A soft-core potential was applied to remove any overlaps between coarse-grained sites (again following the same procedure as applied previously). The resulting system was simulated with a purely repulsive Weeks-Chandler Anderson (WCA) (LJ potential truncated and shifted at its minimum, eqn (4.24)) equivalent of the CG potential in order to allow the chain to relax away from the fully extended conformation to the equilibrium distribution of the bonded parameters given a purely repulsive backbone. Temperature was controlled using a Langevin thermostat. Simulation times with the WCA potentials for 10mers were 100 ns with the

regular (matching DCB) Langevin friction coefficient, and 500 ns for 20 and 30mers with the 10× lower friction coefficient. This time was sufficient that the radius of gyration was no longer decreasing. The non-bonded parameters were then switched back to the LJ parameters and the Langevin friction coefficient returned to the value parameterised to match the diffusion in DCB. 20 independent simulations of 10 μs (for all systems in "good" solvent, and flexible backbones in poor solvent), 15 μs (30mers in poor solvent, regular backbone), 20 μs (20mers in poor solvent, regular backbone), or 25 μs (10mers in poor solvent, regular backbone) each were run to determine an approximate timescale of single-chain folding. The longer simulation times were required for the polymers with regular flexibility backbones in order to obtain an accurate estimate of the folding time, as these systems did not fold as rapidly as the flexible chains.

An additional set of single-chain simulations were conducted at lower friction, to determine the effect of viscosity on the rate of single-chain folding. These low-viscosity simulations were only conducted for 20mers with a regular flexibility backbone in poor solvent. The Langevin friction coefficient in these simulations was 10× lower than in the simulations modelling DCB. After the same setup procedure as described above for 20mers, 20 independent simulations of 5 μs (timestep = 5 fs) each were run to determine the approximate timescale of single-chain folding under these conditions.

4.2.3.2 Multi-chain simulation

In order to examine the multi-chain aggregation behaviour and determine the types of structures that are predicted under conditions of various solvent qualities and backbone stiffness, we studied systems of 10, 20, and 30mers of P(NDI2OD-T2) with parameters corresponding to being in "good", intermediate, and poor solvents, again with the flexible (poor solvent only) and regular (all three solvents) backbones flexibility. The experimental system studied in the SAXS experiments that showed the extended aggregate structures consisted of chains with length of approximately 30 monomers at a concentration of 5 g/L.[25] Assuming a simulation box approx. three times the polymer contour length, a system of 30mers at this concentration contains too many atoms to be easily simulated on the μs timescale. Instead, we focused the majority of this work on the slightly shorter 20mers, which (again with a simulation box approx. three times the contour length) reduces the number of particles by approx. 40%. Shorter (10mer) and longer (30mer) chains were also considered for a few select cases. In order to achieve approximately the same behaviour as the experimental 30mer system, we simulated the shorter chains at a higher concentration, such that the ratio of the polymer volume fraction, ϕ_V, to the overlap volume fraction, ϕ^*, was approximately the same for all chain lengths simulated,

and close to that of the SAXS experiments. Making the crude approximation of ideal chains, $\phi^* \propto 1/N^{1/2}$ for polymer chain length N and so constant ϕ_V/ϕ^* corresponds to constant $\phi_V N^{1/2}$ (see SI Section S4.5 for the derivation of this scaling). Recent work has shown that the concentration of a polymer solution relative to the polymer overlap concentration is a key predictor of OSC device performance due to its effect on the extent and type of aggregation,[43] so we expected that maintaining a constant $\phi_V N^{1/2}$ should give relatively consistent behaviour across different chain lengths. The concentrations that gave the same $\phi_V N^{1/2}$ as the experimental system of 30mers at 5 g/L were 6 g/L for 20mers and 8.5 g/L for 10mers. Unless otherwise stated, the results presented below are for these systems with the same $\phi_V N^{1/2}$. A number of additional systems were studied at different $\phi_V N^{1/2}$: 10mers at 10 g/L (flexible and regular chains), and 20mers at 12 g/L (regular flexibility) and 2 g/L (flexible chains). A detailed list of the systems studied in this work, as well as their values of $\phi_V N^{1/2}$, is given in the SI Table S4.1.

For all systems, the polymers were initially placed in the simulation box at random positions and orientations with a fully extended backbone. The number of polymer chains and box sizes to give the desired concentrations are given in the SI, Table S4.1. As the random packing was likely to lead to overlaps between chains, a soft-core potential was again applied to remove overlapping CG sites (see eqn (4.4), same procedure and parameters as described previously). As with the single-chain simulations, the backbone structure was allowed to relax by initially simulating the system with purely repulsive non-bonded interactions (WCA equivalent of the CG LJ potentials). Simulation times with the WCA potentials for 10mers were 100 ns with the regular (matching DCB) Langevin friction coefficient, and 500 ns for 20 and 30mers with the 10× lower friction coefficient, as described for the single chain simulations. The non-bonded interactions were returned to the LJ potentials, the friction coefficient returned to the desired value (generally that parameterised to match DCB, but 10× lower in some cases), and the systems then simulated for between 1 and 4.5 μs (see SI Table S4.1) using a Langevin thermostat to simulate an implicit solvent environment at a temperature of 300 K. This amount of time was sufficient that extensive aggregation was observed in the poorer solvents. In the poor solvent, the aggregate sizes were approaching the size of the box after approximately 3–4 μs, so further increasing the simulation time was unlikely to yield physically meaningful results without also increasing the system size. Two independent simulations (and in one case, three) were conducted for each set of simulation conditions studied.

4.3 RESULTS AND DISCUSSION

The solution–phase behaviour of P(NDI2OD-T2) (M_n = 31.2 kDa, Đ = 2.1) has previously been examined experimentally via UV-visible absorption spectroscopy and SAXS.[25] The absorption spectrum indicated extensive aggregation in poor solvents TOL and xylene (XY), in which the SAXS measurements suggested the formation of large (high R_g) aggregates with rod-like aspect ratios. These aggregates were measured to have R_g an order of magnitude greater than the same polymer chains in better solvents, and lengths that could not be achieved without multi-chain aggregation (see Table 4.1 for a summary of the experimental results). The formation of extended aggregates as described here is not predicted by existing theories of solution-phase polymer aggregation, by which, based on a conventional understanding of solution–phase behaviour of flexible polymers, the polymer's R_g is expected to decrease with decreasing solvent quality. It is therefore clear that a better understanding of the solution-phase behaviour of P(NDI2OD-T2) is required.

Table 4.1 Published radii of gyration (R_g) and estimated aggregate lengths of P(NDI2OD-T2) in various solvents.[25] A value roughly consistent with single-chain behaviour of M_n = 31.2 kDa (approximately 30mers, see Section 4.3.3, Table 4.2) was observed for the good, moderately good, and moderately poor solvents, but a large increase was observed for poor solvents. Analysis of the SAXS data, conducted in ref 25, indicated the formation of extended rod-like aggregates. The length L of the aggregate was estimated assuming a rod-like structure, for which $R_g^2 = L^2/12$,[127] and the number of monomers calculated from the aggregate length assuming each monomer is 1.4 nm long.

solvent	solvent quality	R_g, lit.[25] (nm)	L (nm)	L (monomers)
CN	good	15.6	54.0	39
DCB	moderately good	11.7	40.5	29
CB	moderately poor	13.4	46.4	33
TOL	poor	255.1	883.7	631
XY	poor	299.8	1038.5	742

While the transition of flexible polymers to a collapsed structure should be favoured in poor solvents, semiflexible polymers, in which the stiffer backbone results in bending being energetically unfavourable, are expected to show behaviour that depends on both stiffness and solvent quality. Previous computational studies of semiflexible polymers have reported a dependence of the equilibrium aggregate structure on both these properties.[134] For relatively stiff backbones, bundles of fully overlapping chains, rather than collapsed globules, are expected due to the unfavourable bending energy. However, while these fully-overlapped bundles are expected to be the equilibrium structure in a poor solvent, due to maximising

favourable polymer–polymer interactions while minimising unfavourable polymer–solvent interactions and bending energy, this structure would not lead to rod-like aggregates of the size observed experimentally, which have lengths much larger than that of a single chain (see Table 4.1).

The CG model for P(NDI2OD-T2) that we have developed allows us to examine its solution-phase behaviour in more detail, enabling the simulation of chain lengths on the order of experimental lengths on a μs time scale while still maintaining enough molecular detail to distinguish the important interactions and accurately represent the highly anisotropic shape of its monomers. We first examine the behaviour of this model of P(NDI2OD-T2) under conditions corresponding to varying solvent quality (Section 4.3.1), observing the formation of multi-chain aggregates with lengths much longer than a single chain in the poorer solvents. For the formation of an extended aggregate to occur, we propose that two conditions must be met: firstly that multi-chain aggregates which are not fully overlapping are sufficiently stable that they do not separate on the timescale of further aggregation (Section 4.3.2), and secondly that single-chain collapse (or folding) occurs on a timescale slower than that of multi-chain aggregation (Section 4.3.3). This points to a possible dependence of aggregation properties on concentration and chain length, potentially explaining the apparent discrepancies between experimental work on this polymer.[22,25]

4.3.1 Solution-phase structure of P(NDI2OD-T2)

We begin by analysing the behaviour of multi-chain systems of P(NDI2OD-T2) in "good", intermediate, and poor solvents, as defined in Section 4.2.2. The multi-chain aggregation behaviour was examined predominantly for P(NDI2OD-T2) 20mers, although 10mers and 30mers in the poor solvent were also considered to determine how (or if) the behaviour depended on chain length. Concentrations were chosen to give the same value of $\phi_V N^{1/2}$, for polymer volume fraction ϕ_V, as a system of 30mers at 5 g/L as described in Section 4.2.3.2, as well as some systems at different concentrations in an attempt to elucidate the effect of concentration on multi-chain aggregation (for a full list of the systems studied, see the SI Table S4.1).

In order to understand the aggregation behaviour, the properties of the aggregate and the kinetics of aggregate formation were analysed in a number of ways. For all analyses, two chains were considered to be in the same aggregate if any of their monomers had a backbone centre-of-mass separation of less than 7 Å. The simplest parameter considered in this work was the aggregate size N_{agg}, where the aggregate's size was simply the number of chains that it contained. The time dependence of the average value of this property is related to the kinetics of aggregation.

The conformation of an aggregate was characterised in terms of its radius of gyration, R_g (that is the radius of gyration of the entire aggregate, not each individual chain), and the shape anisotropy κ^2 (again of the entire aggregate), defined as

$$\kappa^2 = \frac{3}{2}\frac{\lambda_x^4 + \lambda_y^4 + \lambda_z^4}{(\lambda_x^2 + \lambda_y^2 + \lambda_z^2)^2} - \frac{1}{2} \tag{4.8}$$

where λ_i are the eigenvalues of the gyration tensor. This quantity is 0 for a spherical aggregate, and 1 for a linear aggregate, allowing for rod-like aggregates to be distinguished from more disordered structures that are likely to be closer to spherical.

In all cases, aggregation occurred through interactions of the NDI groups (CG site types 2, 3, and 6) in the π-stacking direction. This highly anisotropic aggregation behaviour is consistent with the behaviour expected of conjugated polymers, whose attractions in the π-stacking direction are substantially stronger than via the alkyl side-chains due to the strongly attractive π–π interactions, highlighting the importance of accurately capturing the shape anisotropy of the monomer unit.

Aggregate size (number of chains). We first consider the growth over time of the average aggregate size, $\langle N_{agg}(t)\rangle$, in each solvent (Fig 4.2a). For 20mers in the poor and intermediate solvents, aggregation initially occurred rapidly, with the average aggregate size approaching three chains in the intermediate, and four chains in the poor solvent, after 3 μs. In the better ("good") solvent, aggregation occurred much slower, with the average aggregate size remaining under 2 chains, indicating the presence of many unaggregated chains. The time-dependent aggregation properties presented in Fig. 4.2a appear to be roughly independent of chain length at the same $\phi_V N^{1/2}$ (see SI Fig. S4.18), but show a strong dependence on concentration, which will be discussed further in Section 4.3.3.

In order to get a better understanding of the long-time behaviour in the "good" solvent, which should be representative of solvents in which some aggregation is expected but the formation of rod-like aggregates is not, we conducted the same simulation with lower friction in order to speed up the dynamics of the system. Although this will not accurately capture the kinetics of aggregation in a realistic solvent, the equilibrium behaviour should be the same. Aggregation in this low-friction system occurred faster, as expected, but extensive aggregation was still not observed, with the average aggregate size remaining below 2 (Fig 4.2a). This is consistent with a conventional understanding of aggregation and solvent quality, with aggregates becoming less stable as solvent quality improves due to the effective polymer–polymer interactions becoming more repulsive.

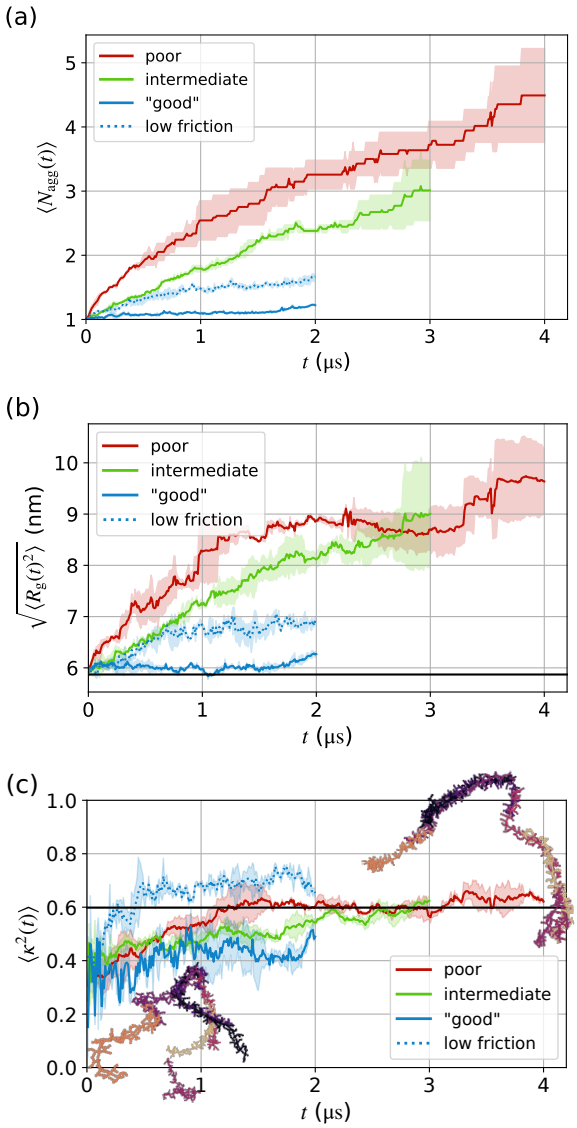

Fig. 4.2 (a) Average aggregate size (number of chains), (b) RMS radius of gyration of aggregates, and (c) average shape anisotropy for aggregates containing at least 2 chains versus time for 20mers in varying solvent qualities. The low-friction results in the "good" solvent are also shown (dotted blue line). Shaded regions indicate 95% confidence intervals based on two replicate simulations. In (a), a system with no aggregation will have an average aggregate size of 1. In (b), the horizontal black line indicates the R_g of a single 20mer in "good" solvent conditions, calculated as the RMS R_g of the final 2 μs of the 20 single chain simulations. In (c), a value of 1 indicates a rod-like structure, and 0 spherical; unaggregated chains (aggregate size = 1) are not included in this plot as we were predominantly interested in the structure of aggregates. Inset images show snapshots of the same aggregate in a poor solvent at 0.7 μs and 4 μs, highlighting the more ordered, rod-like structure at later time. The horizontal black line indicates the shape anisotropy of a single 20mer in "good" solvent, calculated as the average over the final 2 μs of the 20 single-chain simulations.

Radius of gyration and shape anisotropy. The experimental SAXS results showed that the aggregates in extremely poor solvents may be significantly larger than in better solvents, and have a rod-like structure.[25] Over time, as the average aggregate size increased, we observed a corresponding increase in the root-mean squared (RMS) R_g (Fig. 4.2b). Separating this into the R_g of aggregates of a specific size, showed that as aggregate size (N_{agg}, number of chains) increased, the RMS R_g of the aggregate also increased beyond that of a single chain much more rapidly that would be expected if stacking in a perfect π-stacking arrangement (Fig. 4.3a). Though not yet up to the reported hundreds of nanometers, this behaviour is indicative of the formation of extended aggregates where chains are not fully overlapping. Due to computational constraints, it is challenging to model a system large enough to form aggregates with R_g on the order of 300 nm as observed experimentally. These large aggregates would require significantly larger systems (on the order of 20,000 20mers, corresponding to almost 1,000,000 CG sites, to fill a $(500\ \text{nm})^3$ simulation box at a concentration of 6 g/L) and much longer timescales (likely at least 10s of μs) to be observed, which is currently not feasible. However, the trend towards more extended structures as chains are incorporated into the aggregates suggests that the formation of these large, extended aggregates is expected.

Turning to the shape anisotropy, κ^2 (eqn (4.8)), a decrease in this quantity, which classifies how close to a rod ($\kappa^2 = 1$) or sphere ($\kappa^2 = 0$) the structure is, was observed for larger aggregates (Fig. 4.3b). Although this result suggests that the larger aggregates are branched and disordered, rather than rod-like, the formation of more branched aggregates can be attributed to the aggregation mechanism, by which chains initially collide with random orientation of the backbones, before 'zipping' up to form a more rod-like structure. Over time, these structures are expected to become more ordered, as branches collapse onto the growing rod-like backbone of the aggregate. This mechanism is consistent with the time-dependent behaviour of the average κ^2 for aggregates of at least 2 chains (Fig. 4.2c), which initially indicated a structure that was significantly less rod-like than the single chain, before gradually increasing over time towards (and occasionally exceeding) the single-chain values, corresponding to more rod-like structures. The decomposition of the curves in Fig. 4.2c into aggregates of various sizes (SI, Fig S4.17) shows a corresponding increase in κ^2 over time for the smaller aggregates, though it appears possible that perfectly rod-like aggregates will never be achieved. The timescale of this process is likely to become slower as aggregate size increases due to the slower diffusion of the larger branches.

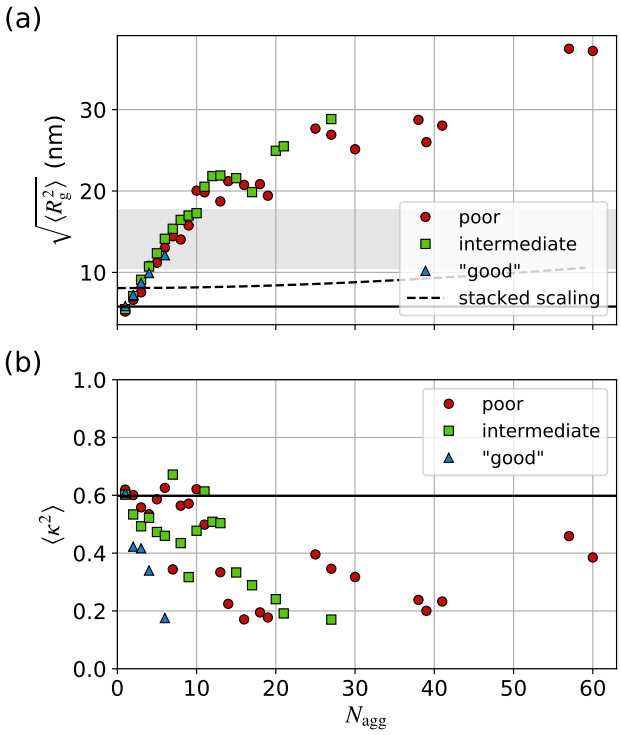

Fig. 4.3 (a) RMS radius of gyration and (b) average shape anisotropy as a function of aggregate size for 20mers in varying solvent qualities, averaged over the entire simulation. The shaded region indicates the reported R_g for good–intermediate solvents, though we note that the experimental systems used chains approximately 30 monomers in length, compared with the 20mers presented in this plot. Horizontal black lines indicate the value of R_g or κ^2 for a single 20mer in the "good" solvent conditions, calculated as described in Fig. 4.2. The dotted black line in (a) is an approximation of the radius of gyration of an aggregate where chains fully overlap, forming a rectangular block, calculated as $R_g^2 = \left(L^2/12\right) + \left(R^2/12\right)$ where L is the length of a single polymer chain (here approximated as 20×1.4 nm for a chain of 20 1.4 nm long monomers), and R the dimension of the aggregate in the π-stacking direction, assuming perfect stacking, where each additional chain is assumed to add an additional 0.4 nm to this dimension.

4.3.2 Partially overlapping chains lead to extended aggregates in poor solvents

The results presented in the previous section show behaviour consistent with the formation of extended, multi-chain aggregates in poor solvents, as observed experimentally.[25] Although we did not observe the order-of-magnitude increases of R_g due to system-size and time-scale limitations, the steadily growing RMS R_g with aggregate size suggests that large aggregates are not unfeasible, with values already reaching multiple times that of a single chain, and increasing much faster than

would be expected for the formation of fully overlapping aggregates.

The aggregation behaviour observed for 20mers depends strongly on the choice of solvent. From previous Monte Carlo simulations of a generic bead–spring model of a semiflexible polymer,[134] it is expected that the thermodynamically favoured aggregate in a poor solvent would be one in which all monomers between two chains overlap to give a fully stacked structure. However, the formation of fully overlapping aggregates would not give rise to the observed order of magnitude increase in R_g for poor solvents, nor to the smaller, though still significant and rapid increase in this property observed in our simulations. Instead, to explain the observed formation of large rod-like structures, chains must not be fully overlapping, allowing for the growth of the aggregate in a brickwork-like fashion. For non-overlapping chains to lead to significant growth of aggregates, it is necessary that these incompletely overlapped chain pairs are sufficiently stable that they are inseparable, or at least do not separate on the time scale of further aggregation, such that they become effectively trapped as additional chains are incorporated into the aggregate.

To characterise whether polymer chains in aggregates were overlapping or not, and whether they were likely to be trapped in those structures, we have defined three order parameters: N_{pair}, N_{total}, and N_{trap} (Fig. 4.4). For all three quantities, monomers were considered to be overlapping if their centre-of-mass separation was less than 7 Å. N_{pair} defines the number of overlapping monomers between a given pair of polymer chains. A value of $< N$ (or $N_{\text{pair}}/N < 1$), where N is the polymer chain length, indicates that two chains are only partially overlapping. N_{total} extends this parameter to include the number of overlapping monomers between a chain and any other chain. Therefore, a value of N (or $N_{\text{total}}/N = 1$) indicates *either* a pair of fully overlapping chains, or a chain that is fully covered by multiple other chains in a partially overlapping fashion. Finally we considered monomers to be trapped in an aggregated structure if they had a monomer on each face. N_{trap} was thus defined as the number of monomers in aggregates overlapping with two other monomers on separate chains. These parameters are illustrated in Fig. 4.4.

Chain overlap fraction. As incompletely overlapping chains are required to give a substantial increase in R_g as aggregates grow, we first examine the number of overlaps between pairs of chains, N_{pair}. Note that only interactions between chains that are considered aggregated (any monomer–monomer centre-of-mass separation < 7 Å) are counted so this variable has a minimum value of 1. It also gives no indication of how much aggregation occurs, as chains which do not interact with any other chains are excluded. Fig. 4.5a shows the evolution of $\langle N_{\text{pair}} \rangle$ over time for 20mers at a concentration of 6 g/L in the three different solvent conditions studied. By approximately 1 μs, the average overlap fraction $\langle N_{\text{pair}} \rangle / N$ of 20mers in the

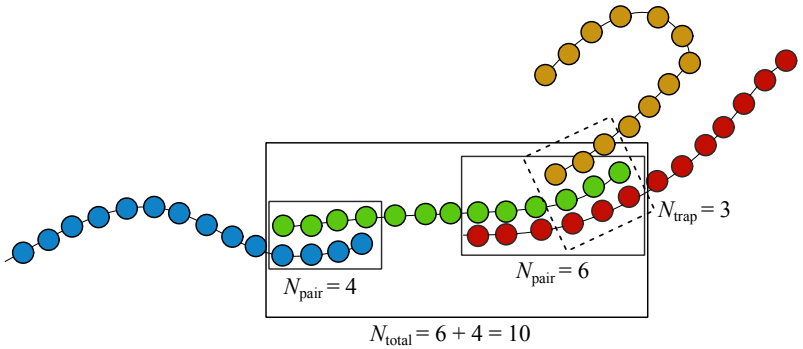

Fig. 4.4 Definition of N_{pair}, N_{total}, and N_{trap} for the green chain. N_{pair} is the number of overlaps between a single pair of chains. N_{total} is the overlaps between a chain and any other chain. N_{trap} is the number of monomers on the specified chain that have a monomer from a different chain on each face.

poorest solvent has converged to 0.4 (8 overlaps) and does not appear to increase further over the rest of the simulation. This is well below the expected 100% overlap predicted previously as the equilibrium structure.[134] In the "good" solvent, however, $\langle N_{pair} \rangle / N$ is still increasing, albeit very slowly. In better solvents, we expect that chains are able to separate rapidly enough that less thermodynamically favourable structures, being those held together by only a few monomers, do not become kinetically trapped by the aggregation of more chains around them. Over time, this behaviour, where thermodynamically less favourable partially overlapping chains can separate, should give aggregates that tend toward the expected thermodynamic minimum of fully overlapping ($\langle N_{pair} \rangle / N = 1$) chains. While the results in Fig. 4.5a suggest that this process may be occurring, especially in the "good" solvent, the timescale of this process appears to be so long that it is unfeasible to observe full rearrangement with the available computational resources. Again, we have compared the behaviour in the "good" solvent with an equivalent system with lower friction to attempt to elucidate the equilibrium behaviour. This low-friction system showed greater overlaps between aggregated chains, indicating that when able, the system appears to converge towards the expected equilibrium (fully overlapping) behaviour.

Comparing the behaviour for different chain lengths at the same $\phi_V N^{1/2}$ (SI Fig. S4.19), a slightly lower average overlap fraction $\langle N_{pair} \rangle / N$ is observed for 20 and 30mers than the shorter 10mers, which may be attributed to slightly faster folding of the longer single chains. This behaviour will be discussed in more detail in Section 4.3.3. It should also be noted that in using $\phi_V N^{1/2}$ to scale the polymer concentration, we have assumed ideal chains, from which the behaviour of our CG model in poor solvents is likely to deviate.

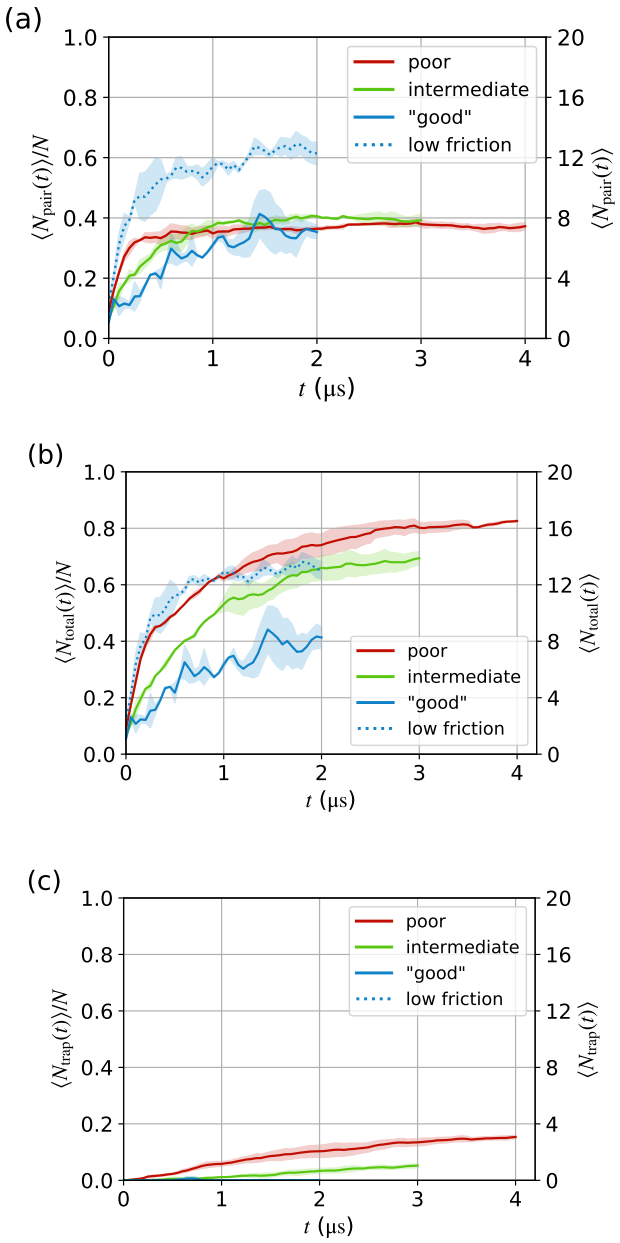

Fig. 4.5 Average (a) chain overlap fraction $\langle N_{\text{pair}}\rangle/N$, (b) total overlap fraction $\langle N_{\text{total}}\rangle/N$, and (c) fraction of trapped monomers $\langle N_{\text{trap}}\rangle/N$ versus time in multi-chain 20mer systems. In all cases, the dotted blue line indicates the simulations conducted in "good" solvent conditions with low friction, which should tend more quickly towards the equilibrium structure. Shaded regions indicate 95% confidence intervals calculated for the two replicate simulations. Only aggregated chains (i.e. those that interact with at least one other chain) were counted in calculating these quantities so in (a) and (b) the value can never be zero. Accordingly, neither (a) nor (b) alone give any insight into how much aggregation is occurring. In (c), a value of zero indicates that all monomers in the system that are interacting with any other chains interact only on one face. For the two "good" solvent plots, this value is always zero.

Stability of partially overlapping chains. The differences in the time evolution of $\langle N_{\text{pair}} \rangle$ in "good" and poor solvents, with the structure able to rearrange towards fully overlapping in the "good" solvent but trapped in partially overlapping structures in poorer solvents, suggests that aggregation through fewer monomers is sufficient to hold two chains together as solvent quality decreases. If partially overlapping chains are effectively inseparable, at least on the timescale of becoming trapped by further aggregation, a build-up of extended aggregates with increasing R_{g} will occur.

The strength of the attraction between two monomers under the different solvent conditions was estimated from the free energy as a function of intermolecular separation (NDI group centre-of-mass distance between two monomers) calculated from OPES simulations (Fig. 4.6). Although this free energy was calculated as a function of distance only (i.e. not considering the orientation of the particles, which is important for distinguishing different aggregate geometries), the minimum at approx. 4 Å is due almost exclusively to conformations close to the π-stacked structure as it is the only conformation that allows such close packing. The well depths from the free energy profiles suggest a preference for aggregation of a pair of monomers of approximately 3.8 kcal/mol (6.4 $k_{\text{B}}T$) in the poor solvent, 2.2 kcal/mol (3.7 $k_{\text{B}}T$) in the intermediate solvent, and 0.9 kcal/mol (1.5 $k_{\text{B}}T$) in the "good" solvent ($k_{\text{B}}T$ at $T = 300\ K$). In the poor solvent, this attraction is sufficiently strong that even chains held together by a single monomer are unlikely to separate often, allowing for the build-up of large aggregates. Additionally, the convergence of $\langle N_{\text{pair}} \rangle / N$ to a value far less than 1 in the poor and intermediate solvents (Fig. 4.5) indicates that with an average N_{pair} of just 8 in the poor solvent, the average number of overlaps is neither decreasing nor increasing. This finding again suggests that chains that are much less than fully overlapping are stable for long periods of time in the poorer solvents.

Trapping of aggregates. Although it appears that aggregates in which chains overlap by only a few monomers are stable enough that the chains become effectively inseparable, further aggregation, where new chains create stacked structures in which parts of a central chain are sandwiched between two other chains, may result in trapping of the non-equilibrium structure, making these partially overlapping structures even more long-lived. We have quantified this as N_{trap}, the number of monomers that have a monomer on each face (Fig. 4.4). This parameter increased over time in the poor and intermediate solvents, but did not go above zero in the "good" solvent over the time simulated (Fig. 4.5c), highlighting again that the chains in the "good" solvent should be able to rearrange towards the fully overlapping structure while those in the poorer solvents will eventually become trapped in the

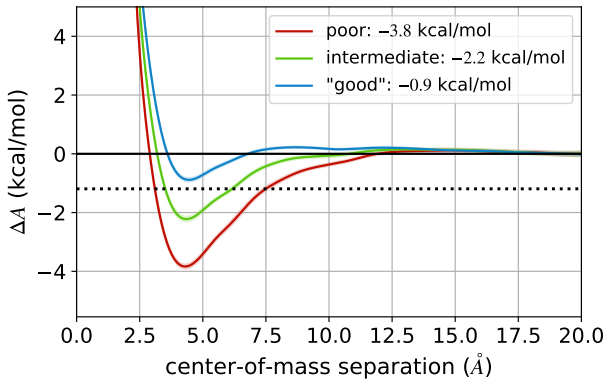

Fig. 4.6 Free energy as a function of centre-of-mass separation of two CG P(NDI2OD-T2) monomers under different solvent conditions. Centres-of-mass were taken as the centre-of-mass of atoms corresponding to the NDI groups (site types 2, 3, 6). Well depths in each system are reported in the legend. The black dotted line indicates $-2k_BT$ at $T = 300\ K$. Error bars (two standard errors) are shown and are approximately the width of the plotted lines. A comparison with the same free energy in the AA system can be found in the SI, Fig. S4.15.

partially overlapping structures.

4.3.3 Single-chain folding is slower than multi-chain aggregation for sufficiently stiff backbones

As it appears that the first condition that we have proposed for the build-up of extended aggregates – that partially overlapping chains are able to hold two chains together long enough for the build up of an extended multi-chain aggregate – holds, we turn our attention to the second, related to the relative rates of multi-chain aggregation and single-chain folding. In poor solvents, flexible polymers are expected to collapse into globules. The single-chain conformations of semiflexible polymers have also been extensively studied,[131–133,135–143] and the equilibrium behaviour predicted to depend on both the backbone rigidity, and the solvent quality (or equivalently the strength of the attractive intermolecular interactions or temperature), with folded conformations such as toroids and hairpins being relatively common. This kind of behaviour – that is, the formation of compact, folded, structures – is neither consistent with the formation of extended aggregates, nor the rod-like aspect ratios observed in the SAXS measurements of P(NDI2OD-T2), although it matches the lower concentration results of Steyrleuthner et al. [22], who attributed shifts in the UV-visible absorption spectra to intramolecular aggregation of P(NDI2OD-T2). We therefore propose that this folding process occurs slower than the multi-chain aggregation of P(NDI2OD-T2) chains at the concentrations studied

via SAXS, if indeed the backbones are flexible enough that folding is favoured at all, and that once aggregated, further folding becomes significantly less favourable. As this is a kinetic effect, it should have a concentration, and possibly chain length, dependence, explaining the discrepancy between the two sets of experimental results for the same polymer/solvent systems.[22,25]

Single-chain folding: expected structure and kinetics. Single CG P(NDI2OD-T2) chains were studied in the extreme solvent conditions (poor and "good") for flexible and regular backbones of length 10, 20, and 30 monomers. Three broad classes of structure were observed and distinguished by their radius of gyration R_g and shape anisotropy κ^2: the extended chain (large radius of gyration, shape anisotropy > 0.5), hairpin (smaller radius of gyration, shape anisotropy > 0.5), and toroid (small radius of gyration, shape anisotropy < 0.5). Over 20 independent 10–25 μs simulations, most chains (whether regular or flexible) displayed a transition to a folded conformation within 10 μs in the poor solvent, but remained extended in the "good" solvent. The exception to this behaviour was for the 10mers, which were too short to consistently give folded structures even within the 25 μs time period in the poor solvent, assuming the folded structure even has significant probability at equilibrium for such short chains. Collapsed structures were either hairpins or toroids, with the 2D distributions as a function of R_g and κ^2, calculated at early (0.5–1 μs, corresponding to the time required to achieve an average aggregate size $\langle N_{agg}(t)\rangle \approx 2$ in the multi-chain simulation), intermediate (4.5–5.5 μs), and late times (9–10 μs) given in Fig. 4.7 (early time), and SI, Fig. S4.20 (intermediate and late time). Fig. 4.7 highlights that, while some chains may have folded by 1 μs, most chains, especially for the regular flexibility backbones, remain extended on the timescale of initial multi-scale aggregation. The more flexible backbones fold faster, and a greater proportion of these are expected to be folded prior to multi-chain aggregation occurring.

To determine an approximate timescale for the folding process, we have fit the mean-squared radius of gyration (averaged over the 20 independent single-chain simulations for each chain length, flexibility, and solvent quality) to an exponential of the form[283]

$$\langle R_g^2(t)\rangle = a\exp(-(t/\tau_s)) + \langle R_{g,min}^2\rangle \tag{4.9}$$

where $\langle R_{g,min}^2\rangle$ is the equilibrium mean squared radius of gyration for each chain length and τ_s is the folding timescale. a is an additional fitting coefficient. $\langle R_{g,min}^2\rangle$ was fit for both chain flexibilities in the poor solvent, but as the chains did not fold in the "good" solvent the values calculated for the corresponding chains in the poor solvent were used to fit the folding time in the "good" solvent. In the poor solvent, flexible chains had τ_s on the order of 1 μs and regular chains between 3–20 μs. This

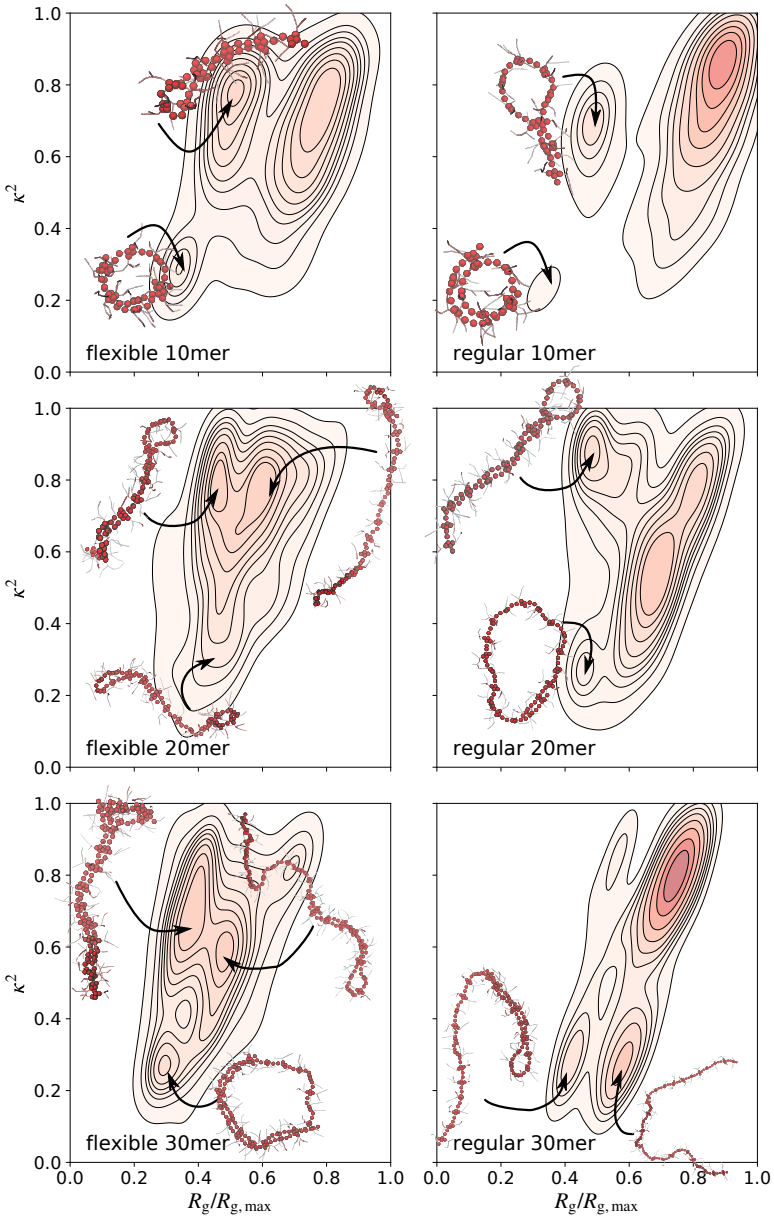

Fig. 4.7 2D histogram of the radius of gyration R_g and shape anisotropy κ^2 calculated over 20 independent simulations of various chain lengths in poor solvent conditions. The distributions were calculated over the period 0.5–1 µs, corresponding to the time by which the average aggregate size $\langle N_{agg}(t)\rangle$ in the poor solvent for both flexible and regular backbones was approximately 2 in the multi-chain simulations. The R_g is normalised by $R_{g,max}$, the R_g of a fully extended rod, with $R_g^2 = L^2/12$ and $L = 1.4$ nm per monomer. Representative structures of some of the more common conformations are shown near their corresponding peak in the distribution. The colour scale is the same in all cases with darker regions corresponding to higher probability.

timescale is indicative of the time for single chains to fold (Fig. S4.22, Table 4.2). Slower chain collapse for stiffer chains is consistent with previously reported studies on the kinetics of single chain behaviour as a function of semiflexibility.[135] In terms of the dependence of the kinetics of chain collapse on molecular weight (chain length), scaling of the folding rate with $N^{1/3}$ has been previously reported.[138] The regular chains in the poor solvent showed behaviour consistent with this scaling (SI Fig. S4.23), while those in the "good" solvent did not fold within 10 μs.

Table 4.2 Fit parameters to eqn (4.9) for the various single-chain systems with chain length N. Fits are shown in Fig. S4.22 and S4.21. The values of $R^2_{g,min}$ calculated for both chain flexibilities in the poor solvent were used for the systems in the "good" solvent. The final two columns list the single chain folding time, τ_s, and approximate coagulation time, τ_c, calculated as the time for the single-chain concentration to drop to 25% of the original concentration for each system. The poor solvent system indicated with a * uses a lower viscosity solvent with friction coefficient 1/10 of the value of the other systems. Where τ_c = N/A, the single-chain concentration in the multi-chain systems remained higher than 25% of the original concentration over the course of the entire simulation. Where τ_c is not given, multi-chain equivalents of these systems were not studied. Coagulation times reported here are for the multi-chain systems at constant $\phi_V N^{1/2}$. The values for systems at different concentrations are given in the SI Table S4.1.

solvent	flexibility	N (monomers)	a (Å^2)	$R^2_{g,min}$ (Å^2)	τ_s (μs)	τ_c (μs)
poor	regular	10	847.64	326.57	19.78	0.42
poor	regular	20	2338.40	934.60	5.61	0.69
poor	regular	30	5532.71	1743.18	3.39	0.60
poor*	regular	20	2694.05	971.07	0.37	0.06
poor	flexible	10	768.04	324.33	1.15	–
poor	flexible	20	2256.38	654.63	1.61	N/A
poor	flexible	30	3015.52	1682.00	1.17	–
"good"	regular	10	910.80	326.57	> 100	–
"good"	regular	20	2736.18	934.60	85.59	N/A
"good"	regular	30	4630.85	1743.18	> 100	–
"good"	flexible	10	648.43	324.33	> 100	–
"good"	flexible	20	1914.58	654.63	> 100	N/A
"good"	flexible	30	2509.32	1682.00	> 100	–

Kinetics of multi-chain aggregation. The aggregation kinetics were approximated based on the depletion of single chains in solution, from which the aggregation time τ_c was approximated as the time for the concentration of unaggregated chains in solution to fall to 25% of the original concentration. The values of τ_c for the

multi-chain systems studied are given in Table 4.2 alongside the timescales of the corresponding single-chain folding. For 20mers of regular backbone flexibility in poor solvent, the aggregation timescale is almost 10 times faster than single-chain folding.

Controlling relative rates of single-chain folding and multi-chain aggregation. As the multi-chain behaviour described above is kinetically controlled, it is expected to depend on the concentration of the system. If it is assumed that multi-chain aggregation is a diffusion-limited bimolecular process, that occurs via binary collisions (all of which lead to aggregation) between spherical aggregates of one chain to give an aggregate of two chains, it can be shown, for the conditions studied here under which coagulation occurs on times scales significantly shorter than R^2/D, where R is the typical size and D the typical diffusion coefficient of the aggregating species, that the coagulation time scale can be approximated as

$$\tau_c \approx f(N)/c^2 \tag{4.10}$$

where $c = CN$ is the monomer concentration (or, equivalently, the mass concentration) for chains of length N and concentration C, and $f(N)$ is some function of N that depends on the simulation system properties and conditions besides c (see derivation in the SI Section S4.10). We define a critical monomer (or mass) concentration, $c^\dagger$, at which multi-chain aggregation, τ_c, is expected to occur on the same timescale as single-chain collapse, τ_s, by setting $\tau_c = \tau_s$. Combined with eqn (4.10), this gives

$$c^\dagger(N) \approx \left(\frac{f(N)}{\tau_s}\right)^{1/2} \tag{4.11}$$

where $f(N)$ can be determined from τ_c and c measured in the multi-chain simulations. The value of this concentration for regular-flexibility backbones of different chain lengths, N, in the poor solvent is shown in Fig. 4.8. Points on this plot correspond to the critical crossover concentration, below which single-chain folding is expected to occur faster than multi-chain aggregation.

The expected scaling of $c^\dagger$ with chain length N can be calculated assuming τ_s scales as $N^{-1/3}$, and that the polymer conformation initially corresponds to that in a good solvent (Flory exponent $\nu \approx 0.6$). In the absence of hydrodynamics, which is neglected in the Langevin dynamics simulations that we have used, the polymer diffusion coefficient should scale with N^{-1}, which gives, under conditions corresponding to this work, a predicted scaling of $c^\dagger \sim N^{0.46}$ (eqn (4.63); see Section S4.10 for a derivation of this expected scaling). Overall, we observe scaling of

$$c^\dagger \approx 0.51 N^{0.42} \tag{4.12}$$

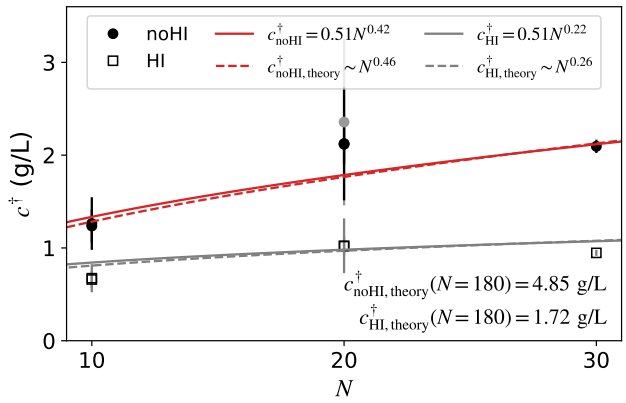

Fig. 4.8 Scaling of the crossover concentration at which the timescale of single chain folding and multi-chain aggregation are expected to be equal, $c^\dagger$, with chain length N. Where multiple points are present for the same chain length, they were calculated using τ_c from multi-chain simulations at different concentrations or solvent viscosity. Solid circles indicate the values of $c^\dagger$ calculated from the Langevin dynamics simulations (i.e. with no hydrodynamics). Lines of best fit to the Langevin dynamics data are shown in red (calculated using the weighted least-squares method as implemented in scipy.optimize.curve_fit), with the dashed line showing the scaling expected from the theory ($\sim N^{0.46}$), and the solid line the observed scaling from simulations. The grey circle for $N = 20$ corresponds to the low friction system in poor solvent. This point was not included in the fit. τ_c was calculated as the time for the concentration of single chains to fall below 25% of their original concentration. Unfilled squares are the values of $c^\dagger$ corrected for hydrodynamic interactions using eqn. (4.13). Grey lines indicate the scaling with the hydrodynamic correction included, calculated from the fits for both the theoretical (dashed lines) and simulation (solid lines) scaling without hydrodynamics (eqn (4.14); with $\bar{c}_0$ and λ taken from the best fit (or theoretical scaling) to the simulation data, given by the red solid (dashed) lines. $\bar{c}_0 = 0.51$ (0.44) and $\lambda = 0.42$ (0.46)). The value of $c^\dagger$ at $N = 180$, corresponding to the work in ref 22, is indicated on the graph. This value was calculated from the theoretical scaling both with ($c^\dagger_{\mathrm{HI,theory}}$) and without ($c^\dagger_{\mathrm{noHI,theory}}$) the hydrodynamic correction.

from the Langevin dynamics simulations, which is remarkably close to the expected scaling of $N^{0.46}$ obtained from the simple theory considering the numerous assumptions that have been made. Probably the most significant of these assumptions is that aggregation only occurs between two single chains to give an aggregate of size 2. This is not the case for the simulations studied in this work, in which many aggregates form containing more than 2 chains (see Fig. 4.3). In addition, the definition of τ_c as the time taken for the concentration of single chains to fall to 25% of the original concentration, although consistent with the notion that the coagulation time scale should correspond to when most chains are in aggregates, is somewhat arbitrary. Nevertheless, an alternative physically motivated measure of τ_c as the

time for the average aggregate size in the simulations to reach 2, gives a similar scaling prediction of $c^\dagger \sim N^{0.47}$, indicating that our definition of τ_c is reasonable. Considering the large uncertainties in the values of $c^\dagger$ for certain chain lengths (which predominantly arise from uncertainty in the rate of multi-chain folding), the simple theory still matches the observed scaling relatively well.

It should be noted here that neither these calculated concentrations, nor the theory presented in the SI, Section S4.10, consider how the process of single-chain folding will affect the multi-chain aggregation rate. As chains fold, they gradually become more compact, which will increase the distance required to diffuse to interact with another polymer chain. There is therefore a complex interdependence between the degree of chain folding at a given time and the collision rate of polymers that cannot be fully captured by the simple model used here. This means that the estimated crossover concentrations are a lower bound: accounting for chain collapse during aggregation will increase the concentration at which aggregation dominates single-chain collapse. Nevertheless, especially for the shorter chains, for which the size difference between a fully extended and collapsed chain is less significant, the calculated concentrations should be a reasonable approximation to the actual concentrations at which folding may occur faster than interchain aggregation.

Although these simulations used Langevin dynamics, in which hydrodynamic interactions are neglected, an approximate correction to account for the effect of hydrodynamics on the polymer diffusion coefficient can be applied (see SI Section S4.10, eqns (4.66)–(4.74)). This amounts to

$$c^\dagger_{\mathrm{HI}} = c^\dagger_{\mathrm{noHI}} \left(\frac{N^\nu}{N + N^\nu} \right)^{1/2} \tag{4.13}$$

where the subscripts "noHI" and "HI" indicate the absence and presence of hydrodynamic interactions, respectively. For $N \gg 1$ and $\nu < 1$, the expected scaling of $c^\dagger$ with N becomes

$$c^\dagger_{\mathrm{HI}}(N) \to \bar{c}_0 N^{\lambda + \frac{1}{2}(\nu - 1)} \tag{4.14}$$

where $\bar{c}_0$ is a constant, and λ a scaling exponent obtained from the fit of the Langevin dynamics simulation values of $c^\dagger$ for which $c^\dagger_{\mathrm{noHI}}(N) = \bar{c}_0 N^\lambda$. The values of $c^\dagger$ obtained from eqn (4.13) are included in Fig. 4.8, along with the theoretical scaling of $c^\dagger_{\mathrm{HI}}$ with N from eqn (4.14). Note that the rate of single-chain folding was not adjusted for hydrodynamics as it is expected to depend on the rate of monomer diffusion rather than that of the whole polymer. The monomer diffusion coefficient was parameterised in the CG Langevin dynamics simulations to match that in the explicit-solvent AA simulations, which include hydrodynamic interactions. Accordingly, the Langevin dynamics simulations effectively account for hydrodynamics at the monomer level.

Examining the value of $c^\dagger$ at conditions corresponding to those used in the work of refs 25 (30mers, $c \approx 5$ g/L) and 22 (180mers, $c < 1$ g/L) highlights the utility of this parameter. For 30mers, such as those used in ref 25 for which extended rod-like aggregates were observed, the critical concentration is predicted to be approximately 1 g/L accounting for hydrodynamics, well below the concentrations used in the experiments. At concentrations of 5 g/L (roughly corresponding to the concentrations used in the simulations conducted in this work) multi-chain aggregation is therefore expected in preference to chain collapse, giving rise to the observed rod-like aggregates. The effect of concentration on the behaviour of a number of different systems that are otherwise identical is given in the SI, Fig. S4.24, highlighting that more rapid aggregation, and the formation of larger aggregates, is indeed observed at higher concentrations. Extrapolating the observed chain length dependence (Fig. 4.8) to longer chains (e.g. 180mers, consistent with ref 22), single-chain folding is expected to be the dominant pathway at concentrations up to approximately 2 g/L. These concentrations are above those used in the experiments of up to 1 g/L.[22] The predicted folding behaviour is therefore consistent with the experimental observations for these longer chains at lower concentrations. This kinetic effect, by which the relative rates of single chain folding and multi-chain aggregation are important for predicting the structure of any aggregates, reconciles the apparent discrepancy in the experimental studies, and highlights the importance of both concentration and chain length for achieving the desired thin-film morphology.

It is important to note here that $c^\dagger$ has very different scaling with N from the overlap volume fraction ϕ^*, which has been used previously[43] to predict aggregation properties. The work of ref 43, which considered only a single polymer (DPP-DTT, which is significantly different chemically to P(NDI2OD-T2)) at concentrations close to the overlap concentration, suggested that the optimal concentration for achieving high performing organic field-effect transistor (OFET) devices is the polymer overlap concentration. If this is the case, the optimal concentration is expected to decrease with N, and $c^\dagger$ should be constant for constant $\phi_V N^{1/2}$. Fig. S4.25a shows that this is not the case for the simulations in this work, with the value of $\phi_V N^{1/2}$ at which $\tau_s = \tau_c$ showing a dependence on N. This chain length dependence would not be expected if $\phi_V N^{1/2}$ were a good parameter for controlling aggregation. Our work suggests that there is a lower concentration (at least for some range of chain lengths) that might more accurately predict the transition to extended aggregates correlated with good device performance. This concentration is determined by the relative rates of single-chain collapse and multi-chain aggregation and scales in the opposite way with N compared with the overlap concentration. It should be noted, however, that the model presented in this work (SI Section S4.10) breaks

down at the overlap concentration as aggregation will be instantaneous at this concentration (giving $\tau_c = 0$), and so the crossover concentration becomes ill-defined. The values of $c^\dagger$ calculated from the short chain simulations are well below this overlap concentration (approx. 25 g/L for 30mers, assuming the size is the radius of gyration in a good solvent, and higher for shorter chains), though are approaching the estimated overlap concentration for 180mers (approx. 6 g/L, calculated using the scaling of R_g with N obtained from the shorter chains in good solvent). This calculated overlap concentration is, however, a lower bound on the value, which will be higher in poor solvents where single chains are more collapsed, so the estimated values of $c^\dagger$ for 180mers are still expected to be reasonable.

Effect of solvent viscosity on relative rates of single-chain folding and multi-chain aggregation. All of the previous analysis was conducted using the same solvent viscosity (friction coefficient chosen to match monomer MSD of CG system with AA monomers in DCB) in order to facilitate comparison between different solvent qualities. However, the viscosity of TOL (0.560 mPa·s at 25°C) is approximately half that of DCB (1.324 mPa·s at 25°C).[284] It is therefore important that the effect of viscosity on the competition between single-chain folding and multi-chain aggregation be considered, as it should affect the rates of both processes. Based on the theory presented in the SI Section S4.10, the rates of both single-chain folding[285] and multi-chain aggregation are expected to scale linearly with viscosity, as they both depend on the diffusion coefficient of either the monomer or polymer, which from the Stokes-Einstein equation are inversely proportional to solvent viscosity.

To determine the effect of viscosity in the simulations, the single-chain folding and multi-chain aggregation timescales were calculated for a system with Langevin friction coefficient $\gamma = 1/10\gamma_{DCB}$, where γ_{DCB} is the value used for all other simulations in implicit DCB. The calculated time constants for single-chain folding (τ_s) and multi-chain aggregation (τ_c) are given alongside the DCB-viscosity results in Table 4.2. Both the single- and multi-chain aggregation timescales were found to scale approximately linearly with γ, indicating that while viscosity will change τ_c and τ_s, it will do in such a way that it is not expected to change the calculated value of $c^\dagger$. Indeed, the low viscosity system is included as one of the 20mer points in Fig. 4.8 and shows roughly the same scaling of $c^\dagger$ with N as the higher viscosity points.

Effect of aggregation on backbone stiffness. The structure of P(NDI2OD-T2) consists of a fused-ring NDI system, connected through a bTh group. Any flexibility of the backbone must therefore come from the rotatable Th–Th and Th–NDI bonds. As aggregation occurs in a manner in which both the NDI and the Th groups π stack, aggregation has the effect of reducing the flexibility of the chain. The Kuhn

length b of a single 30mer, and each chain in a pair of aggregated (fully overlapping, $N_{pair}/N = 1$) 30mers are compared in Table 4.3. The Kuhn length increased from approximately 8 in the single chain case, to 20 monomers in the fully overlapping aggregate, corresponding to a substantial increase in bending rigidity ($\kappa_b = bk_BT/2$ for a worm-like chain[286]). This increased backbone stiffness means that folding of sections of the polymer where aggregation has occurred (meaning a monomer is interacting with at least one other monomer) becomes highly unlikely.

Table 4.3 Kuhn length b (number of monomers) and bending rigidity κ_b of either a single chain (30mer, regular backbone flexibility, poor solvent, averaged over 20 independent simulations over the 0.9-1 μs time period of the 10 μs simulations described above), or a single chain in a pair of fully overlapping chains (30mers, regular backbone flexibility, poor solvent, averaged over each chain in the aggregate over the final 100 ns of a 1 μs simulation). The values for the more flexible chain, and both chains in the "good" solvent, are given in the SI Table S4.3. The Kuhn length is reported as the number of monomers, where each monomer is assumed to be 14 Å long.

system	b (monomers)	κ_b (kcal/mol.Å)
single chain	7.66	31.98
aggregated chains	20.00	83.44

To determine whether this regime, where the chains are so covered as to prevent further folding, is relevant for the aggregation observed here, the fraction of monomers in aggregates that interacted with other monomers in any other chain was calculated. This variable, N_{total}/N, defined in Fig. 4.4, gives the total number of monomer–monomer interactions between one chain and any other chain. In the poor and intermediate solvents, this quantity was in excess of 80% of the full chain length (about 16 monomers for 20mers; Fig. 4.5b) after 4 μs of simulation, indicating that chains that are in aggregates are almost fully covered by other chains. Although the small regions where chains are not overlapped may still be able to fold, the aggregates will be substantially stiffer than the single chains, and effectively stuck in an extended state, from which the further build up of extended rod-like structures can occur.

Effect of backbone flexibility on multi-chain aggregation. To better understand the effect of the single-chain folding kinetics on the multi-chain aggregation properties, we examined the same P(NDI2OD-T2) polymer with an artificially flexible backbone. The flexible backbone had angle bending and dihedral coefficients between NDI and thiophene groups reduced to 1% of the values for the regular flexibility chain. Single chains of this flexible polymer exclusively collapsed into more compact structures within the 10 μs single-chain simulations, with relaxation times on the order of

1 μs, rather than remaining extended (Figs. 4.7, S4.20, and S4.22). At the same concentration as the regular flexibility 20mers (6 g/L), the flexible 20mers did not meet either of the metrics discussed above for the calculation of τ_c (single chain concentration fallen to 25% of the original concentration, or an average aggregate size of 2) within the simulation time of 3 μs. Given the value of τ_s of ≈ 1 μs for these chains, this corresponds to a critical concentration $c^\dagger$ of > 6 g/L. It is therefore expected that much more single-chain collapse would be expected here than in the corresponding stiffer chain system, in which multi-chain aggregation should generally occur before chains have a chance to collapse.

Comparing the aggregate size (number of monomers) and radius of gyration of the flexible and regular backbones showed a slower rate of aggregate growth, and generally more compact structures for the flexible chains than the stiffer regular chains (Fig. 4.9) as expected from the relative rates of folding and aggregation. This behaviour can be attributed to a more rapid collapse into hairpin/toroid structures, which has the twofold effect of reducing the collision rate due to the more compact structures, and giving more compact structures when collisions do occur as chains may already be partially collapsed. Examining a system with an even lower concentration showed the same behaviour, with very little multi-chain aggregation observed over the simulated time period (Fig. 4.9a). While there was still a brief initial aggregation period, during which chains that were initially positioned close to each other were able to aggregate prior to folding, little aggregation was observed after this point with the average aggregate size remaining well below 1 over the entire simulation period. Although multi-chain aggregation is not *completely* prevented at this lower concentration, it is greatly suppressed and could be expected to lead to different final aggregate properties, as observed experimentally.[22,25]

The lower radius of gyration of the flexible chains in poor solvent observed in Fig. 4.9b could be attributed to both less aggregation than for the regular-flexibility backbone and more compact aggregates even when consisting of many chains. From the behaviour in Fig. 4.9a, the flexible-chain aggregates were generally smaller (contained fewer polymer chains) than those with the regular backbone flexibility, indicating that less aggregation does occur as previously discussed. From examination of the R_g and κ^2 of aggregates of various sizes (Fig. 4.10) it can also be seen that when larger aggregates did form with the flexible backbone, they were generally more compact (lower R_g) than their regular-flexibility counterparts, though the scaling of κ^2 with aggregate size, particularly in the poor solvent, appeared random, likely due to the fewer aggregates of each size leading to poorer statistics. Overall, it appears that the more rapid single-chain collapse of the flexible polymer leads to a stronger preference for intrachain aggregation compared with the regular flexibility chain. This has the combined effect of reducing the number of aggregates, due to

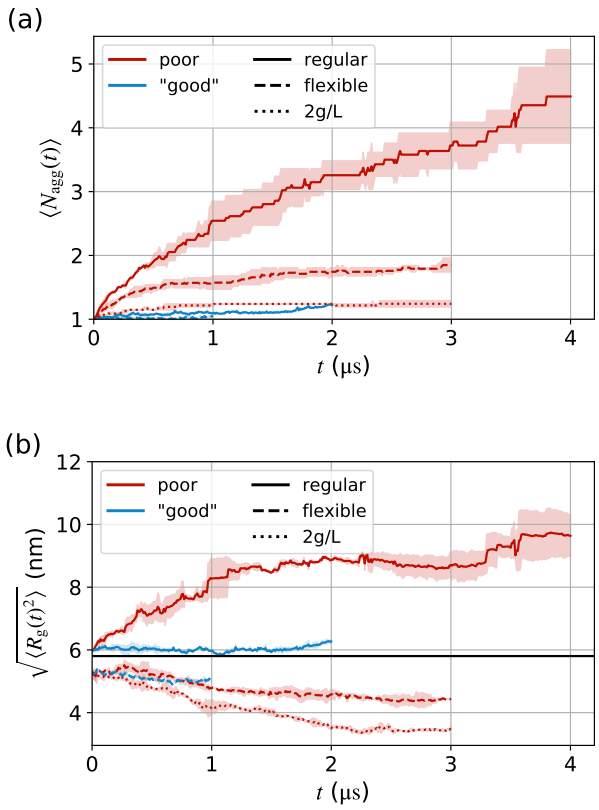

Fig. 4.9 Comparison of the multi-chain aggregation kinetics of flexible and regular 20mers in "good" and poor solvent. (a) Average aggregate size (number of chains in aggregate, $\langle N_{agg}(t) \rangle$) and (b) RMS R_g over time. The horizontal black line in (b) indicates the value of the RMS R_g for single, regular flexibility, chains in the "good" solvent, calculated as described in Fig. 4.2. The results for flexible chains in the poor solvent at two concentrations that are expected to be lower than $c^\dagger$ (2 and 6 g/L) are also presented (dotted and dashed red lines).

the greater distance required for the more compact aggregates to diffuse in order to aggregate, and giving slightly more compact aggregates where aggregation does occur. Similar behaviour could likely be obtained in a more dilute system of stiffer chains, which, although they take longer to fold, could be expected to collapse prior to extensive multi-chain aggregation at low enough concentration.

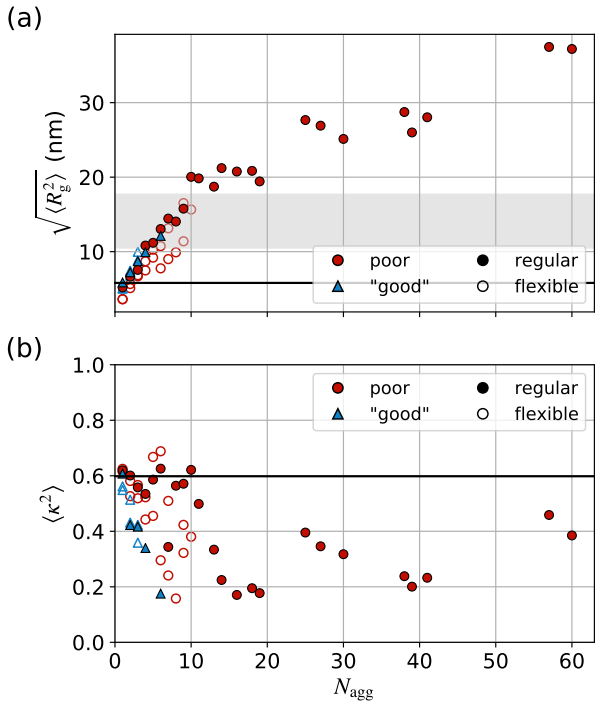

Fig. 4.10 (a) RMS R_g and (b) average shape anisotropy κ^2 as a function of aggregate size for regular (filled symbols) and flexible (unfilled symbols) backbones in a "good" (blue triangles) or poor (red circles) solvent at a concentration of approximately 6 g/L. Horizontal grey lines indicate the values of R_g and κ^2 for single 20mers of the regular backbone in "good" solvent.

4.4 CONCLUSIONS

The solution-phase morphology and dynamics of OSC polymer P(NDI2OD-T2) was studied using CG MD simulation in order to understand the reported formation of extended rod-like aggregates in poor solvents. We found that sufficiently strong intermolecular attractions (equivalent to poor solvent quality), for which interaction through only a few monomers resulted in effectively inseparable chains, led to the build up of extended aggregates of partially overlapping chains. Although we were not able to observe the formation of aggregates of the size observed experimentally (on the order of 100s of nm) due to computational limitations, the formation of aggregates with radius of gyration exceeding that of a single chain in the simulations suggests that these larger aggregates should indeed be able to form. Over time, a trend towards more linear, rod-like aggregates was also observed, consistent with the experimental results.

We proposed that this behaviour, which is not predicted by existing theories of polymer solubility in which decreasing solvent quality is conventionally asso-

ciated with chain collapse, is due to the relative rates of multi-chain aggregation and single-chain folding. The formation of extended aggregates is expected under conditions in which aggregation occurs faster than folding, assuming interchain attraction is strong enough to hold chains together in an only partially overlapping chain configuration. Firstly, we have shown that under conditions that correspond to P(NDI2OD-T2) in poor solvent toluene, at concentrations representative of experiments where rod-like aggregates were observed, aggregated chains overlap by only around 40% of their full chain length. Under conditions corresponding to a better solvent, this overlap fraction is still increasing over the timescale of the simulations, and is expected to reach upwards of 70% overlap. This finding is consistent with the difference between the experimentally observed behaviour in good–intermediate and poor solvents, with rod-like aggregates observed in the poor solvents, and structures in the better solvents showing sizes consistent with single chains, despite some aggregation occurring, suggesting almost fully overlapping chains.

For semiflexible polymers, a class that describes many OSCs, the folding of a single polymer chain is expected to depend on the chain stiffness. By comparing CG simulations of P(NDI2OD-T2) with a backbone parameterised to match the flexibility of the all-atom model with those of a much more flexible equivalent, we found more rapid folding of the flexible chain than that with regular flexibility. In both cases, the folding rate also displayed a chain-length dependence, increasing with increasing chain length as has previously been reported.[138] By comparing the approximate time for single-chain folding and that characterising multi-chain aggregation in the poor solvent, we were able to determine approximate concentrations at which each of these processes should be expected as the dominant pathway. A theory relating this critical concentration to chain length was developed, and the simulations were found to be in excellent agreement with the predictions. The critical concentration depended both on backbone flexibility, with a more flexible backbone expected to result in predominantly single-chain folding at higher concentrations than a more rigid one, and chain length, with longer chains transitioning from single-chain folding to multi-chain aggregation at higher concentrations due to their more rapid folding. In comparing the simulated solution-phase behaviour of flexible and regular P(NDI2OD-T2) chains, this proposed dependence was observed, with the more flexible chains giving more compact structures and less multi-chain aggregation. This finding rationalises apparent discrepancies between experimental measurements of the P(NDI2OD-T2):TOL system[22,25] and emphasises the importance of both concentration and chain length on predicting solution-phase behaviour.

Overall, multi-chain aggregation, resulting in the formation of extended rod-like

aggregates, is expected to occur under conditions in which

1. partially overlapping chains are inseparable over large timescales such that they do not rearrange to the energetically favourable fully-overlapped chains before becoming trapped, and

2. single-chain folding occurs slow enough that it is not expected to occur before multi-chain aggregation prevents further folding.

The relative rates of the single- and multi-chain pathways that control the second of these conditions depend on the the polymer concentration, chain length, and backbone flexibility. Although we have assumed these processes to be independent, they are likely to show a complex interdependence, with the progress along the single-chain folding pathway affecting the aggregation rate. A more complex model that accounts for these processes more completely, as well as explicitly including the effects of hydrodynamics, and potentially considering polydisperse systems rather than the monodisperse ones considered here, will further improve understanding of the solution-phase behaviour of semiflexible polymers. Finally, we have studied this behaviour using a CG model systematically parameterised to accurately represent P(NDI2OD-T2). However, these results are not expected to be specific to just this molecule, with the reported dependence of the solution-phase morphology on solvent quality, backbone flexibility, concentration, and chain length, likely applicable more generally to any semiflexible polymer.

Supporting Information

S4.1 PARAMETERISATION OF ALL-ATOM MODEL OF P(NDI2OD-T2)

The all-atom model of P(NDI2OD-T2) was parameterised following the method outlined in ref 24 for conjugated polymers in the OPLS force field.[24,202] As described in the main text, the charges were averaged over atoms in the same chemical environment to reduce the number of parameters.

The full set of parameters, as well as the definition of atom and bond types for each site are given in Section S4.14 of this document.

To increase the symmetry and reduce the number of atom types required, a monomer of P(NDI2OD-T2) was considered as a symmetric equivalent to its more commonly represented naphthalene diimide (NDI)–bithiophene (bTh) structure, with the bTh group split between the ends of the monomer (Fig. S4.1). Within a polymer chain, this will give exactly the same structure, with the only difference being at the terminal monomers.

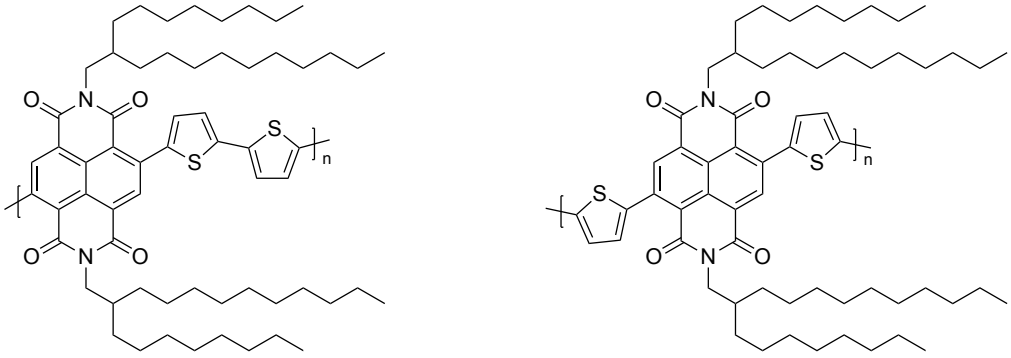

(a) Asymmetric **(b)** Symmetric

Fig. S4.1 Structures of the (a) more commonly used asymmetric, and (b) our symmetric representation of monomers of P(NDI2OD-T2).

s4.1.1 atomic point charges

Atomic point charges were calculated separately for the bTh and NDI conjugated entities of the backbone as described in ref 24. Each unit was terminated with a thiophene ring at each end to mimic the environment of a fully conjugated backbone, the alkyl sidechains on the NDI group truncated to methyl groups after the tertiary carbon (i.e. –N–CH_2–CH–$(CH_3)_2$), and the geometry optimised at the B3LYP/6-31+G** level. ChelpG charges for the optimised geometries were used as atomic point charges. Due to the symmetry of the P(NDI2OD-T2) monomer, atoms in the same chemical environment were assigned the same atom type (see Fig. S4.29 for the P(NDI2OD-T2) atom types), and their charge averaged over equivalent atoms in the system. Any excess molecular charge, related to the introduction of the terminal thiophenes and truncation of the side-chains, was added to the carbon atoms that connect the side-chains to the backbone (i.e. the CH_2 group bonded to the N, site type 955 for monomer unit or central monomer of polymer, 957 for terminal monomer of polymer; see Fig. S4.29 for definitions). OPLS charges[202,268–273] were used for the atoms in the alkyl chains.

s4.1.2 bonded potentials

While most bonded parameters were obtained from a combination of the OPLS force-field parameters for equivalent atom types and the optimised geometries of a P(NDI2OD-T2) monomer, with the bond lengths and angles from the optimised geometries and the force constants from the OPLS force field, the parameters for the bond lengths and angles between the NDI and thiophene (Th) conjugated entities were obtained from quantum-chemical calculations. Specifically, the NDI–Th bond and the NDI–Th and Th–Th dihedrals were explicitly parameterised using constrained geometry optimisations.

NDI–Th bond

The NDI–Th bond was parameterised from the energy of the entire asymmetric monomer unit (B3LYP/6-31+G**) with the length of the NDI–Th bond fixed at 0.01 Å intervals from $l_0 - 0.1$ to $l_0 + 0.1$, where l_0 is the bond length determined from the unconstrained optimisation. The potential energy was fit to a harmonic potential of the form

$$U_{\text{bond}}^{\text{harm}}(l)(l) = k_{\text{b}}(l - l_0)^2 \tag{4.15}$$

where k_{b} is the bond stretching coefficient (half the force constant), and l_0 again the bond length in the unconstrained optimisation (Fig. S4.2).

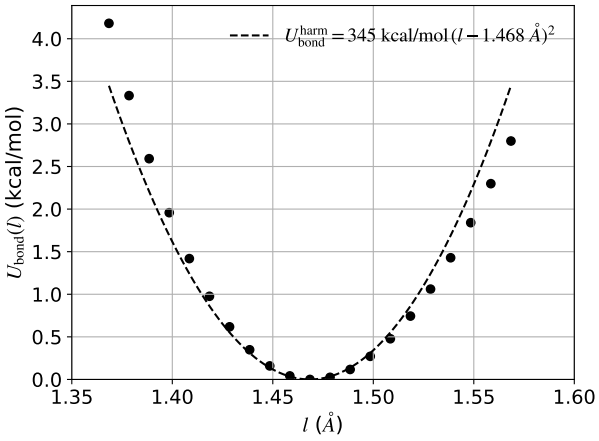

Fig. S4.2 Fit to the NDI–Th bond potential. Constrained optimisations were performed at each of the points shown, at 0.1 Å intervals from the optimised bond length of 1.468 Å. Dashed line indicates the fit to the form $U_{\text{bond}} = k_{\text{b}}(l - l_0)^2$, where l_0 is the value of the bond length in the unconstrained optimisation. All data with $U_{\text{bond}} < 2$ kcal/mol were used for the fit.

Dihedral potentials

The explicitly parameterised dihedral potentials in this work used the form

$$U_{\text{dihed}}^{\text{m/h}}(\phi_i)(\phi) = \sum_{n=0}^{m} k_n \cos^n(\phi) \tag{4.16}$$

where ϕ is the dihedral and k_n are fit parameters. In LAMMPS this is implemented as the "multi/harmonic" dihedral style for $m = 4$. For the Th–Th and NDI–NDI dihedrals we use $m = 4$ and 8 respectively. For $m = 4$, the dihedral form in eqn (4.16) is equivalent to the more commonly used OPLS dihedral, which has the form

$$U_{\text{dihed}}^{\text{OPLS}}(\phi) = \frac{1}{2}k_1\left[1 + \cos(\phi)\right] + \frac{1}{2}k_2\left[1 - \cos(2\phi)\right] + \frac{1}{2}k_3\left[1 + \cos(3\phi)\right] + \frac{1}{2}k_4\left[1 - \cos(4\phi)\right] \tag{4.17}$$

where k_n are fit parameters, but is more flexible when $m \geq 5$. The more flexible form of eqn (4.16) with $m = 8$ was required to accurately capture the height of the barrier at $\phi = 0$ for the NDI–NDI dihedral, but $m = 4$ was found to be adequate for the NDI–Th dihedral (see Fig. S4.3)

For both the NDI–Th and Th–Th dihedrals, 4 different combinations of atoms define the same dihedral due to the connectivity of the conjugated units. Rather than parameterise four interdependent dihedral potentials to define the dihedral between each unit, we have set the parameters of three of these to zero, and parameterised the one remaining, effectively capturing the effect of all four possible dihedrals in one set of parameters. The definition of the two dihedrals, and the atoms used for their parameterisation, is shown in Fig. S4.4.

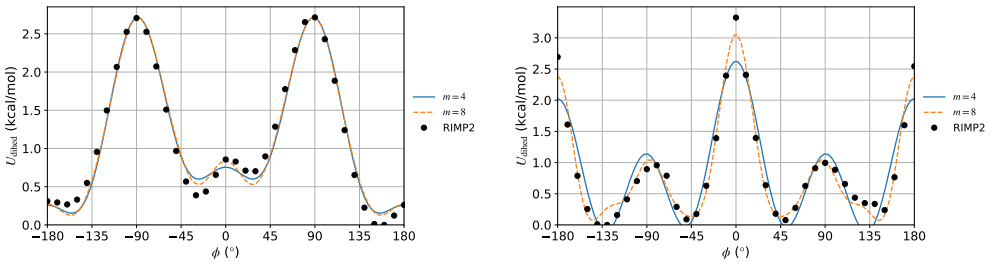

(a) Th–Th **(b)** NDI–Th

Fig. S4.3 Comparison of the dihedral form (eqn. (4.16)) with $m = 4$ or $m = 8$ for fitting to the (a) Th–Th and (b) NDI–Th dihedrals. The points labelled RIMP2 are the energies obtained from quantum calculations. For the final parameters we use the fit parameters with $m = 4$ for the Th–Th potential, and $m = 8$ for the NDI–Th.

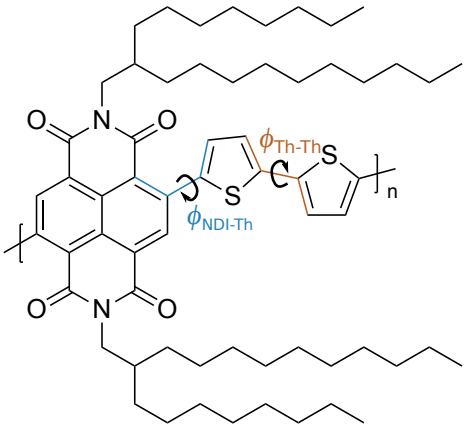

Fig. S4.4 The structure of a P(NDI2OD-T2) monomer unit, with the atoms used to define the NDI–Th (blue) and Th–Th (orange) dihedrals highlighted.

In order to calculate the dihedral potentials, the following procedure was followed, as outlined in ref 24:

1. Geometry was optimised (B3LYP/6-31+G**) with the dihedral of interest fixed at 10° increments from −180 to 180°. Each optimisation started from the optimised geometry of the immediately preceding calculation, leading to structures getting trapped in non-optimised geometries, particularly around 0 and 180°, giving a non-symmetric potential. To obtain a symmetric potential, additional optimisations were carried out in the opposite direction from −160 to −180°, and from 20 to 0°, both at 5° intervals and the energy of these structures used.

2. RIMP2/cc-pVTZ single-point energy calculations on the optimised geometries with the single dihedral fixed were used to construct the MP2 dihedral poten-

tial, which was fit to eqn (4.16) to give the five (or nine) coefficients k_n. The results of these calculations, and the fits to the obtained potentials are shown in Fig. S4.3.

3. The potential energy as a function of dihedral angle in an molecular dynamics (MD) system, including other bonded and non-bonded interactions, was obtained and compared to the previously obtained RIMP2 potential. As the dihedral energy in the MD simulation will be influenced by the non-bonded interactions (in OPLS the 1–4 interactions, being those between atoms separated by three bonds, are set to 0.5× their full value, which has been done in this work), the dihedral potential obtained from the quantum calculations cannot be used as is. The relevant dihedral potential for accurately modelling the behaviour in the MD simulation is the difference between the RIMP2 potential, and that obtained from an equivalent MD system, again calculated with the dihedral constrained at various positions over the whole 360° interval. For the NDI–Th dihedral, an energy minimisation at each constrained dihedral sometimes resulted in the structure becoming trapped in local minima (similarly to in the geometry optimisations outlined in step 1), so the MD potential was calculated using the following cooling protocol:

   a) Dihedral of interest restrained to ϕ_0 at 10° intervals between 0 and 360°with a restraining potential of the form

   $$U_{\text{rest}} = k_{\text{rest}}\left[1 + \cos(n\phi - (\phi_0))\right] \tag{4.18}$$

   with $k_{\text{rest}} = 5000$ kcal/mol and $n = 1$.

   b) The system was cooled from 100 K to 0 K, with temperature controlled using a Langevin thermostat ($\gamma = 0.01$, see eqn. (4.2)) over 100 ps.

   c) The system was run for an additional 10 ps at 0 K, then the energy minimised.

   d) This final minimised energy at each value of the dihedral constraint was used to construct the potential energy in the same way as for Fig. S4.3.

   For the Th–Th dihedral, the energy with the dihedral restrained as outlined above was simply calculated from an energy minimisation of the structure rather than following the cooling procedure.

4. The potential obtained from the MD energy minimisation procedure was then fit to the same form as that from the quantum calculations (eqn (4.16) with $m = 4$ or 8). The difference in the coefficients from the quantum fit and the MD fit then gives the final coefficients for the potential in the MD force field.

A comparison between the dihedral potentials calculated from the quantum calculation and the final MD force field parameterisation is shown in Fig. S4.5.

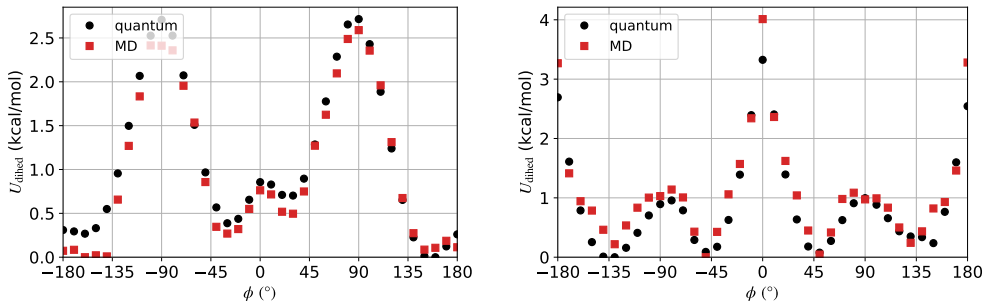

(a) Th–Th **(b)** NDI–Th

Fig. S4.5 Comparison of dihedral potentials calculated from quantum calculations (black circles) or MD simulation with the final force field parameters (red squares) for (a) the Th–Th torsion, or (b) the NDI–Th torsion. Both show reasonable agreement between the two methods.

S4.2 COARSE-GRAINING OF P(NDI2OD-T2)

All coarse-grained (CG) simulations in this work used an implicit solvent, modelled using Langevin dynamics. The friction coefficient γ (eqn (4.2)) was chosen to give good agreement between the mean squared displacement (MSD) of monomers in the all-atom (AA) (in *o*-dichlorobenzene (DCB)) and CG representations, shown in Fig. S4.6.

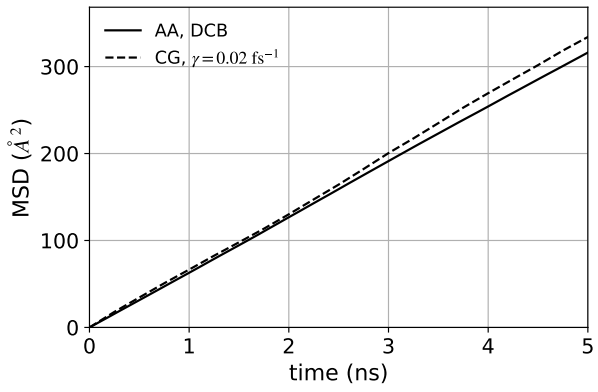

Fig. S4.6 MSD of P(NDI2OD-T2) monomers in the AA (solid lines), and CG (dashed lines) simulation of P(NDI2OD-T2) monomers with friction coefficient set to $\gamma = 0.02$ fs^{-1} to match the diffusion in DCB.

P(NDI2OD-T2) was coarse-grained from simulations of monomers in DCB. The AA simulations (described in the main text) were deemed to be at equilibrium by 50 ns of the 200 ns simulation based on the time dependence of the monomer center-of-mass radial distribution function (RDF) (Fig. S4.7).

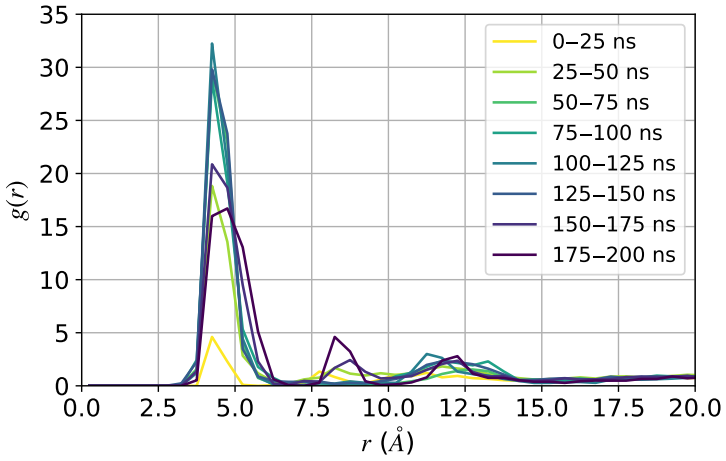

Fig. S4.7 Monomer center-of-mass RDF for P(NDI2OD-T2) monomers in DCB averaged over various time slices of the simulation.

The bonded interactions were parameterised from simulations of trimers, again in DCB. The equilibration period of these simulations was estimated from the time dependence of the bonded distributions. While most converged within 1 ns, the time dependence of the slowest varying distribution – the 3–1–7–3 dihedral – is shown below (Fig. S4.8). A 50 ns equilibration time was used based on the time dependence of this dihedral distribution.

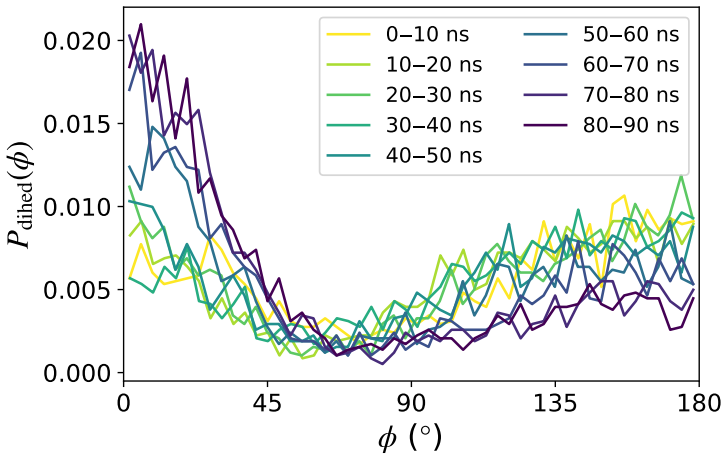

Fig. S4.8 Distribution of the 3–1–7–3 (site types defined in Fig. S4.31) dihedral in DCB, averaged over various time slices of the simulation. Each line is the distribution calculated over the indicated 10 ns block.

s4.2.1 analytical forms of bonded and non-bonded potentials

The following analytical functions were fit to the CG potentials to facilitate simulation. See Fig. 4.1 for site type definitions.

Bonds. For the bonds that did not contain side-chains atoms, a harmonic potential (eqn (4.19a)) was used. For those that did (site-types 4–5 and 5–5), a quartic potential was used (implemented in LAMMPS as the "class2" bond style).

$$U_{\text{bond}}^{\text{harm}}(l)(l) = k_2(l - l_0)^2 \tag{4.19a}$$

$$U_{\text{bond}}^{\text{class2}}(l)(l) = k_2(l - l_0)^2 + k_3(l - l_0)^3 + k_4(l - l_0)^4 \tag{4.19b}$$

In both cases k_i are the bond stretching coefficients, and l_0 the equilibrium bond length between two bonded sites with bond length l.

Angles. Angles 3–2–4 and 3–6–4 were modelled with a harmonic angle potential (eqn (4.20a)). The others used a quartic potential (eqn (4.20b)).

$$U_{\text{angle}}^{\text{harm}}(\theta)(\theta) = k_2(\theta - \theta_0)^2 \tag{4.20a}$$

$$U_{\text{angle}}^{\text{quart}}(\theta)(\theta) = k_2(\theta - \theta_0)^2 + k_3(\theta - \theta_0)^3 + k_4(\theta - \theta_0)^4 \tag{4.20b}$$

k_i are the angle bending coefficients, and θ_0 the equilibrium angle between three bonded sites at angle θ.

Dihedrals. All dihedrals were modelled with the dihedral form given by eqn (4.21):

$$U_{\text{dihed}}^{\text{m/h}}(\phi_i)(\phi) = \sum_{n=0}^{m} k_n \cos^n(\phi) \tag{4.21}$$

with $m = 4$ where k_n are fit parameters and ϕ the dihedral angle between four bonded sites. Note this is the same as eqn (4.16) used for the AA simulation

Improper dihedrals. A cosine improper dihedral style was used (eqn. (4.22), implemented in LAMMPS as the cvff improper style):

$$U_{\text{impro}}^{\text{cvff}}(\psi)(\psi) = k\,[1 + d\cos(n\psi)] \tag{4.22}$$

where k is an energy parameter, $d = 1$ or -1 and n is the multiplicity (an integer). Here we use $d = -1$ and $n = 2$.

Non-bonded interactions. Non-bonded interactions were fit to a Lennard Jones (LJ) potential (eqn (4.23)), with interactions cut off and shifted to zero at $r_c = 15$ Å:

$$U_{\mathrm{LJ}} = \begin{cases} 4\epsilon_{ij}\left[\left(\frac{\sigma_{ij}}{r}\right)^{12} - \left(\frac{\sigma_{ij}}{r}\right)^{6}\right], & r < r_c \\ 0, & \text{otherwise} \end{cases} \tag{4.23}$$

where σ_{ij} and ϵ_{ij} are the interaction diameter and strength, respectively. A purely repulsive form of this potential was also used in order to relax the backbone structure prior to simulation with attractive non-bonded interactions. The Weeks-Chandler Anderson (WCA) potential was used:

$$U_{\mathrm{WCA}} = \begin{cases} 4\epsilon_{ij}\left[\left(\frac{\sigma_{ij}}{r}\right)^{12} - \left(\frac{\sigma_{ij}}{r}\right)^{6}\right] + \epsilon_{ij}, & r < 2^{1/6}\sigma_{ij} \\ 0, & \text{otherwise} \end{cases} \tag{4.24}$$

where all symbols are as defined for the LJ potential. The potential is shifted to zero at the cutoff of $2^{1/6}\sigma_{ij}$ (the position of the LJ energy minimum) to give a purely repulsive potential.

s4.2.2 Convergence of non-bonded parameters

Non-bonded parameters were optimised following the iterative Boltzmann inversion (IBI) protocol described in refs 172, 281. The convergence of the RDFs was monitored using eqn (4.5), as shown in Fig. S4.9. The parameters from iteration 12 (highlighted in orange in Fig. S4.9) were used as the final P(NDI2OD-T2) CG parameters. The behaviour of the RDFs, and corresponding LJ potentials, for the 5 iterations leading up to iteration 12 are shown in Fig. S4.10.

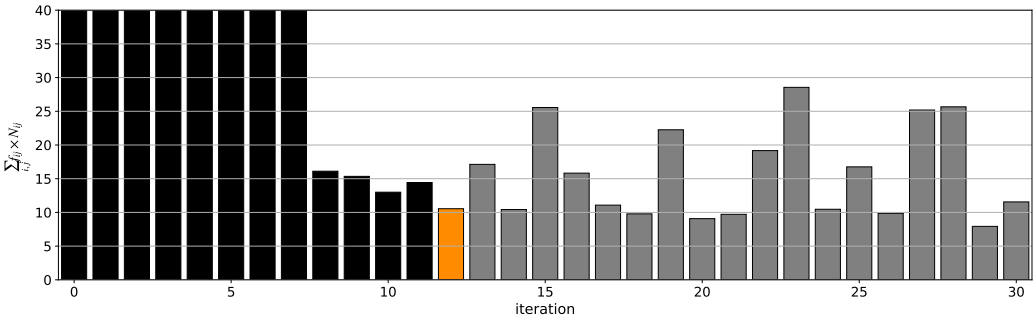

Fig. S4.9 Convergence of the IBI procedure for the coarse-graining of the P(NDI2OD-T2) non-bonded interactions from simulations of monomers in DCB. The orange bar indicates the iteration that was used for further simulation, as all subsequent iterations showed little to no improvement.

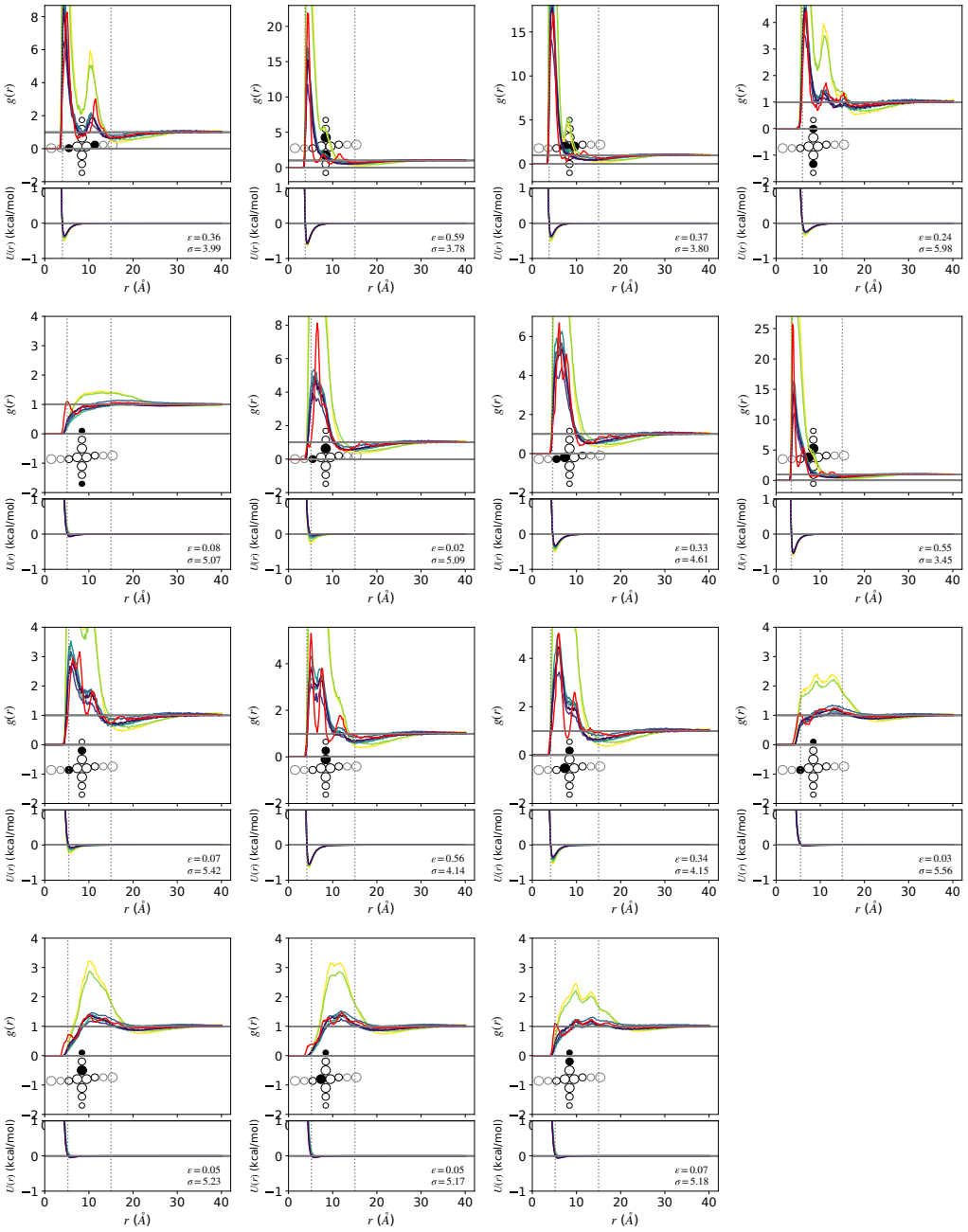

Fig. S4.10 Comparison of the target AA (red) and CG site–site RDFs for the final 5 iterations prior to the one that was used (coloured by iteration with yellow the earliest and purple the final iteration, number 12). The inset diagrams indicates the site-types that the distribution is calculated for (for sites on different monomers). The LJ potential that resulted in the plotted distributions is shown in the lower plots, with the parameters of the final iteration (12) listed. The plots of the LJ potentials follow the same colour mapping as the RDFs.

S4.2.3 Comparison of coarse-grained and all-atom distributions

Following the parameterisation of both the bonded and non-bonded interactions, all the bonded distributions were recalculated with the final non-bonded interactions to determine whether the parameterisation of the non-bonded interactions affected the previously obtained bonded distributions. Distributions between additional bonded sites, which were not explicitly parameterised as their behaviour should be captured by the combination of other parameters, were also examined to determine whether they behaved as expected. The simulations used to generate these were set up identically to the CG trimer simulations used to parameterise the bonded interactions (18 trimers in (87 Å)^3 box). The same soft potential as for the previous simulations was used to remove overlaps, and the simulations run for a total of 100 ns (timestep = 5 fs), with the bonded distributions calculated from the final 50 ns. In all cases, good agreement was found between the AA (solid grey line) and CG (dotted black line) distributions, even for the potentials that were not explicitly parameterised.

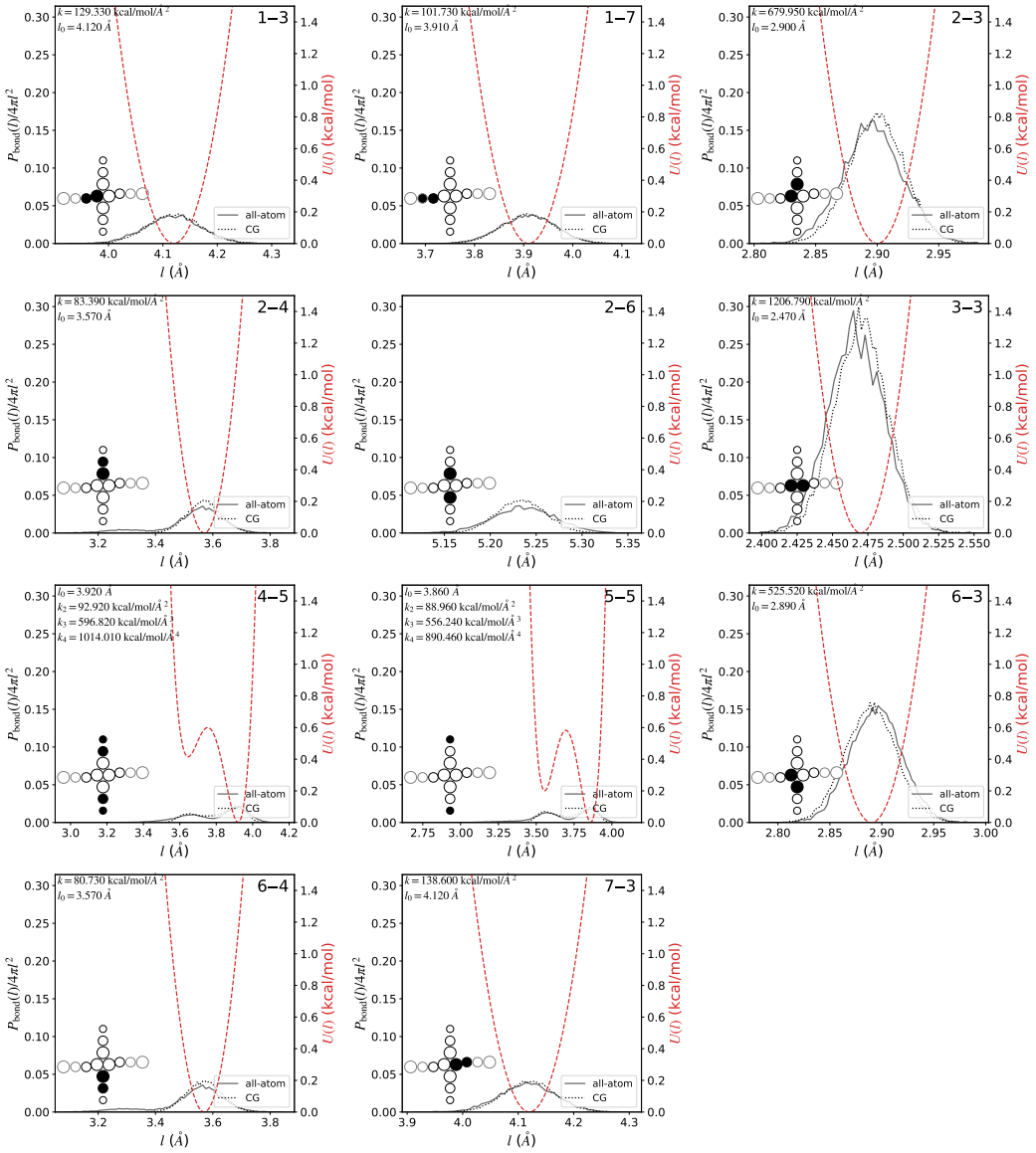

Fig. S4.11 Final bond distributions calculated from simulations with the full set of optimised parameters (including non-bonded). Where the bond length was explicitly parameterised, the final potential is shown in red, and its parameters given in the top left corner of each plot. An inset diagram shows a representation of P(NDI2OD-T2) with the pair of atoms defining the bond highlighted.

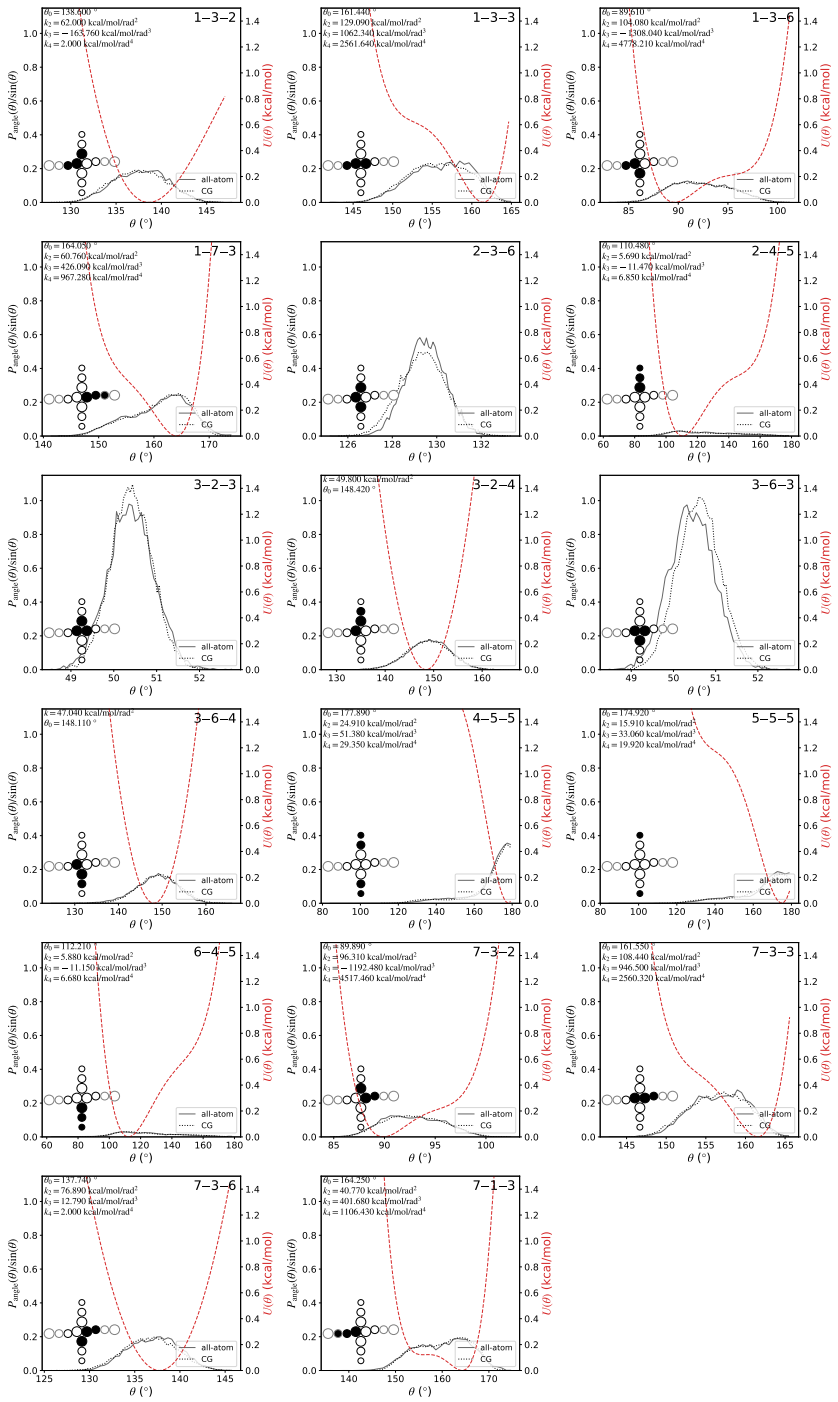

Fig. S4.12 Final angle distributions calculated from simulations with the full set of optimised parameters (including non-bonded). Where the angle was explicitly parameterised, the final potential is shown in red, and its parameters given in the top left corner of each plot. An inset diagram shows a representation of P(NDI2OD-T2) with the trio of atoms defining the angle highlighted.

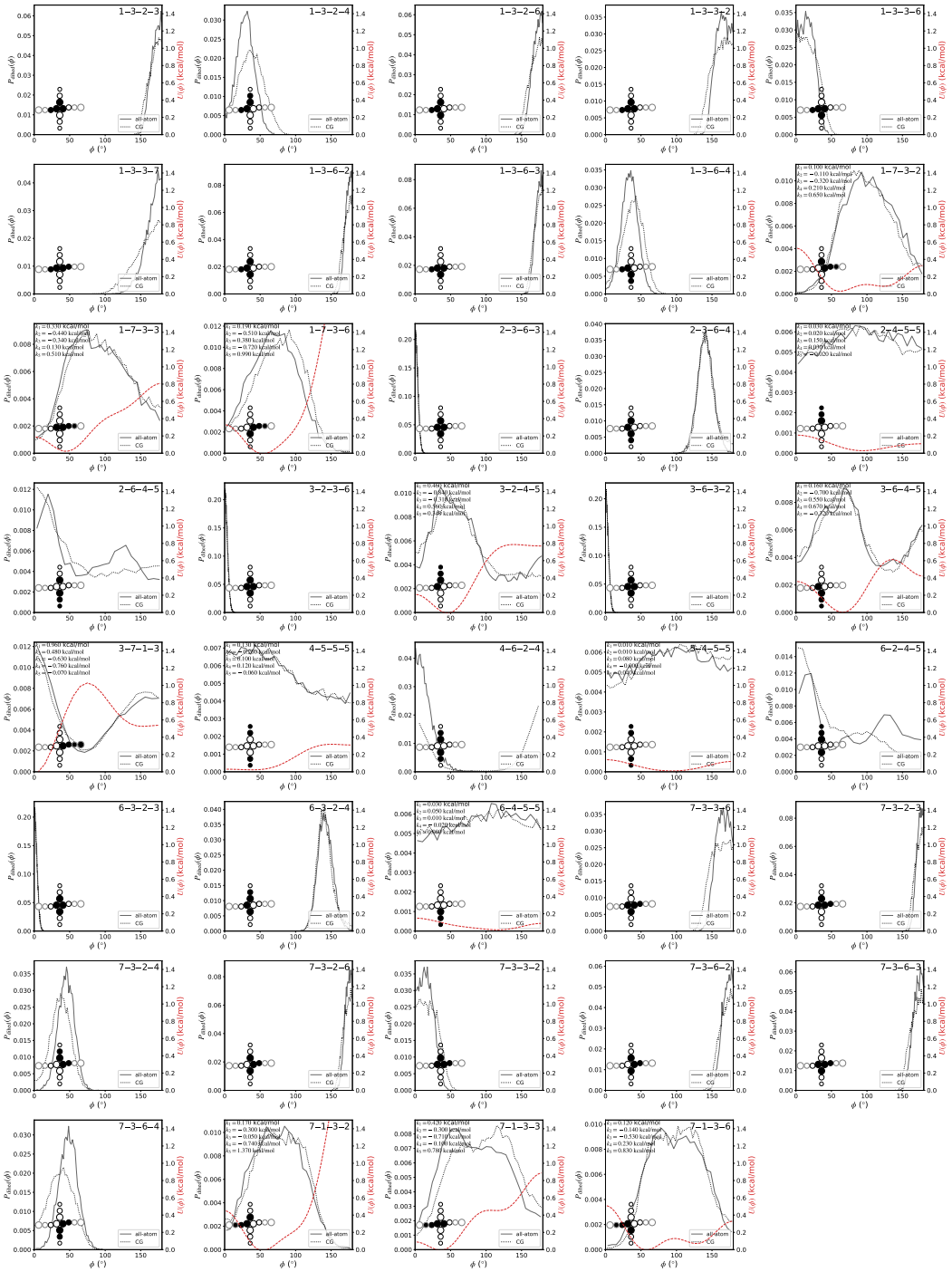

Fig. S4.13 Final dihedral distributions calculated from simulations with the full set of optimised parameters (including non-bonded). Where the dihedral was explicitly parameterised, the final potential is shown in red, and its parameters given in the top left corner of each plot. An inset diagram shows a representation of P(NDI2OD-T2) with the four atoms defining the dihedral highlighted.

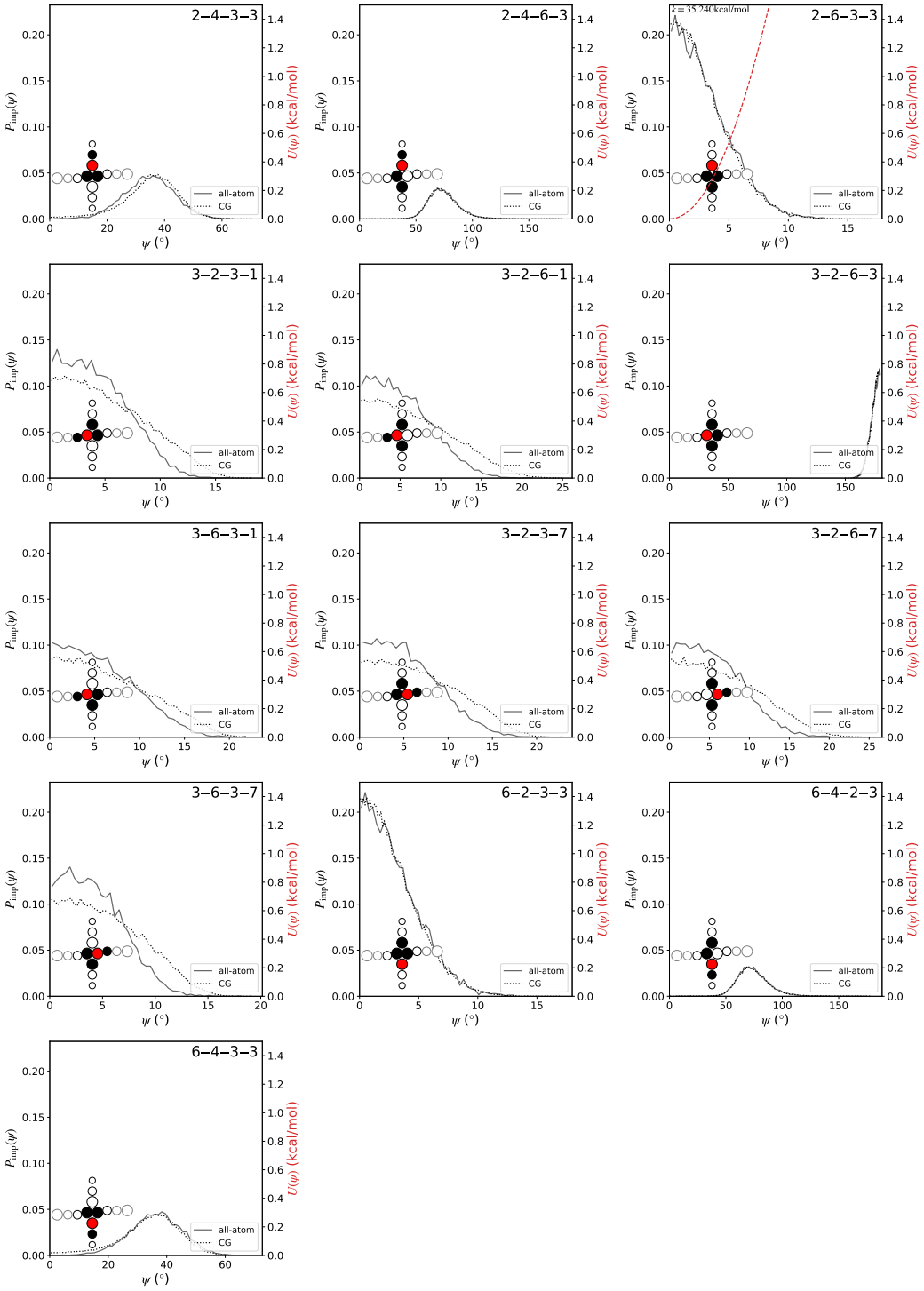

Fig. S4.14 Final improper distributions calculated from simulations with the full set of optimised parameters (including non-bonded). Where the improper was explicitly parameterised, the final potential is shown in red, and its parameters given in the top left corner of the plot. An inset diagram shows a representation of P(NDI2OD-T2) with the four sites defining the improper highlighted (central site highlighted in red).

S4.3 OPES SIMULATIONS

s4.3.1 reweighting procedure

Free-energy calculations for the AA and CG monomer systems were used to estimate the relative strength of the interactions between monomers in different solvents. These calculations used the on-the-fly probability enhanced sampling (OPES) procedure.[209] As OPES biases the behaviour of the monomers, the free energy cannot simply be calculated from the probability distribution in these simulations, but must be reweighted to properly account for the effect of this bias. The sampled distribution $P_{\text{bias}}(s)$ is related to the unbiased equilibrium distribution $P(s)$, where s is the collective variable(s) that is (are) being biased (here the center-of-mass separation) through the addition of a bias $V(s)$, where

$$V(s) = k_{\text{B}}T \ln\left(\frac{P_{\text{bias}}(s)}{P(s)}\right). \tag{4.25}$$

The bias introduced by the harmonic wall that restrains the center-of-mass separation of the monomers to be less than 20 Å is also accounted for in this manner. The weights to return to the unbiased distribution are then simply $w = \exp\left(\frac{V(s)}{k_{\text{B}}T}\right)$. This can be used to calculate an estimate of unbiased distribution, which in PLUMED[211,212] is done using kernel density estimation, as

$$\langle \hat{P}(s,t) \rangle = \frac{\sum_{t'=0}^{t} w(t') K(s - s(t'), \sigma_{\text{K}})}{\sum_{t'=0}^{t} w(t')} \tag{4.26}$$

where $w(t')$ is the weight at time t' ($w(t') = \exp(V(s,t')/k_{\text{B}}T)$), and $K(s - s(t'), \sigma_{\text{K}})$ are kernels (here Gaussians), centered at $s(t)$ with bandwidth σ_{K} (here 0.25 Å) and summed over all times between t' and t. This procedure is implemented in PLUMED as `reweight_bias`, combined with the `histogram` functionality to calculate weighted probability densities.[211,212]

s4.3.2 comparison of aa and cg opes results

To validate the choice of scaled parameters, where the interactions corresponding to P(NDI2OD-T2) in a better and poorer solvent are obtained by uniform scaling of the parameters from DCB, we have compared the free energy as a function of center-of-mass separation of the three sets of CG parameters used in this work, and the AA equivalent in toluene (TOL) (a poor solvent for P(NDI2OD-T2), and one in which rod-like aggregates are observed experimentally), *o*-dichlorobenzene (DCB) (the solvent the intermediate solvent interactions were parameterised in), and 1-chloronaphthalene (CN) (a good solvent for P(NDI2OD-T2)). In all three cases, the scaled parameters give reasonable agreement between the CG and AA

free energies. Importantly, the poor solvent parameters are a good representation of the TOL environment in which the formation of extended rod-like aggregates is expected.

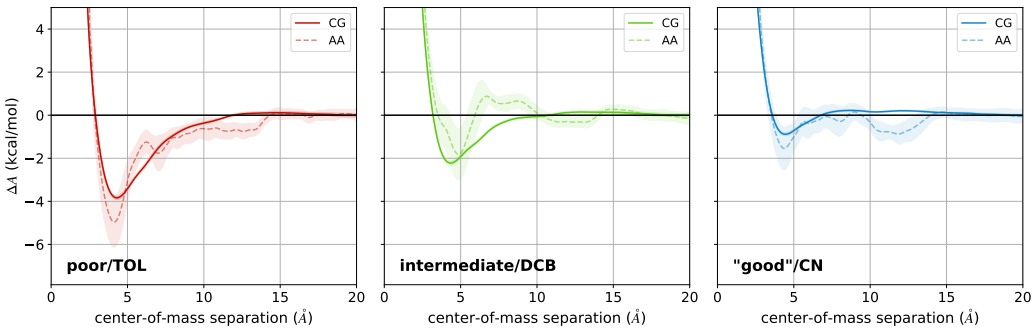

Fig. S4.15 Free energy as a function of center-of-mass separation for the interaction between two monomers of P(NDI2OD-T2) as either the AA (dashed lines) or CG (solid lines) representation. Error bars (shaded) indicate two standard errors, calculated by block averaging (they are approximately the thickness of the line for the CG curves). The poor solvent parameters were obtained by scaling the parameters obtained from AA simulations in DCB to be 20% stronger, while the good solvent parameters are 20% weaker than the DCB parameterisation.

S4.4 PROPERTIES OF THE CG P(NDI2OD-T2) POLYMER CHAIN

We have quantified the flexibility of the polymer chains with regular and flexible backbones as the Kuhn length, b, calculated from simulations of single chains of length 10, 20, or 30 monomers under "good" solvent conditions. The flexible chains, where the bonded parameters that define the flexibility (see Section S4.15) were set to 1% of the original parameters, have a Kuhn length approximately 30–40% shorter than the regular backbone (Fig. S4.16). The Kuhn length b was calculated as

$$b = \frac{\langle R_{ee}^2 \rangle}{R_{max}} \tag{4.27}$$

where R_{ee} is the end-to-end distance, measured as the distance between the centers-of-mass of the first and last monomers, and R_{max} the contour length, approximated as (14 Å)×N, where 14 Å is the approximate distance between equivalent thiophene groups of adjacent monomers and N the number of monomers in the chain.

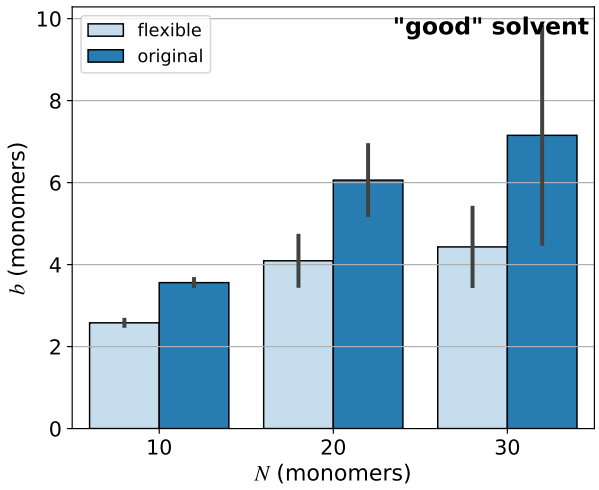

Fig. S4.16 Kuhn length b of P(NDI2OD-T2) with the flexible and regular flexibility backbone in the "good" solvent. Error bars are the standard deviation of the mean Kuhn length calculated over 1–10 μs of the 20 independent simulations for each chain length and flexibility.

S4.5 POLYMER OVERLAP VOLUME FRACTION, ϕ^*

For comparing chains of different lengths, we conducted simulations at concentrations intended to give a constant value of the ratio of ϕ_V, the polymer volume fraction, to ϕ^*, the overlap volume fraction. For an ideal chain, the overlap volume fraction, ϕ^*, is defined as

$$\phi^* = \frac{N v_{\text{mon}}}{V} \tag{4.28}$$

where N is the chain length (number of monomers), v_{mon} is the volume of a monomer, and V is the pervaded volume with $V = R^3$ where R is the size of the chain. Here we have used $R = \langle R_g^2 \rangle^{1/2}$ giving

$$\phi^* = \frac{N v_{\text{mon}}}{\langle R_g^2 \rangle^{3/2}}. \tag{4.29}$$

The radius of gyration R_g of an ideal chain is

$$\langle R_g^2 \rangle = \frac{\langle R_{ee}^2 \rangle}{6} \tag{4.30}$$

where R_{ee} is the end-to-end distance, with $\langle R_{ee}^2 \rangle \propto N$. Thus,

$$R_g \propto \sqrt{N} \tag{4.31}$$

and

$$\begin{aligned}\phi^* &\propto \frac{N}{\left(\sqrt{N}\right)^3} \\ &\propto \frac{1}{N^{1/2}}.\end{aligned} \tag{4.32}$$

Constant ϕ_V/ϕ^* is therefore equivalent to constant $\phi_V N^{1/2}$.

The volume fraction of the polymer chain ϕ_V was calculated as

$$\phi_V = c v_{mon} \tag{4.33}$$

where c is the monomer concentration.

S4.6 LIST OF COARSE-GRAINED SYSTEMS STUDIED

A variety of systems with different chain lengths N, concentration, and flexibility were used to study the effect of these properties on the aggregation behaviour of P(NDI2OD-T2). Table S4.1 summarises the conditions of each simulation, including the number of chains and box size used to achieve the target concentration, as well as the calculated coagulation time, τ_c, for each system. To examine the average behaviour of most systems, a number of systems were simulated starting from multiple independent starting configurations. The number of independent systems is given in the "replicates" column of Table S4.1.

Table S4.1 List of the multi-chain systems studied in this work. N is the length (number of monomers) of the polymer chain, and "time" the simulation time of each replicate simulation (where multiple independent simulations were run starting from different initial configurations). The entries marked with asterisks were simulated with a lower Langevin friction coefficient of 0.002 fs^{-1} (compared to 0.02 fs^{-1} for all others) to attempt to speed up the dynamics and understand the equilibrium behaviour of these systems. $\phi_V N^{1/2}$ for the different system concentrations and the number of chains packed in to a box with the given side length are also included. The aggregation time for all systems, measured as the time for the concentration of single chains to drop to 25% of the original concentration, is given in the final column. Where this value is "N/A", the single-chain concentration never dropped to below 25% the original concenration.

N	solvent	C (g/L)	flexibility	# chains	side length (Å)	$\phi_V N^{1/2}$	replicates	time (μs)	τ_c (μs)
10	poor	8.5	regular	112	600	0.014	2	1.5	0.42
20	poor	6	regular	94	800	0.014	2	4	0.69
20	poor	6	flexible	94	800	0.014	2	3	N/A
20*	poor	6	regular	94	800	0.014	2	1	0.06
20	intermediate	6	regular	94	800	0.014	2	3	1.34
20	"good"	6	regular	94	800	0.014	2	2	N/A
20*	"good"	6	regular	94	800	0.014	2	2	N/A
20	"good"	6	flexible	94	800	0.014	2	1	N/A

Continued on next page

N	solvent	C (g/L)	flexibility	# chains	side length (Å)	$\phi_V N^{1/2}$	replicates	time (μs)	τ_c (μs)
30	poor	5	regular	101	1000	0.014	2	1	0.60
10	poor	10	regular	39	400	0.016	3	2	0.32
10	poor	10	flexible	39	400	0.016	1	5	0.86
20	poor	12	regular	187	800	0.027	2	1	0.18
20	poor	2	flexible	31	800	0.0046	2	3	N/A

* Low friction system

S4.7 TIME EVOLUTION OF SHAPE ANISOTROPY

The evolution of the average shape anisotropy, $\langle\kappa^2\rangle$, over time for aggregates of various sizes in the three solvent conditions is shown in Fig. S4.17. In the poor solvent, although aggregates initially formed in a relatively disordered structure, they became more rod-like over time ($\langle\kappa^2\rangle$ increasing) as the chains "zipped up" to form aligned aggregates. This was especially notable for the smaller aggregates (consisting of 1–5, or 6–10 chains). The larger aggregates formed later in the simulation (and therefore had less time to organise), and also displayed slower dynamics, so the trends are not as clear. These longer chains are, however, expected to eventually show a similar increase in $\langle\kappa^2\rangle$ to the smaller aggregates. Note that data for large aggregates is quite sparse, as only a few aggregates of this size formed. Discontinuities in the data arise from the continuously increasing size of many aggregates, where aggregates with N_{agg} within a specific range may only exist for a finite amount of time before further aggregation pushes them to the next bracket. This becomes particularly noticeable for intermediate to large aggregate size, where only a few aggregates of this size typically form.

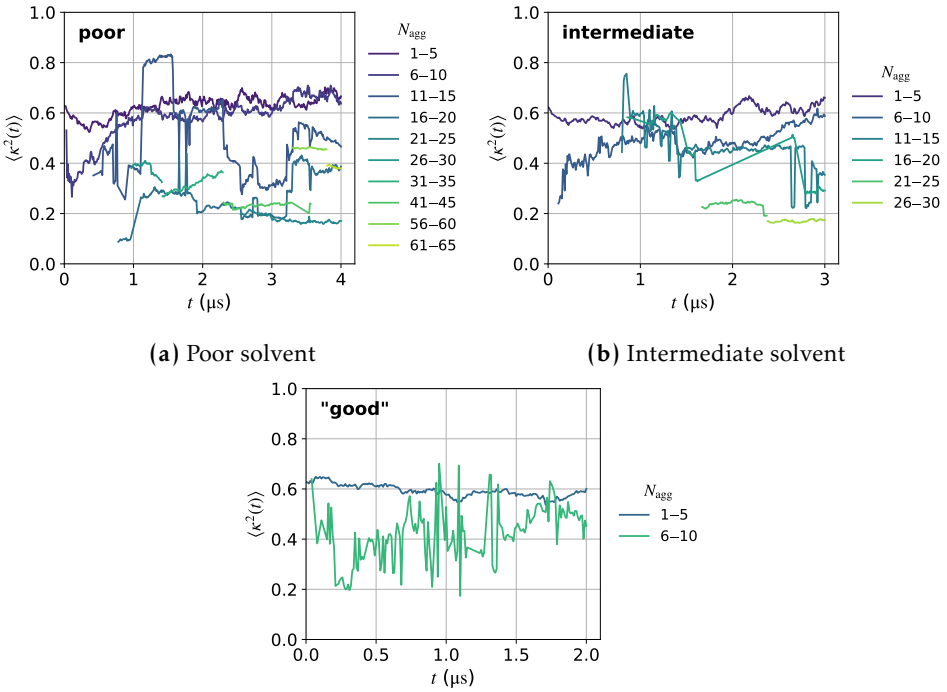

(a) Poor solvent **(b)** Intermediate solvent

(c) "Good" solvent

Fig. S4.17 Evolution of the average shape anisotropy $\langle\kappa^2\rangle$ for aggregates of regular flexibility 20mers (6 g/L) in (a) poor, (b) intermediate, and (c) "good" solvent conditions. $\kappa^2 = 1$ corresponds to a rod-like structure, and $\kappa^2 = 0$ to a sphere. To make the plots clearer, data has been combined for aggregates made up of 1–5, 6–10, etc. chains.

S4.8 CHAIN LENGTH AND CONCENTRATION DEPENDENCE OF AGGREGATION PROPERTIES

The effect of chain length and concentration on the evolution of aggregate size and structure over time is shown in Figs. S4.18 and S4.19. The rate of aggregate growth appears to be roughly independent of chain length, particularly at early time (Fig. S4.18a), indicating that the choice of constant $\phi_V N^{1/2}$ is a reasonable way to compare systems with different chain lengths. The number of overlaps between aggregated chains appears to decrease slightly for the 20 and 30mers (Fig. S4.19a).

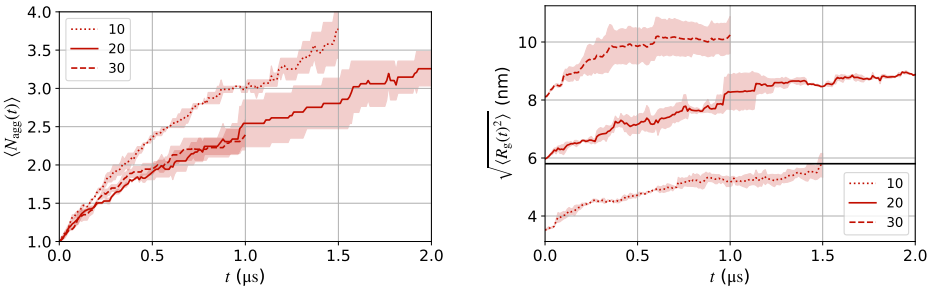

(a) Average aggregate size

(b) Radius of gyration

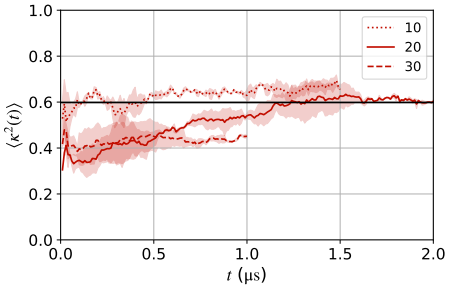

(c) Shape anisotropy

Fig. S4.18 Dependence of (a) average aggregate size (b) root-mean squared (RMS) radius of gyration, and (c) shape anisotropy on polymer chain length under poor solvent conditions. All systems were at the same $\phi_V N^{1/2}$ where ϕ_V is the polymer volume fraction and N the chain length. Only the first 2 μs are shown. Horizontal black lines in (b) and (c) indicate the R_g and κ^2, respectively, of a single 20mer in good solvent for reference.

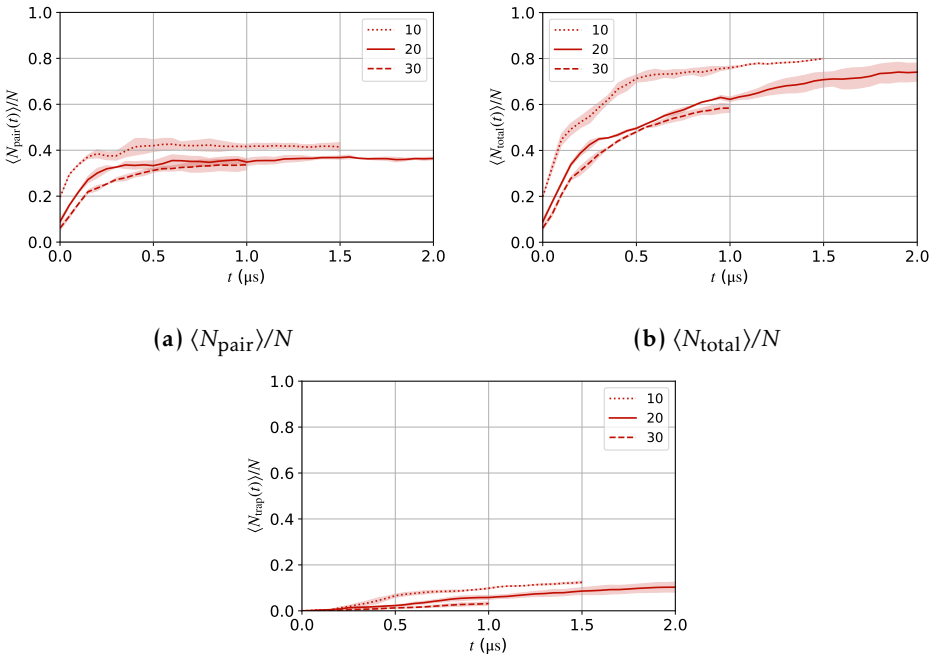

(a) $\langle N_{\text{pair}} \rangle / N$

(b) $\langle N_{\text{total}} \rangle / N$

(c) $\langle N_{\text{trap}} \rangle / N$

Fig. S4.19 Dependence of (a) $\langle N_{\text{pair}} \rangle / N$, (b) $\langle N_{\text{total}} \rangle / N$, and (c) $\langle N_{\text{trap}} \rangle / N$ on chain length in the poor solvent. Again, all systems are at the same $\phi_{\text{V}} N^{1/2}$ and only the first 2 μs are shown.

S4.9 SINGLE-CHAIN FOLDING KINETICS

s4.9.1 INTERMEDIATE- AND LATE-TIME 2D HISTOGRAMS OF SINGLE-CHAIN BEHAVIOUR

The distribution of single chain structures at intermediate (4.5–5.5 μs) and late (9–10 μs) times (early time given in the main text) in the poor solvent are shown in Fig. S4.20. This highlights that the flexible chains fold more readily than the chains with regular flexibility. A variety of structures were observed, corresponding to extended coils (high R_g, high κ^2), hairpins/racquets (lower R_g, high κ^2), and toroids (lower R_g, lower κ^2). At late time, toroid structures appear to be generally favoured for the flexible backbones, especially the shorter chains, while both hairpins and toroids were common for the regular flexibility backbones and the longer flexible chains.

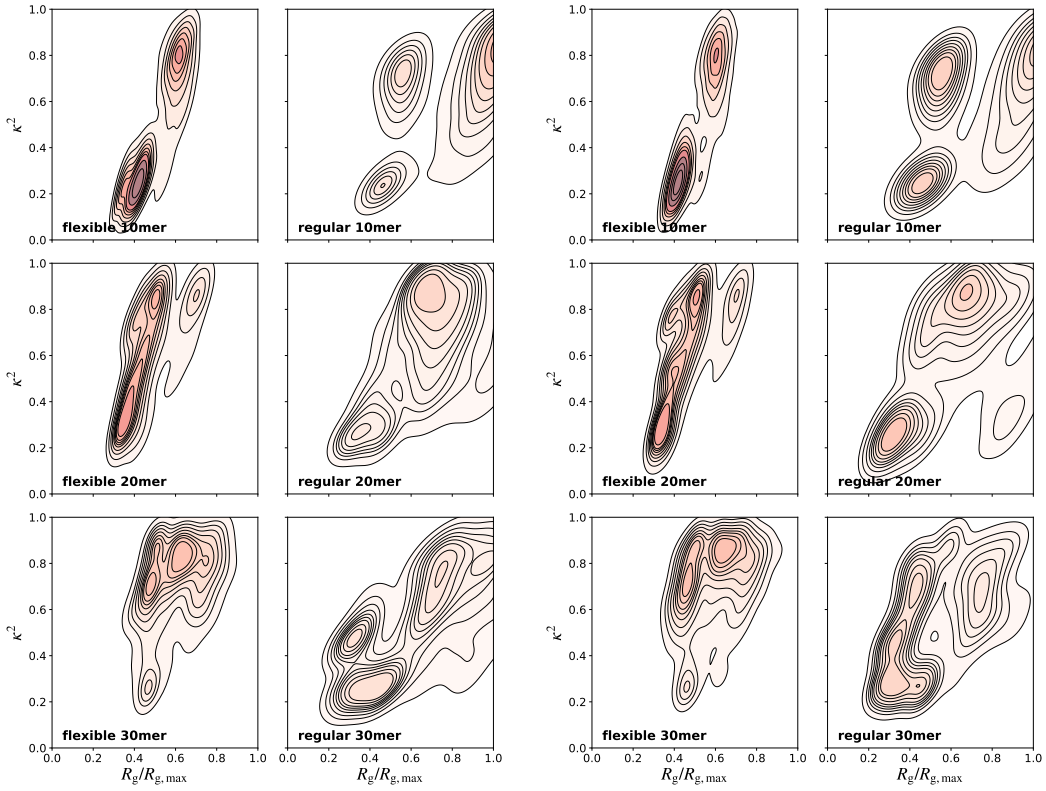

(a) 4.5–5.5 μs **(b)** 9–10 μs

Fig. S4.20 2D histograms of the radius of gyration, R_g, and shape anisotropy, κ^2, for 20 independent simulations of various chain lengths in poor solvent conditions. Early time distributions (0.5–1 μs) can be found in the main text (Fig. 4.7). The R_g is normalised by $R_{g,max}$, the R_g of a fully extended rod, with $R_g^2 = L^2/12$[127] and $L = 1.4$ nm per monomer. The colour scale is the same for all plots, with darker colours corresponding to higher probability.

S4.9.2 DETERMINING TIME CONSTANT FOR FOLDING OF SINGLE-CHAINS.

As described in the main text, the approximate timescale for single-chain folding was determined from fit of the mean-squared R_g, averaged over the 20 independent single-chain simulations, to a exponential function (eqn (4.9)). The plots of the decay in $\langle R_g^2 \rangle$ over time for each set of systems (varying chain length, solvent quality, and flexibility) and the lines of best fit are given in Fig. S4.21 for the low viscosity systems ($\gamma = 0.002$ fs^{-1}), and in Fig. S4.22 for the systems with regular viscosity ($\gamma = 0.02$ fs^{-1}).

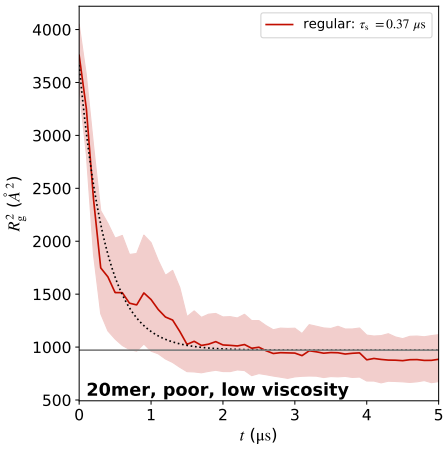

Fig. S4.21 Decay of mean-squared radius of gyration over time for single-chains of P(NDI2OD-T2) with regular flexibility backbone of length 20 in poor solvent with friction coefficient 1/10× that of the other simulations. Shaded regions indicating the 95 % confidence intervals calculated over 20 independent simulations. Dotted line is the fit of eqn (4.9) to the simulation data used to determine τ_s. Fit parameters are given in Table 4.2 of the main text. The horizontal grey line indicates the value of $R^2_{g,min}$ calculated from the fitting procedure.

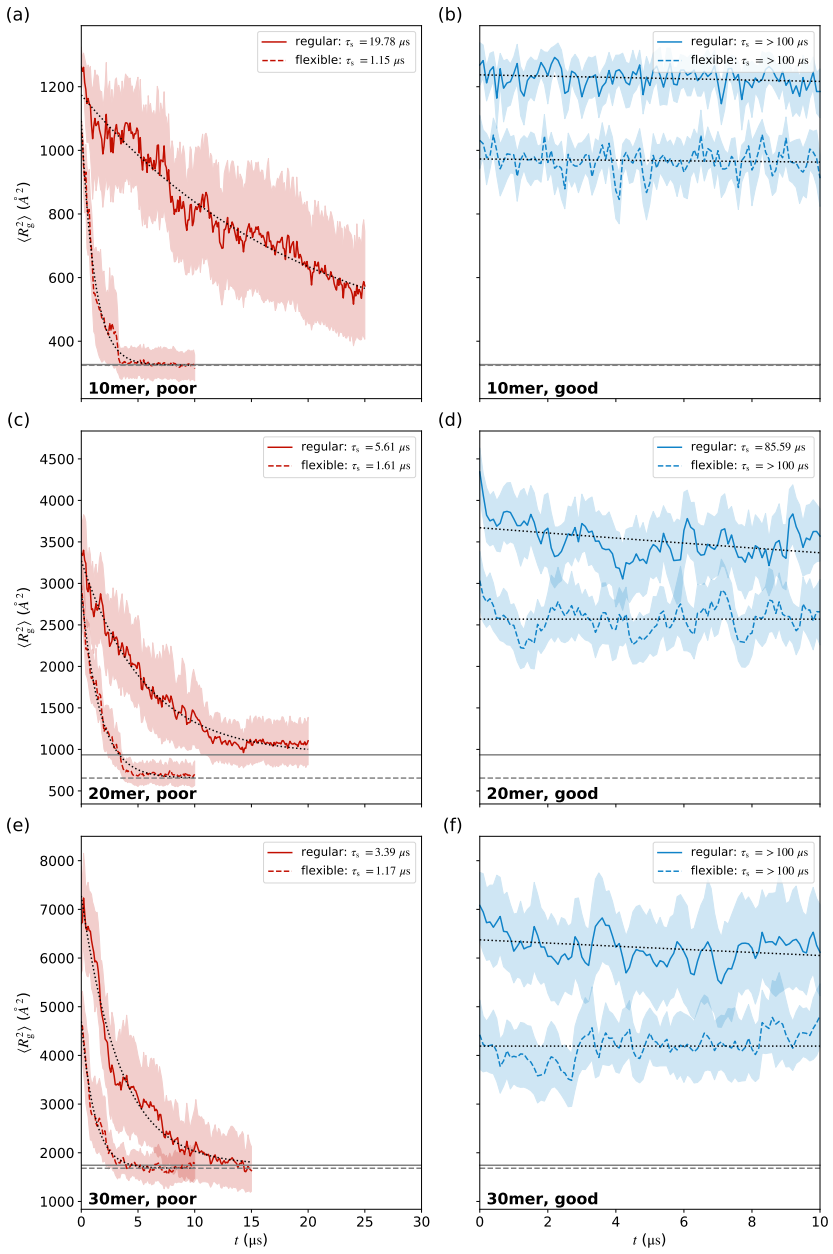

Fig. S4.22 Decay of mean-squared radius of gyration over time for single-chains of length 10 (a,b), 20 (c,d), and 30 (e,f) with parameters are representative of being immersed in a poor (a,c,e) or better (b,d,f) solvent with regular (solid lines) or flexible (dashed lines) backbones. Coloured shaded regions indicating the 95 % confidence intervals calculated over 20 independent simulations. Dotted lines are the fits of eqn (4.9) to the simulation data used to determine the single-chain folding time, τ_s. Fit parameters are given in Table 4.2 of the main text. Grey lines indicate the value of $R^2_{g,min}$ calculated from the fitting procedure (dashed line for flexible, and solid line for regular backbone). The values of $R^2_{g,min}$ for the good solvent fits were fixed as the values for the corresponding flexibility backbone in the poor solvent.

S4.9.3 SCALING OF FOLDING RATE WITH CHAIN LENGTH

The rate of single-chain folding for semiflexible polymers has been previously shown to scale with $N^{1/3}$ for chains of length N.[138] We have fit the folding rate (calculated as $1/\tau_s$ where τ_s is calculated from the fit to the single chain folding data in Fig. S4.22) to an equation of the form $1/\tau_s = aN^{1/3} + b$ and found that this scaling accurately describes the behaviour of the regular flexibility backbones (Fig. S4.23). The fitting parameter b shifts the x-intercept of the plot to higher N (here $N \approx 7.5$), which is consistent with single-chains not folding ($\tau_s \to \infty$ and so $1/\tau_s \to 0$) for chains with length on the order of a single Kuhn length (approx 6–8 monomers for the model here).

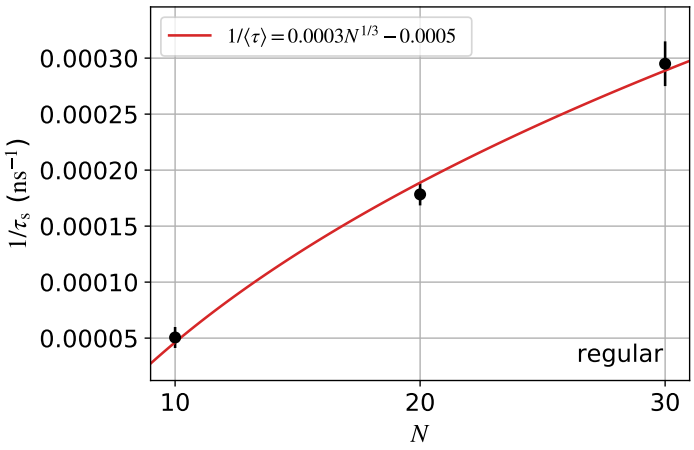

Fig. S4.23 Scaling of folding rate $1/\tau_s$ with $N^{1/3}$ for the single chain simulations with regular flexibility backbone in poor solvent. Error bars are two standard deviations from the estimate of the fit parameter τ_s.

S4.10 SCALING OF KINETICS OF MULTI-CHAIN AGGREGATION VS SINGLE-CHAIN COLLAPSE

The derivation of the scaling relationships for the crossover concentration with chain length, and a correction for hydrodynamic interactions, is given below.

SINGLE-CHAIN FOLDING, τ_s

Consider a system of polymer chains of degree of polymerisation N and chain concentration C (monomer concentration $c = NC$) transferred from a good to a poor solvent at time $t = 0$. Assume that the time scale for single-chain folding collapse

follows the scaling

$$\tau_s = \frac{L_0^2}{D_0} N^{\alpha} \tag{4.34}$$

where D_0 is the monomer diffusion coefficient, L_0 some length scale, and α a scaling exponent. Based on previous work,[138] and the simulations here of single-chain folding (Fig. S4.23), $\alpha = -\frac{1}{3}$. Examination of the single-chain folding rate with Langevin friction coefficient (where Langevin friction coefficient $\propto \frac{1}{D_0}$; Fig. S4.21) shows the expected[285] $\tau_s \propto \frac{1}{D_0}$ scaling.

multi-chain aggregation, τ_c

Let's assume that multi-chain aggregation is diffusion limited and occurs via binary collisions between spherical aggregates, with the radius and diffusion coefficient of an aggregate of i chains R_i and D_i respectively (note that the effect of chain collapse on R_i is ignored). The kinetics of aggregation is governed by a series of kinetic equations for the concentration C_i of aggregates of size i:[188]

$$\frac{dC_i}{dt} = \frac{1}{2}\sum_{j=1}^{i-1} K_{j,i-j} C_j C_{i-j} - \sum_{j=1}^{\infty} K_{i,j} C_i C_j, \quad i \geq 2 \tag{4.35}$$

$$\frac{dC_1}{dt} = -\sum_{j=1}^{\infty} K_{1,j} C_1 C_j \tag{4.36}$$

where (see ref 287), assuming all collisions lead to aggregation,

$$K_{i,j} = 4\pi(D_i + D_j)(R_i + R_j)\left[1 + \frac{(R_i + R_j)}{\sqrt{\pi(D_i + D_j)t}}\right] \tag{4.37}$$

Note that the derivation of this equation assumes that there are particles in the system that are initially separated by more than $(R_i + R_j)$, since aggregation occurs when particles reach a separation of $(R_i + R_j)$. Above the overlap concentration, all particles will on average be separated from their nearest neighbours by less than this distance, so aggregation will be instantaneous (the coagulation time will be zero), and so the crossover concentration becomes ill-defined.

Eqns 4.35–4.37 are typically solved ignoring the time-dependent term in eqn 4.37, for which analytical solutions exist in some cases (e.g. constant $K_{i,j} = K$). But this term can only be ignored if

$$\frac{(R_i + R_j)}{\sqrt{\pi(D_i + D_j)t}} \ll 1 \tag{4.38}$$

i.e.

$$t \gg \frac{(R_i + R_j)^2}{\pi(D_i + D_j)} \tag{4.39}$$

Comparing an estimate of this time scale using the RMS radius of gyration and diffusion coefficient from the simulations of single chains in the "good" solvent with the aggregation time from multi-chain simulations, this condition does not appear to hold, and, in fact, the time-independent part of eqn (4.37) appears negligible for large N (see Table S4.2; here, $R_i = R_j = R_1$, $D_i = D_j = D_1$, and so $\frac{(R_i+R_j)^2}{\pi(D_i+D_j)} = \frac{2R_1^2}{\pi D_1}$, and we take $R_1 \approx R_g(t = 0)$ from simulations of single chains).

Table S4.2 Properties of single-chain diffusion and aggregation, compared to the multi-chain aggregation time, all measured in poor solvent with viscosity corresponding to implicit DCB. D_1 and R_1 are the diffusion coefficient and size of a single polymer chain of length N, and τ_c the coagulation time, measured as the time for the concentration of single chains to drop to 25% of the initial concentration. All data is for the chains with regular backbone flexibility, and the multi-chain simulations at the concentrations that gave constant $\phi_V N^{1/2}$.

N	D_1 (Å^2/ns)	R_1^2 (Å^2)	$2R_1^2/\pi D_1$ (μs)	τ_c (μs)
10	1.23	1200	0.6	0.42
20	0.85	3400	2.5	0.69
30	0.47	8000	11	0.60

In all cases, coagulation occurs on a shorter timescale (and much shorter for $N \geq 20$) than for which $K_{i,j}$ is constant. Furthermore, we are interested in the conditions for which $\tau_s \approx \tau_c$. As τ_s decreases with increasing N, we expect the time-dependant part of $K_{i,j}$ to be come dominant for larger N.

Unfortunately, we cannot solve eqns (4.35)–(4.37) in this case, so we just consider the reaction of single chains to form aggregates of size 2, which should accurately approximate the kinetics at short enough times when the population of larger aggregates is small. In this case, eqns (4.35) and (4.36) become (with $K \equiv K_{1,1}$)

$$\frac{dC_1}{dt} = -KC_1^2 \tag{4.40}$$

$$\frac{dC_2}{dt} = KC_1^2 \tag{4.41}$$

and eqn (4.37) becomes (with $R \equiv R_1$ and $D \equiv D_1$)

$$\begin{aligned} K = K_{1,1} &= 16\pi DR\left(1 + \frac{\sqrt{2}R}{\sqrt{\pi Dt}}\right) \\ &\equiv A + Bt^{-1/2} \end{aligned} \tag{4.42}$$

where

$$A = 16\pi DR \tag{4.43}$$

and

$$B = 16\sqrt{2\pi}D^{1/2}R^2 \tag{4.44}$$

Combining eqns (4.40) and (4.42):

$$\frac{\mathrm{d}C_1}{\mathrm{d}t} = -(A + Bt^{-1/2})C_1 \tag{4.45}$$

which can be solved with initial condition $C_1(0) = C$ to give

$$\frac{1}{C_1(t)} = \frac{1}{C} + At + 2Bt^{1/2} \tag{4.46}$$

Defining the characteristic coagulation time τ_c as the time for the concentration of single chains to fall to a fraction x of the initial concentration, i.e.

$$C_1(\tau_c) = x\frac{c}{N} \tag{4.47}$$

then inserting eqn (4.47) into eqn (4.46) and rearranging gives

$$0 = A\tau_c + 2B\tau_c^{1/2} + \left(\frac{x-1}{x}\right)\frac{N}{c} \tag{4.48}$$

which has the general solution

$$\tau_c = \frac{2B^2 - AG \pm 2\sqrt{B^4 - AB^2G}}{A^2} \tag{4.49}$$

where

$$G \equiv \left(\frac{x-1}{x}\right)\frac{N}{c}. \tag{4.50}$$

We will restrict ourselves to two cases:

1. $A\tau_c \gg 2B\tau_c^{1/2}$
2. $A\tau_c \ll 2B\tau_c^{1/2}$

noting that case 2 appears to correspond to the conditions in this work.

Case 1: $A\tau_c \gg 2B\tau_c^{1/2}$

Under these conditions, eqn (4.48) becomes

$$\tau_c = -\frac{G}{A} = \frac{N}{Ac}\left(\frac{1-x}{x}\right) \tag{4.51}$$

Inserting the definition of A from eqn (4.43) gives

$$\tau_c = \frac{1}{16\pi DR}\left(\frac{1-x}{x}\right)\frac{N}{c} \tag{4.52}$$

If we assume

$$D = D_0 N^{\beta} \tag{4.53}$$

and

$$R = R_0 N^{\nu} \tag{4.54}$$

$$\tag{4.55}$$

then

$$\tau_c = \frac{1}{16\pi D_0 R_0}\left(\frac{1-x}{x}\right)\frac{N^{(1-\beta-\nu)}}{c} \propto \frac{N^{(1-\beta-\nu)}}{c} \tag{4.56}$$

Defining the critical monomer concentration, $c^{\dagger}$, as c where $\tau_c = \tau_s$, combining eqns (4.56) and (4.34) gives

$$c^{\dagger} = \frac{1}{16\pi R_0 L_0^2}\left(\frac{1-x}{x}\right)N^{(1-\alpha-\beta-\nu)} \propto N^{(1-\alpha-\beta-\nu)} \tag{4.57}$$

Case 2: $A\tau_c \ll 2B\tau_c^{1/2}$

Under the conditions corresponding to case 2, eqn (4.48) gives

$$\tau_c = \frac{N^2}{4B^2c^2}\left(\frac{1-x}{x}\right)^2 \tag{4.58}$$

Insterting the definition of B from eqn (4.44):

$$\tau_c = \frac{1}{2^{11}\pi DR^4}\left(\frac{1-x}{x}\right)^2\frac{N^2}{c^2} \tag{4.59}$$

Using eqns (4.53) and (4.54)

$$\tau_c = \frac{1}{2^{11}\pi D_0 R_0}\left(\frac{1-x}{x}\right)^2\frac{N^{(2-\beta-4\nu)}}{c^2} \propto \frac{N^{(2-\beta-4\nu)}}{c^2} \tag{4.60}$$

Again defining the critical monomer concentration, $c^{\dagger}$, where $\tau_c = \tau_s$, combining eqns (4.60) and (4.34) gives

$$c^{\dagger} = \frac{1}{(2^{11}\pi R_0)^{1/2}L_0}\left(\frac{1-x}{x}\right)N^{(1-\alpha/2-\beta/2-2\nu)} \propto N^{(1-\alpha/2-\beta/2-2\nu)} \tag{4.61}$$

The scaling of $c^{\dagger}$ with N is therefore quite different in cases 1 (eqn (4.61)) and 2 (eqn (4.57)).

Comparison of scaling

As described above, from both the literature[138] and the simulations in this work, $\alpha \approx -1/3$. Given no hydrodynamic interactions in the Langevin dynamics simulations, $\beta = -1$. Assuming polymer conformation (initially) corresponds to a good solvent, $\nu \approx 0.6$. With these exponents, from eqns (4.57) in case 1 and (4.61) in case 2:

$$\textbf{Case 1:} \quad c^{\dagger} \propto N^{(1-\alpha-\beta-\nu)} = N^{(1+1/3+1-0.6)} = N^{1.73} \tag{4.62}$$

$$\textbf{Case 2:} \quad c^{\dagger} \propto N^{(1-\alpha/2-\beta/2-2\nu)} = N^{(1+1/6+1/2-2\times 0.6)} = N^{0.46} \tag{4.63}$$

Note that case 2 corresponds to the time-scale regime of the simulation in which the time-dependent part of the coagulation rate coefficient dominates.

CALCULATION OF $c^{\dagger}$

To determine $c^{\dagger}$ from Langevin dynamics simulations for case 2 (which is the case for the simulations conducted in this work), the fraction x of single unaggregated chains in solution used to define the coagulation time was chosen to be $x = 0.25$. This value is kept fixed for all the analysis. From eqn (4.60)

$$\tau_{\mathrm{c}} = \frac{f(N)}{c^2} \tag{4.64}$$

where $f(N)$ is a function of N that depends on the simulation system properties and conditions but not on c. From τ_{c} and c measured in the simulation, $f(N)$ for each chain length N simulated can be determined. Then, setting $\tau_{\mathrm{c}} = \tau_{\mathrm{s}}$, where τ_{s} is the single-chain collapse time measured in the simulation , $c^{\dagger}$ for each N simulated can be determined as

$$c^{\dagger}(N) = \left(\frac{f(N)}{\tau_{\mathrm{s}}}\right)^{1/2} \tag{4.65}$$

CORRECTING THE SCALING FOR HYDRODYNAMIC INTERACTIONS

The simulations in this work used Langevin dynamics, in which hydrodynamic interactions (HI) are ignored. The scaling relationships in eqns (4.62) and (4.63) therefore need to be corrected to account for the effect of hydrodynamic interactions. From ref 288, the Kirkwood formula[289] for the translational diffusion coefficient of a polymer of degree of polymerisation N is

$$D = \frac{D_0}{N} + \frac{k_{\mathrm{B}}T}{6\pi\eta}\left\langle\frac{1}{R_{\mathrm{H}}}\right\rangle \tag{4.66}$$

where D_0 is the monomer diffusion coefficient and R_{H} the hydrodynamic radius, with

$$\left\langle\frac{1}{R_{\mathrm{H}}}\right\rangle = \frac{1}{N^2}\sum_{i\neq j}\left\langle\frac{1}{r_{\mathrm{ij}}}\right\rangle \tag{4.67}$$

where r_{ij} is the distance between monomers i and j.

From Zimm theory (see e.g. refs 127, 290)

$$\frac{k_B T}{6\pi\eta}\left\langle\frac{1}{R_H}\right\rangle = \frac{D_0^*}{N^\nu} \tag{4.68}$$

where ν is the scaling exponent for polymer size, and D_0^* is the segmental diffusion coefficient, which is expected to be similar to the monomer diffusion coefficient D_0. Assuming $D_0^* \approx D_0$, and combining eqns (4.68) and (4.66):

$$D \approx D_0\left(\frac{1}{N} + \frac{1}{N^\nu}\right) \tag{4.69}$$

Note that eqn (4.69) is incorrect for $N = 1$, but should be reasonably accurate for $N \gg 1$.

Since the scaling of the τ_c and $c^\dagger$ involves D in the denominator (see eqns (4.56), (4.60)), which contributes a scaling of $c^\dagger$ with $N^{-\beta}$ for case 1 and $N^{-\beta/2}$ for case 2, correcting the $c^\dagger$ for $\beta = -1$ from Langevin dynamics simulations involves multiplying $c^\dagger$ calculated from the simulations by

$$\textbf{Case 1:}\quad \frac{1}{N}\left(\frac{1}{N} + \frac{1}{N^\nu}\right)^{-1} = \frac{N^\nu}{N + N^\nu} \tag{4.70}$$

$$\textbf{Case 2:}\quad \frac{1}{N^{1/2}}\left(\frac{1}{N} + \frac{1}{N^\nu}\right)^{-1/2} = \left(\frac{N^\nu}{N + N^\nu}\right)^{1/2} \tag{4.71}$$

From eqn. (4.61) we expect $c^\dagger(N)$ from the Langevin dynamics simulation to have the form

$$c^\dagger_{\text{noHI}}(N) = \bar{c}_0 N^\lambda \tag{4.72}$$

where "noHI" denotes the absence of hydrodynamic interactions, $\bar{c}_0$ is a constant (which depends on the system type, but not on concentration or N) and λ is a scaling exponent. To correct this relationship for hydrodynamic interactions, we multiply eqn. (4.72) by eqn. (4.71) (for case 2):

$$c^\dagger_{\text{HI}}(N) \approx \bar{c}_0 N^\lambda \left(\frac{N^\nu}{N + N^\nu}\right)^{1/2} \tag{4.73}$$

For $N \gg 1$ and $\nu < 1$:

$$c^\dagger_{\text{HI}}(N) \to \bar{c}_0 N^{\lambda + \frac{1}{2}(\nu - 1)} \tag{4.74}$$

So given values of $\bar{c}_0$ and λ from fitting the data for $c^\dagger$ vs N without hydrodynamic interactions, and assuming a value of ν (e.g. 0.6 for a good solvent), $c^\dagger$ with hydrodynamic interactions can be predicted using eqn (4.74) for $N \gg 1$.

S4.11 CONCENTRATION EFFECTS

S4.11.1 EFFECT OF CONCENTRATION ON AGGREGATE SIZE

The effect of concentration on the average aggregate size was examined by comparing three sets of simulations with the same chain length and properties, but different concentrations: regular flexibility 10mers at 8.5 and 10 g/L, regular flexibility 20mers at 6 and 12 g/L, and flexible 20mers at 2 and 6 g/L. More rapid aggregate growth, and the formation of larger aggregates, was observed at higher concentration. Comparing the 6 and 12 g/L simulations, τ_c is approx. 4× faster at the higher concentration (see Table S4.1), consistent with the predicted $1/c^2$ scaling from the theory (eqn. (4.60)).

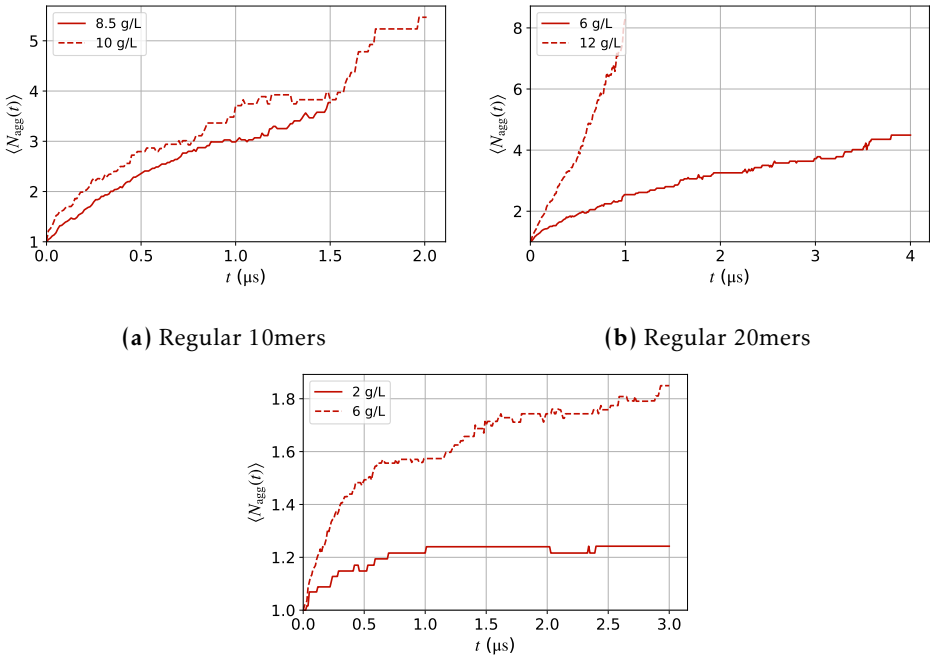

(a) Regular 10mers

(b) Regular 20mers

(c) Flexible 20mers

Fig. S4.24 Average aggregate size (number of chains) versus time at different concentrations for different chain lengths and flexibilities. Higher concentrations (dashed lines) give more rapid aggregate growth and overall larger aggregates.

S4.11.2 EFFECT OF FLEXIBILITY ON CRITICAL CONCENTRATION

The critical concentration $c^\dagger$ was calculated from simulations of multiple chain lengths, at different concentrations, and for polymers with different flexibility. While the results for the regular flexibility backbones are presented in the main text, Fig. 4.8, the effect of chain flexibility was not presented. An additional data point

from the more flexible chains is shown in Fig. S4.25, as well as a breakdown of the original flexibility points into the concentration of the multi-chain simulations.

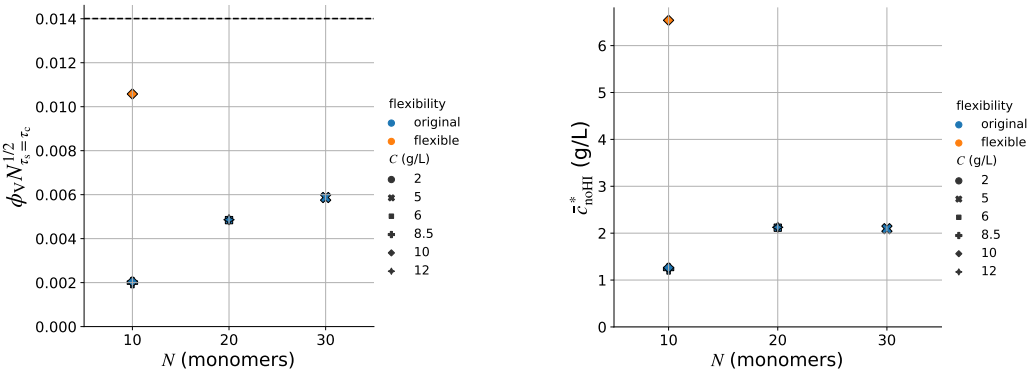

(a) Volume fraction relative to overlap concentration

(b) Concentration

Fig. S4.25 Scaling of the concentration where $\tau_s = \tau_c$ with chain length N, presented as either (a) $\phi_V N^{1/2}$ or (b) concentration (g/L). The points corresponding to different concentrations were calculated using the coagulation time from multi-chain simulations at the labelled concentration. The horizontal dashed line in (a) indicates the value of $\phi_V N^{1/2}$ used for the majority of simulations in this work. Systems at concentrations below the points on these plots are expected to favour single-chain folding, while higher concentrations should lead to more prominent multi-chain aggregation.

The majority of simulations in this work were conducted at concentrations higher than $c^\dagger$ ($\phi_V N^{1/2}$ given by dashed black line in Fig. S4.25a), though the flexible chain simulations approached, or dropped below, this critical concentration. Accordingly, although all simulations in poor solvents showed some degree of multi-chain aggregation, there was substantially less in the case of flexible chains. The scaling of this critical concentration with chain length N is discussed in the main text, and can explain the conflicting behaviour in the two published experimental studies.[22,25] We also examined one system at a concentration expected to be well below the critical concentration for the flexible 20mers in poor solvent (2 g/L). Although this system initially still showed a small amount of aggregation, due to random placement of chains in the box resulting in chains that were close enough to aggregate before they folded, there was significantly less multi-chain aggregation observed in this case, and almost none after the initial aggregation (Fig. S4.24c).

S4.12 EFFECT OF VISCOSITY ON MULTI-CHAIN AGGREGATION

As the experimental viscosity of DCB and TOL differ significantly,[284] it is important to consider the effect of this parameter on the single- and multi-chain behaviour of the CG model. The effect of this change in viscosity on the multi-chain aggregation properties is shown in Figs. S4.26 and S4.27. τ_c in the low viscosity solvent is approx. 10× faster than in implicit DCB (0.06 vs 0.7 µs, calculated as the time for the single-chain concentration to fall below 25% its original concentration). This scaling is consistent with the 10× smaller friction coefficient for the low viscosity solvent.

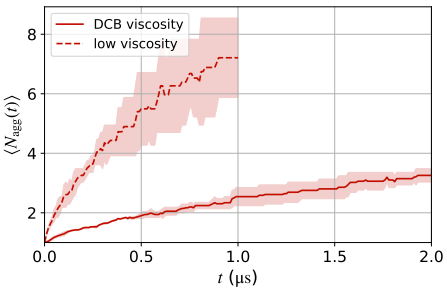

(a) Average aggregate size

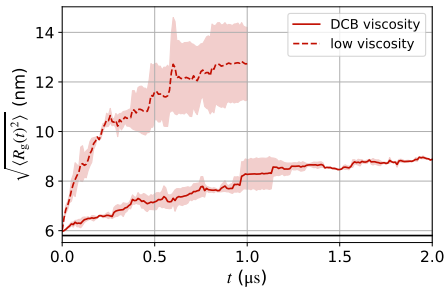

(b) Radius of gyration

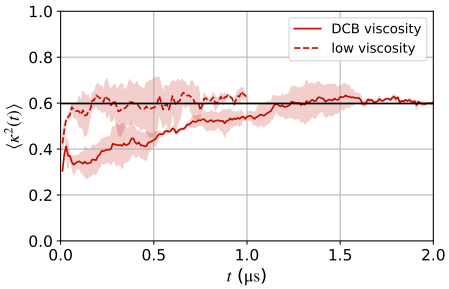

(c) Shape anisotropy

Fig. S4.26 (a) Average aggregate size (b) RMS radius of gyration, and (c) average shape anisotropy as a function of time for different solvent viscosities under poor solvent conditions. Horizontal black lines in (b) and (c) indicate the R_g and κ^2 respectively of a single 20mer in good solvent for reference.

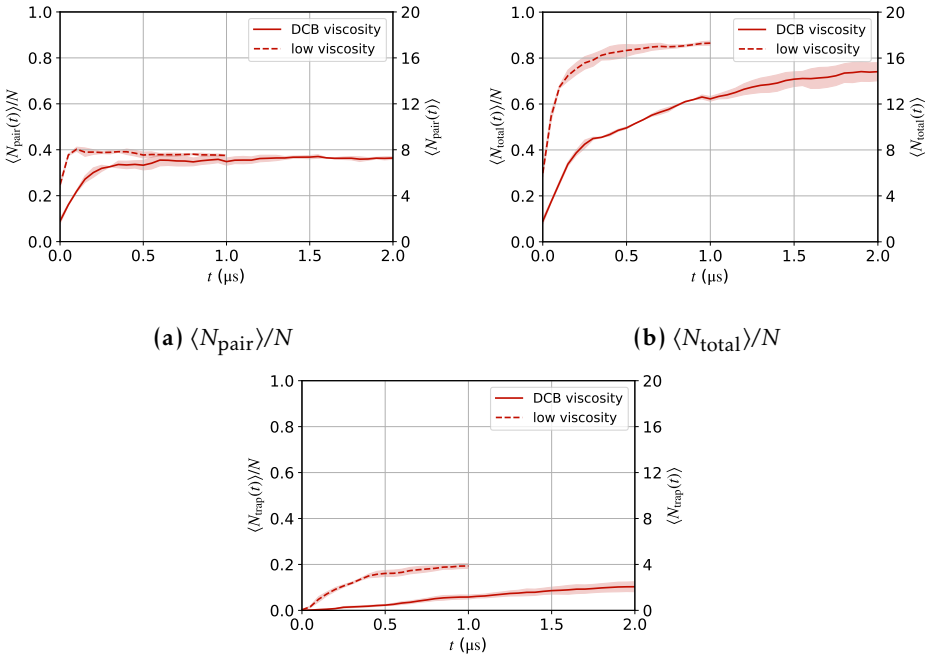

(a) $\langle N_{\mathrm{pair}}\rangle/N$ **(b)** $\langle N_{\mathrm{total}}\rangle/N$

(c) $\langle N_{\mathrm{trap}}\rangle/N$

Fig. S4.27 (a) $\langle N_{\mathrm{pair}}\rangle/N$, (b) $\langle N_{\mathrm{total}}\rangle/N$, and (c) $\langle N_{\mathrm{trap}}\rangle/N$ as a function of time for different solvent viscosities under poor solvent conditions.

S4.13 BACKBONE FLEXIBILITY

S4.13.1 EFFECT OF OVERLAPS AND BACKBONE FLEXIBILITY ON KUHN LENGTH AND BENDING RIGIDITY

The effect of backbone aggregation on chain flexibility is discussed briefly in the main text. Fully overlapping chains were shown to increase the overall rigidity of the aggregate backbone, with a 3–5-fold increase in Kuhn length observed on going from a single free chain to an aggregated pair, even on transitioning from a good to a poor solvent. The Kuhn length and bending rigidity for the single-chain systems not listed in the main text, and for a fully overlapping aggregate of flexible chains in poor solvent, are given in Table S4.3.

Table S4.3 Kuhn length, b (Å or number of monomers), and bending rigidity, κ_b, for 30mers with different backbone and solvent conditions. Where b is given as a number of monomers, each monomer was assumed to be 14 Å long. Systems labelled "aggregated" are from a single 1 μs simulation of two fully overlapping 30mers, with listed values averaged over the final 100 ns for each chain in the aggregate pair. The single chain simulations (labelled "single") use data from the same 10–15 μs single-chain simulations described previously, using the values averaged over the 0.9–1 μs period in each of the 20 independent simulations.

flexibility	solvent	system	b (Å)	b (monomers)	κ_b (kcal/mol.Å)
flexible	poor	single	24.04	1.72	7.16
flexible	poor	aggregated	287.28	20.52	85.63
regular	poor	single	107.29	7.66	31.98
regular	poor	aggregated	279.91	20.00	83.44
flexible	good	single chain	57.04	4.07	17.00
regular	good	single chain	100.17	7.15	29.86

S4.13.2 EFFECT OF BACKBONE FLEXIBILITY ON CHAIN OVERLAPS

The effect of backbone flexibility on some of the properties defining the aggregate structure of P(NDI2OD-T2) in both good and poor solvents is shown below. The overall aggregate size (in terms of number of monomers and R_g) is given in the main text Fig. 4.9, and chain overlap fractions (N_{pair}/N, N_{total}/N, and N_{trap}/N) are shown in Fig. S4.28. For the poor solvent, a similar degree of overlap was observed for aggregated chains with the flexible and regular backbones. This indicates that, although less aggregation was observed overall (Fig. 4.9), where aggregation did occur, it was in a similar manner to the regular backbone, with partially overlapping chains. Overall, some chain collapse prior to aggregation, as observed for flexible

chains, resulting in less aggregation and an overall lower R_g (due to collapse of either single chains or partially overlapping aggregates), though the initial aggregation process followed a similar path for both backbones, giving partially overlapping chains with $N_{pair}/N \approx 0.4$ in the poor solvent. The difference was more prominent in the good solvent, in which aggregation did not initially occur irreversibly as it did in the poor solvent. The more compact chains formed with the flexible backbones resulted in both less aggregation and fewer overlaps in the good solvent compared with the same system with the stiffer backbone. These chains were able to collapse more prior to extensive aggregation, with R_g^2 of the single flexible chains being approximately 60% of the regular ones in the good solvent.

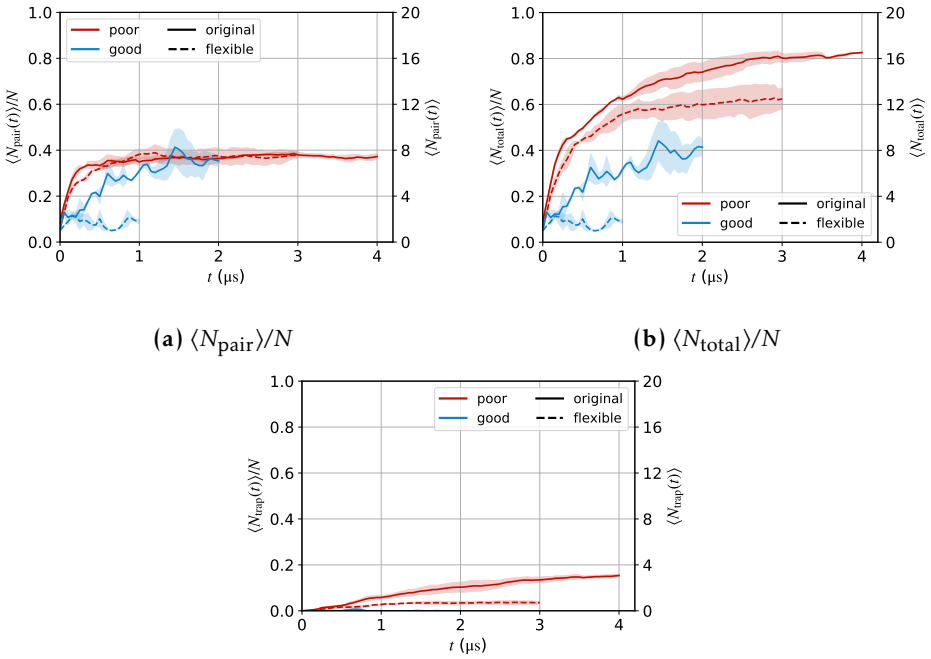

(a) $\langle N_{pair}\rangle/N$

(b) $\langle N_{total}\rangle/N$

(c) $\langle N_{trap}\rangle/N$

Fig. S4.28 (a) $\langle N_{pair}\rangle/N$, (b) $\langle N_{total}\rangle/N$, and (c) $\langle N_{trap}\rangle/N$ as a function of time for different backbone flexibilities of 20mers at 6 g/L for good and poor solvent conditions.

S4.14 ALL-ATOM PARAMETERS

The all-atom parameters for the symmetric P(NDI2OD-T2) model are reproduced below. The atom and bond types are defined in Fig. S4.29. Where parameters were not parameterised explicitly (for the side-chains for example), they were taken directly from the OPLS force field for equivalent atom types.[202,268–273]

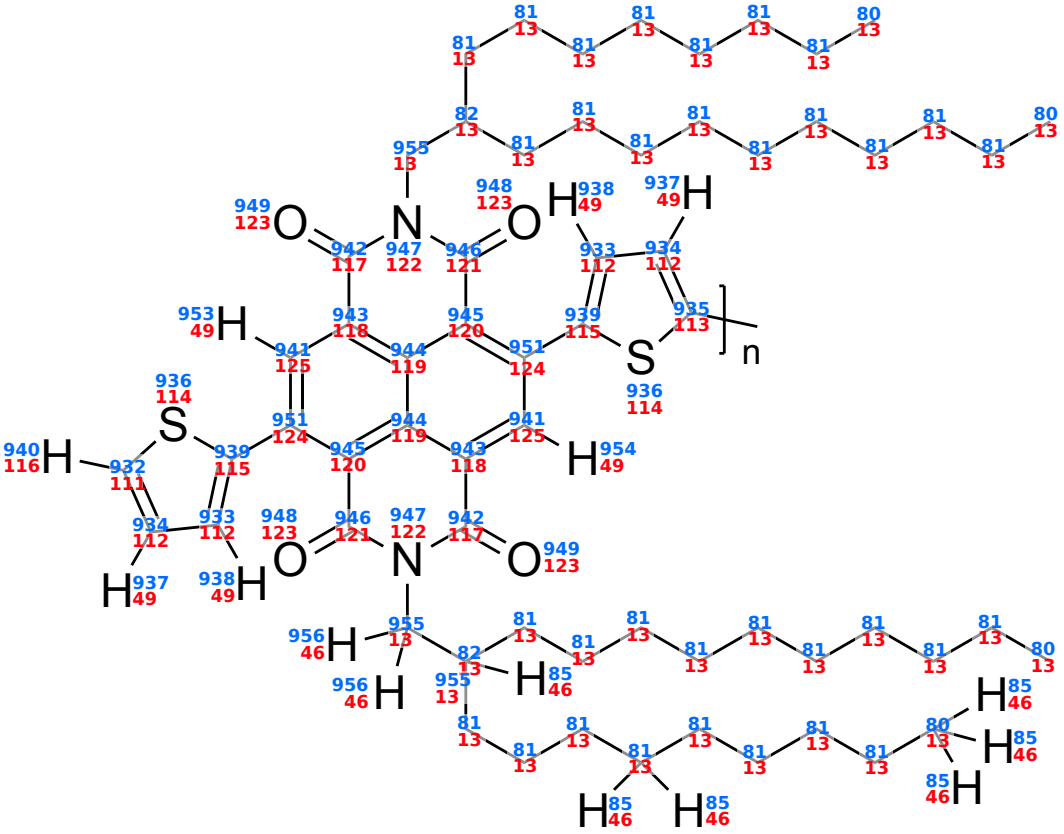

Fig. S4.29 Definition of the different atom (blue) and bond (red) types for this parameterisation of P(NDI2OD-T2). Atom types with values 932 and above differ from those in the OPLS force field, with their partial charges obtained from quantum-chemical calculations, but van der Waals (vdW) parameters from the OPLS force-field for equivalent atom types. Bond types with values 110 and above also differ from those in the OPLS force field, with the bond lengths and angles obtained from the optimised geometry, and force constants from the OPLS force field for equivalent atom types. The energy parameters for the 113–113 bond length, and the 120–124–113–112, and 112–113–113–112 dihedrals were explicitly parameterised (as described in Section S4.1) as these potentials were not expected to be accurately represented by the OPLS force field. For the sake of representing both a terminal and central monomer of a polymer chain in a single image, the left terminus is shown with the site types corresponding to a terminal monomer, and the right to a central monomer (connecting to another monomer). For clarity, only a few side-chain hydrogens are shown.

S4.14.1 NON-BONDED PARAMETERS

Table S4.3 Masses, partial charges, and LJ parameters for the AA symmetric P(NDI2OD-T2) monomer model. The non-bonded potential between two particles of type i and j is defined as

$$U_{\mathrm{NB}}(r_{ij}) = 4\epsilon_{ij}\left[\left(\frac{\sigma_{ij}}{r_{ij}}\right)^{12} - \left(\frac{\sigma_{ij}}{r_{ij}}\right)^{6}\right] + \frac{q_i q_j}{4\pi\epsilon_0 r_{ij}}$$

where σ_{ii} is the homonuclear LJ diameter, ϵ_{ii} the homonuclear LJ interaction strength, and q_i the charge. Geometric mixing rules were used to define the heteronuclear parameters from the homonuclear ones: $\sigma_{ij} = \sqrt{\sigma_i \sigma_j}$ and $\epsilon_{ij} = \sqrt{\epsilon_i \epsilon_j}$. The excess charge of the system, resulting from the truncation of the side-chains in the model parameterisation and the use of OPLS charges for the final side-chain atoms, was added to atom type 955 (or 957 for teminal monomers of polymer chain) to enforce charge neutrality. The optimised charge of this atom type was approx. −0.08 e, but the charges used in the force-field depended on whether the monomer was an isolated monomer (955^{m}), central polymer unit (955^{pc}), or terminal polymer unit (957) in order to maintain charge neutrality. Charges and LJ parameters for atom types 80, 81, 82, and 85 came directly from the OPLS force field.

atom type (i)	mass (g/mol)	q_i (e)	ϵ_{ii}	σ_{ii}
932	12.01	0.126 452	0.07	3.55
933	12.01	−0.222 396	0.07	3.55
934	12.01	−0.271 944	0.07	3.55
935	12.01	0.120 963 5	0.07	3.55
936	32.06	−0.126 013 5	0.25	3.55
937	1.008	0.194 494 5	0.03	2.42
938	1.008	0.189 001 5	0.03	2.42
939	12.01	0.110 991	0.07	3.55
940	1.008	0.182 183	0.03	2.42
941	12.01	−0.099 982	0.07	3.55
942	12.01	0.665 569 5	0.105	3.75
943	12.01	−0.205 615	0.07	3.55
944	12.01	0.083 396	0.07	3.55
945	12.01	−0.179 475 5	0.07	3.55
946	12.01	0.594 664 5	0.105	3.75
947	14.01	−0.344 225	0.17	3.25
948	16.00	−0.454 13	0.21	2.96

Continued on next page

atom type (i)	mass (g/mol)	q_i (e)	ϵ_{ii}	σ_{ii}
949	16.00	−0.535 615 5	0.21	2.96
950	12.01	0.149 833	0.07	3.55
951	12.01	0.132 339	0.07	3.55
952	1.008	0.128 893	0.03	2.42
953	1.008	0.043 813	0.03	2.42
954	1.008	0.128 152	0.03	2.42
955^{m}	12.01	−0.066 702 5	0.066	3.5
955^{pc}	12.01	0.120 969	0.066	3.5
956	1.008	0.070 512 75	0.03	2.42
957	12.01	0.040 045	0.066	3.5
80	12.01	−0.18	0.066	3.5
81	12.01	−0.12	0.066	3.5
82	12.01	−0.06	0.066	3.5
85	1.008	0.06	0.03	2.5

^{m} charge for monomer

^{pc} charge for central monomer of polymer chain

S4.14.2 BONDED PARAMETERS

Bonds, angles, dihedrals, and impropers for the AA model of P(NDI2OD-T2) are listed in terms of their bond types (red numbers in Fig. S4.29).

Table S4.4 Bond length parameters. Bond stretching coefficients, k_2, were taken directly from the OPLS force field with the exception of the identical 115–124 and 111–124 bonds, which were parmeterised explicitly. Most equilibrium bond lengths (l_0) were obtained from the optimised geometry of P(NDI2OD-T2). Bonds 13–13 and 13–46 contain only side-chain atoms so both k_2 and l_0 were taken from the OPLS force field. The harmonic bond length potential is defined in eqn (4.19a).

bond	bond style	k_2 (kcal/mol/Å^2)	l_0 (Å)
49–112	harmonic	367	1.084
111–112	harmonic	546	1.371
111–114	harmonic	250	1.733
112–112	harmonic	469	1.419
112–113	harmonic	546	1.383

Continued on next page

bond	bond style	k_2 (kcal/mol/Å^2)	l_0 (Å)
112–115	harmonic	546	1.379
113–113	harmonic	512	1.449
113–114	harmonic	250	1.751
114–115	harmonic	250	1.757
115–124*	harmonic	345	1.468
116–111	harmonic	367	1.081
117–118	harmonic	400	1.486
117–122	harmonic	490	1.400
117–123	harmonic	570	1.225
118–119	harmonic	469	1.417
118–125	harmonic	469	1.382
119–119	harmonic	469	1.424
119–120	harmonic	469	1.420
120–121	harmonic	400	1.492
120–124	harmonic	469	1.400
121–122	harmonic	490	1.408
121–123	harmonic	570	1.224
122–13	harmonic	337	1.482
124–49	harmonic	367	1.084
124–125	harmonic	469	1.415
125–49	harmonic	367	1.084
111–124*	harmonic	345	1.468
13–13	harmonic	268	1.529
13–46	harmonic	340	1.090

* Bonds for which force constant was explicitly parameterised

Table S4.5 Bond angle parameters. Angle bending coefficients, k_2, were taken directly from the OPLS force field. Most equilibrium bond angles (θ_0) were obtained from the optimsed geometry of P(NDI2OD-T2). Angles 13–13–13, 46–13–13, and 46–13–46 contain only side-chain atoms so both k_2 and θ_0 were taken from the OPLS force field. The harmonic bond angle potential is defined in eqn (4.20a).

angle	angle style	k_2 (kcal/mol/rad^2)	θ_0 (°)
111–112–112	harmonic	70	112.8
112–112–49	harmonic	35	123.6
112–112–113	harmonic	70	113.5
112–113–113	harmonic	70	128.9
112–113–114	harmonic	74	110.2
113–114–111	harmonic	74	91.8
113–114–115	harmonic	74	92.3
114–111–112	harmonic	70	111.7
114–113–113	harmonic	74	120.8
114–115–112	harmonic	74	110.0
115–112–49	harmonic	35	122.8
115–112–112	harmonic	70	113.9
112–115–124	harmonic	70	129.6
115–124–125	harmonic	70	116.2
115–124–120	harmonic	70	125.6
124–125–49	harmonic	35	120.2
124–125–118	harmonic	63	121.7
124–120–119	harmonic	63	119.9
114–115–124	harmonic	70	120.1
125–124–120	harmonic	63	119.0
125–118–119	harmonic	63	120.4
125–118–117	harmonic	85	119.2
118–119–119	harmonic	63	118.4
118–119–120	harmonic	63	121.0
118–117–123	harmonic	80	122.0
118–117–122	harmonic	35	116.8
118–125–49	harmonic	35	118.1
117–118–119	harmonic	85	120.5

Continued on next page

angle	angle style	k_2 (kcal/mol/rad^2)	θ_0 (°)
117–122–121	harmonic	70	124.7
117–122–13	harmonic	50	117.6
122–121–120	harmonic	70	117.5
122–121–123	harmonic	80	120.0
122–117–123	harmonic	80	121.2
122–13–46	harmonic	35	106.2
122–13–13	harmonic	80	114.9
121–122–13	harmonic	50	117.4
121–120–119	harmonic	85	118.9
121–120–124	harmonic	85	121.1
123–121–120	harmonic	80	122.5
120–119–119	harmonic	63	120.6
120–124–49	harmonic	35	119.0
116–111–112	harmonic	35	132.1
116–111–114	harmonic	35	125.0
113–112–49	harmonic	35	123.4
13–13–13	harmonic	38.35	112.7
46–13–13	harmonic	37.5	110.7
46–13–46	harmonic	33	107.8

Table S4.6 Dihedral parameters. Unless otherwise stated, parameters were taken directly from the OPLS force field for equivalent atom types. The "multi/harmonic" dihedral styles are of the form in eqn (4.16) with $m = 4$ or 8 for the multi/harmonic4 and multi/harmonic8 potentials, respectively. The "opls" style dihedral has the form given in eqn (4.17). X is a wild-card atom. For the three dihedrals that were explicitly parameterised (112–113–113-112, 112–115–124–120, and 112–111–124–120), the other dihedrals involving the same two central atoms had all energy parameters set to zero, such that the dihedral was completely controlled by the one set of parameters. All energy parameters k_i have units of kcal/mol.

dihedral	dihedral style	k_0	k_1	k_2	k_3	k_4	k_5	k_6	k_7	k_8
X–114–111–X	opls	0	2.8	0	0					
X–111–112–X	opls	0	7.25	0	0					
X–112–112–X[a]	opls	0	7.25	0	0					
X–112–113–X	opls	0	7.25	0	0					
X–113–114–X	opls	0	2.8	0	0					
112–113–113–114[b]	opls	0	0	0	0					
112–113–113–112[b]	multi/harmonic4	2.542	0.042	−7.139	−0.351	3.121				
114–113–113–114[b]	opls	0	0	0	0					
X–114–115–X	opls	0	2.8	0	0					
X–115–112–X	opls	0	7.25	0	0					

Continued on next page

dihedral	dihedral style	k_0	k_1	k_2	k_3	k_4	k_5	k_6	k_7	k_8
112–115–124–120[b]	multi/harmonic8	0.802	0.321	−2.186	−1.377	−24.648	0.893	48.435	0.984	−30.962
112–115–124–125[b]	opls	0	0	0	0					
114–115–124–125[b]	opls	0	0	0	0					
114–115–124–120[b]	opls	0	0	0	0					
112–111–124–120[b]	multi/harmonic8	0.802	0.321	−2.186	−1.377	−24.648	0.893	48.435	0.984	−30.962
112–111–124–125[b]	opls	0	0	0	0					
114–111–124–125[b]	opls	0	0	0	0					
114–111–124–120[b]	opls	0	0	0	0					
X–124–125–X	opls	0	7.25	0	0					
X–125–118–X	opls	0	7.25	0	0					
X–118–117–122	opls	0	1.1	0	0					
X–118–117–123	opls	0	2.1	0	0					
118–117–122–121[c]	opls	0	7.25	0	0					
118–117–122–13[c]	opls	0	7.25	0	0					
123–117–122–X[c]	opls	0	2.1	0	0					
120–121–122–117[c]	opls	0	7.25	0	0					
120–121–122–13[c]	opls	0	7.25	0	0					
123–121–122–X[c]	opls	0	2.1	0	0					
X–122–13–X	opls	0	0	0	0					
X–120–121–123	opls	0	2.1	0	0					
X–120–121–122	opls	0	1.1	0	0					

Continued on next page

dihedral	dihedral style	k_0	k_1	k_2	k_3	k_4	k_5	k_6	k_7	k_8
X–119–120–X	opls	0	7.25	0	0					
X–118–119–X	opls	0	7.25	0	0					
X–119–119–X	opls	0	7.25	0	0					
X–120–124–X	opls	0	7.25	0	0					
13–13–13–13	opls	1.3	−0.05	0.2	0					
46–13–13–13	opls	0	0	0.3	0					
46–13–13–46	opls	0	0	0.3	0					

[a] ref 24

[b] parameterised in this work

[c] ref 291

Table S4.7 Improper torsion parameters. All parameters are from the OPLS force-field for equivalent atom types. The cosine potential defined in eqn (4.22) (implemented in LAMMPS as "cvff") was used for all improper torsions.

improper	improper style	k (kcal/mol)	d	n
X-X-117-123	cvff	10.5	−1	2
X-X-118-X	cvff	1.1	−1	2
X-X-119-X	cvff	1.1	−1	2
X-X-120-X	cvff	1.1	−1	2
X-X-121-123	cvff	10.5	−1	2
X-X-122-X	cvff	1.1	−1	2
X-X-124-X	cvff	1.1	−1	2
X-X-125-X	cvff	1.1	−1	2
X-X-111-X	cvff	1.1	−1	2
X-X-112-X	cvff	1.1	−1	2
X-X-115-X	cvff	1.1	−1	2
X-X-113-X	cvff	1.1	−1	2

S4.14.3 SOLVENT (DCB) PARAMETERS

All-atom simulations were conducted in an explicit solvent of *o*-dichlorobenzene (DCB). All parameters for this molecule were taken directly from the OPLS force-field,[202,268–273] but we have reproduced them below for clarity. The structure of the molecule and the atom/bond types are given in Fig. S4.30 and the parameters in the following tables. Atom and bond type numbering follows the `opls aa.prm` file distributed with Tinker.[292] The numbers for the atom and bond types of P(NDI2OD-T2) described above were chosen to not overlap with the existing OPLS atom types from this source.

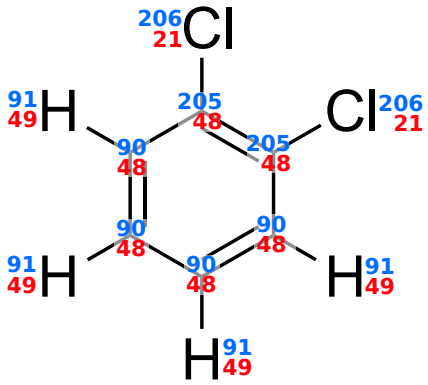

Fig. S4.30 Atom (blue) and bond (red) types for the AA model of DCB used as the solvent for parameterisation of the CG system. These atom/bond types are referenced in the tables below for the parameters of this molecule.

Table S4.8 Masses, partial charges q_i, and homonuclear LJ parameters ϵ_{ii} and σ_{ii} for the AA DCB model, with parameters taken directly from the OPLS force field.

atom type (i)	mass (g/mol)	q_i (e)	ϵ_{ii}	σ_{ii}
90	12.01	−0.115	0.07	3.55
91	1.008	0.115	0.03	2.42
205	12.01	0.18	0.07	3.55
206	35.453	−0.18	0.3	3.4

Table S4.9 Bond length parameters. All parameters come directly from the OPLS force field. The harmonic bond potential has the form given in eqn (4.19a).

bond	bond style	k_2 (kcal/mol/Å^2)	l_0 (Å)
48–48	harmonic	469	1.4
48–21	harmonic	300	1.725
48–49	harmonic	367	1.08

Table S4.10 Bond angle parameters. All parameters come directly from the OPLS force field. The harmonic angle potential has the form given in eqn (4.20a).

angle	angle style	k_2 (kcal/mol/rad^2)	θ_0 (°)
48–48–48	harmonic	63	120.0
48–48–49	harmonic	35	120.0
21–48–48	harmonic	75	120.0

Table S4.11 Dihedral parameters. All parameters come directly from the OPLS force field. The opls style dihedral potential has the form given in eqn (4.17)

dihedral	dihedral style	k_0	k_1	k_2	k_3
X–48–48–X	opls	0	7.25	0	0

Table S4.12 Improper torsion parameters. All parameters come directly from the OPLS force field. The cosine (cvff) style potential has the form given in eqn (4.22).

improper	improper style	k (kcal/mol)	d	n
X-X-48-X	cvff	1.1	−1	2

S4.15 COARSE-GRAINED MODEL PARAMETERS

The parameters for the coarse-grained model are given in this section. The forms of the potentials, and the definitions of the parameters are given in Section S4.2.1. Although it is included in the main text, we replicate the image of the site-type definitions and their relationship to the all-atom model for clarity, as we will refer to the sites by their number in the following tables.

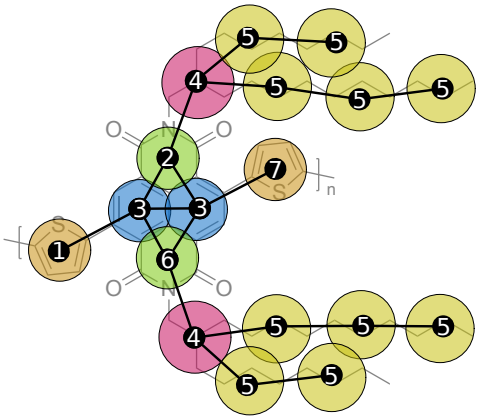

Fig. S4.31 Definition of site types for the CG P(NDI2OD-T2) model. Sites are coloured and labelled according to their site types, with sites that have the same non-bonded parameters (though not necessarily the same bonded parameters) shown as the same colour.

s4.15.1 SITE MASSES

Table S4.13 Site masses for the CG representation of P(NDI2OD-T2). Masses correspond to the mass of the particles in the AA representation that make up the CG site. Where atoms are shared between multiple CG sites, the mass is split evenly among those sites.

site type	mass (g/mol)
1	84.116
2	86.050
3	45.040
4	55.096
5	42.078
6	86.050
7	82.116

S4.15.2 NON-BONDED PARAMETERS

The non-bonded parameters for the P(NDI2OD-T2) model corresponding to the three solvent conditions are given in Table S4.14, and plotted in Fig. S4.32.

Table S4.14 Non-bonded interaction parameters for the three solvent conditions. ϵ_{DCB} is the as-parameterised parameters. ϵ_{good} and ϵ_{poor} are the same parameters scaled by ± 20 %. All ϵ are given in units of kcal/mol. The same values of σ_{ij} are used for all three sets of parameters (units of Å). The WCA cutoff is the cutoff used for the setup simulations with repulsive particles (units of Å). It is equal to $2^{1/6}\sigma_{ij}$ and the potential is shifted to zero at this point. Note that some parameters (e.g. 1–1 and 7–7) are identical, as the site types are chemically equivalent. They are assigned different site types as the bonded interactions differ, but the non-bonded interactions have been constrained to be the same.

pair	ϵ_{DCB}	ϵ_{good}	ϵ_{poor}	σ_{ij}	WCA cutoff
1–1	0.364	0.291	0.437	3.987	4.475
1–2	0.023	0.018	0.028	5.089	5.712
1–3	0.331	0.265	0.397	4.605	5.169
1–4	0.070	0.056	0.084	5.425	6.089
1–5	0.027	0.022	0.032	5.556	6.236
1–6	0.023	0.018	0.028	5.089	5.712
1–7	0.364	0.291	0.437	3.987	4.475
2–2	0.586	0.469	0.703	3.778	4.241
2–3	0.551	0.441	0.661	3.449	3.871
2–4	0.555	0.444	0.666	4.141	4.648
2–5	0.050	0.040	0.060	5.230	5.870
2–6	0.586	0.469	0.703	3.778	4.241
2–7	0.023	0.018	0.028	5.089	5.712
3–3	0.369	0.295	0.443	3.798	4.263
3–4	0.338	0.270	0.406	4.153	4.662
3–5	0.047	0.038	0.056	5.165	5.798
3–6	0.551	0.441	0.661	3.449	3.871
3–7	0.331	0.265	0.397	4.605	5.169
4–4	0.243	0.194	0.292	5.977	6.709
4–5	0.068	0.054	0.082	5.182	5.817

Continued on next page

pair	ϵ_{DCB}	ϵ_{good}	ϵ_{poor}	σ_{ij}	WCA cutoff
4–6	0.555	0.444	0.666	4.141	4.648
4–7	0.070	0.056	0.084	5.425	6.089
5–5	0.076	0.061	0.091	5.068	5.689
5–6	0.050	0.040	0.060	5.230	5.870
5–7	0.027	0.022	0.032	5.556	6.236
6–6	0.586	0.469	0.703	3.778	4.241
6–7	0.023	0.018	0.028	5.089	5.712
7–7	0.364	0.291	0.437	3.987	4.475

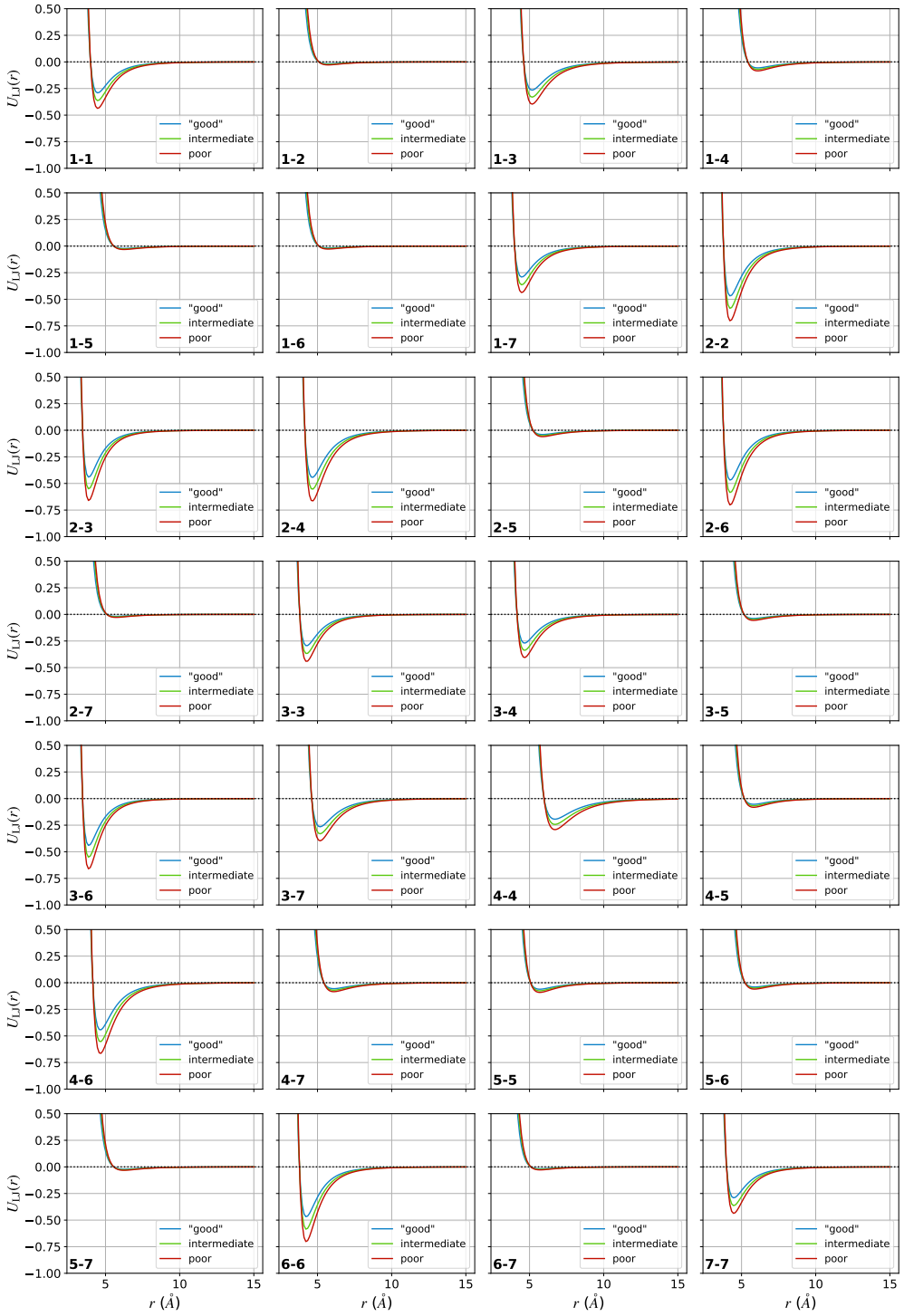

Fig. S4.32 LJ non-bonded potentials for all possible pairs of interactions in the CG P(NDI2OD-T2) model. The "good" solvent has parameters that are 20% weaker than those obtained in DCB, while the "poor" solvent interactions are 20% stronger. The as-parameterised model (from DCB) is labelled as "intermediate". The site types for the interactions are listed in the bottom left of each plot.

S4.15.3 BONDED PARAMETERS

For the bonds, two different potentials were used for the stretching parameters: a harmonic potential (eqn (4.19a)), and a quartic potential that uses the LAMMPS "class2" bond style (eqn (4.19b)). Angles also made use of two different potential forms: a harmonic (eqn (4.20a)) and a quartic potential (eqn (4.20b)). All dihedrals were modelled with the dihedral style described in eqn (4.21) with $m = 4$. The improper torsion was modelled with a cosine form (eqn (4.22)).

In order to model the flexible backbone, the 1–7–3 and 7–1–3 angles, and the 3–7–1–3 dihedrals were reduced to 1% of their original stiffness (Fig. S4.33). The modified parameters are given in Tables S4.16 and S4.17. All other parameters are the same as for the regular backbone

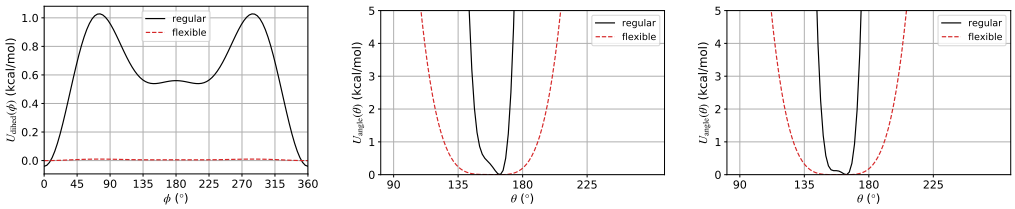

(a) Dihedral 3–7–1–3 **(b)** Angle 1–7–3 **(c)** Angle 7–1–3

Fig. S4.33 (a) Dihedral and (b)–(c) angle potentials used to tune the flexibility of the polymer backbone from regular (black lines) to flexible (red dashed line). In all three cases, the coefficients were reduced to 1% of their original values.

Table S4.15 Bond length parameters for the CG model of P(NDI2OD-T2). Bond stretching coefficients k_i are in units of kcal/mol/Å^i. The forms of the harmonic and quartic bond styles are given in eqns (4.19a) and (4.19b) respectively. Note that the quartic bond potential is implemented in LAMMPS as the "class2" bond style.

bond	bond style	l_0 (Å)	k_2	k_3	k_4
1–3	harmonic	4.12	129.33		
1–7	harmonic	3.91	101.73		
2–3	harmonic	2.90	679.95		
2–4	harmonic	3.57	83.39		
3–3	harmonic	2.47	1206.79		
6–3	harmonic	2.89	525.52		
6–4	harmonic	3.57	80.73		

Continued on next page

bond	bond style	l_0 (Å)	k_2	k_3	k_4
7–3	harmonic	4.12	138.60		
4–5	quartic	3.92	92.92	596.82	1014.01
5–5	quartic	3.86	88.96	556.24	890.46

Table S4.16 Bond angle parameters for the CG model of P(NDI2OD-T2). Angle bending coefficients k_i are in units of kcal/mol/rad^i. The parameters for the flexible backbone are also included (see Fig. S4.33). These replace the corresponding angle of the regular flexibility backbone. The forms of the harmonic and quartic angle styles are given in eqns. (4.20a) and (4.20b) respectively.

angle	angle style	θ_0 (°)	k_2	k_3	k_4
1–3–2	quartic	138.60	62.00	−163.76	2.00
1–3–3	quartic	161.44	129.09	1062.34	2561.64
1–3–6	quartic	89.61	104.08	−1308.04	4778.21
1–7–3	quartic	164.05	60.76	426.09	967.28
2–4–5	quartic	110.48	5.69	−11.47	6.85
4–5–5	quartic	177.89	24.91	51.38	29.35
5–5–5	quartic	174.92	15.91	33.06	19.92
6–4–5	quartic	112.21	5.88	−11.15	6.68
7–3–2	quartic	89.89	96.31	−1192.48	4517.46
7–3–3	quartic	161.55	108.44	946.50	2560.32
7–3–6	quartic	137.74	76.89	12.79	2.00
7–1–3	quartic	164.25	40.77	401.68	1106.43
3–2–4	harmonic	148.42	49.80		
3–6–4	harmonic	148.11	47.04		
1–7–3*	quartic	164.05	0.61	4.26	9.67
7–1–3*	quartic	164.25	0.41	4.02	11.06

* Flexible backbone parameters

Table S4.17 Dihedral parameters for the CG model of P(NDI2OD-T2). Energy parameters k_i are in units of kcal/mol. All dihedrals use the dihedral potential defined in eqn (4.16) with $m = 4$ (implemented in LAMMPS as the "multi/harmonic" style). The parameters for the flexible backbone are also given (see Fig. S4.33). This replaces the corresponding dihedral of the regular flexibility backbone.

dihedral	dihedral style	k_0	k_1	k_2	k_3	k_4
1–7–3–2	multi/harmonic	0.10	−0.11	−0.32	0.21	0.65
1–7–3–3	multi/harmonic	0.33	−0.44	−0.34	0.13	0.51
1–7–3–6	multi/harmonic	0.19	−0.51	0.38	−0.72	0.99
2–4–5–5	multi/harmonic	0.03	0.02	0.15	0.03	−0.02
3–2–4–5	multi/harmonic	0.46	−0.84	−0.31	0.56	0.34
3–6–4–5	multi/harmonic	0.16	−0.70	0.55	0.67	−0.32
3–7–1–3	multi/harmonic	0.96	0.48	−0.63	−0.76	−0.07
4–5–5–5	multi/harmonic	0.13	−0.26	0.10	0.12	−0.06
5–4–5–5	multi/harmonic	0.01	0.01	0.08	0.00	0.04
6–4–5–5	multi/harmonic	0.03	0.05	0.01	−0.02	0.08
7–1–3–2	multi/harmonic	0.17	−0.30	−0.05	−0.74	1.37
7–1–3–3	multi/harmonic	0.42	−0.30	−0.71	−0.10	0.78
7–1–3–6	multi/harmonic	0.12	−0.14	−0.53	0.23	0.83
3–7–1–3*	multi/harmonic	0.010	0.005	−0.006	−0.008	−0.001

* Flexible backbone parameters

Table S4.18 Improper torsion parameters for the CG model of P(NDI2OD-T2). Energy parameter k is in units of kcal/mol. The form of the cosine style improper is given in eqn (4.22).

improper	improper style	k	d	n
2–6–3–3	cosine	35.24	−1	2

5

Solution–phase aggregation of N2200: effect of solvent and side-chains

"There is an art to the business of making sandwiches which it is given to few ever to find the time to explore in depth."

— Douglas Adams, *Mostly Harmless*

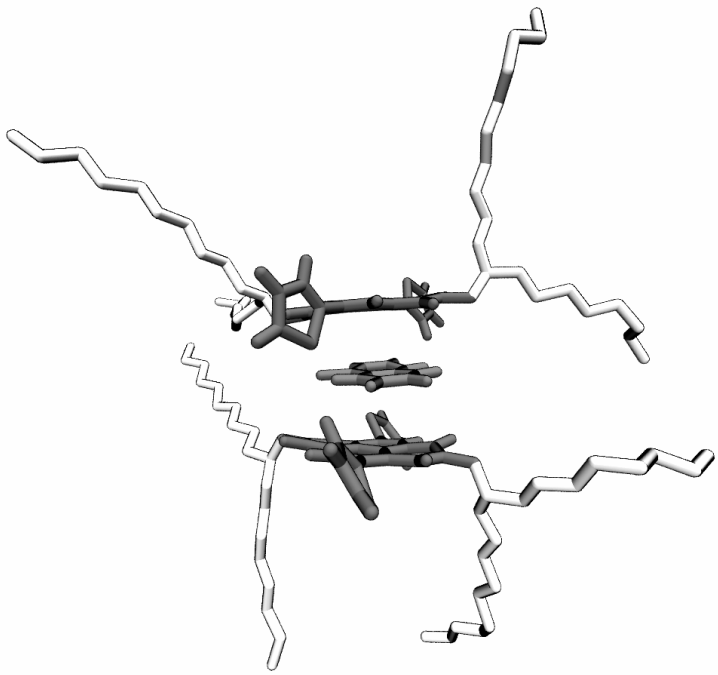

Unpublished work written in manuscript style

Abstract

The effect of side-chain chemical structure on the aggregate morphology and solution-phase behaviour of the organic semiconductor (OSC) polymer P(NDI2OD-T2), also known as N2200, is examined using molecular dynamics simulations. While Flory-Huggins theory has been commonly used in the past to understand the solution-phase behaviour of OSCs, we show that, while it gives results that are qualitatively consistent with certain experimental techniques, it neglects important aspects of the solution-phase behaviour. For a derivative of N2200 with ethylene oxide (EO) side-chains, wrapping of these chains around the backbone is shown to lead to a more disordered aggregate structure, without the backbone planarisation that appears characteristic of aggregates of N2200 with the conventional alkyl (A) side-chains. This side-chain wrapping has not been reported previously for any OSC molecule, but appears to be important for fully understanding how the structure with EO side-chains aggregates in solution. We also examine the behaviour of the conventional polymer (A side-chains) in 1-chloronaphthalene, which has shown contradictory aggregation properties when measured using different experimental techniques. These experimental contradictions are reconciled through a proposed solvent-separated, sandwich-like structure in this solvent, where strong solvent–backbone interactions may allow the build-up of a large aggregate, without increasing the electronic coupling between or along the polymer backbone. Overall, this work highlights that simple solubility theories, while generally thought to be at least qualitatively accurate for OSCs, can fail to account for how specific interactions may influence the overall aggregation behaviour. In cases where, for example, interactions between solvent and backbone, or backbone and side-chains are important, this can lead to qualitatively incorrect predictions.

5.1 INTRODUCTION

Organic semiconductors (OSCs), molecules whose conjugated backbone imparts interesting optical and electronic properties, are likely to play a large role in many future technologies, from energy efficient, flexible displays, to lightweight photovolatics. Although already finding prominence in energy efficient lighting and displays, their use in other applications is more limited, due to their generally poorer performance than current inorganic counterparts. Although performance is improving, greater progress is hampered by the unpredictability of the morphology and device electronic properties of OSCs, with many factors – ranging from, among others, molecular weight,[27,30] solvent,[21,22,25,39–41] and chemical structure,[32,35–38] – all impacting the solution-phase behaviour and the final thin-film structure of the commonly polymeric OSC. As many of the promising applications of these molecules stem from their ability to be solution-processed,[2] it is important that this behaviour be better understood.

The importance of solution-phase behaviour for OSC device performance, particularly for OSC polymers, has been well studied, with strong correlations observed between solution-phase structure, thin-film microstructure, and device performance.[21,25,30,44] While at least some aggregation is generally required to give sufficiently ordered structures, fully crystalline structures are not required for good charge transport,[38] with ordered nanoscale domains connected by long-tie chains giving as good, if not better charge mobility.[26] Of the number of ways of controlling thin-film microstructure and device performance, the nature of the sidechains,[31,32,36,37] and the choice of solvent,[21,22,25,39,40] are known to be particularly important.

Solution-phase aggregation properties are commonly examined experimentally through UV-visible spectroscopic measurements, in which electronic coupling between aggregated chains (or within a single chain) induces changes in the spectrum.[293] The solution-phase aggregation properties of high-performing OSC polymer P(NDI2OD-T2) (also known as N2200, by which we will refer to it) have been extensively studied by UV-vis spectroscopy,[22,27] with aggregation typically associated with a strong red shift in the absorption spectrum. The effect of the alignment of monomers (that is, whether the naphthalene diimide (NDI) groups in different chains are directly stacked, or offset; see Fig. 5.1 for chemical structure of the monomer) within the aggregate has also been studied,[294] but was reported to have only minor effects on the shape of the absorption spectrum. Interestingly, recent work on a derivative of N2200, where the alkyl (A) side-chains are replaced with ethylene oxide (EO) chains (see Fig. 5.1), has shown significant differences in the shape of the absorption spectrum in the same solvents.[295] The difference

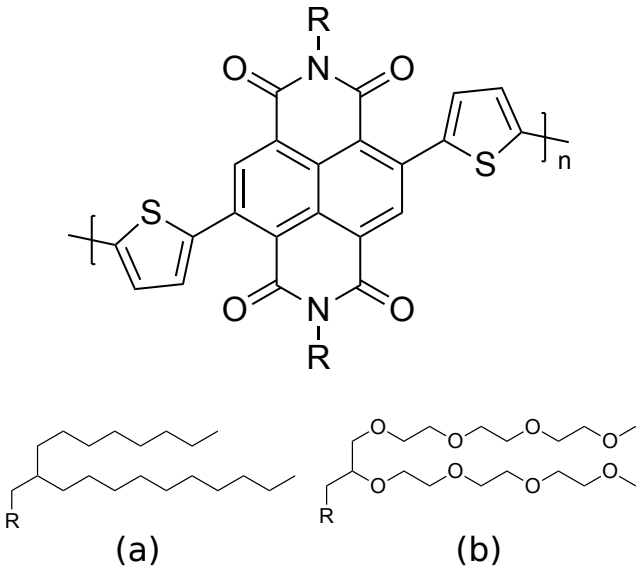

Fig. 5.1 Structure of (top) the symmetric N2200 backbone and (bottom) side-chains where R = (a) gives N2200-A and R = (b) N2200-EO.

between the spectral shapes for these two variants of N2200 has not been previously explained, though it suggests significant differences in the aggregate structure.

Side-chains are often considered only in terms of the changes in solubility they impart to the overall polymer, and therefore the overall degree of aggregation, rather than how they may change the aggregate structure. Details of specific interactions between backbone and side-chains are therefore often neglected. These specific interactions are also not typically amenable to study through experimental techniques. In Section 5.3.1 we have used molecular dynamics (MD) simulations to examine the aggregate structures of N2200 with the typical alkyl (A) side-chains (referred to here as N2200-A for simplicity) and with the modified ethylene oxide (EO) side-chains (referred to here as N2200-EO). Side-chains were found to change the aggregate structure, as well as to modify the backbone structure of single chains in aggregates, highlighting that, under certain circumstances, side-chains act as more than just solubilising agents. Understanding the specifics of the side-chain–backbone interactions is therefore an important, though generally neglected, factor in understanding the solution-phase aggregation properties, with implications for thin-film microstructure and charge transport.

In addition to the differences in behaviour between N2200-A and N2200-EO, both polymers show interesting aggregation behaviour when studied using different experimental techniques: in certain solvents in which no aggregation is indicated by the UV-vis absorption spectrum, poor solubility (or extensive aggregation) is observed using other experimental techniques.[295,296] For N2200-EO, the absorption spectrum suggests no aggregation in chloroform (CF), while size-exclusion chro-

matography (SEC) measurements suggest the formation of structures many times the molecular weight of a single chain.[295] Similarly for N2200-A, the UV-vis absorption spectrum in 1-chloronaphthalene (CN) again suggests no aggregation, though anecdotal evidence suggests that CN may, in fact, be a poor solvent for N2200-A.[296] While MD simulation techniques have been used to study the solubility of N2200-A in CN in the past,[129] the measures of solubility used in the previous work considered only the relative interactions between the components of the mixture, rather than considering any specific interactions. Particularly strong solvent–polymer attractive interactions may, for example, lead to a stacked, sandwich-like, structure in which ordered solvent molecules separate the N2200-A backbones. The final aggregate structure may therefore involve both polymer and solvent molecules. This kind of behaviour has been observed in a co-crystal of an NDI derivative (which is similar in structure to the backbone of an N2200 monomer) with CN, in which the CN molecules stacked in between the planes of the NDI groups.[297] However, it is not clear whether this behaviour could translate to solution.

In the following sections, we have examined the solution-phase behaviour of N2200 with the commonly used A (N2200-A), or EO side-chains (N2200-EO), using MD simulation (see Fig. 5.1 for chemical structures). We have also used Flory-Huggins theory[127] to determine the relative strength of the polymer–polymer, solvent–solvent, and polymer–solvent interactions, while also considering the backbone–side-chain, side-chain–solvent, and backbone–solvent interactions (Section 5.3.1.1). Flory-Huggins interaction parameters calculated from MD have previously been used relatively successfully to understand the solution phase behaviour of OSC polymers, and understand how the structure of the polymer aggregate,[130] and the choice of solvent,[128–130] affect polymer solubility. However, their application for understanding the relative solubilities of polymer components, and especially the differing interactions between various side-chain structures and the polymer backbone as in this work, is novel. Additionally, although differences in the absorption spectra of N2200-A and N2200-EO have previously been reported,[295] the differences in spectral features have not been explained. These features can be qualitatively explained through an analysis of the structure of aggregates of the two polymers, which appear to be strongly influenced by the interactions between side-chains and backbone in a way that cannot be fully described by Flory-Huggins theory calculations (Section 5.3.1.2).

Finally, the possible formation of unconventional aggregate structures in which the backbones do not interact in the typical π-stacking manner is of interest for understanding the discrepancies between different experimental techniques for both N2200-A and N2200-EO. These experimental discrepancies are expected to result from aggregation that occurs without strong electronic coupling between or within

chains, leading to a lack of an observable shift in the UV-vis absorption spectrum. One of the advantages of MD simulation in this regard is the atom-scale resolution, which potentially allows for the observation of structures that may explain the experimental behaviour. An in-depth analysis of the aggregation behaviour of N2200-A in CN is presented in Section 5.3.2, and the behaviour of N2200-EO in CF is discussed briefly in Section 5.3.3. The molecular-level insight obtained from MD simulations highlights the importance, in some cases, of considering specific molecular interactions in order to accurately predict the solution-phase aggregation properties. In many cases, it may not be sufficient to rely purely on simple theories of solubility, such as Flory-Huggins theory, as has been done in the past.[129,130] Similarly, care must be taken when using a single experimental technique, especially one in which assumptions must be made about the behaviour of aggregated molecules such as UV-visible spectroscopy, for understanding solution-phase behaviour. A number of challenges associated with molecular simulation of OSC polymers are discussed in Section 5.3.4.

5.2 METHODS

In this work, we have used all-atom molecular dynamics (MD) simulations to study the solution-phase behaviour of N2200-A and N2200-EO. All simulations have used the LAMMPS software package,[244,263–265] and visualisation and analysis conducted with ovito,[245] and VMD.[266]

5.2.1 FORCE-FIELD PARAMETERISATION

Although general purpose force-fields exist, their parameters are often not suited to capturing the rigid backbones and extended conjugation of OSC polymers,[267] which will affect the charge distribution and certain bonded parameters, especially those connecting conjugated segments. We have previously developed a set of parameters for N2200-A consistent with the OPLS force-field (see Chapter 4), following a method previously outlined in the literature.[24] The OPLS force-field is particularly suited to the study of organic liquids, such as the solvents studied here, and when combined with the explicit parameterisation of certain important bonded parameters has been shown to accurately represent a wide variety of OSC polymers.[24]

In comparing the behaviour of N2200-A and N2200-EO, the aim in this work is to isolate the effect of side-chains on the polymer behaviour and aggregation properties. We have therefore kept the same backbone (partial charges, van der Waals, bond, angle, dihedral, and improper) parameters, and simply changed the

side-chains from the A to EO structure. Both A and EO side-chains used parameters directly from the OPLS force-field with no further modification.[202,268–273] The parameters that are not defined in Chapter 4 can be found in the SI Section S5.1.

The backbone and side-chain structures were also modelled individually as separate units in order to elucidate the effect of each of the components on the overall solubility. To model the backbone, the side-chains were truncated to a methyl group (R = CH_3 in Fig. 5.1). This required the addition of an extra hydrogen to the methylene group directly attached to the backbone relative to the full monomer. This hydrogen had the same type and charges as in the monomer (atom type 931, see Chapter 4) and the charge of the methyl carbon was adjusted to absorb the excess charge ($q = -0.137215e$). The single A side-chains were modelled as decane ($CH_3(CH_2)_8CH_3$), and the EO side-chains as $CH_3(OCH_2CH_2)_3OCH_3$. In both cases, all parameters were obtained directly from the OPLS force-field (see SI Section S5.1 for the EO parameters, and Chapter 4 for the A side-chains).

5.2.2 molecular dynamics simulation

All-atom MD simulations were conducted for N2200-A and N2200-EO in a variety of solvents in which the solubility of the two polymers has been studied experimentally.[22,25,295] Three solvents were examined for N2200-EO: chlorobenzene (CB, a poor solvent for N2200-EO), chloroform (CF, a good solvent for N2200-EO from UV-vis spectrum, but inconsistent with other experimental techniques), and 1-chloronaphthalene (CN, a good solvent), in which N2200-EO has varied solubility. For N2200-A, CN (good from UV-vis spectrum, but inconsistent with other experimental techniques), *o*-dichlorobenzene (DCB, good), and toluene (TOL, poor) were examined, as well as CF (poor) for comparison with the behaviour of N2200-EO. Simulations of monomers were initially used to qualitatively examine the side-chain and polymer behaviour and how this may affect the aggregation properties (Section 5.2.2.1). Larger simulations of oligomers consisting of 6 monomer units (6mers), either initialised as randomly positioned or aggregated chains, were also examined to determine whether the behaviour of an oligomer (which should be closer to that of an experimental polymeric system) is consistent with the monomer simulations (Section 5.2.2.2). Finally, to investigate the relative strength of the different interactions in the system, smaller monomer simulations were conducted from which Flory-Huggins parameters were calculated (Section 5.2.2.3).

In all cases, non-bonded interactions were calculated using a truncated and shifted Lennard Jones (LJ) potential with a cutoff of 11 Å, consistent with the parameterisation of the OPLS force-field.[202,268–273] The electrostatics were calculated using the particle–particle particle–mesh (PPPM) method.[201] Non-bonded interactions between atoms separated by 1 (1–2), or 2 (1–3) bonds were set to zero, and

those between atoms separated by 3 (1–4) bonds to 0.5 of their full strength, again consistent with the OPLS force-field. The SHAKE algorithm was used to constrain the hydrogen containing bonds to their equilibrium bond-length, allowing for the use of a 2 fs timestep. Simulations were conducted at constant temperature and pressure (NPT ensemble) with temperature and pressure controlled with a Nosé-Hoover thermostat[196,279] and barostat,[198] respectively.

Unless otherwise specified, all simulations followed a similar setup procedure: molecules were placed with random positions and orientations using Packmol[277] in a large box at low density in order to prevent overlaps and interlocking rings, and the energy of the system minimised. With the target density defined as the experimental density of the pure solvent system, the box was shrunk linearly in all three dimensions to a density approx. 25% higher than the target density, then expanded to a size approximately consistent with the target density, as described in the literature.[278] Velocities of all particles were then assigned from the Maxwell-Boltzmann distribution at 300 K. The initial, intermediate, and final box sizes are given for all systems in the SI, Table S5.6.

Although N2200 is typically represented as an asymmetric unit (i.e. NDI–bithiophene), we use a symmetric equivalent in this work where the bithiophene group is split to either side of the NDI group (thiophene (Th)–NDI–Th) as described in Chapter 4 and shown in Fig. 5.1.

5.2.2.1 Monomer simulations

We initially modelled both N2200-A and N2200-EO immersed in each of the five solvents. Using monomers means the system can be smaller than required for even short oligomers, due to the shorter range of intermolecular correlations, allowing simulations to reach longer timescales than what would be possible for larger systems. Monomers also diffuse faster than oligomers, allowing aggregation to occur more rapidly. Simulations were conducted at a concentration of approx. 55 g/L, with 18 monomers immersed in approx. 3000 solvent molecules (see SI Table S5.6 for the exact number of solvent molecules for each system). The setup procedure describe above was followed (initial random placement at low density, shrinking to high density over 40 ps, then expansion to target density over 20 ps), then the simulations run for 100–300 ns at constant temperature (300 K) and pressure (1 atm). The resulting trajectories were examined to determine the aggregation properties.

5.2.2.2 Oligomer simulations

Although monomers are expected to diffuse faster through the solvent, and therefore likely to aggregate faster than polymers or oligomers, the aggregation properties of longer chains are not necessarily well represented by the behaviour of monomers. Accordingly, we examine 6mers of both N2200-A and N2200-EO at approximately

the same concentration as the monomer simulations. Larger box sizes, chosen to be approx. twice the length of a fully extended 6mer, were required to contain the oligomers, with all systems containing approx. 20,000 solvent molecules (see SI Table S5.6). Systems were set up following the same procedure outlined above (shrinking over 40 ps, expansion over 20 ps), followed by 25–60 ns of simulation at 300 K and 1 atm.

A number of oligomer simulations were also conducted starting from an aggregated structure. To initialise these simulations, three 6mer chains were positioned at the center of the box, with center-of-mass separation of 4 Å, aligned with their backbones parallel, such that they were close to the expected π-stacked aggregate structure. Solvent (either CB, CF or CN for N2200-EO, and CF, CN, or DCB for N2200-A) was packed randomly around the polymers at low density and the setup procedure outlined above was followed (shrinking over 40 ps, expansion over 20 ps). Each system was run for between 20–100 ns at 300 K and 1 atm (see Table S5.6 for details).

To examine some of the more interesting structures proposed to form in CN, N2200-A 6mers were studied starting from a solvent-separated structure in CN and DCB. To initialise these structures, three oligomers were positioned with a center-of-mass separation of 9 Å between each chain in the π-stacking direction and perfectly aligned in the other directions. The simulation setup procedure was modified slightly to allow the solvent to penetrate into the stacked polymer structure. The energy of the system was initially minimised with the centers-of-mass of each monomer (approximated as the two carbons in the center of the naphthalene ring of the NDI group) fixed. The simulation box was then shrunk and expanded as described for all other simulations, but with the positions of all the polymer atoms fixed. The constraints on the entire polymer were then released, and the system equilibrated with the monomer centers-of-mass fixed (this allowed for the side-chains and other backbone atoms to rearrange while preventing unwanted aggregation of the chains) for 5 ns. The restraints on the monomer positions were then released and the unconstrained system run for a total of 40 ns in CN and 20 ns in DCB.

5.2.2.3 Flory-Huggins theory calculations

Flory-Huggins theory was used to predict the solubility of both N2200-A, N2200-EO, and the various components of the polymer (backbone or side-chains) in different solvents. Methods based on MD simulation have been used in the past to calculate Flory-Huggins interaction parameters of OSC polymers,[128–130] and we have used a method inspired by these works in the following calculations. Flory-Huggins theory quantifies the free energy of mixing in terms of the chain length, volume

fraction, and relative interaction energy. The Flory-Huggins parameter, χ_{FH}, can be obtained from the energetic component of this free energy, and is related to the relative strength of the polymer–polymer, solvent–polymer, and solvent–solvent interactions in a lattice-site model of a binary mixture. χ_{FH} can be calculated as[129,130]

$$\chi_{FH} = \frac{U_{mix}}{N\phi_p\phi_s k_B T} \tag{5.1}$$

where ϕ_p and ϕ_s are the polymer and solvent volume fractions respectively in the mixture, and N the number of lattice sites in the mixture. U_{mix} is the energy of mixing, with[130]

$$U_{mix} = U_m - N_s U_s - N_p U_p \tag{5.2}$$

where U_m is the total potential energy (non-bonded + bonded interaction energy) of the mixture containing N_s solvent molecules and N_p polymer monomers, U_s is the total potential energy per solvent molecule in a pure solvent system, and U_p is the total potential energy per monomer in a pure polymer system. Previous MD calculations of Flory-Huggins parameters have used the cohesive energy density – that is the total intermolecular non-bonded interactions per unit volume – to calculate U_{mix}, and accordingly χ_{FH}.[129] As MD force-fields artificially separate the bonded (especially dihedral) and non-bonded interactions, which may still be strongly interdependent, using only the non-bonded for the calculation of U_{mix} may result in the neglect of important interactions for mixing. The total potential energy used in this work is therefore expected to give a more accurate estimate of U_{mix}. To facilitate comparison between the different solvents, we have calculated an effective χ_{FH} for which the volume of a lattice site was assumed to be the volume of a CF molecule, calculated as the total volume of a pure CF system divided by the number of solvent molecules in that system (1000).

As eqn. (5.2) includes the energy of pure polymer and solvent systems, simulations of these pure phases, as well as the polymer–solvent mixtures were required in order to calculate χ_{FH}. For the pure solvent simulations, systems of 1000 solvent molecules were set up by placing the molecules with random position and orientation in a cubic simulation box at low density (see SI Table S5.6 for simulation box sizes). The setup procedure outlined above was followed (with shrinking over 100 ps, expansion over 20 ps) and the final system simulated for 10–15 ns (or 80 ns for CF) at constant pressure and temperature (1 atm, 300 K), from which the total potential energy of the system was calculated. The time required for equilibration of this property was calculated using pymbar's timeseries module,[248,249] in which the equilibration time is calculated to maximise the number of uncorrelated samples (see ref. 250 for details), and the energy calculated only using data from this equilibrated period.

The structure of the pure polymer phase, whether amorphous or crystalline, has been shown to affect the value of Flory-Huggins parameters calculated from MD simulations.[130] However, as we are interested predominantly in the *relative* solubility of the N2200 variants in the different solvents rather than the absolute values, the choice of polymer structure is less important. We have used a monomer crystal (that is, monomers arranged in a crystalline structure) as the pure polymer phase in this work for consistency with the solution-phase simulations of monomers. The monomer-crystal was constructed by positioning monomer centers-of-mass at the approximate coordinates, and in the correct orientation, to give previously reported spacing in the π-stacking, lamellar stacking, and backbone directions for the N2200-A crystal.[129] For N2200-A, monomers were positioned at intervals of 15 Å in the direction along the backbone (10 monomers), 25 Å in the side-chain stacking direction (3 monomers), and 4 Å in the π-stacking direction (10 monomers) to give a crystalline structure containing 300 monomers. The same setup was used for the N2200-EO monomer-crystal, with the exception of using 16 Å spacing in the backbone direction. For the backbone (no side-chain) monomer-crystal, the π-stacking spacing remained at 4 Å, and the backbone at 16 Å, but the spacing in the side-chain direction was reduced to 11.5 Å. The initial box size was chosen to give exact continuation of this spacing into the adjacent periodic images. As these crystal structures as defined are not necessarily in a minimum energy structure, an annealing procedure was followed to attempt to reach the thermodynamic minimum. The energy of the monomer crystal was initially minimised, then the system simulated at constant volume and energy for 40 ps to initialise the packing. Particle velocities were assigned from a Maxwell-Boltzmann distribution at 300 K and the system heated at constant pressure (1 atm, box sizes in x, y, and z dimensions allowed to vary independently) from 300 to 450 K over 200 ps. The simulation was then run at 450 K for 2 ns at constant temperature and pressure before cooling slowly over 10 ns from 450 to 300 K. The system was then run at 300 K for 2 ns, from which the equilibrium properties were calculated (equilibration time again calculated using pymbar, based on the fluctuations of the total potential energy). Representative structures of all of these crystals as initially defined, and following the equilibration procedure, are given in the SI, Section S5.2.2.

Mixtures were simulated as 4 monomers (either N2200-A, N2200-EO, or the N2200 backbone without side-chains) at a polymer volume fraction of approx. 5% (approx. 600 solvent molecules, see SI Table S5.6 for exact numbers). Flory-Huggins theory is a lattice model that makes a number of assumptions, one of which is that, in the homogeneous mixture, lattice sites of type A interact with the other sites in the system, whether also of type A or B, in proportion to their relative volume fractions in the solvent. For this assumption to hold, the system should not

aggregate in the MD simulations used to calculate χ_{FH}, which can be particularly challenging in the poorer solvents. To prevent as much aggregation as possible, monomers were initially positioned in the center of four of the eight octants of a $(100\ \text{Å})^3$ box to start at maximum separation. As with the other simulations, the box was shrunk over 40 ps to high density, then expanded over 20 ps to the target density. The simulations were each run for 4 ns, over which time minimal aggregation was observed. The equilibration time was determined using pymbar[248–250] as described previously and the total potential energy calculated from the data after this time.

Finally, the solubility of backbone monomers (with no side-chains) in a "solvent" of side-chains, as well as the solubility of the free side-chains in each solvent, were studied using Flory-Huggins theory. The same setup procedure as outlined above for the monomer mixtures was followed in all cases. Pure side-chain systems contained 1000 side-chain molecules, while the backbone–side-chain mixtures were set up to have approximately the same polymer volume fraction as the simulations for the monomer–solvent Flory-Huggins theory calculations (4 monomers, approx. 300 side-chain molecules). Side-chain–solvent mixtures used 72 side-chain molecules in 3000–4000 solvent molecules to give approximately the same solute volume fraction as in the monomer simulations described in Section 5.2.2.1. See SI Table S5.6 for details.

5.2.2.4 Free energy calculations

A number of free energy calculations were conducted for N2200-A monomers in various solvents. These use the OPES methodology,[209] which, similar to metadynamics,[210] periodically deposits repulsive gaussians in collective-variable space in order to bias the system away from sampling regions it has already visited. All free energy calculations were conducted exactly as outlined in Chapter 4, using the PLUMED software package.[211,212] Free energies were calculated as a function of three collective variables: the backbone center-of-mass separation, and two angles that define the orientation of the monomers. These angles, $\theta_{v_1-v_2}$ and $\theta_{v_1-v_C}$, where v_1 and v_2 are the vectors normal to the plane of the NDI groups of monomers 1 and 2 respectively, and v_C the vector connecting the centers-of-mass of the NDI groups of each monomer, are defined in more detail in the SI Fig. S5.5.

5.3 RESULTS AND DISCUSSION

A number of differences have been reported experimentally between the behaviour of N2200-A and N2200-EO in different solvents, despite having the same backbone structure. Based on published UV-vis absorption spectra of N2200-A[22,25] and N2200-EO,[295] changing the side-chains appears to have a significant effect on the

solubility of the polymer, as well as potentially changing the aggregate structure in solvents where the polymers are comparably soluble. In Section 5.3.1 the differences between N2200-A and N2200-EO are examined in more detail: Section 5.3.1.1 highlights the differences in solubility of the backbone and side-chain components and how this influences the overall solubility of the polymer. The structure of the aggregate is discussed in Section 5.3.1.2. For both N2200-EO and N2200-A, experimental techniques show contradictory results under certain conditions. In CF, the UV-vis absorption spectrum of N2200-EO suggests that the polymer does not aggregate, while SEC shows the formation of structures with molecular weight exceeding that of a single chain.[295] Similarly for N2200-A, the UV-vis absorption spectrum in CN suggests no aggregation, while preliminary results using other experimental techniques show that significant aggregation does occur in this solvent.[296] Some possible explanations for the observed behaviour are given in Sections 5.3.2 and 5.3.3. This work highlights a number of challenges for both molecular simulation and experimental measurements of OSC polymers which will be discussed in Section 5.3.4.

5.3.1 comparison of n2200-a and n2200-eo

Despite their similar chemical structures, the UV-vis absorption spectra of N2200-A and N2200-EO (Fig. 5.2) indicate different solubility of the two polymers based on the red shift of the absorption maximum (especially in CF, in which N2200-A is poorly soluble while N2200-EO appears to be very soluble), as well as featuring significantly different shapes. The solubility difference is expected to be related to the relative solubility of the side-chains in the different solvents, which is examined in Section 5.3.1.1 using Flory-Huggins theory, though the exclusion of solvent from the backbone due to different side-chain structures has also been proposed to be a critical factor for polymer solubility.[161] The structure of the aggregates of each polymer in a selection of these solvents is examined in Section 5.3.1.2, and can be used to explain the differences in the absorption spectra of the two polymers.

5.3.1.1 Backbone and side-chain Flory-Huggins parameters

The difference between the relative solubilities of N2200-A and N2200-EO was examined using Flory-Huggins theory. Although often used to determine the overall solubility of a polymer (e.g. refs 129, 130), here we extend this analysis to examine the relative solubilities of the backbone and side-chains, and relate this to the solubility of the entire monomer. This separation into backbone and side-chain Flory-Huggins parameters highlights the importance of the chemical nature of both the side-chain and backbone for the design of OSCs with a particular microstructure, and also some of the limitations of Flory-Huggins theory. In the analysis that follows,

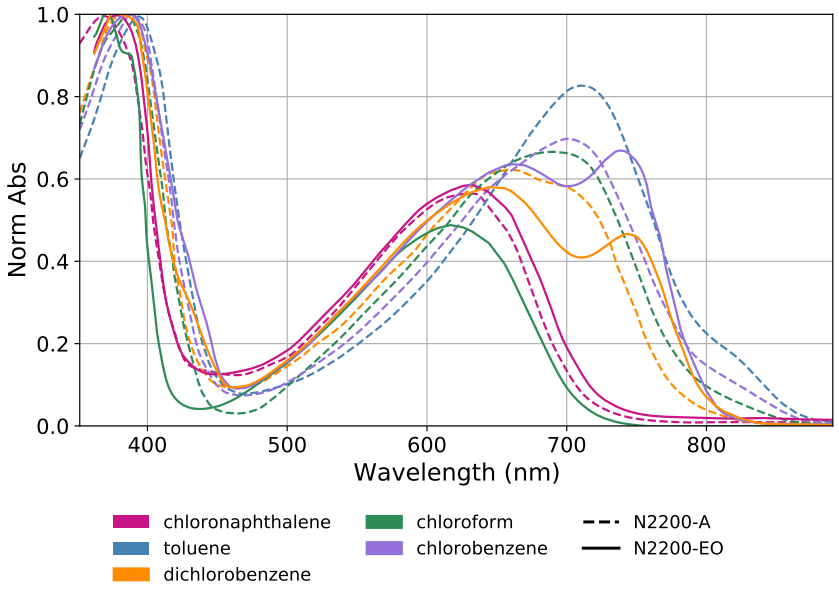

Fig. 5.2 Experimental UV-vis absorption spectra of N2200-A (dashed lines) and N2200-EO (solid lines) at room temperature, reproduced from refs 25 and 295, respectively.

we consider only the relative values of the Flory-Huggins parameters as the absolute values are expected to strongly depend on the choice of pure polymer phase,[130] which will be discussed further below.

We first address the difference in solubility between N2200-A, and N2200-EO, which we propose is due to differences in the relative solubility of the backbone and side-chains. Examining the Flory-Huggins parameters of the different components (backbones and the two types of side-chains), and the entire monomers, showed solubility trends consistent with the red shifts in the UV-vis measurements (Fig. 5.3):[22,25] N2200-A showed greater solubility than N2200-EO in CN (although the Flory-Huggins parameters are within error), poorer solubility in CF, and similar solubility in CB. In the absence of side-chains, the backbone showed poor solubility in all three solvents, though was most soluble in CN. The greater solubility in CN can be explained by the chemical similarity of the naphthalene ring of CN and the NDI group of the backbone, which likely results in strong solvent–backbone interactions as has been discussed previously.[129] The Flory-Huggins parameters of the side-chains, combined with the previously obtained backbone parameters, are consistent with the different solubility of the overall polymers. The good solubility of the A side-chains, combined with the better solubility of the backbones in this solvent compared to other solvents, means the lack of aggregation of N2200-A in CN, as suggested by the UV-visible absorption spectrum, is not unexpected. Similarly, the poorer solubility of the A side-chains in CB and CF relative to CN, combined with

the poorer solubility of the backbones, is consistent with the poorer solubility of the entire monomer. In comparison, the EO side-chains showed much greater solubility in CF than the other solvents. These highly soluble side-chains explain the lack of observed aggregation (from the absorption spectrum) of the overall N2200-EO monomer in this solvent compared with either of the other solvents despite the comparatively less soluble backbone. The poorer solubility of the EO side-chains in CN and CB is again translated to poorer solubility of the entire monomer.

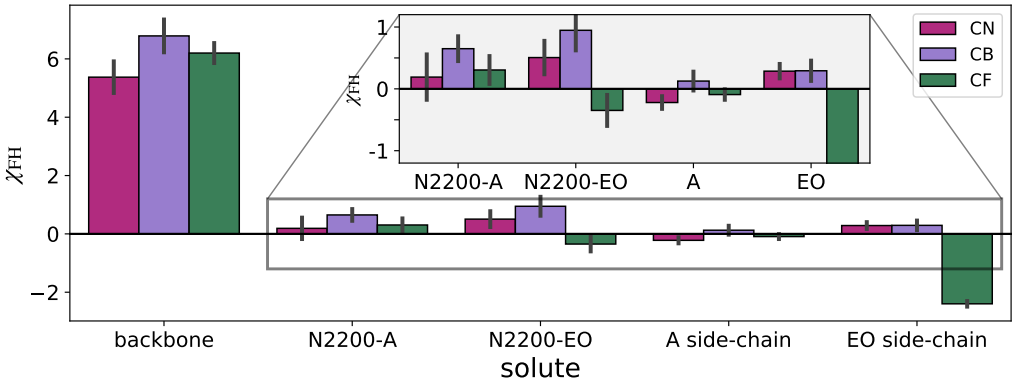

Fig. 5.3 Flory-Huggins parameters, χ_{FH}, of the polymers with the two different side-chains (N2200-A, and N2200-EO), and the individual components of the polymers (backbone, A side-chain, EO side-chain) in 3 solvents of interest (1-chloronaphthalene (CN), chlorobenzene (CB), and chloroform (CF)). Error bars are ± two standard errors.

All of the behaviour described above is consistent with the UV-vis absorption spectra of N2200-A and N2200-EO, though it does not explain the potentially contradictory behaviour of N2200-EO in CF, or N2200-A in CN, for which different experimental techniques give contrasting predictions of the solubility. Nor can it explain the different shaped spectra for N2200-A and N2200-EO. While it therefore seems that Flory-Huggins theory performs relatively well for predicting the solution-phase behaviour of OSCs as has been shown in the past[128–130] – at least compared with UV-visible absorption data – it does not necessarily tell the whole story.

At this point, we note that there are a number of limitations to Flory-Huggins theory which must be considered when analysing the results presented above. Firstly, as discussed briefly earlier, Flory-Huggins theory is a lattice model which assumes that each site in the homogeneous mixture interacts with other sites in proportion to their volume fractions. The use of an off-lattice simulation technique like MD means that this is not necessarily the case. Though we have ensured that aggregation in the mixture simulations is minimal, the vast discrepancy between the sizes of the molecules, where in the most extreme case, an N2200-A monomer is approx. 11 times the size of a CF molecule, means that the distribution of lattice sites will

never be homogeneous (Fig. 5.4). This problem is exacerbated for polymer chains, in which monomers are bonded together, pushing the system further from the ideal case of homogeneously distributed lattice sites. For this reason, we have used monomers to calculate the Flory-Huggins parameter, while previous studies have used oligomers.[129,130]

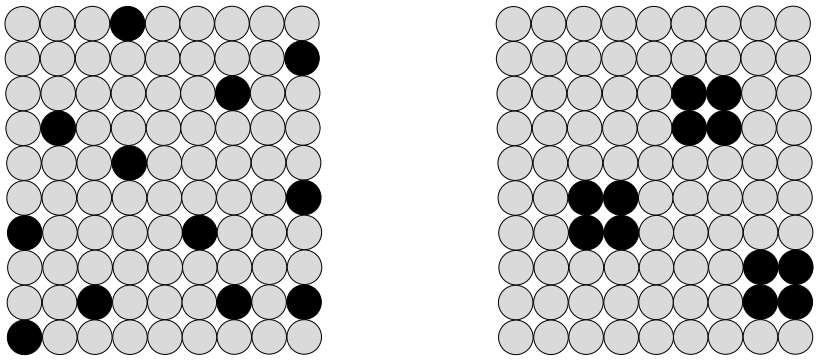

(a) Ideal behaviour **(b)** Actual behaviour

Fig. 5.4 Representation of the (a) ideal (homogenous distribution of lattice sites) and (b) actual (homogenous distribution of monomers) behaviour of the lattice model used here for Flory-Huggins theory calculations. Note that we have represented the system as a lattice in this diagram, but this is also an assumption that is not directly applicable to MD, which is by nature an off-lattice technique.

Secondly, although not necessarily an assumption of the theory itself, the structure of the pure polymer phase must be assumed in the MD simulations used in the calculation of χ_{FH}. Importantly, different structures, whether amorphous or crystalline, have been recently shown to give different absolute values of χ_{FH} for OSC polymers.[130] We have assumed crystalline structures of the polymers and backbone, while the solvents and the pure side-chain systems were liquids at the simulation temperature (300 K). In terms of comparing the *relative* solubilities of a specific polymer in different solvents, the choice of pure polymer phase is unimportant as it will only affect the absolute values of χ_{FH}, i.e. changing the structure of the pure polymer phase will shift the values of χ_{FH} up or down by the same amount for each solvent. This does, however, mean that quantitatively comparing the values between different polymers (or between polymer, backbone, and side-chain) is less straightforward. The effect of the pure polymer structure on Flory-Huggins parameters of OSC polymers has been recently studied so will not be discussed further here.[130] Nevertheless, despite the many associated assumptions, Flory-Huggins theory has proven to generally provide accurate predictions of the mixing of OSC solutions.[128–130]

As mentioned previously, calculations of Flory-Huggins parameters from MD have, in the past, used only the cohesive energy density, rather than the total

potential energy, to calculate U_{mix}, and accordingly χ_{FH}.[129] While this appears to have given reasonable results, it ignores the possible effect of changes in the bonded distributions (bond lengths, angles, and dihedrals), that may occur on aggregation, on the mixing energy. Additionally, in parameterising an MD force-field, dihedral and non-bonded potentials are arbitrarily partitioned. This means that important contributors to the non-bonded energy could be neglected if not considering changes in dihedral potentials that occur on mixing. It is therefore important that these bonded interactions are also accounted for in order to obtain a reliable estimate of χ_{FH}. These interactions have been included in this work by using the total potential energy (that is the inter- and intramolecular non-bonded interactions, plus the bonded energies) for the calculation of U_{mix}. It should be noted, however, that if the intramolecular conformation does not change significantly between the pure systems and the mixture, these intramolecular interactions should not contribute to the calculated Flory-Huggins parameter.

5.3.1.2 Aggregation behaviour

Although Flory-Huggins parameters calculated from MD have recently been shown to correlate relatively well to the aggregation properties of specific OSC polymers,[130] other studies have shown that solubility parameters (albeit the simpler Hildebrand solubility parameter rather than χ_{FH}) do not accurately predict the experimental solubility of these polymers.[161] The work presented in the previous section showed that Flory-Huggins parameters were consistent with the UV-vis absorption spectra of N2200-A and N2200-EO, but the different shapes of the spectra could not be explained through this simple theory. Flory-Huggins theory also could not provide any evidence for why CF may be a poor solvent for N2200-EO, and CN for N2200-A, despite the absorption spectra (and Flory-Huggins parameters) suggesting that both of these polymer–solvent pairs should be highly miscible. Examining the structure of aggregates of N2200-A and N2200-EO in the various solvents, a number of differences between the behaviour of the two polymer derivatives were observed. These differences are useful for understanding the differences between the absorption spectra of the two polymers.

EO side-chains wrap around the N2200 backbone. The first of the observed differences between N2200-A and N2200-EO is the wrapping of the EO side-chains around the monomer backbone in all three solvent studied, which does not occur for N2200-A (Fig. 5.5). The prevalence of this wrapping behaviour was confirmed by the analysis of the distribution of side-chain atoms relative to backbone atoms (Fig. 5.6), which shows the clear preference for EO side-chains to interact with the backbone, while A side-chains remained extended. Note that this behaviour was most significant in CF, but was also observed for N2200-EO in CB, albeit to a slightly lesser extent, and even

slightly in CN. The reduced prevalence of this side-chain wrapped structure in CB and CN is likely due to the stronger backbone–solvent interactions in the aromatic solvents. Side-chain wrapping was never observed for N2200-A. Side-chain position distributions for the other solvents and polymers can be found in the SI Fig. S5.6.

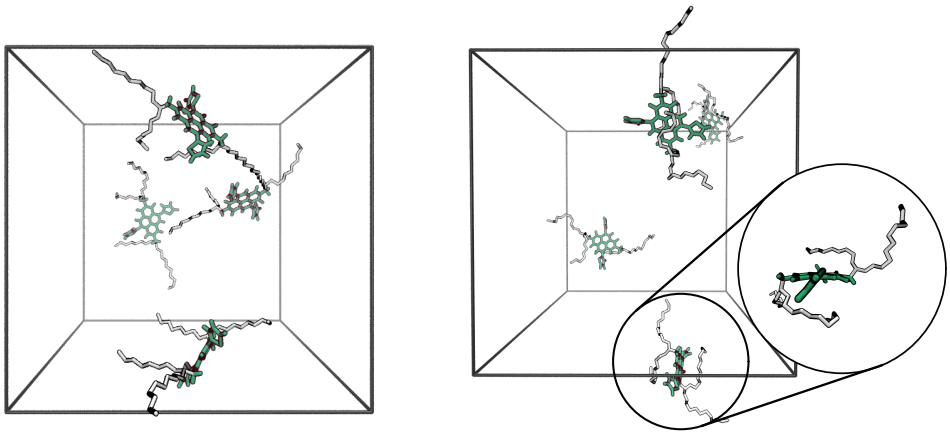

(a) N2200-A in CF **(b)** N2200-EO in CF

Fig. 5.5 Snapshot of a simulation of 4 monomers of (a) N2200-A and (b) N2200-EO in CF (solvent molecules and side-chain hydrogens removed for clarity). The side-chains of N2200-EO are observed to wrap around the backbone, effectively shielding it from interactions with the solvent, while those of N2200-A remain extended.

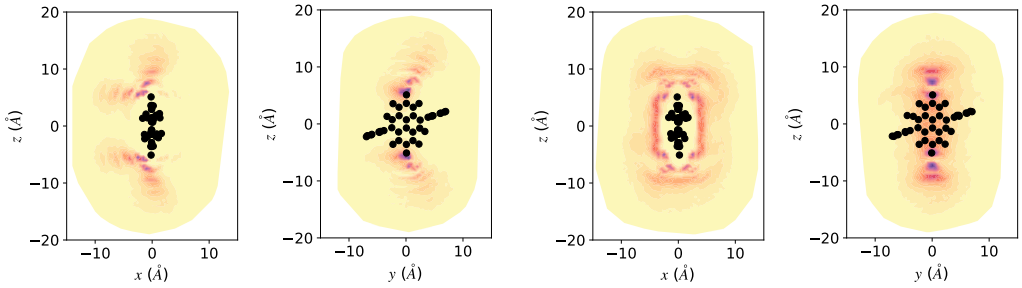

(a) N2200-A **(b)** N2200-EO

Fig. 5.6 Probability distribution of side-chain atom positions around the backbone for both (a) N2200-A and (b) N2200-EO in CF from a side-on (in xz plane) or front-on (in yz plane) perspective, calculated from the simulations of 4 monomers used for the Flory-Huggins theory simulations. Darker colours indicate higher probability of finding side-chain atoms in that position, with the same colour scale used across all four plots. The positions of the backbone atoms are given as black circles.

The side-chain position probability distributions can be converted to a free energy in order to determine an approximate free energy preference for side-chain wrapping for N2200-EO relative to N2200-A, and in the different solvents. The free

energy preference for side-chain wrapping has been calculated here as the difference between the free energy of an extended chain compared with a wrapped one. The probability distribution of just the 6–8th heavy atoms in each of the side-chains (where the first side-chain atom is the one directly bonded to the tertiary carbon, see Fig. 5.1) was used to calculate the free energy as these atoms are expected to be those that interact most closely with the backbone when wrapped. Side-chain atoms were considered to be in a wrapped configuration when between $x = \pm 6$ Å, $y = \pm 4$ Å, and $z - \pm 4$ Å (where the center of mass of the N2200 backbone is at $x = y = z = 0$). The unwrapped configuration was defined for regions of the same total volume with the same x and y limits, but with $8 < z < 12$ and $-12 < z < -8$ Å, chosen to capture the region of highest probability of the three side-chain atom positions in the z dimension. The x, y, and z coordinates are as shown in Fig. 5.6. The free energy preference for side-chain wrapping was then calculated from the probabilities of the selected side-chain atoms existing in either the wrapped (P_{wrapped}) or extended (P_{extended}) regions as $\Delta G = -k_{\text{B}} T \ln(P_{\text{wrapped}}/P_{\text{extended}})$. While we emphasise that this measure is qualitative, giving the relative stability of the two different structures, with the absolute value depending strongly on the choice of region used to define wrapped and unwrapped side-chains, in the most extreme cases, the wrapping of side-chains is up to 0.5 kcal/mol more favourable compared to remaining extended for N2200-EO, while remaining extended is up to 0.75 kcal/mol more favourable than wrapping for the N2200-A side-chains.

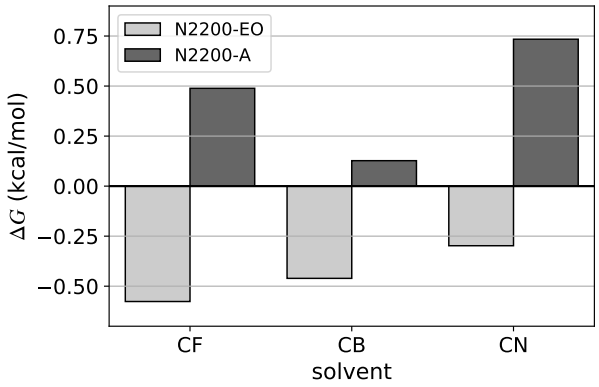

Fig. 5.7 Free energy difference between wrapped and extended side-chains. A negative value indicates side-chain wrapping is favoured. The free energy difference is calculated from the probability of side-chain atoms being in the regions $-6 < x < 6$ Å, $-4 < y < 4$ Å, and $8 < z < 12$ Å (and $-12 < z < -8$ Å) for the extended chains, and $-6 < x < 6$ Å, $-4 < y < 4$ Å, and $-4 < z < 4$ Å for the wrapped chains.

As the backbone and solvent are the same for both N2200-A and N2200-EO, the side-chain wrapping must be attributed to either changes in the side-chain–solvent, or side-chain–backbone, interactions. In this case, the cause appears to be

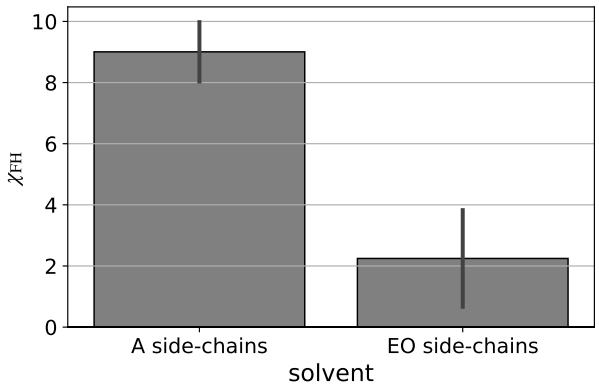

Fig. 5.8 Flory-Huggins parameters calculated for the backbone–side-chain systems where backbone monomers were immersed in a "solvent" of side-chains.

the strength of the side-chain–backbone interactions, which are strong enough to displace a solvent molecule and give the wrapped structure. The relative strength of the A side-chain–backbone and EO side-chain–backbone interactions were investigated through calculation of χ_{FH} of backbone monomers (with no side-chains) immersed in a "solvent" of side-chains (Fig. 5.8). Based on the difference between the Flory-Huggins parameters, the EO–backbone interactions were much stronger than those between the A side-chains and backbone. For solvents such as CF and CB, in which the backbone–solvent interactions are relatively weak (higher χ_{FH}, see Fig. 5.3), this leads to a strong preference for side-chain wrapping. As backbone–solvent interactions become stronger, such as in CN, the preference for wrapped side-chains diminishes as it becomes more difficult to displace a solvent molecule.

An alternative explanation for the side-chain wrapping behaviour is that the EO side-chains are less soluble than the A side-chains, with side-chain wrapping resulting in the structure which minimises side-chain–solvent interactions. However, calculations of the Flory-Huggins parameter indicates that EO side-chains are much more soluble than A side-chains in CF (Fig. 5.3), suggesting that less soluble side-chains are not the predominant cause for the side-chain wrapping.

Based on previous work studying the effect of side-chain structure on polymer solubility,[161] side-chains that exclude solvent from the backbone are expected to increase the solubility of the polymer. The wrapping of EO side-chains around the backbone has this solvent-excluding effect and is therefore expected to increase the solubility of N2200-EO even further than what could be expected from energetics alone in solvents such as CF and CB. This increased solubility would not be captured by Flory-Huggins theory, again highlighting the importance of not considering Flory-Huggins theory a black box for predicting the solubility of OSCs.

EO side-chains disrupt backbone packing. Differences in the experimental UV-vis absorption spectra for N2200-A and N2200-EO under conditions in which they both show aggregation (e.g. in CB, see Fig. 5.2) indicate that the structure of the aggregated polymer may vary with side-chains. Given the observed wrapping of the EO side-chains around the N2200 backbone, it stands to reason that the aggregate structures will be different. As the aggregation process is expected to be slow, and the system size for solvated systems of oligomers prohibitively large to reach the necessary timescales, the effect of the observed side-chain wrapping on the structure of the aggregate was examined through simulation of systems of 6mers beginning in a fully aggregated state. Stacks of three chains were considered in order to mimic a crystal-like environment where a chain interacts with other polymers on each face. Two key differences were observed between the behaviour of N2200-EO and N2200-A 6mer aggregates: greater structural disorder and a shift of the peak in the NDI–NDI radial distribution function (RDF) to shorter separation for the polymer with EO side-chains, and significant planarisation of the N2200-A backbone which was not observed for N2200-EO (Fig. 5.9).

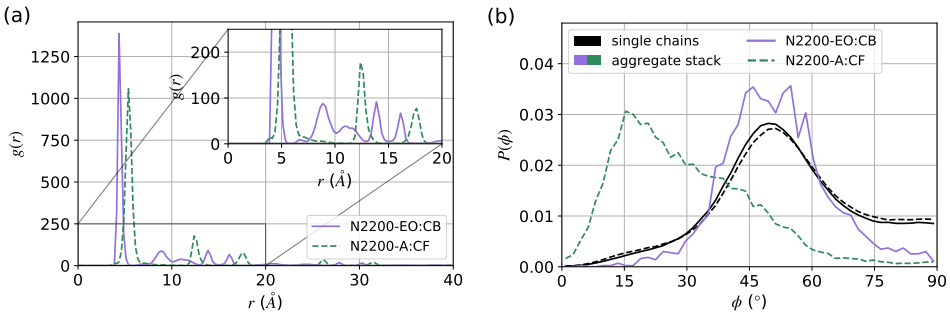

Fig. 5.9 Comparison of some properties of the aggregate structure of N2200-A and N2200-EO in solvents where aggregation unambigously occurs (CB for N2200-EO and CF for N2200-A). (a) NDI–NDI RDF, $g(r)$, calculated between NDI groups in the central chain (sandwiched between the other chains) and NDI groups in either of the other chains of N2200-EO (purple, solid line) or N2200-A (green, dashed line). (b) NDI–Th dihedral distribution. The dihedral is defined as in Chapter 4. The behaviour of this dihedral in the central chain in the aggregate stack (green or purple) or in a system starting from random positions of chains where no aggregates with a fully surrounded chain are observed (black) is shown for N2200-EO (lines) or N2200-A (dashed lines).

Examining the RDFs of N2200-EO and N2200-A in solvents where aggregation is unambigously known to occur (CB for N2200-EO and CF for N2200-A; Fig. 5.9a) showed strong crystalline ordering of N2200-A in this solvent (and indeed in all solvents studied in this work, Fig. S5.7a). While N2200-EO was also quite crystalline, some disorder was observed (e.g. the region at around r = 10 Å). This disorder corresponds to a shift of one of the outer aggregate chains away from the directly

stacked structure in order to allow for the side-chains to interact more readily with the backbones. This third chain eventually almost fully dissociated in both CF and CB over the course of 80–100 ns. In comparison, all three of the N2200-A backbones remained almost fully aggregated in a highly crystalline structure over the entire simulation (up to almost 120 ns in CF), though the NDI groups were slightly offset (shifted marginally towards a structure in which NDI groups stack over Th groups; see SI Fig. S5.8) relative to the structure of the N2200-EO aggregate. The slightly offset structure for N2200-A resulted in the large peak in the RDF being shifted to larger separation. However, given that even a full shift from a NDI–NDI-stacked to NDI–Th stacked structure results only in subtle changes to the UV-vis spectrum,[294] this slight displacement is unlikely to be the major cause for the differences in the UV-vis spectra.

More significant changes were observed when examining the dihedral distribution for the dihedral between the NDI and Th groups within the central chain of the stacked aggregate (Fig. 5.9b). Planarisation of the N2200-A backbone has been previously reported as a significant contributor to the spectral shift in the UV-visible absorption spectrum.[22] Comparing the distribution of the NDI–Th dihedral in unaggregated (or at most aggregated with one other chain) oligomers with the same dihedral in the central chain of the stack of 6mers showed significant planarisation of the N2200-A backbone, as well as a restriction of the rotation about the NDI–Th bond in the aggregated stacks compared with the unaggregated chains. While the rotation about the bond was similarly restricted in aggregated N2200-EO, planarisation was not observed, with the dihedral distribution peaked around approximately the same angle as the unaggregated chains. Note that the planarisation of the N2200-A backbones was only observed for the central chains (i.e. those that had another chain on each face) for both N2200-A and N2200-EO. The exterior chains showed behaviour that was much closer to that of the unaggregated chains.

The effect of polymer conformation and aggregate morphology on the UV-vis absorption spectrum can be understood through analysis of the relative amounts of inter- and intrachain coupling.[293,298] Where intrachain coupling dominates, the aggregate can be considered to be J-like in character (characterised by a red shift and a stronger 0-0 – lower energy – vibronic peak), while strong interchain coupling gives a more H-like aggregate (characterised by a blue shift and a stronger 0-1 – higher energy – vibronic peak). In reality, the aggregate is likely to fall between these two extremes giving intermediate H-J aggregates in which the observed spectral shift and vibronic features will be a result of the relative amounts of the competing H and J character of the aggregate.[293,298]

Examining the effect of aggregation on the intrachain behaviour of N2200-EO and N2200-A, the significant planarisation of the N2200-A backbone is expected

to result in both a red shift and an increase in the 0-0 vibronic peak as aggregation occurs. This is due to the stronger intrachain coupling that is expected to be induced by the backbone planarisation, as has been studied previously.[22] Assuming the peak at approx. 810 nm in the N2200-A spectra in CF, CB, and TOL (Fig. 5.2) corresponds to the 0-0 vibronic peak, the observed red-shift and the emergence of this peak as solvent quality decreases agrees well with the behaviour observed in the simulations. However, the size of the N2200-A 0-0 peak is small, especially compared with the N2200-EO spectra, in which the higher wavelength peak is much more significant despite the weaker intrachain coupling expected due to the lack of backbone planarisation. The large 0-1 peak for N2200-A suggests that the H-character of this polymer is significantly greater than in N2200-EO, and sufficient to greatly enhance the size of the 0-1 peak relative to the 0-0 peak in the N2200-A spectra. Our MD simulations of aggregates support this behaviour, with the greater disorder in the N2200-EO aggregates expected to reduce interchain coupling relative to the highly crystalline N2200-A aggregates. It also appears that the locking of backbone dihedrals in N2200-EO enhances the intrachain coupling sufficiently that its strength is on the order of the weaker interchain coupling, despite the absence of backbone planarisation.

Overall, the different shapes of the UV-vis absorption spectra of N2200-A and N2200-EO can be explained in terms of the behaviour of aggregated chains. N2200-A formed a highly crystalline aggregate with a more planar backbone, resulting in increasing J-character as aggregation occurs whilst maintaining strong H-character due to the crystallinity. On the other hand, N2200-EO formed a more disordered structure, likely due to the strong side-chain–backbone interactions, in which H-character is reduced enough that the 0-1 and 0-0 peaks are roughly equal in size despite the weaker intrachain coupling compared with N2200-A.

5.3.2 N2200-A in chloronaphthalene

While the previous section highlights the differences between the aggregate structures of N2200-A and N2200-EO, and the effects this may have on the measured UV-vis absorption spectrum, neither Flory-Huggins parameters, nor the structures observed when starting from already-aggregated polymer chains, appear to give any insight into the experimentally reported behaviour of N2200-A in CN. The UV-visible spectrum of N2200-A in this solvent suggests that the polymer does not aggregate, while the observation of precipitates at low polymer concentration show CN to be a poor solvent for N2200-A.[296] Based on observations from unbiased MD simulations of monomers, we propose an aggregation mechanism through which a CN molecule becomes sandwiched between two N2200-A backbones. This solvent-separated structure would prevent the direct backbone aggregation that

results in changes to the UV-vis absorption spectrum whilst still giving extensive aggregation that may be observed through other experimental techniques. The solution-phase behaviour of N2200-A was examined in various solvents, observing transient solvent-separated structures only in CN, though not the formation of persistent aggregates (Section 5.3.2.1). To attempt to further explain this behaviour, the strength of the polymer–solvent interactions were examined through the analysis of Flory-Huggins parameters (Section 5.3.2.2). As this proved to be inconclusive, more extensive free-energy calculations were conducted to determine the existence of any possible free-energy minima that may explain the experimental discrepancies (Section 5.3.2.3).

5.3.2.1 Observation of solvent-separated structure

The discrepancy between experimental results – with UV-visible spectroscopy showing no aggregation of N2200-A in CN, while precipitation methods suggest that it is insoluble in this solvent – is expected to be due to aggregation that occurs in such a way that the backbones are not electronically coupled and therefore gives no shift in the UV-vis absorption spectrum. In examining the trajectories of monomer simulations in this solvent, we observed the formation of semi-persistent solvent-separated structures, in which two N2200-A monomers were separated by a single solvent molecule sandwiched between the backbones (Fig. 5.10). The RDF of monomers (measured as the RDF of centers-of-mass of the backbone atoms) and the orientation of monomer pairs as a function of center-of-mass separation (Fig. 5.11), showed a small peak in the RDF of N2200-A in CN at the separation corresponding to the solvent-separated structure (≈ 7.5 Å). The orientation of pairs at this separation also showed a preference for a close-to face-face alignment, which was not observed in either DCB or TOL. The peak in the RDF in all three solvents at approx 10–15 Å corresponds to the interaction between monomer thiophene groups, which is an effect that is expected to be significantly reduced in oligomers (see SI Fig. S5.10 for RDFs of 6mers).

While this solvent-separated structure was observed, and may explain the experimental discrepancies (the interdigitated solvent molecule preventing electronic coupling of the backbones), it appeared only transiently in monomer simulations, persisting for only approx. 10 ns, with no build up of aggregates containing this motif observed. It is possible that these transient sandwich structures, though not strong enough to hold monomers together over long timescales, may, if many form between a pair of longer oligomers, be sufficiently strong in concert that they can hold longer chains together in such a way that larger aggregates can form. We have therefore examined the aggregation behaviour of 6mers, beginning with randomly positioned and oriented oligomers. Again, a small peak was observed at 7.5 Å

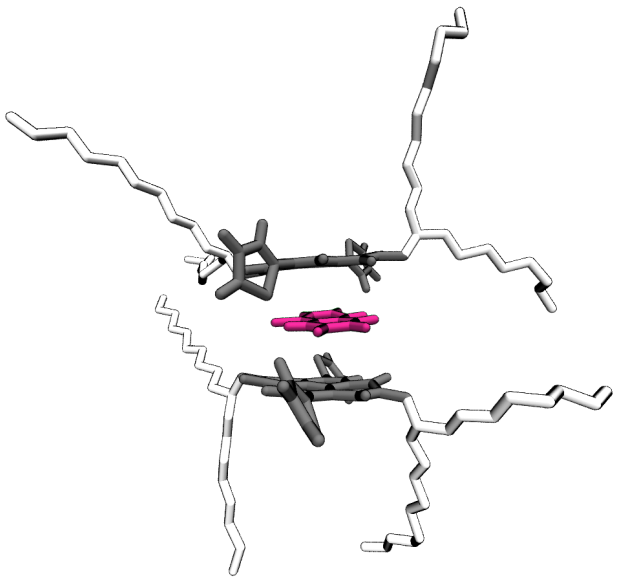

Fig. 5.10 Representative structure of the N2200-A–CN solvent-separated structure taken from the monomer simulations of N2200-A in CN. Side-chain hydrogens and all other solvent molecules are removed for clarity. Backbone atoms are coloured dark grey, side-chains white, and the CN molecule pink.

with orientation corresponding to the solvent-separated structure (see SI Fig. S5.10). However, these structures were not particularly persistent, again lasting only approx. 10 ns. Notably, the proposed structure in which chains are held together by multiple solvent-separated monomers was never observed, with all observed instances of a solvent-separated structure occurring between terminal monomers of oligomers. The absence of the multi-solvent separated structure may possibly be attributed to the relatively short timescale of the simulations (on the order of 60 ns). However, due to the large size of the fully solvated systems, it is difficult to go far beyond this timescale to observe the long-time behaviour which may be more indicative of the experimental behaviour.

In an attempt to circumvent the timescale limitation, simulations were conducted in DCB (a good solvent in which aggregates should not be stable) and CN (in which the solvent-separated structure may be stable) with three polymer chains initialised in a solvent-separated stack. The fully-overlapping sandwich structure persisted for at least 40 ns in CN (the entire simulation length), while the same structure in DCB dissociated within 10 ns. After the 40 ns simulation in CN, the structure was not significantly different from the starting structure, giving no indication that it would dissociate on even longer timescales. While not conclusive, the persistence of this solvent-separated polymer stack suggests that, when involving multiple monomer–solvent–monomer interactions, the solvent-separated structure may be sufficiently stable that it could lead to the build up of extended aggregates. A representative

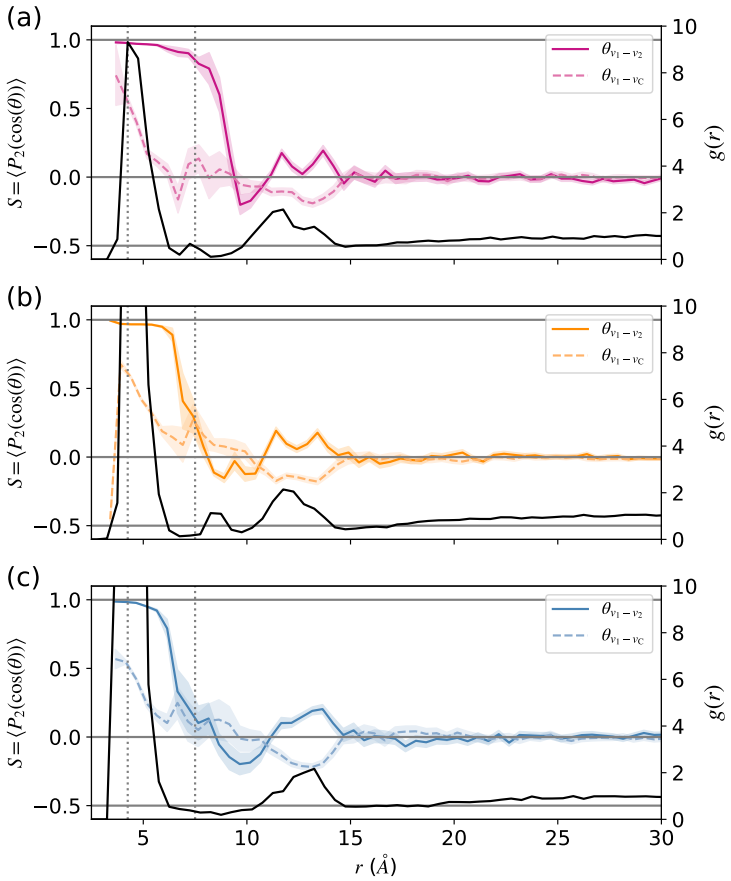

Fig. 5.11 Average orientation of monomer pairs in (a) CN, (b) DCB and (c) TOL at separation r ($S = \langle P_2(\cos(\theta)) \rangle$, coloured lines, averaged over time) defined by two angles: $\theta_{v_1-v_2}$, the angle between the vectors normal to the plane of each monomer's NDI group, and $\theta_{v_1-v_C}$, the angle between the normal to the plane of the NDI group of one monomer, and the vector connecting the two monomer's centers-of-mass (see Fig. S5.5 for pictorial definition). θ is the angle between the two vectors in each case. A value of $S = 1$ indicates that the vectors are parallel, and $S = -0.5$ that they are perpendicular. Randomly oriented monomers will have $S = 0$. The RDF, $g(r)$, is shown as a black line. In DCB and TOL, the tops of the RDFs are cut off to better observe the behaviour corresponding to the potential solvent-separated structure at approx $r = 7.5$ Å. The full RDFs are shown in the SI Fig. S5.9a. Vertical dashed lines indicate the separations that roughly correspond to a face-face pair (4.25 Å), or a solvent separated pair (7.5 Å).

snapshot of the solvent-separated structure of N2200-A in CN is shown in Fig. 5.12. Although not all pairs of monomers appear to be separated by a solvent, enough are that the aggregate appears to be stable and not prone to either collapse into the fully aggregated structure, or separation into single chains. In some cases in which a solvent molecule was not observed between monomer backbones, the side-chains (not shown) penetrated into the aggregate structure instead.

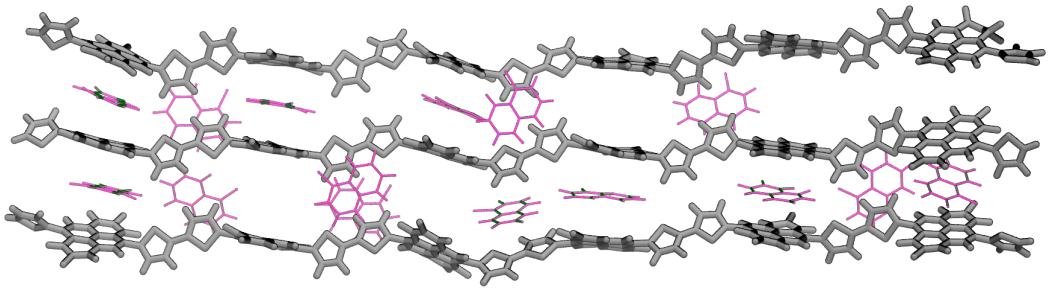

Fig. 5.12 Snapshot of the solvent-separated structure of N2200-A in CN beginning from this structure. Snapshot is taken after 40 ns of simulation. Side-chains are not shown for clarity. Only solvent molecules within 4 Å of the backbone atoms of two different oligomers are shown, and are coloured pink.

Comparing the dihedral distribution of N2200-A in the CN sandwich structure with that of either the conventionally π-stacked aggregate or the unaggregated chains shows that intramolecularly, the solvent-separated aggregate behaved similarly to unaggregated chains (Fig. 5.13). This suggests that the solvent molecule separating the N2200 backbones is able to prevent the restriction of rotation about the NDI–Th bond that appears to be a significant contributor to the spectral shifts observed on aggregation, as discussed earlier in Section 5.3.1.2. The formation of this kind of aggregate is therefore likely to not show significant changes in the UV-vis absorption spectrum relative to an unaggregated chain.

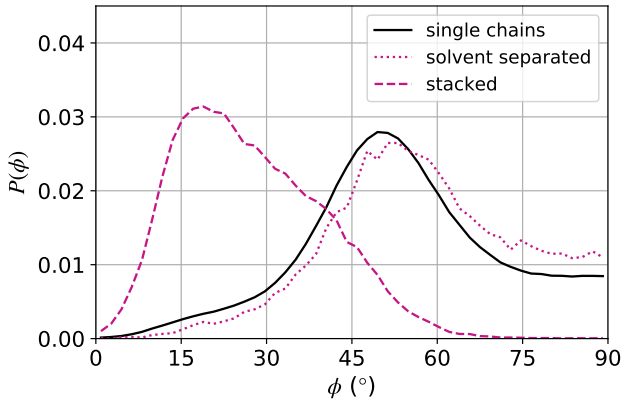

Fig. 5.13 NDI–Th dihedral distribution for N2200-A chains in the solvent-separated aggregate (dotted line), fully aggregated (dashed line) structure, or free in solution (black solid line).

5.3.2.2 Relative solvent–backbone interaction strength

In order to understand why the solvent-separated N2200-A structure may form in CN, but not in other solvents, Flory-Huggins parameters for various N2200-A–solvent mixtures were calculated. Flory-Huggins parameters were calculated as

described in Section 5.3.1.1 for the comparison of N2200-EO and N2200-A. Three different solvents were considered: CN, the solvent for which experimental techniques show discrepancy and UV-visible spectrum indicates no aggregation; DCB, in which the UV-visible spectrum indicates low aggregation; and TOL, in which UV-visible spectrum indicates extensive aggregation. We have again broken the Flory-Huggins parameters down into parameters for the backbone and side-chain components, as well as the entire monomer (Fig. 5.14). The relative Flory-Huggins parameters are again consistent with the behaviour predicted by the UV-vis absorption spectrum: poor solubility in TOL, and much better solubility in CN and DCB. Based on the behaviour of the backbone and side-chains individually, these solubility trends can be attributed to the better solubility of both the side-chains and backbone in CN and DCB.

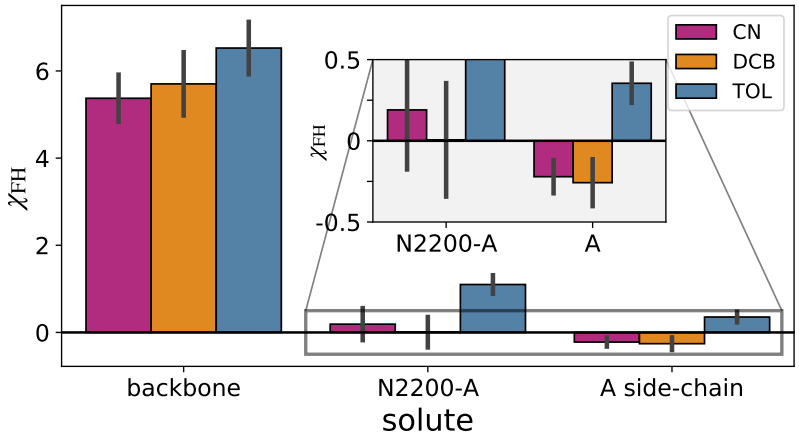

Fig. 5.14 Flory-Huggins parameters for the N2200 backbone, N2200-A, and the A side-chains in CN, DCB, and TOL.

The lower values of χ_{FH} for the N2200 backbone in CN suggest strong backbone–solvent interactions, which is a requirement for the formation of the solvent-separated structure. Examining the distribution of solvent molecules directly above the backbone (Fig. 5.15) a stronger preference for CN, compared with the other solvents, to interact with the plane of the NDI group of N2200-A was observed. This is consistent with behaviour observed previously[129] where CN molecules were seen to interact strongly with the backbones of N2200-A. Although not conclusive evidence for the formation of the solvent-separated structure in CN, it is plausible that the strong backbone–solvent interactions may lead to this unexpected behaviour.

5.3.2.3 Free-energy calculations

Although the unbiased simulations presented above provide some circumstantial evidence for the formation of a stable solvent-separated structure that would explain

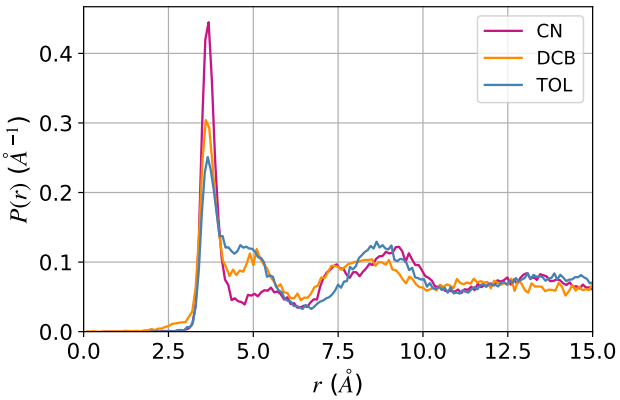

Fig. 5.15 Probability density of finding a solvent molecule directly above the plane of the NDI group of a monomer at distance r, where r is the is the x component (perpendicular to the plane of the NDI group) of the center-of-mass separation. Given a monomer where the plane of the NDI group is in the yz plane, r is the absolute distance in the x direction between solvent and NDI centers-of-mass for all solvents with $|y| < 5$ Åand $|z| < 5$ Å. This restriction on the y and z coordinates approximately selects only particles that are directly above the plane of the NDI group. The probability density was calculated from the monomer simulations used for the Flory-Huggins theory calculations where little aggregation was observed over the timescale of the simulations (4 ns). As aggregation occurs over time, the distribution of solvent directly above the NDI group is expected to change as it is displaced by other monomers.

the conflicting experimental results,[296] the transient nature of these structures casts some doubt onto their relevance for aggregation over an experimental timescale. Additionally, as large-scale simulations of longer oligomers are hampered by both the large system size required to fully solvate these longer chains and the slower diffusion of the longer polymer, potential solvent-separated structures – in which chains are connected through multiple instances of this behaviour – become challenging to observe. This is largely due to the timescale required for favourable oligomer–solvent–oligomer encounters. However, if these multi-monomer solvent-separated structures *are* able to be formed under equilibrium conditions, they do appear to be stable based on the behaviour of simulations starting from the solvent-separated aggregate of 6mers. To obtain a better understanding of the equilibrium behaviour, we have mapped the full distance and orientation dependent free-energy landscape for a pair of solvated monomers.

The free-energy calculations described in this section use the OPES method,[209] biasing the backbone (NDI and Th groups) center-of-mass separation between the two monomers, and the three angles defined in Fig. S5.5: $\theta_{v_1-v_2}$, $\theta_{v_1-v_C}$, and $\theta_{v_2-v_C}$. Free energy surfaces as a function of combinations of $\theta_{v_1-v_2}$, $\theta_{v_1-v_C}$, and separation for N2200-A in CN are shown in Fig. 5.16. Additional plots at shorter separation

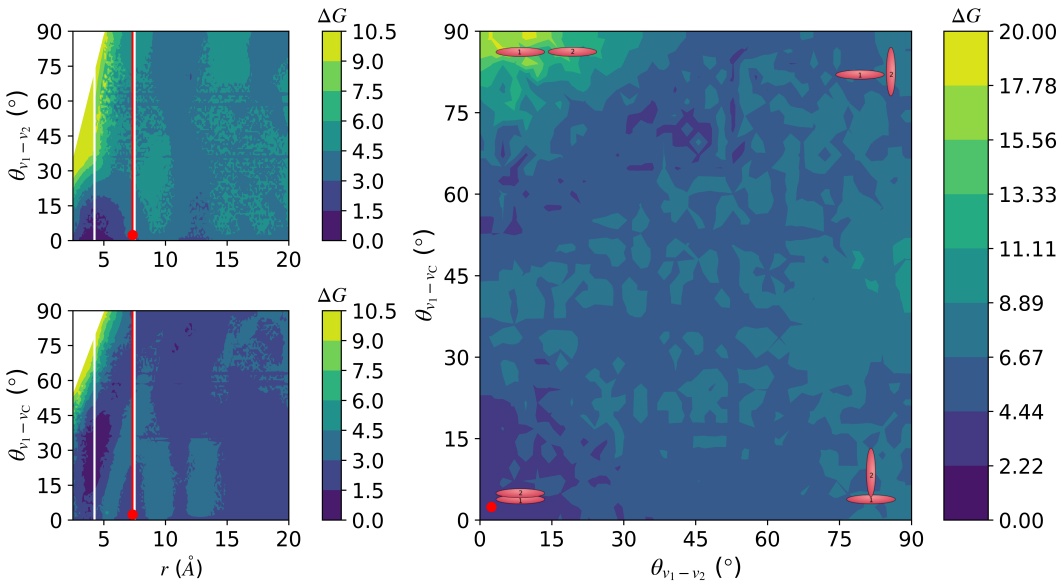

Fig. 5.16 Free energy surfaces (in units of kcal/mol) as a function of distance and angle ($\theta_{v_1-v_2}$ or $\theta_{v_1-v_C}$, small left plots), or two angles ($\theta_{v_1-v_2}$ and $\theta_{v_1-v_C}$ at 7.33 Å separation, large right plot) for N2200-A in CN. Colour indicates the free energy, with the minimum at $\Delta G = 0$ kcal/mol. The orientations of the backbone planes at certain extreme configurations are overlaid on the angle–angle plot. Vertical white lines on the distance–angle plots indicate the separations corresponding to the directly face-face aggregated structure, and the expected position of the solvent-separated structure. The red points indicate the position of the free energy minimum at $r = 7.33$ Å. Note that data was collected over the full 0–180° range, but due to the symmetry of the molecule, we combine this into 0–90°.

and for the other solvents are given in the SI Figs. S5.13– S5.15. Note that $\theta_{v_1-v_C}$ and $\theta_{v_2-v_C}$ are equivalent for identical monomers.

A free energy minimum was observed corresponding to the solvent-separated structure in CN (separation ≈ 7.5 Å, $\theta_{v_1-v_2} \approx \theta_{v_1-v_C} \approx 0$), though it is not the global minimum (Fig. 5.16). While a minimum corresponding to the solvent-separated structure was also observed in DCB (SI Fig. S5.14), it appears less significant than in CN. However, further considering the behaviour in CN, a barrier of ≈ 2 kcal/mol surrounding the solvent separated structure was observed, which may limit access to this structure.

While Fig. 5.16 shows that the the solvent-separated structure is expected to be stable in CN, examining the overall free energy as a function of separation (i.e. averaged over all orientations; Fig. 5.17) shows little difference between N2200-A in DCB and CN. While, again, N2200-A is expected to show the poorest solubility in TOL due to the substantially deeper minimum at 4.5 Å, there is no clear evidence for the formation of any other structures in CN that may describe the experimental discrepancies. One notable feature of the free energy as a function of intermolecular

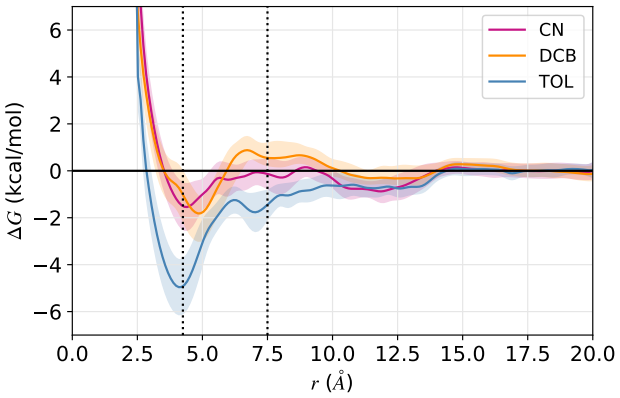

Fig. 5.17 Free energy as a function of only intermolecular separation r, calculated from the OPES simulations described above. Shaded regions indicate two standard errors, calculated by block averaging.

separation is the broad minimum at 10–13 Å in CN. This minimum corresponds to a structure in which monomers are interacting through the Th groups in a side-side/L-shaped manner (see Fig. S2.18). While this does appear to be an important interaction for N2200-A in CN, indicating potentially poorer solubility of the Th groups, this direct Th–Th interaction is expected to be less important for polymers, in which these groups are shielded by the connected monomers. This structure may, however, still be an important factor for explaining the experimental discrepancies in solubility. It is important to emphasise that these free energy calculations were conducted for systems of monomers, rather than oligomers or polymers. Longer chains, in which multiple instances of the solvent-separated structure can hold chains together more strongly, as described above, may have a deeper minimum at this position. The aggregation pathway may also change on going to longer chains, which may improve access to the solvent-separated structure.

Although the results presented above for the formation of a solvent-separated structure in CN are somewhat inconclusive, they do highlight that solubility theories, such as Flory-Huggins theory, that consider only the intermolecular interactions, may sometimes be inadequate for accurately describing, even qualitatively, the solution-phase behaviour of OSCs. This is especially true when specific interactions, such as between backbone and solvent molecules, may play an important role. Similarly, experimental techniques such as UV-vis spectroscopy, which is heavily relied upon in the field for understanding aggregation properties, may also fail when predicting solution-phase behaviour as it is sensitive only to specific changes in the local environment. The use of multiple experimental techniques, coupled with molecular simulation methods that can give greater insight into the molecule-scale behaviour of polymer and solvent, is therefore vital for obtaining a comprehensive

understanding of how OSC polymers behave in solution.

5.3.2.4 *Alternative structures*

Although the solvent-separated sandwich structure proposed above is a plausible explanation for the experimental behaviour of N2200-A in CN, there are a number of other alternate structures which may be able to describe this behaviour similarly well. One possible candidate involves the interaction of Th groups, which is shown to be another relatively deep free-energy minimum in CN. However, although some interaction between terminal Ths was observed in oligomer simulations, there was no evidence that would suggest the formation of large aggregates with this interaction motif. However, due to the large system size (approx. 300,000 atoms) the timescales accessible to these simulations are short; being able to examine the long-time behaviour may give more conclusive results.

Another possible structure is an aggregate in which, instead of stacking with the NDI groups directly face-face, an NDI–Th stacked structure forms. Examining the NDI–Th RDF, calculated from unbiased simulations of 6mers starting from random positions and orientations, a small peak at short separation in CN that is absent in the DCB systems as well as a somewhat different shape to the DCB and TOL distributions (Fig. 5.18), was observed. These differences in the RDF may indicate a preference for a different aggregation geometry. However, even if this offset aggregate is preferred to the directly stacked one, there still remains the question of overall solubility, which is expected to be good in CN due to the strong interactions between the NDI group and CN molecules, as well as the good solubility of the side-chains. Both the monomer and oligomer simulations show this behaviour, with substantially less aggregation observed in CN than in either DCB or TOL. Additionally, differences in the UV-vis absorption spectrum due to a staggered aggregation mode have been shown to be minimal,[294] so it is unlikely that this structure is the source of the discrepancies between experimental techniques. The solvent-separated structure, therefore, appears to still be the best explanation for the inconsistent results between different experimental techniques.

5.3.3 N2200-EO IN CHLOROFORM

While the solvent-separated structure appears to be a plausible explanation for the discrepancies between experimental techniques in measuring the solubility of N2200-A in CN, a similar structure for N2200-EO in CF is unlikely to be the cause of the experimental inconsistencies for this polymer–solvent pair. Though solvent–backbone interactions are strong between N2200 and CN, they are much weaker in CF. However, based on the wrapping of the side-chains around the N2200-EO backbone, which was not observed for N2200-A (see Section 5.3.1.2), it is possible

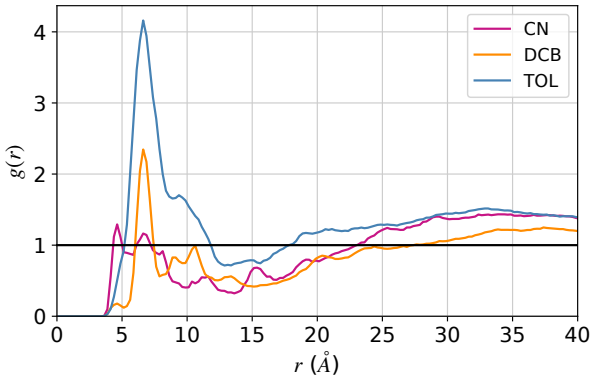

Fig. 5.18 NDI–Th RDFs in CN, DCB, and TOL. The NDI–NDI, and Th–Th distributions are given in the SI, Fig. S5.17. Note that RDFs do not go to one at 40 Å as the 6mers are longer than this, meaning there are still correlations out to this larger separation.

that a structure in which the backbones are separated by the side-chains, in much the same way that CN separates the N2200-A backbones, could be responsible for the experimental discrepancies. While this explanation is appealing, no evidence of a side-chain separated structure was observed in simulations, with monomer–monomer RDFs and orientation profiles showing no orientation preference at distances corresponding to the approximate position where the side-chain–separated structure should be observed (approx. 7–8 Å, Fig. 5.19a). Interestingly, a small peak was observed in the RDFs for N2200-EO 6mers in CB at this separation (Fig. S5.12b), which, due to the poorer solubility of the side-chains, is expected to be due to stronger aggregation of the polymer in the poorer solvent. As in Fig. 5.11, the peaks in the RDFs at 10–15 Å correspond to the interaction between thiophene groups in the monomer simulations, which is not expected to be a significant effect in polymeric systems (see SI Fig. S5.12 for RDFs of 6mers).

As with N2200-A in CN, although the results here are inconclusive, they again highlight the importance of expanding the analysis of polymer solubility and solution-phase behaviour beyond simple solubility theories. While measures such as Flory-Huggins parameters are valuable, and generally give a good estimate of the expected solution-phase behaviour of OSCs, it can be dangerous to rely too heavily on them as they may not capture sufficient detail to even qualitatively predict the correct behaviour in some cases. It is tempting, when comparing the good agreement between Flory-Huggins parameters and UV-vis absorption aggregation trends, to assume that both methods are accurate. However, it appears that even standard experimental techniques may occasionally fail to capture the aggregation properties of certain OSCs under specific conditions. The work in this chapter also shows that,

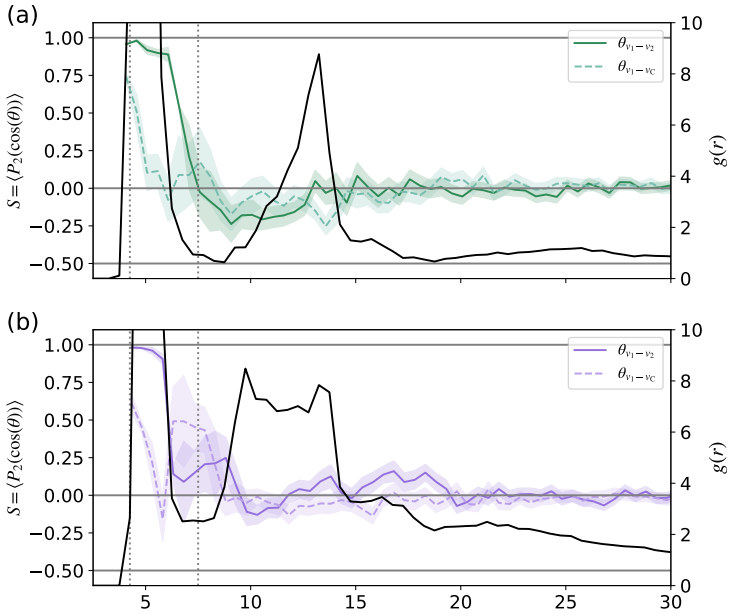

Fig. 5.19 Average orientation of N2200-EO monomer pairs in (a) CF and (b) CB at separation r defined as $S = \langle P_2(\cos(\theta)) \rangle$, shown as coloured lines. Two angles were used to define the orientation: $\theta_{v_1-v_2}$, and $\theta_{v_1-v_C}$ (defined in Fig. S5.5). θ is the angle between the two vectors in each case. A value of $S = 1$ indicates that the vectors are parallel, and $S = -0.5$ that they are perpendicular. Randomly oriented vectors will have $S = 0$. The RDF, $g(r)$, is overlaid as a black line (only shown up to 10 to better observe the behaviour at larger separation). The full RDFs are shown in Fig. S5.11a. Vertical dashed lines indicates the position where the directly face-face interacting monomer pair (approx. 4.25 Å) or the proposed side-chain separated structure (approx. 7.5 Å) are expected to be observed.

while MD is a powerful technique for examining solution-phase behaviour with molecular detail, it has a number of limitations which will be discussed below.

5.3.4 Challenges for molecular simulation of OSC polymers

Overall, while it does appear that a solvent-separated structure can form in CN, and is the free-energy minimum at the corresponding center-of-mass separation, it is not clear whether this structure is accessible enough in polymers to impart changes to the large-scale aggregation behaviour. Additionally, although side-chain wrapping was observed for N2200-EO, neither a structure in which these wrapped side-chains resulted in a side-chain separated aggregate structure, nor any other structure that may explain the discrepancies between the measurements of different experimental techniques,[295] were observed in CF. There are a number of reasons which may explain the inability of these unbiased MD simulations, and even the extensive free-energy calculations, to provide conclusive evidence for the formation

of unconventional aggregates, and the likely effect of these aggregates on the final aggregate structure.

Considering the behaviour of N2200-A in CN, it is possible that the proposed structure is simply not the cause of the experimental behaviour. Though it is shown to form in the unbiased simulations, is stable when a simulation is initialised from this structure, and corresponds to a free-energy minimum, there may be other more significant structures which better explain the observed experimental behaviour. We have examined a number of possible structures in Section 5.3.2.4, and although the solvent-separated structure still appeared to be the most plausible, there may be other structures that have not been considered. Similarly for N2200-EO, although a structure in which wrapped side-chains become sandwiched between the N2200 backbones is consistent with the experimental results, there may be other structures that can equally well describe the behaviour. However, as no structures were observed in the unbiased simulations that could explain the behaviour, it is impossible to draw further conclusions from these simulations, other than to say that the behaviour may be related to the wrapping of the EO side-chains around the N2200-EO backbone as this was the only significant difference observed between N2200-A and N2200-EO.

As previously mentioned, the timescales accessible for all-atom oligomer simulations is a limiting factor, meaning only short-time behaviour can be examined for longer chains. We have therefore predominantly focused on monomer simulations in order to reach longer timescales and potentially observe the formation of structures relevant to the experimental behaviour. There is, however, the possibility that the experimental behaviour is due to the interaction of many monomers in a polymer chain, meaning the behaviour may not be accurately translated to a system of monomers. Interactions that occur between multiple monomers on two chains will likely require entire chains to be in a specific orientation. This concerted aggregation mechanism is expected to significantly increase the time required to observe the formation of ordered oligomer structures to beyond the reach of all-atom simulations. Simulations of oligomers initialised from the aggregate structures have been used in this work to address this issue, but, whether or not the aggregated structures spontaneously form under experimental conditions remains unclear. Enhanced sampling methods are likely to be more useful in determining where any free energy minima lie, but these also become more difficult for longer polymer chains due to the introduction of more slowly-varying collective variables which must be biased. Hybrid simulations, in which, for example, the polymer and first few solvation shells of each polymer chain are modelled atomistically, while the rest of the solvent is either treated implicitly or coarse-grained, are a potentially useful alternative for reaching larger timescales while retaining the interaction specificity required

for the formation of structures such as the solvent-separated structure proposed here. The Adaptive Resolution Simulation (AdResS) method,[299,300] which allows for an atomistic and coarse-grained (CG) region to be defined is one such means of achieving this, and has been shown to agree well with full atomistic simulations.[300]

Finally, we note that the OPLS force-field used in this work is a general-purpose force-field parameterised to accurately capture the structure and thermodynamics of small organic molecules. As conjugated polymers can differ significantly from the set of molecules used in the original parameterisation, we have specifically parameterised the partial charges, and the bonded parameters that are expected to deviate most significantly from the general OPLS parameterisation, for N2200. However, the non-bonded LJ parameters were taken directly from the force-field without further optimisation, which may introduce inaccuracies into the calculation. Although good agreement between structural and thermodynamic properties calculated either using the OPLS force-field or experimentally has been found in the past for certain OSCs,[274] there is no guarantee that simulations will yield quantitatively accurate results. Additionally, the OPLS force-field does not include polarisability. Of the three solvents studied here for N2200-A, and also the additional two studied for N2200-EO, CN is the most polarisable (Table S5.7).[284] It is possible that including polarisability would further stabilise the N2200-A–CN solvent-separated structure through stronger backbone–CN interactions, or uncover an alternate aggregate structure that satisfies the experimental observations. Polarisable force-fields do exist (see refs 301–303), though are computationally more demanding, and extending this work to include the effect of polarisability may lead to more conclusive results. As it stands, however, while the formation of a solvent-separated structure for N2200-A in CN is appealing, in that it satisfies the experimental observations whilst still remaining consistent with the stronger backbone–solvent interactions, the results presented above cannot unambiguously show that this structure is indeed the driving force behind the discrepancy between experimental techniques.

5.4 CONCLUSIONS

The effect of solvent and side-chains on the aggregation behaviour of high performing OSC P(NDI2OD-T2), also known as N2200, was studied through classical MD simulations. Significant differences have been observed experimentally between the UV-vis absorption spectra of N2200 with the conventional A side-chains (N2200-A) and a derivative with EO side-chains (N2200-EO),[25,295] though these differences have not been explained in the past. In this work, Flory-Huggins theory calculations of the solubility of the different components (backbone, side-chains) of each polymer showed that, without side-chains, the N2200 backbone is expected to be

highly insoluble in all solvents studied. With side-chains, the relative solubilities of the polymers in each solvent can accurately describe the aggregation properties as measured by UV-vis absorption spectroscopy, as has been recently shown for other OSC polymers.[130] Flory-Huggins parameters cannot, however, account for the different shapes of the spectra of N2200-A and N2200-EO, nor can they explain the potential discrepancies between experimental techniques for the solubility of N2200-A in CN or N2200-EO in CF.

From analysis of the aggregate structure of N2200-A and N2200-EO in various solvents, the shape changes in the UV-vis absorption spectra can be attributed to differing aggregate structures. While N2200-A formed a highly crystalline aggregate which induced significant backbone planarisation relative to the single chain, the N2200-EO aggregate was significantly more disordered and less stable. The greater disorder in the N2200-EO aggregate structure appeared to be due to the wrapping of the EO side-chains around the N2200 backbone, a phenomenon that has not been previously reported. For N2200-EO, although the backbone was also locked into a specific conformation in the aggregate, it was not planarised significantly compared to a single chain. In terms of the effect on the balance between H and J character of the aggregate, and how this is expected to affect the absorption spectra, all of the observed behaviour is consistent with the different shapes of the experimental spectra of these two polymers.

Two interesting experimental results have also been examined using MD simulation. Both involve formation of aggregates in specific solvents that appear to be invisible to UV-vis absorption spectroscopy, but not to other experimental techniques such as SEC or simple precipitation-based methods. This behaviour has been reported for N2200-A in CN,[296] and N2200-EO in CF.[295] We have proposed the behaviour of N2200-A in CN to be due to the formation of a solvent-separated sandwich-like structure, where the intercalation of a solvent molecule between two monomer backbones prevents electronic coupling whilst still resulting in significant aggregation. Although some evidence for the formation of this structure was observed, and it does appear to be stable if it is able to form with the concerted aggregation of multiple monomer–solvent–monomer pairs in a chain, free energy calculations of monomers were inconclusive and it is unclear whether this structure is likely to be a significant contributor to the experimental-scale aggregation properties. For N2200-EO in CF no evidence of the formation of any structure that could explain the experimental behaviour was observed in unbiased MD simulations. The observed side-chain wrapping may be related to the interesting experimental behaviour, but it is not yet clear exactly how this may be.

A number of important points have come out of this work, particularly in relation to best practices for predicting solubility from MD simulation, and how solubility

parameters compare to experimental solubility. As previous studies,[129,130] and the work here, have shown, good agreement can be found between Flory-Huggins interaction parameters and the aggregation properties of polymers as measured by UV-vis absorption spectroscopy. It can therefore be tempting to conclude that Flory-Huggins theory accurately captures the aggregation behaviour of OSCs polymers. While this may be true in many cases, it does not appear to be so for two of the cases studied here, and likely others in the literature. Specific interactions between, for example, solvent and backbone, or backbone and side-chains, may be able to disrupt the aggregate structure in such a way that no changes to the UV-vis absorption spectra are observed. These interactions should not be ignored. Specific solvent (or side-chain)–backbone interactions are challenging to observe with experimental techniques, so combined experimental–computational approaches become important. There are, however, challenges associated with detailed molecular simulations, most notably accessing the relevant length- and time-scales to observe experimentally-important behaviour. Enhanced sampling methods can be applied to attempt to circumvent these issues, but are still expensive, especially for oligomeric systems. The development of more efficient models, and the improvement of computer hardware, should allow these kinds of calculations to become more routine in the future, giving greater insight into the molecular scale behaviour of OSC polymers in solution.

Supporting Information

S5.1 ALL-ATOM PARAMETERS FOR N2200-A AND N2200-EO

All parameters for N2200-A, and the backbone of N2200-EO, are exactly as described for the all-atom simulations in Chapter 4. The parameters for the EO side-chains were obtained directly from the OPLS force-field[202,268–273] and are reproduced in the tables below. The atom types and their relationship to the all-atom structure are shown in Fig. S5.1.

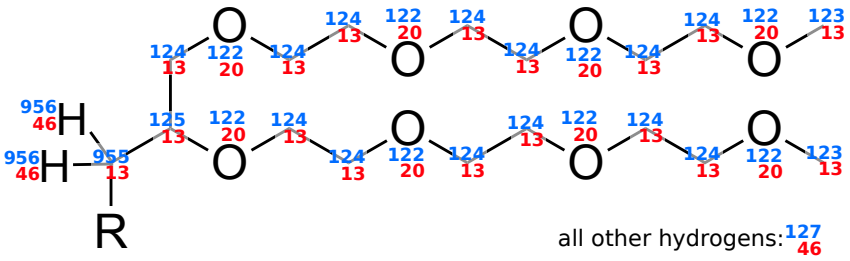

Fig. S5.1 Definition of the site types for the EO side-chains. Atom type 955 and 956 are defined in Chapter 4 while all other parameters are directly from the OPLS force field.

Table S5.1 Masses, partial charges, and LJ parameters for the all-atom N2200-EO side-chains. The non-bonded potential between two particles of type i and j is defined as

$$U_{\mathrm{NB}}(r_{ij}) = 4\epsilon_{ij}\left[\left(\frac{\sigma_{ij}}{r_{ij}}\right)^{12} - \left(\frac{\sigma_{ij}}{r_{ij}}\right)^{6}\right] + \frac{q_i q_j}{4\pi\epsilon_0 r_{ij}}$$

where σ_{ii} = is the homonuclear LJ diameter, ϵ_{ii} = homonuclear LJ interaction strength, and q_i = the charge. Geometric mixing rules were used for ij interactions: $\sigma_{ij} = \sqrt{\sigma_i \sigma_j}$; $\epsilon_{ij} = \sqrt{\epsilon_i \epsilon_j}$. Charges and LJ parameters for all five side-chain atom types come directly from the OPLS force-field. Parameters for atom types 955 and 956 are given in Chapter 4.

atom type (i)	mass (g/mol)	q_i (e)	ϵ_{ii}	σ_{ii}
122	15.999	−0.4	0.14	2.9
123	12.01	0.11	0.066	3.5
124	12.01	0.14	0.066	3.5
125	12.01	0.17	0.066	3.5
127	1.008	0.03	0.03	2.5

Table S5.2 Bond length parameters. All parameters come directly from the OPLS force-field. The harmonic potential has the form $U_{\mathrm{bond}}(l) = k_l(l - l_0)^2$ where k is the bond stretching coefficient, and l_0 the equilibrium bond length.

bond	bond style	k_l (kcal/mol/Å^2)	l_0 (Å)
13–13	harmonic	268	1.529
13–20	harmonic	320	1.41
13–46	harmonic	340	1.09

Table S5.4 Bond angle parameters. All parameters come directly from the OPLS force-field. The harmonic angle potential has the form $U_{\mathrm{angle}}(\theta) = k_\theta(\theta - \theta_0)^2$, where k is the angle bending coefficient and θ_0 the equilibrium bond angle.

angle	angle style	k_θ (kcal/mol/rad^2)	θ_0 (°)
13–20–13	harmonic	60	109.5
20–13–46	harmonic	35	109.5
13–13–46	harmonic	37.5	110.7
13–13–13	harmonic	58.35	112.7

Table S5.5 Dihedral parameters. All parameters come directly from the OPLS force-field. The OPLS style dihedral potential has the form

$$U_{\text{dihed}}(\phi) = \frac{1}{2}k_1[1+\cos(\phi)]+\frac{1}{2}k_2[1-\cos(2\phi)]+\frac{1}{2}k_3[1+\cos(3\phi)]+\frac{1}{2}k_4[1-\cos(4\phi)]$$

X is a wild-card atom. All energy parameters k_i have units of kcal/mol.

dihedral	dihedral style	k_1	k_2	k_3	k_4
20–13–13–20	OPLS	−0.55	0	0	0
13–13–13–20	OPLS	1.3	−0.05	0.2	0
46–13–13–46	OPLS	0	0	0.3	0
20–13–13–46	OPLS	0	0	0.468	0
13–13–13–46	OPLS	0	0	0.3	0
X–13–20–13	OPLS	−0.521	−2.018	1.996	0

S5.2 SYSTEM SETUP

s5.2.1 SETUP PARAMETERS

Table S5.6 Details of all the systems studied in this work. The number of solvent and polymer molecules for each system are given in the N_{solv} and N_{poly} columns respectively. L_{init}, L_{int}, and L_{final} give the initial, intermediate, and final box sizes used in the setup procedure described in the main text (all in units of Å). For the pure solvent systems, the target density is also listed. Pure polymer systems (N2200-A, N2200-EO, backbone) were initialised in a crystalline structure, described in the main text and below. The systems labelled "Flory" were used for the Flory-Huggins parameter simulations, and set up with 4 monomers positioned in opposite corners of the simulation box. Those labelled "6mer stack" were initialised with the three 6mer chains aligned in the π-stacked configuration, and "6mer SS-stack" in the solvent-separated π-stacked configuration. All other systems were initialised with the polymer molecules randomly positioned and oriented in the simulation box. Solvents are chlorobenzene (CB), chloroform (CF), 1-chloronaphthalene (CN), *o*-dichlorobenzene (DCB), and toluene (TOL). Where the solvent is listed as "A" or "EO", the backbone was immersed in a bulk fluid of alkyl (A) or ethylene oxide (EO) side-chain molecules.

system	solvent	N_{solv}	polymer	N_{poly}	L_{init}	L_{int}	L_{final}	density (g/cm^3)	simulation time (ns)
monomer:CB	CB	3274	N2200-EO 1mers	18	124	76	82.5	–	160
monomer:CF	CF	4350	N2200-A 1mers	18	124	76	82.5	–	270
			N2200-EO 1mers	18	124	76	82.5	–	270
monomer:CN	CN	2437	N2200-A 1mers	18	124	76	82.5	–	140
			N2200-EO 1mers	18	124	76	82.5	–	150
monomer:DCB	DCB	2937	N2200-A 1mers	18	124	76	82.5	–	170
monomer:TOL	TOL	3135	N2200-A 1mers	18	124	76	82.5	–	110

Continued on next page

system	solvent	N_{solv}	polymer	N_{poly}	L_{init}	L_{int}	L_{final}	density (g/cm^3)	simulation time (ns)
6mer:CB	CB	26192	N2200-EO 6mers	24	244	152	165	–	30
6mer:CF	CF	34800	N2200-EO 6mers	24	244	152	165	–	50
6mer:CN	CN	19496	N2200-A 6mers	24	244	152	165	–	60
6mer:DCB	DCB	23488	N2200-A 6mers	24	244	152	165	–	50
6mer:TOL	TOL	25080	N2200-A 6mers	24	244	152	165	–	25
6mer stack:CB	CB	11599	N2200-EO 6mers	3	344	120	125	–	80
6mer stack:CF	CF	14680	N2200-A 6mers	3	344	120	125	–	120
			N2200-EO 6mers	3	344	120	125	–	115
6mer stack:CN	CN	8622	N2200-A 6mers	3	344	120	125	–	95
			N2200-EO 6mers	3	344	120	125	–	30
6mer stack:DCB	DCB	23488	N2200-A 6mers	3	344	120	125	–	60
6mer SS-stack:CN	CN	8622	N2200-A 6mers	3	344	120	125	–	40
6mer SS-stack:DCB	DCB	23488	N2200-A 6mers	3	344	120	125	–	20
pure CB	CB	1000	–	–	80	50	55	1.11	12
pure CF	CF	1000	–	–	80	50.5	51.05	1.49	80
pure CN	CN	1000	–	–	104	60	64.14	1.194	30
pure DCB	DCB	1000	–	–	70	55	57	1.3	13

Continued on next page

system	solvent	N_{solv}	polymer	N_{poly}	L_{init}	L_{int}	L_{final}	density (g/cm^3)	simulation time (ns)
pure TOL	TOL	1000	–	–	84	53	56.03	0.87	10
pure N2200-A	–	–	N2200-A 1mers	300	–	–	–	–	2
pure N2200-EO	–	–	N2200-EO 1mers	300	–	–	–	–	2
pure backbone	–	–	backbone 1mers	300	–	–	–	–	2
pure A	–	–	A side-chains	1000	104	64	68.66	–	15
pure EO	–	–	EO side-chains	1000	104	60	64.14	–	15
N2200-A:CB, Flory	CB	759	N2200-A 1mers	4	100	45	50	–	4
N2200-A:CF, Flory	CF	957	N2200-A 1mers	4	100	45	50	–	4
N2200-A:CN, Flory	CN	563	N2200-A 1mers	4	100	45	50	–	4
N2200-A:DCB, Flory	DCB	678	N2200-A 1mers	4	100	45	50	–	4
N2200-A:TOL, Flory	TOL	722	N2200-A 1mers	4	100	45	50	–	4
N2200-EO:CB, Flory	CB	751	N2200-EO 1mers	4	100	45	50	–	4
N2200-EO:CF, Flory	CF	950	N2200-EO 1mers	4	100	45	50	–	4
N2200-EO:CN, Flory	CN	559	N2200-EO 1mers	4	100	45	50	–	4
N2200-EO:DCB, Flory	DCB	673	N2200-EO 1mers	4	100	45	50	–	4
N2200-EO:TOL, Flory	TOL	716	N2200-EO 1mers	4	100	45	50	–	4
backbone:CB, Flory	CB	552	backbone 1mers	4	100	41	45	–	4
backbone:CF, Flory	CF	699	backbone 1mers	4	100	41	45	–	4
backbone:CN, Flory	CN	411	backbone 1mers	4	100	41	45	–	4

Continued on next page

system	solvent	N_{solv}	polymer	N_{poly}	L_{init}	L_{int}	L_{final}	density (g/cm^3)	simulation time (ns)
backbone:DCB, Flory	DCB	495	backbone 1mers	4	100	41	45	–	4
backbone:TOL, Flory	TOL	527	backbone 1mers	4	100	41	45	–	4
backbone:A, Flory	A	279	backbone 1mers	4	100	41	45	–	4
backbone:EO, Flory	EO	305	backbone 1mers	4	100	41	45	–	4
A:CB, Flory	CB	3274	A side-chains	72	124	76	82.5	–	80
A:CF, Flory	CF	4350	A side-chains	72	124	76	82.5	–	100
A:CN, Flory	CN	2437	A side-chains	72	124	76	82.5	–	70
A:DCB, Flory	DCB	2936	A side-chains	72	124	76	82.5	–	80
A:TOL, Flory	TOL	3135	A side-chains	72	124	76	82.5	–	60
EO:CB, Flory	CB	3274	EO side-chains	72	124	76	82.5	–	80
EO:CF, Flory	CF	4350	EO side-chains	72	124	76	82.5	–	100
EO:CN, Flory	CN	2437	EO side-chains	72	124	76	82.5	–	30

s5.2.2 CRYSTAL STRUCTURES

The structures of the monomer crystals as initialised, and following the annealing procedure are shown below. The dimensions of the cell, initialised to give periodic packing in all three dimensions, are also given. Over the course of the simulation, the x, y, and z box side-lengths were allowed to vary independently.

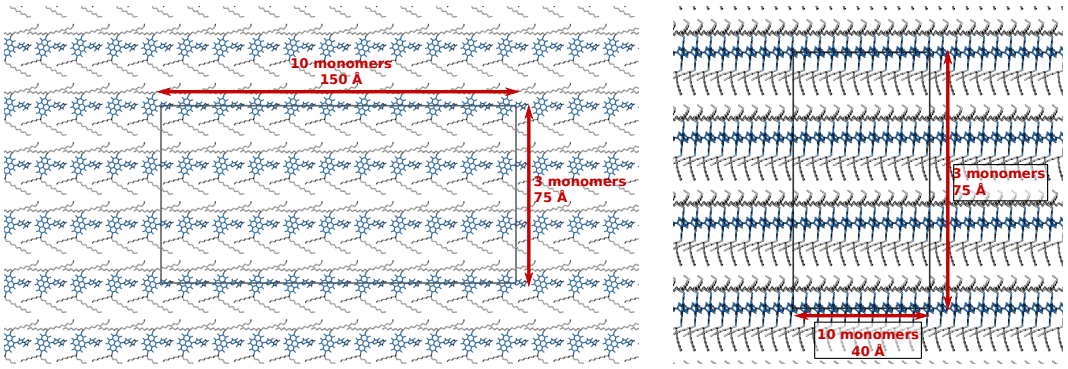

(a) Starting structure from a (left) front-on or (right) side-on view

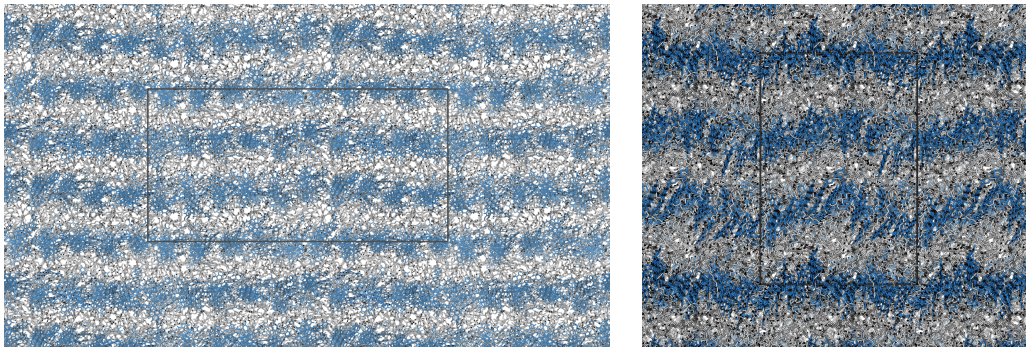

(b) Final structure from a (left) front-on or (right) side-on view

Fig. S5.2 (a) Starting and (b) final (post-annealing) structure of the N2200-A monomer crystal. The periodic box is indicated on each image (black square) and the number of monomers in each direction and initial box size labelled on the starting structures. Backbone (blue) and side-chains (grey) are coloured separately, and side-chain hydrogens are not shown for clarity.

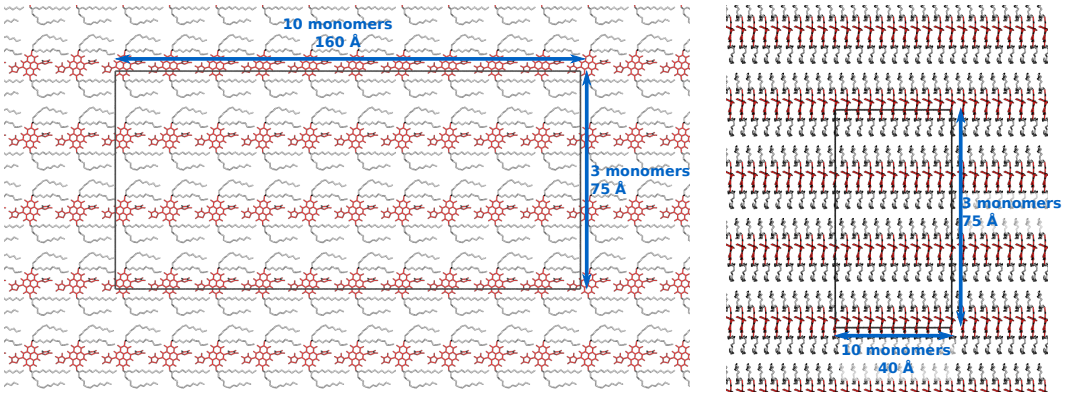

(a) Starting structure from a (left) front-on or (right) side-on view

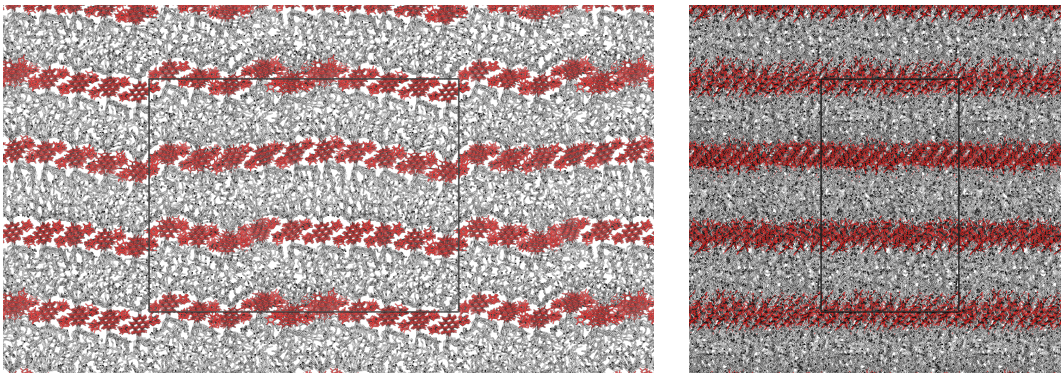

(b) Final structure from a (left) front-on or (right) side-on view

Fig. S5.3 (a) Starting and (b) final (post-annealing) structure of the N2200-EO monomer crystal. The periodic box is indicated on each image (black square) and the number of monomers in each direction and initial box size labelled on the starting structures. Backbone (red) and side-chains (grey) are coloured separately, and side-chain hydrogens are not shown for clarity.

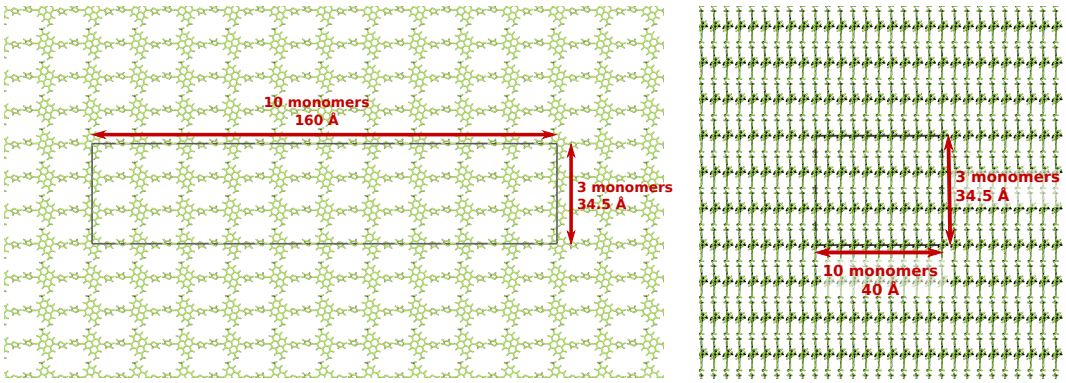

(a) Starting structure from a (left) front-on or (right) side-on view

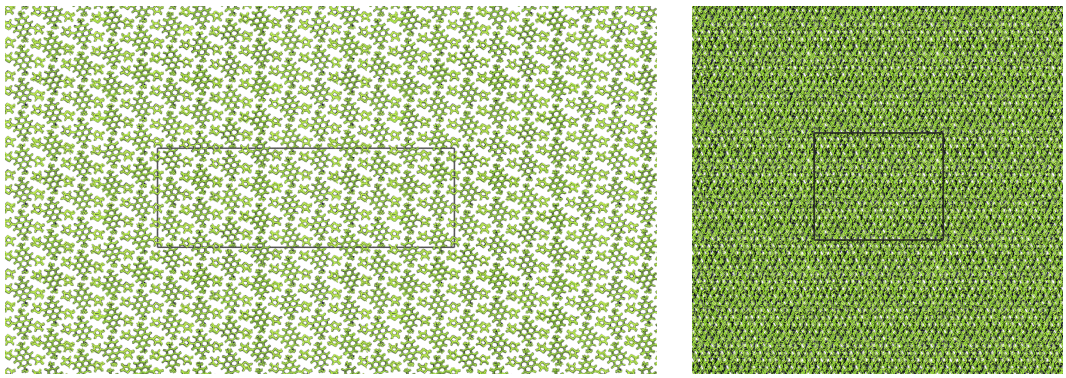

(b) Final structure from a (left) front-on or (right) side-on view

Fig. S5.4 (a) Starting and (b) final (post-annealing) structure of the backbone monomer crystal. The periodic box is indicated on each image (black square) and the number of monomers in each direction and initial box size labelled on the starting structures.

S5.3 ORIENTATION-ANGLE DEFINITIONS

The orientation of two monomers has been described in this work using two angles: $\theta_{v_1-v_2}$, and $\theta_{v_1-v_C}$. These angles are defined in Fig. S5.5. Note that this definition does not distinguish between rotations about the v_1 axis so will not uniquely define the relative orientation of molecules that do not have in-plane symmetry. While the presence of side-chains, and the asymmetry of the monomer unit, mean that this in-plane symmetry is lacking for N2200 (and therefore that the same values of $\theta_{v_1-v_2}$ and $\theta_{v_1-v_C}$ may describe different relative orientations), the effect of rotation about the v_1 axis is expected to be minimal compared to changes in the orientation of the planes of the molecules. The angle $\theta_{v_2-v_C}$ also exists, but is equivalent to $\theta_{v_1-v_C}$ for identical monomers.

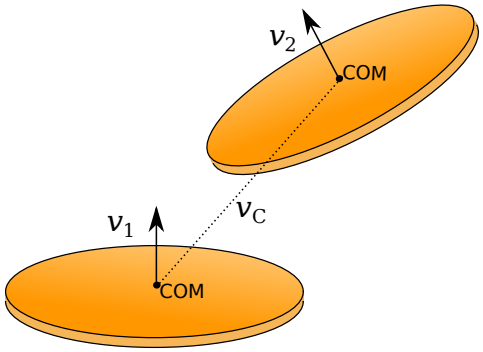

Fig. S5.5 Definition of the angles used to define the orientation of two planar, disk-like particles. $\theta_{v_1-v_2}$ is the angle between the vectors normal to the plane of each molecule. $\theta_{v_1-v_C}$ and $\theta_{v_2-v_C}$ are the angles between the normal to the plane, and the vector connecting the centers-of-mass.

S5.4 PROBABILITY DISTRIBUTIONS FOR EXTENDED AND WRAPPED SIDE-CHAINS

The free energy difference between extended and wrapped side-chains was calculated from the probability distributions of the side-chain positions relative to the N2200 backbone for both N2200-A and N2200-EO. The probability distributions for all solvents are shown in Fig. S5.6.

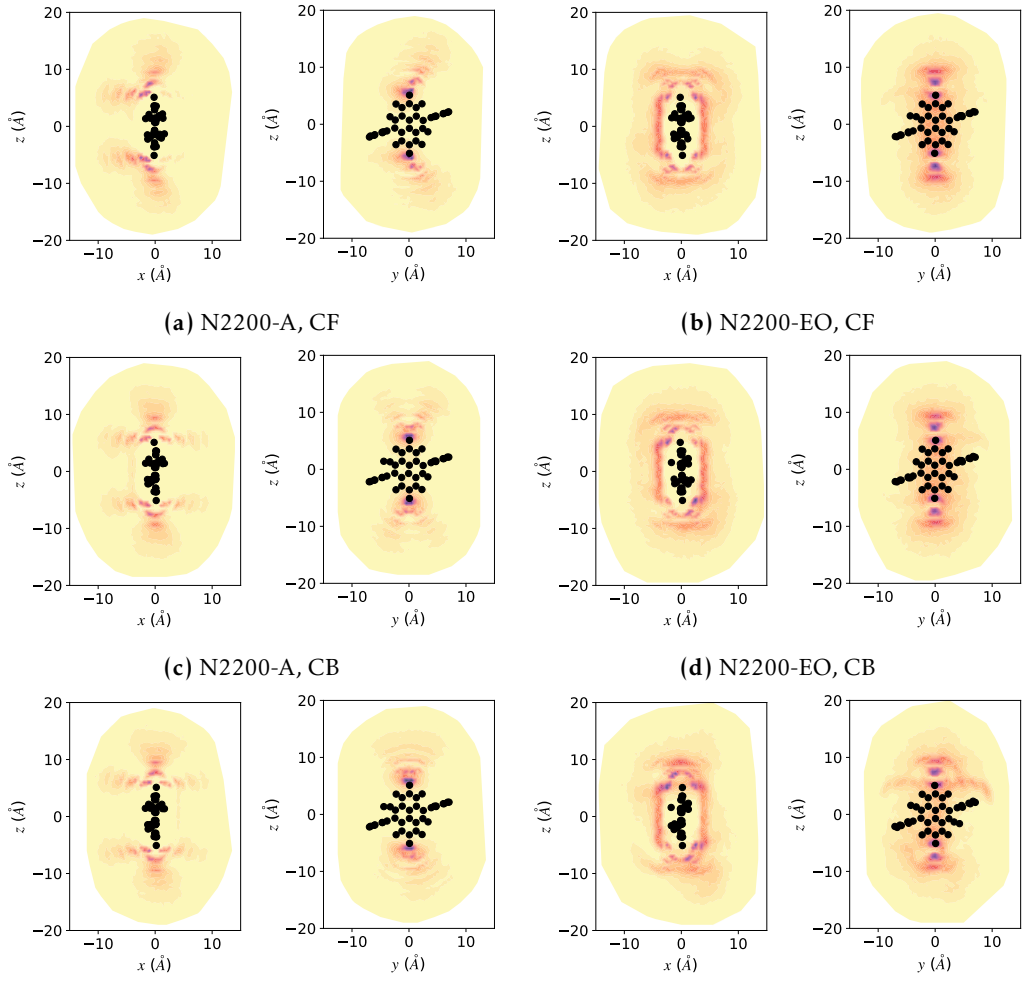

(a) N2200-A, CF **(b)** N2200-EO, CF

(c) N2200-A, CB **(d)** N2200-EO, CB

(e) N2200-A, CN **(f)** N2200-EO, CN

Fig. S5.6 Probability distributions of side-chain atom position around the backbone for both (a,c,e) N2200-A and (b,d,f) N2200-EO in (a,b) CF, (c,d) CB, or (e,f) CN. Both a side-on (in *xz* plane) or front-on (in *yz* plane) perspective are shown. Darker colours indicate higher probability of finding side-chain atoms in that position, with the same colour scale used across all plots. The positions of the backbone atoms are given as black circles.

S5.5 AGGREGATE STACK BEHAVIOUR

A number of systems were examined starting from a fully aggregated structure. These contained three 6mer chains in order to give a crystal-like environment for one of the chains, in which it interacts with two other chains, one on each face. Most of the analysis below will therefore be conducted for the central chain of the stack (the one that interacts with both other chains if fully aggregated).

s5.5.1 RADIAL DISTRIBUTION FUNCTIONS

The NDI–NDI RDF, $g(r)$, of the central chain of the N2200-A and N2200-EO stacks is shown below for all the solvents studied. In all solvents, the structure of N2200-A remained highly crystalline, while N2200-EO became slightly more disordered.

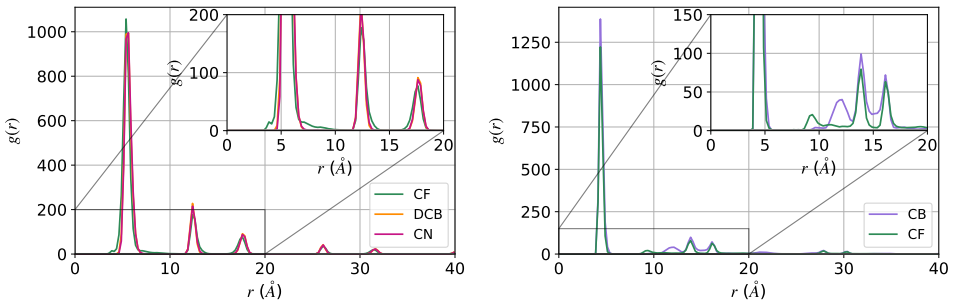

(a) N2200-A **(b)** N2200-EO

Fig. S5.7 NDI–NDI RDF of the central chain of a stack of 3 N2200 6mers with either (a) A or (b) EO side-chains in various solvents.

S5.5.2 STRUCTURE OF AGGREGATES IN CHLOROFORM

Representative structures of the N2200-A and N2200-EO aggregates in CF (after 100 ns for N2200-A, and 40 ns for N2200-EO), starting from the stacked structure, are shown below. N2200-A shows slightly offset NDI groups, resulting in the first peak in the RDF occurring at larger separation than for N2200-EO.

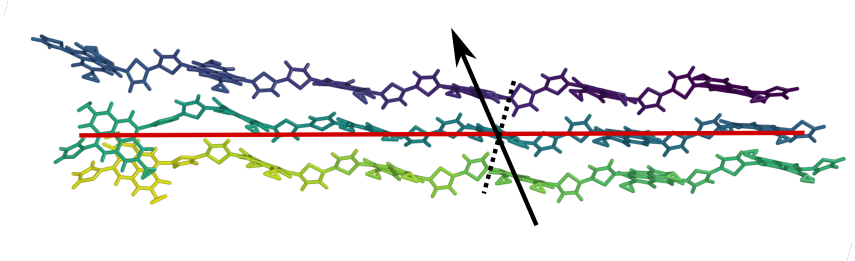

(a) N2200-A

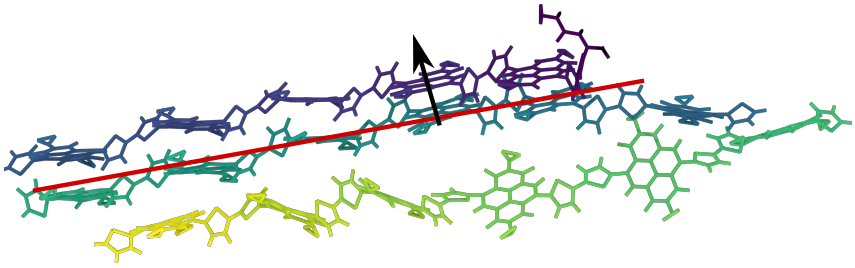

(b) N2200-EO

Fig. S5.8 (a) Representative final aggregate structure (after 100 ns) of N2200-A in CF. (b) Representative aggregate structure after 40 ns (prior to full dissociation of the third (yellow–green) chain of N2200-EO in CF. Side-chains are not shown for clarity. In both (a) and (b), the red line indicates the approximate direction of the polymer backbone, the black arrow the direction of stacking between chains (i.e. connecting the monomer centers-of-mass), and the dotted black line where the arrow would be if chains were arranged with NDI groups directly stacked (i.e. perpendicular to the plane of an NDI group of a monomer in the central chain). In (b), the dotted black line and arrow are indistinguishable.

S5.6 ADDITIONAL RDFS AND ORIENTATION PROFILES

A number of additional RDFs and distance–orientation profiles are given in the following sections.

S5.6.1 N2200-A

The RDFs shown in Fig. 5.11 are cut off at the top to better visualise the behaviour at separations corresponding to the potential solvent-separated structure. The full RDFs are given in Fig. S5.9 for both monomers and 6mers. Note that the 6mer RDFs do not appear to go to one at large separation as the size of the 6mer is larger than the maximum 40 Å plotted to here, meaning there are still correlations out to this large separation, particularly when chains are aggregated.

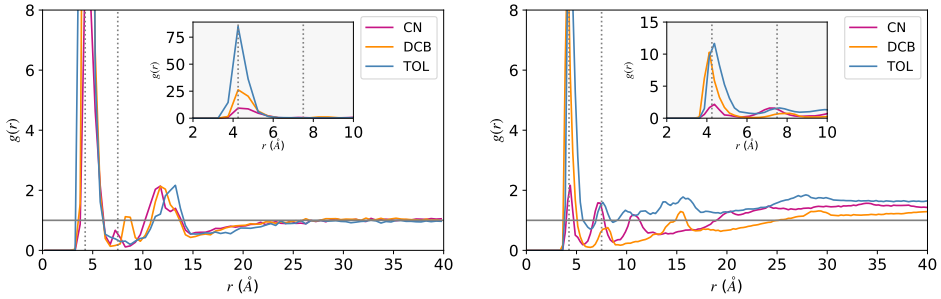

(a) Monomers **(b)** 6mers

Fig. S5.9 RDFs of N2200-A (a) monomers, (b) 6mers in various solvents. Vertical dotted lines indicate the separations expected to correspond to a fully face-on pair of monomers (4.25 Å) and a solvent-separated structure (7.5 Å). Inset plots show the full height of the first peak at approx 4.25 Å. In the 6mer plots, the RDF is calculated between all pairs of monomers on different chains.

RDFs and orientation profiles as a function of intermonomer separation r are shown for 6mers of N2200-A in various solvents in Fig. S5.10. A small peak is observed at approx. 7.5 Å in CN with orientation that is consistent with the solvent-separated structure. The behaviour of N2200-A in DCB at this position is also similar, though the peak in the RDF is smaller and the directly interacting structure is much more prominent. As described previously, the 6mer RDFs do not converge to one because of the length of the oligomers, which is greater than 40 Å.

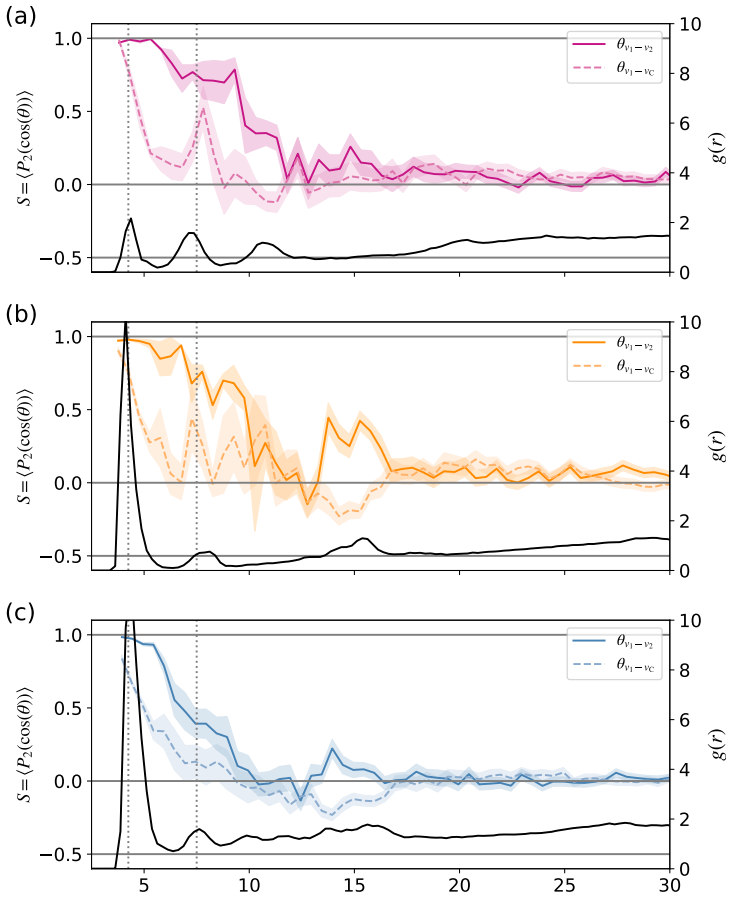

Fig. S5.10 Average orientation of N2200-A monomer pairs in 6mers at separation r (i.e. the average orientation at monomer–monomer separation r between two monomers on different oligomers) defined as $S = \langle P_2(\cos(\theta)) \rangle$ in (a) CN, (b) DCB, and (c) TOL. Two angles are used to define the orientation: $\theta_{v_1-v_2}$, $\theta_{v_1-v_C}$ (defined in Fig. S5.5). θ is the angle between the two vectors (v_1, v_2, or v_C) in each case. A value of $S = 1$ indicates that the vectors are parallel, and $S = -0.5$ that they are perpendicular. Randomly oriented vectors will have $S = 0$. The RDF, $g(r)$, is overlaid as a black line (only shown up to 10 to better observe the behaviour at larger separation. The full RDFs are shown in Fig S5.9. Vertical dashed line indicates the position where the directly face-face interacting monomer pair (approx. 4.25 Å) or the solvent-separated structure (approx. 7.5 Å) are expected to be observed. Shaded regions indicate two standard errors, calculated using block averaging.

S5.6.2 N2200-EO

Equivalent plots to those shown in section S5.6.1 for N2200-EO are shown in Figs. S5.11 and S5.12.

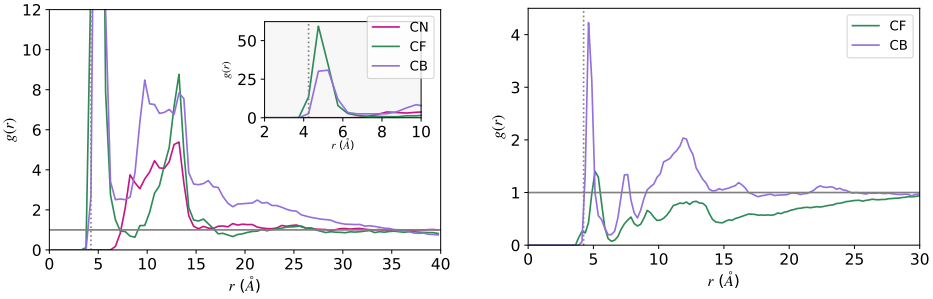

(a) Monomers **(b)** 6mers

Fig. S5.11 RDFs of N2200-EO (a) monomers, and (b) 6mers in various solvents. Vertical dotted lines indicate the separations expected to correspond to a fully face-on pair of monomers (4.25 Å) and a solvent-separated structure (7.5 Å). In the 6mer plots, the RDF is calculated between all pairs of monomers on different chains.

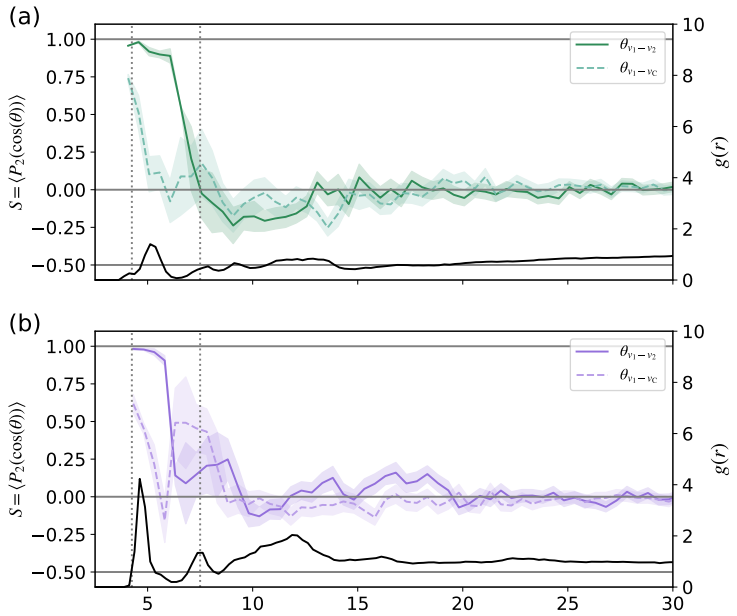

Fig. S5.12 Average orientation of N2200-EO monomer pairs in 6mers at separation r (i.e. the average orientation at monomer–monomer separation r between two monomers on different oligomers) defined as $S = \langle P_2(\cos(\theta)) \rangle$ in (a) CF, and (b) CB. All features are as defined in the caption to Fig. S5.10. Shaded regions indicate two standard errors in S calculated by block averaging.

S5.7 FREE-ENERGY SURFACES AT POINTS OF INTEREST

Monomer–monomer free energy surfaces, calculated using OPES simulations, for N2200-A in CN, DCB, and TOL are shown in Figs. S5.13, S5.14, and S5.15, respectively. The angle–angle surfaces are shown at two different separations, corresponding to the directly face-face pair, and the distance where a solvent-separated structure should be observed. While a slip-stacked, face-face structure appears to be the global minimum in all cases, an additional minimum was observed corresponding to the solvent-separated structure in CN and DCB, though this was much more strongly favoured in CN than in DCB.

A representation of the minimum of the free energy at various separations is given in Fig S5.16. Again, this shows that the position and orientation corresponding to the solvent-separated structure is stable in CN, and to a lesser extent in DCB, but was not observed in TOL. Note that these orientations simply represent the orientation corresponding to the minimum free energy at each separation. There is no guarantee of a physical pathway linking these states. Other, slightly less stable, but more accessible, states may therefore be more representative of the orientation along the "actual" aggregation pathway.

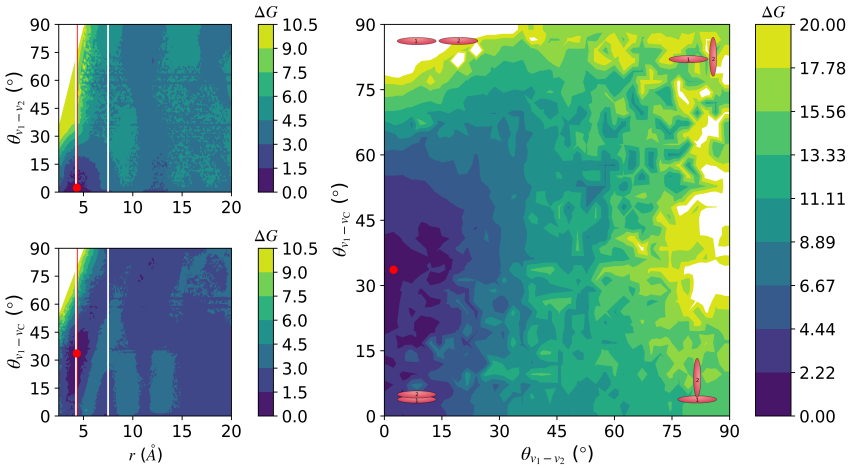

(a) 4.33 Å

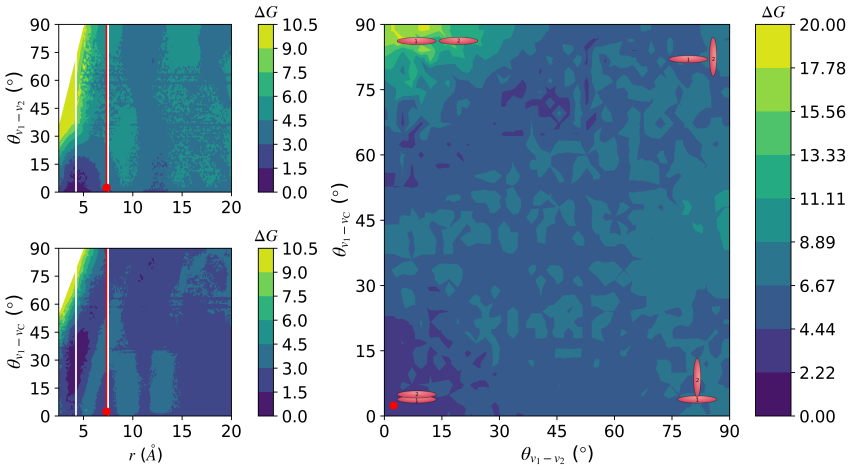

(b) 7.33 Å

Fig. S5.13 Free energy surfaces for N2200-A in CN calculated from OPES simulations of two monomers with the distance, r, and the three angles defining the orientation, $\theta_{v_1-v_2}$, $\theta_{v_1-v_C}$, and $\theta_{v_2-v_C}$ (see Fig. S5.5 for definitions of angles), biased. In each plot, the minimum of the free energy (reported in kcal/mol) is shifted to zero. The red points indicate the free energy minimum for each plot. Vertical white lines on the distance–angle plots indicate the approximate separations where the directly face-face (4.25 Å) and solvent-separated (7.5 Å) structures are expected to be observed. Diagrams corresponding to the combination of $\theta_{v_1-v_2}$ and $\theta_{v_1-v_C}$ are overlaid on the angle–angle plot.

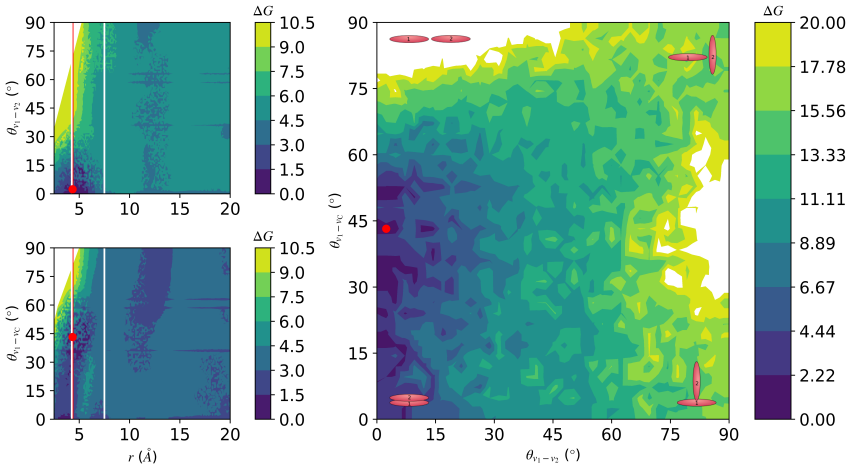

(a) 4.33 Å

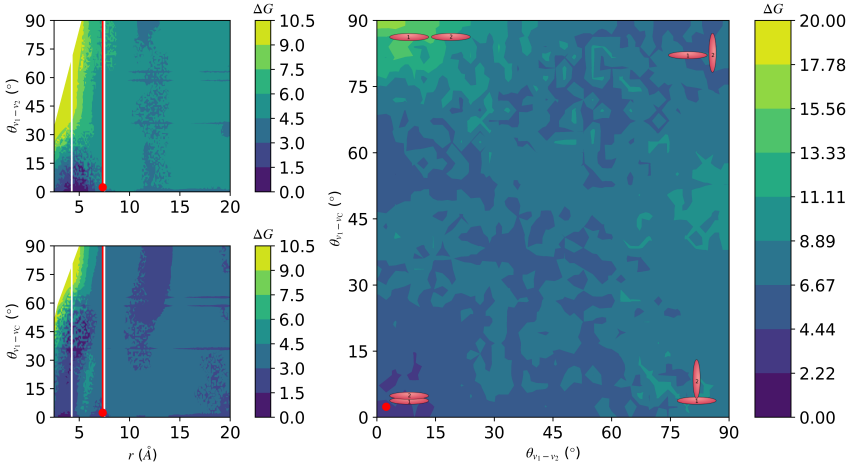

(b) 7.33 Å

Fig. S5.14 Free energy surfaces for N2200-A in DCB calculated from OPES simulations of two monomers with the distance, r, and the three angles defining the orientation, $\theta_{v_1-v_2}$, $\theta_{v_1-v_C}$, and $\theta_{v_2-v_C}$ (see Fig. S5.5 for definitions of angles), biased. In each plot, the minimum of the free energy (reported in kcal/mol) is shifted to zero. The red points indicate the free energy minimum for each plot. Vertical white lines on the distance–angle plots indicate the approximate separations where the directly face-face (4.25 Å) and solvent-separated (7.5 Å) structures are expected to be observed. Diagrams corresponding to the combination of $\theta_{v_1-v_2}$ and $\theta_{v_1-v_C}$ are overlaid on the angle–angle plot.

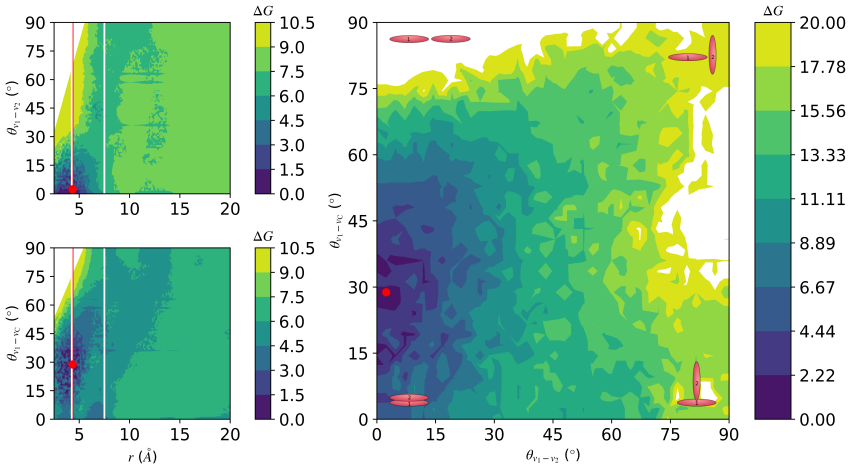

(a) 4.33 Å

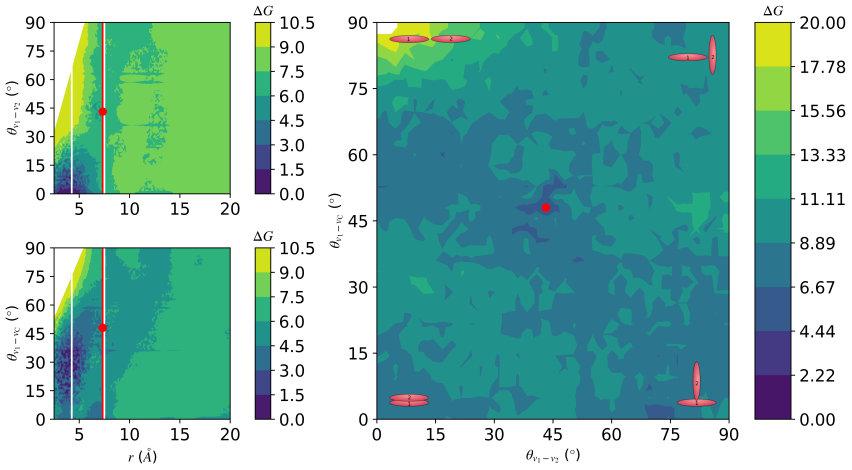

(b) 7.33 Å

Fig. S5.15 Free energy surfaces for N2200-A in TOL calculated from OPES simulations of two monomers with the distance, r, and the three angles defining the orientation, $\theta_{v_1-v_2}$, $\theta_{v_1-v_C}$, and $\theta_{v_2-v_C}$ (see Fig. S5.5 for definitions of angles), biased. In each plot, the minimum of the free energy (reported in kcal/mol) is shifted to zero. The red points indicate the free energy minimum for each plot. Vertical white lines on the distance–angle plots indicate the approximate separations where the directly face-face (4.25 Å) and solvent-separated (7.5 Å) structures are expected to be observed. Diagrams corresponding to the combination of $\theta_{v_1-v_2}$ and $\theta_{v_1-v_C}$ are overlaid on the angle–angle plot.

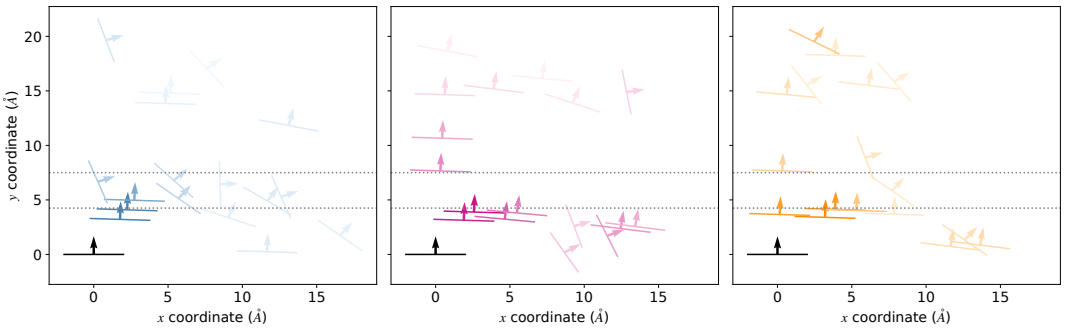

Fig. S5.16 Relative positions and orientations of monomer pairs at the free energy minimum for each separation coloured by free energy in (left) TOL, (center) CN, and (right) DCB. Each monomer is represented as a line corresponding to looking down the plane of the NDI group and separation and orientation given relative to the black reference molecule. The arrows indicate the direction of v_1 (or v_2) – the vectors normal to the plane of the monomer's backbone – and are positioned at the center-of-mass of the particle. Dotted lines indicate the separation that corresponds approximately to the directly interacting (4.25 Å) or solvent-separated (7.5 Å) structures. Lines/arrows are coloured according to the depth of the free energy minimum at this separation, with more stable structures darker than less stable ones.

S5.8 NDI–TH DISTRIBUTIONS

The RDFs, $g(r)$, between the NDI–NDI, NDI–Th, and Th–Th groups from simulations of 6mers are given in Fig. S5.17. These show slight differences in the spontaneous aggregation behaviour of N2200-A in CN compared with the other solvents, though, overall, little aggregation in this solvent was observed.

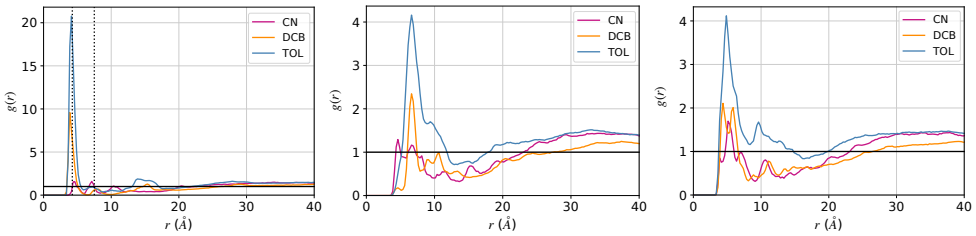

(a) NDI–NDI **(b)** NDI–Th **(c)** Th–Th

Fig. S5.17 (a) NDI–NDI, (b) NDI–Th, and (c) Th–Th distributions of N2200-A 6mers in CN, DCB, or TOL. Distributions are calculated between all pairs of monomers in different oligomer chains.

S5.9 SOLVENT POLARISABILITIES

Table S5.7 Polarisability of the organic solvents examined in this work.[284] Where two values are listed, two different sources were available (see references within ref. 284).

solvent	polarisability (Å^3)
1-chloronaphthalene (CN)	19.30
o-dichlorobenzene (DCB)	14.17
toluene (TOL)	11.80 (12.25)
chlorobenzene (CB)	14.10 (12.30)
chloroform (CF)	9.50 (8.23)

6

Conclusions

"Now, I'm fairly confident I've come up with several valuable insights – in fact, I'm sure of it – but, uh, I've only slept six hours in the last few days, so, um..."

— Rodney McKay, *Stargate: Atlantis*

6.1 SUMMARY AND FUTURE DIRECTIONS

The previous chapters present an in-depth analysis of the behaviour of organic semiconductors (OSCs) in solution and at interfaces. Molecular simulation techniques have been used to obtain molecular-level insights into the kinetics and thermodynamics of various important aspects of OSC morphology, rationalising previously unexplained, or unexpected, experimental behaviour, and leading to novel methods for predicting this morphology.

Orientation of OSCs at interfaces with solid and vapour can be simply predicted

Chapter 3 presented an analysis of how small-molecule OSCs align at solid and vapour interfaces. Using generic coarse-grained (CG) ellipsoids, with parameters chosen to represent a range of typical OSC-like particles, universal scaling of the orientation of interfacial particles with a simple free energy parameter was observed. In most cases, the equilibrium orientation of the interfacial layer of an isotropic liquid at a solid substrate was found to be face on, and side-on at the interface with a vapour. This has implications for the fabrication of OSC devices in which a particular interface orientation may be required for high performance. A number of strategies for controlling the orientation at both the solid and vapour interfaces were proposed, based on the scaling of orientation with the components of the free energy. Changing the shape anisotropy was found to be a useful method for controlling the orientation at both interfaces, while the orientation at the solid interface can perhaps be most easily controlled by changing the substrate to one that interacts more strongly with either the face or the side of the molecule. It should be noted that, under circumstances where the electronic structure of the substrate, for example, is important for achieving good device performance, it may become challenging to change the strength of the substrate interactions without losing performance on other fronts. However, as the substrate does not necessarily always play an active role in the device, it may be possible to change the substrate to optimise the OSCs' interfacial orientation without compromising other aspects of device performance.

The work in Chapter 3 exclusively examined interfaces with bulk isotropic liquids of disk-shaped small molecules. This is only a small subset of possible OSC structures, which also include rod-like particles, polymers, and molecules with side-chains, as well as materials that form bulk anisotropic liquid-crystalline phases. It is likely that many of the same principles – that is, the balance between entropic and energetic contributions which can be tuned by changing particle shape and interaction anisotropy – can be applied to these other classes of molecules. Examining other structures in more detail may confirm the generality of the predictor, increasing its utility beyond the cases studied in this work. While the behaviour of

nematic fluids of anisotropic particles has been studied previously at the vapour interface,[84] it would also be interesting to examine how well our predictor translates to bulk anisotropic systems, including to interfaces of such systems with a solid interface. Likely the interactions with adjacent layers would need to be considered to maintain good predictive power.

General models such as that used in Chapter 3 are also potentially valuable for studying non-equilibrium processes such as solution-phase deposition or solvent evaporation. While molecular dynamics (MD) studies of these kind of processes do exist,[169,175,304,305] they have typically looked at specific systems rather than using general models. While the observations from these specific studies are interesting, it is difficult to formulate general design rules from them. The use of more general models, parameterised to be within the range of typical OSCs, as done in the work in Chapter 3, would therefore be useful for better understanding the processes that govern solution-phase deposition.

Rapid formation of partially overlapping chains leads to rod-like aggregates

In Chapter 4, we parameterised an all-atom (AA) model of high-performance OSC polymer P(NDI2OD-T2), also known as N2200, which was used to develop a CG model of this polymer. N2200 has been shown experimentally to form large, rod-like aggregates in poor solvents, with size up to an order of magnitude larger than a single polymer chain, indicative of a directional, multi-chain aggregation process.[25] This observation contradicts all known theories of polymer solubility – which predict chain collapse in poor solvents – as well as earlier studies on the same polymer that suggested it formed single-chain, collapsed structures.[22] CG simulations at conditions approximating those studied in ref. 25 showed the formation of multi-chain aggregates in poor solvent, in which chains held together by interactions between only a fraction of their constituent monomers were sufficiently stable that they did not separate on the timescale of further aggregation. This led to chains becoming trapped in structures that are not the expected thermodynamic minimum of fully overlapping chains, and to the build-up of large extended aggregates. Importantly, whether a single-chain folding, or multi-chain aggregation, pathway is followed was found to depend on the relative rates of these two competing processes: if multi-chain aggregation occurred faster than single-chain folding, extended aggregates formed, while faster single-chain folding gave more collapsed structures, and no build up in aggregate size. The relative rates of these processes can be controlled by changing backbone stiffness and length, as well as polymer concentration. A critical crossover concentration was determined for N2200, above which multi-chain aggregation is expected to be favoured, reconciling the apparently contradictory experimental results. Overall, this work provides a novel and general theoretical

framework for predicting, and thus controlling, OSC polymer aggregate morphology. This could be exploited to design better OSC devices, given the experimentally observed correlation between the formation of extended rod-like aggregates and charge-carrier mobility.

The quantitative accuracy of the prediction of the critical crossover concentration from the MD simulations conducted here could be further improved by including hydrodynamic interactions in the simulations. Although we have estimated the effect of hydrodynamic interactions on the behaviour of the multi-chain systems, a number of assumptions were made in this process. Whilst these assumptions appear to be generally reasonable, explicitly including hydrodynamics, such as by using a Lattice-Boltzmann fluid,[208,306–308] should allow for better predictions of the critical crossover concentration with direct applications to experimental systems.

In terms of accurately modelling the aggregation properties, the effect of including dipoles or quadrupoles may be another interesting extension to this work. While the work here is a first approximation, and provides valuable insights into the behaviour of OSC polymers in solution, many OSCs molecules have significant quadrupoles which may play an important role in their solution-phase and aggregation behaviour. To the best of our knowledge, no CG models of OSCs have included either dipoles or quadrupoles, so the development, and use, of these models would be an important next step in achieving greater understanding of OSC behaviour.

The ability to control whether polymer chains aggregate or collapse in poor solvents is hugely important for the development of high-performing OSC devices as the solution-phase structure has implications for the final thin-film structure and, accordingly, the charge transport properties. Although this work only examined a single OSC polymer (N2200) the presence of some critical concentration which controls the preference for single- or multi-chain behaviour in poor solvents should not be unique to this polymer. The extension of this work to other OSC polymers, particularly those that deviate significantly in structure from N2200, would be valuable for confirming the transferability of this theory. Additionally, while the simulation results presented here are consistent with both experimental sources,[22,25] further experiments studying, for example, the effect of concentration on solution-phase behaviour in poor solvent, would be useful for both validating the computational results, and determining the quantitative accuracy of the calculated critical crossover concentration and its dependence on chain length.

Specific molecular interactions may be important for solution-phase behaviour

Solution-phase behaviour of OSC polymer N2200 was further studied in Chapter 5 using the AA model parameterised in Chapter 4. This chapter examined solution-phase aggregation in more detail, looking at a number of chemical factors that may

influence both the aggregation process, and the final aggregate structure: the solvent and side-chains. In general, it was found that Flory-Huggins theory, which has been used in the past to explain the solution-phase behaviour of OSC polymers, fails under certain circumstances where it appears specific molecular interactions may be important. It is also unable to explain differences in aggregate structure, which may account for observed differences in, for example, the UV-visible absorption spectrum of N2200 with either alkyl (A, referred to as N2200-A), or ethylene oxide (EO, referred to as N2200-EO) side-chains. Examining the simulations, wrapping of the side-chains around the N2200-EO backbone was observed in solvents where the backbone showed poor solubility (and to a lesser extent when the backbone was more soluble), leading to a more disordered aggregate structure that can explain the differences in the absorption spectrum. This kind of specific side-chain–backbone interaction has not been reported previously.

A sandwich-like solvent-separated structure was observed for monomers of N2200-A in 1-chloronaphthalene, which may reconcile differences in behaviour of this polymer–solvent pair when using different experimental techniques.[296] Evidence from simulations of monomers and oligomers, as well as calculations of the monomer–monomer free energy surface in a variety of solvents, supported this proposed sandwich structure, but was not conclusive. Further investigation into the prevalence of this structure in oligomeric systems was hampered by the large system size, which drastically reduced the timescale accessible to simulations. Although enhanced sampling methods may be useful here, the additional slowly-varying collective variables introduced by extending the length of the polymer chain, make these calculations challenging. The aggregation behaviour of N2200-EO in chloroform has also shown inconsistencies when measured using different experimental techniques.[295] Although the observed side-chain wrapping may be related to this discrepancy, no evidence was observed in either monomer or oligomer simulations for an aggregate structure that could explain the experimental behaviour. Nevertheless, these results highlight that simple solubility theories, such as Flory-Huggins theory, which is commonly applied to OSC polymer solutions, may not accurately describe the solution-phase behaviour, particularly when specific (e.g. side-chain–backbone, or solvent–backbone) interactions may be important. Capturing the polarisability of both the solvent and polymer may also prove a useful next step towards better understanding the contradictory experimental results. As an alternative to using expensive, fully polarisable force-fields, partial charges could be modified to enhance the strength of the dipole, for example, allowing for the effect of solvent polarisability to be examined.

CG simulations could be employed to access the longer time and polymer length scales possibly required to conclusively determine the source of experi-

mental discrepancies between techniques for measuring the aggregation N2200-A in 1-chloronaphthalene and N2200-EO in chloroform. Models like that described in Chapter 4 only account for solvent implicitly, so could not capture the proposed solvent-separated structure for N2200-A in 1-chloronaphthalene. Models with explicit, but CG, solvent could, however, be used to further study these systems on longer timescales while still maintaining some of the specificity of the AA model. Alternatively, hybrid models, where the polymer and nearby solvent is treated atomistically and all other solvent either coarse-grained or accounted for implicitly, may also be valuable.

Finally, more definitive experimental studies on the solution-phase aggregation behaviour of N2200 are required to confirm the contradictory observations from different experimental techniques. While anecdotal evidence suggests that N2200-A is insoluble in 1-chloronaphthalene, in contrast to all previous experimental studies and the UV-vis spectroscopic data, these experimental results remain unpublished, and it is therefore challenging to compare to the simulation results with any certainty. Unfortunately, experiments by our collaborators that could confirm these interesting solubility properties have been hindered by the Covid-19 pandemic.

Combining solution-phase and interfacial behaviour

While the work presented in Chapter 3 focused on the behaviour of pure liquids at interfaces, and that of Chapters 4 and 5 on bulk solutions, the intersection of these studies – OSC solutions at interfaces – is also significant. Pre-aggregation in solution has been shown to affect the alignment of OSC polymers at a solid interface,[16,66,67] which in turn has implications for charge transport. Understanding how these multi-component systems behave, and what factors influence their interfacial behaviour, is an important next step. The work conducted in the previous chapters lays the groundwork for further increasing understanding of the processes that impact the final thin-film structure, particularly at device interfaces.

Many device fabrication methods involve the deposition of OSCs onto a substrate from solution. Understanding the dual nature of how OSC molecules aggregate in solution, and how these aggregates (or free molecules) behave at the interfaces both in the initial solution, and as solvent is evaporated, is therefore an important step towards optimising the fabrication process. Being able to choose, or even design, molecules that behave in solution in such a way that they give the optimal interface structure after solvent evaporation, should help improve OSC-based device efficiency, and bring them closer towards commercial viability.

Appendix A

Authorship Statements

Boehm, B. J.; Nguyen, H. T. L.; Huang, D. M. The Interplay of Interfaces, Supramolecular Assembly, and Electronics in Organic Semiconductors. *J. Phys: Condens. Matter* **2019**, *31*, 423001.

Principal author (candidate): Belinda J. Boehm
Contribution: 60%
Literature search, writing, and drafting of the majority of the paper. This paper constitutes a literature review I conducted during the period of my Higher Degree by Research candidature and is not subject to any obligations or contractual agreements with a third party that would constrain its inclusion in this thesis. I am the primary author of this paper.

Signature: Date: 22/02/2022

Co-author contributions

By signing the Statement of Authorship, each author certifies that:

1. the candidate's stated contribution to the publication is accurate (as detailed above);
2. permission is granted for the candidate to include the publication in the thesis; and
3. the sum of all co-author contributions is equal to 100% less the candidate's stated contribution

Co-Author: Huong T. L. Nguyen
Contribution: 15%
Literature search and summary of parts of this paper related to coarse-graining methods for anisotropic particles. Assisted in revision of the manuscript.

Signature: Date: 23/02/2022

Co-Author: David M. Huang
Contribution: 25%
Wrote sections related to continuum methods (not included in this thesis). Assisted with literature search and summary, and revision of the manuscript. Acted as corresponding author.

Signature: Date: 22/02/2022

Boehm, B. J.; Huang, D. M. A Simple Predictor of Interface Orientation of Fluids of Disk-like Anisotropic Particles and Its Implications for Organic Semiconductors. *Soft Matter* **2022**, *18*, 1843–1857.

Principal author (candidate): Belinda J. Boehm
Contribution: 85%
Designed coarse-grained model and carried out simulations and analysis. Construction of figures. Conception, writing, and drafting of manuscript. This paper reports on original research I conducted during the period of my Higher Degree by Research candidature and is not subject to any obligations of contractual agreements with a third party that would constrain its inclusion in this thesis. I am the primary author of this paper.

Signature: Date: 22/02/2022

Co-author contributions

By signing the Statement of Authorship, each author certifies that:

1. the candidate's stated contribution to the publication is accurate (as detailed above);
2. permission is granted for the candidate to include the publication in the thesis; and
3. the sum of all co-author contributions is equal to 100% less the candidate's stated contribution

Co-Author: David M. Huang
Contribution: 15%
Conceived project, supervised the model development, simulations, interpretation of results, and the conception and revision of manuscript. Acted as corresponding author.

Signature: Date: 22/02/2022

References

(1) Boehm, B. J.; Nguyen, H. T. L.; Huang, D. M. The Interplay of Interfaces, Supramolecular Assembly, and Electronics in Organic Semiconductors. *J. Phys: Condens. Matter* **2019**, *31*, 423001.

(2) Arias, A. C.; MacKenzie, J. D.; McCulloch, I.; Rivnay, J.; Salleo, A. Materials and Applications for Large Area Electronics: Solution-Based Approaches. *Chem. Rev.* **2010**, *110*, 3–24.

(3) Krebs, F. C.; Tromholt, T.; Jørgensen, M. Upscaling of Polymer Solar Cell Fabrication Using Full Roll-to-Roll Processing. *Nanoscale* **2010**, *2*, 873–886.

(4) Forrest, S. R. The Path to Ubiquitous and Low-Cost Organic Electronic Appliances on Plastic. *Nature* **2004**, *428*, 911–918.

(5) Sirringhaus, H.; Ando, M. Materials Challenges and Applications of Solution-Processed Organic Field-Effect Transistors. *MRS Bull.* **2008**, *33*, 676–682.

(6) Noriega, R.; Salleo, A.; Spakowitz, A. J. Chain Conformations Dictate Multiscale Charge Transport Phenomena in Disordered Semiconducting Polymers. *Proc. Natl. Acad. Sci. USA* **2013**, *110*, 16315–16320.

(7) Tumbleston, J. R.; Collins, B. A.; Yang, L.; Stuart, A. C.; Gann, E.; Ma, W.; You, W.; Ade, H. The Influence of Molecular Orientation on Organic Bulk Heterojunction Solar Cells. *Nat. Photon.* **2014**, *8*, 385–391.

(8) Lee, C.; Giridhar, T.; Choi, J.; Kim, S.; Kim, Y.; Kim, T.; Lee, W.; Cho, H.-H.; Wang, C.; Ade, H.; Kim, B. J. Importance of 2D Conjugated Side Chains of Benzodithiophene-Based Polymers in Controlling Polymer Packing, Interfacial Ordering, and Composition Variations of All-Polymer Solar Cells. *Chem. Mater.* **2017**, *29*, 9407–9415.

(9) Ye, L.; Jiao, X.; Zhou, M.; Zhang, S.; Yao, H.; Zhao, W.; Xia, A.; Ade, H.; Hou, J. Manipulating Aggregation and Molecular Orientation in All-Polymer Photovoltaic Cells. *Adv. Mater.* **2015**, *27*, 6046–6054.

(10) Osaka, I.; Takimiya, K. Backbone Orientation in Semiconducting Polymers. *Polymer* **2015**, *59*, A1–A15.

(11) Yoneya, M.; Matsuoka, S.; Tsutsumi, J.; Hasegawa, T. Self-Assembly of Donor–Acceptor Semiconducting Polymers in Solution Thin Films: A Molecular Dynamics Simulation Study. *J. Mater. Chem. C* **2017**, *5*, 9602–9610.

(12) Bagchi, K.; Jackson, N. E.; Gujral, A.; Huang, C.; Toney, M. F.; Yu, L.; de Pablo, J. J.; Ediger, M. D. Origin of Anisotropic Molecular Packing in Vapor-Deposited Alq3 Glasses. *J. Phys. Chem. Lett.* **2019**, *10*, 164–170.

(13) Muccioli, L.; D'Avino, G.; Zannoni, C. Simulation of Vapor-Phase Deposition and Growth of a Pentacene Thin Film on C60 (001). *Adv. Mater.* **2011**, *23*, 4532–4536.

(14) Youn, Y.; Yoo, D.; Song, H.; Kang, Y.; Kim, K. Y.; Jeon, S. H.; Cho, Y.; Chae, K.; Han, S. All-Atom Simulation of Molecular Orientation in Vapor-Deposited Organic Light-Emitting Diodes. *J. Mater. Chem. C* **2018**, *6*, 1015–1022.

(15) Walters, D. M.; Antony, L.; de Pablo, J. J.; Ediger, M. D. Influence of Molecular Shape on the Thermal Stability and Molecular Orientation of Vapor-Deposited Organic Semiconductors. *J. Phys. Chem. Lett.* **2017**, *8*, 3380–3386.

(16) Chen, M. S.; Lee, O. P.; Niskala, J. R.; Yiu, A. T.; Tassone, C. J.; Schmidt, K.; Beaujuge, P. M.; Onishi, S. S.; Toney, M. F.; Zettl, A.; Fréchet, J. M. J. Enhanced Solid-State Order and Field-Effect Hole Mobility through Control of Nanoscale Polymer Aggregation. *J. Am. Chem. Soc.* **2013**, *135*, 19229–19236.

(17) Dalal, S. S.; Walters, D. M.; Lyubimov, I.; de Pablo, J. J.; Ediger, M. D. Tunable Molecular Orientation and Elevated Thermal Stability of Vapor-Deposited Organic Semiconductors. *Proc. Natl. Acad. Sci. USA* **2015**, *112*, 4227–4232.

(18) Senes, A.; Meskers, S. C. J.; Greiner, H.; Suzuki, K.; Kaji, H.; Adachi, C.; Wilson, J. S.; Janssen, R. A. J. Increasing the Horizontal Orientation of Transition Dipole Moments in Solution Processed Small Molecular Emitters. *J. Mater. Chem. C* **2017**, *5*, 6555–6562.

(19) Osaka, I.; Saito, M.; Koganezawa, T.; Takimiya, K. Thiophene–Thiazolothiazole Copolymers: Significant Impact of Side Chain Composition on Backbone Orientation and Solar Cell Performances. *Adv. Mater.* **2014**, *26*, 331–338.

(20) Chen, M. S.; Niskala, J. R.; Unruh, D. A.; Chu, C. K.; Lee, O. P.; Fréchet, J. M. J. Control of Polymer-Packing Orientation in Thin Films through Synthetic Tailoring of Backbone Coplanarity. *Chem. Mater.* **2013**, *25*, 4088–4096.

(21) Luzio, A.; Criante, L.; D'Innocenzo, V.; Caironi, M. Control of Charge Transport in a Semiconducting Copolymer by Solvent-Induced Long-Range Order. *Sci. Rep.* **2013**, *3*, 3425.

(22) Steyrleuthner, R.; Schubert, M.; Howard, I.; Klaumünzer, B.; Schilling, K.; Chen, Z.; Saalfrank, P.; Laquai, F.; Facchetti, A.; Neher, D. Aggregation in a High-Mobility n-Type Low-Bandgap Copolymer with Implications on Semicrystalline Morphology. *J. Am. Chem. Soc.* **2012**, *134*, 18303–18317.

(23) Steyrleuthner, R.; Di Pietro, R.; Collins, B. A.; Polzer, F.; Himmelberger, S.; Schubert, M.; Chen, Z.; Zhang, S.; Salleo, A.; Ade, H.; Facchetti, A.; Neher, D. The Role of Regioregularity, Crystallinity, and Chain Orientation on Electron Transport in a High-Mobility n-Type Copolymer. *J. Am. Chem. Soc.* **2014**, *136*, 4245–4256.

(24) Jackson, N. E.; Kohlstedt, K. L.; Savoie, B. M.; Olvera de la Cruz, M.; Schatz, G. C.; Chen, L. X.; Ratner, M. A. Conformational Order in Aggregates of Conjugated Polymers. *J. Am. Chem. Soc.* **2015**, *137*, 6254–6262.

(25) Nahid, M. M.; Welford, A.; Gann, E.; Thomsen, L.; Sharma, K. P.; McNeill, C. R. Nature and Extent of Solution Aggregation Determines the Performance of P(NDI2OD-T2) Thin-Film Transistors. *Adv. Electron. Mater.* **2018**, *4*, 1700559.

(26) Noriega, R.; Rivnay, J.; Vandewal, K.; Koch, F. P. V.; Stingelin, N.; Smith, P.; Toney, M. F.; Salleo, A. A General Relationship between Disorder, Aggregation and Charge Transport in Conjugated Polymers. *Nat. Mater.* **2013**, *12*, 1038–1044.

(27) Nahid, M. M.; Matsidik, R.; Welford, A.; Gann, E.; Thomsen, L.; Sommer, M.; McNeill, C. R. Unconventional Molecular Weight Dependence of Charge Transport in the High Mobility N-Type Semiconducting Polymer P(NDI2OD-T2). *Adv. Funct. Mater.* **2017**, *27*, 1604744.

(28) Dixon, A. G.; Visvanathan, R.; Clark, N. A.; Stingelin, N.; Kopidakis, N.; Shaheen, S. E. Molecular Weight Dependence of Carrier Mobility and Recombination Rate in Neat P3HT Films. *J. Polym. Sci. B: Polym. Phys.* **2018**, *56*, 31–35.

(29) Zhou, Q.; Shi, G. Conducting Polymer-Based Catalysts. *J. Am. Chem. Soc.* **2016**, *138*, 2868–2876.

(30) Bartelt, J. A.; Douglas, J. D.; Mateker, W. R.; Labban, A. E.; Tassone, C. J.; Toney, M. F.; Fréchet, J. M. J.; Beaujuge, P. M.; McGehee, M. D. Controlling Solution-Phase Polymer Aggregation with Molecular Weight and Solvent Additives to Optimize Polymer-Fullerene Bulk Heterojunction Solar Cells. *Adv. Energy Mater.* **2014**, *4*, 1301733.

(31) Liu, Z.; Zhang, G.; Zhang, D. Modification of Side Chains of Conjugated Molecules and Polymers for Charge Mobility Enhancement and Sensing Functionality. *Acc. Chem. Res.* **2018**, *51*, 1422–1432.

(32) Liu, X.; He, B.; Garzón-Ruiz, A.; Navarro, A.; Chen, T. L.; Kolaczkowski, M. A.; Feng, S.; Zhang, L.; Anderson, C. A.; Chen, J.; Liu, Y. Unraveling the Main Chain and Side Chain Effects on Thin Film Morphology and Charge Transport in Quinoidal Conjugated Polymers. *Adv. Funct. Mater.* **2018**, *28*, 1801874.

(33) Lee, C. S.; Dadmun, M. D. Important Thermodynamic Characteristics of Poly(3-Hexyl Thiophene). *Polymer* **2014**, *55*, 4–7.

(34) Siebbeles, L. D. A.; Grozema, F. C.; de Haas, M. P.; Warman, J. M. Effect of Backbone Structure on Charge Transport along Isolated Conjugated Polymer Chains. *Radiat. Phys. Chem.* **2005**, *72*, 85–91.

(35) Liu, J.; Ma, L.-K.; Li, Z.; Hu, H.; Kit Sheong, F.; Zhang, G.; Ade, H.; Yan, H. Donor Polymer Based on Alkylthiophene Side Chains for Efficient Non-Fullerene Organic Solar Cells: Insights into Fluorination and Side Chain Effects on Polymer Aggregation and Blend Morphology. *J. Mater. Chem. A* **2018**, *6*, 23270–23277.

(36) Alkan, M.; Yavuz, I. Intrinsic Charge-Mobility in Benzothieno[3,2-b][1]Benzothiophene (BTBT) Organic Semiconductors Is Enhanced with Long Alkyl Side-Chains. *Phys. Chem. Chem. Phys.* **2018**, *20*, 15970–15979.

(37) Kang, B.; Kim, R.; Lee, S. B.; Kwon, S.-K.; Kim, Y.-H.; Cho, K. Side-Chain-Induced Rigid Backbone Organization of Polymer Semiconductors through Semifluoroalkyl Side Chains. *J. Am. Chem. Soc.* **2016**, *138*, 3679–3686.

(38) Yang, G.; Li, Z.; Jiang, K.; Zhang, J.; Chen, J.; Zhang, G.; Huang, F.; Ma, W.; Yan, H. Optimal Extent of Fluorination Enabling Strong Temperature-Dependent Aggregation, Favorable Blend Morphology and High-Efficiency Polymer Solar Cells. *Sci. China Chem.* **2017**, *60*, 545–551.

(39) Zheng, Y.-Q.; Yao, Z.-F.; Lei, T.; Dou, J.-H.; Yang, C.-Y.; Zou, L.; Meng, X.; Ma, W.; Wang, J.-Y.; Pei, J. Unraveling the Solution-State Supramolecular Structures of Donor–Acceptor Polymers and Their Influence on Solid-State Morphology and Charge-Transport Properties. *Adv. Mater.* **2017**, *29*, 1701072.

(40) Hu, H.; Zhao, K.; Fernandes, N.; Boufflet, P.; H. Bannock, J.; Yu, L.; de Mello, J. C.; Stingelin, N.; Heeney, M.; P. Giannelis, E.; Amassian, A. Entanglements in Marginal Solutions: A Means of Tuning Pre-Aggregation of Conjugated Polymers with Positive Implications for Charge Transport. *J. Mater. Chem. C* **2015**, *3*, 7394–7404.

(41) Huang, Y.; Cheng, H.; Han, C. C. Temperature Induced Structure Evolution of Regioregular Poly(3-Hexylthiophene) in Dilute Solution and Its Influence on Thin Film Morphology. *Macromolecules* **2010**, *43*, 10031–10037.

(42) Cheng, P.; Yan, C.; Li, Y.; Ma, W.; Zhan, X. Diluting Concentrated Solution: A General, Simple and Effective Approach to Enhance Efficiency of Polymer Solar Cells. *Energy Environ. Sci.* **2015**, *8*, 2357–2364.

(43) Venkatesh, R.; Zheng, Y.; Vierson, C.; Liu, A.; Silva, C.; Grover, M.; Reichmanis, E. Data Science Guided Experiments Identify Conjugated Polymer Solution Concentration as a Key Parameter in Device Performance. *ACS Mater. Lett.* **2021**, 1321–1327.

(44) Li, M.; Bin, H.; Jiao, X.; Wienk, M. M.; Yan, H.; Janssen, R. A. J. Controlling the Microstructure of Conjugated Polymers in High-Mobility Monolayer Transistors via the Dissolution Temperature. *Angew. Chem. Int. Ed.* **2020**, *59*, 846–852.

(45) Sirringhaus, H.; Brown, P. J.; Friend, R. H.; Nielsen, M. M.; Bechgaard, K.; Langeveld-Voss, B. M. W.; Spiering, A. J. H.; Janssen, R. a. J.; Meijer, E. W.; Herwig, P.; de Leeuw, D. M. Two-Dimensional Charge Transport in Self-Organized, High-Mobility Conjugated Polymers. *Nature* **1999**, *401*, 685–688.

(46) Yokoyama, D. Molecular Orientation in Small-Molecule Organic Light-Emitting Diodes. *J. Mater. Chem.* **2011**, *21*, 19187–19202.

(47) Kim, K.-H.; Lee, S.; Moon, C.-K.; Kim, S.-Y.; Park, Y.-S.; Lee, J.-H.; Woo Lee, J.; Huh, J.; You, Y.; Kim, J.-J. Phosphorescent Dye-Based Supramolecules for High-Efficiency Organic Light-Emitting Diodes. *Nat. Commun.* **2014**, *5*, 4769.

(48) Komino, T.; Tanaka, H.; Adachi, C. Selectively Controlled Orientational Order in Linear-Shaped Thermally Activated Delayed Fluorescent Dopants. *Chem. Mater.* **2014**, *26*, 3665–3671.

(49) Lee, T.; Caron, B.; Stroet, M.; Huang, D. M.; Burn, P. L.; Mark, A. E. The Molecular Origin of Anisotropic Emission in an Organic Light-Emitting Diode. *Nano Lett.* **2017**, *17*, 6464–6468.

(50) Liu, C.-F.; Lin, Y.; Lai, W.-Y.; Huang, W. Understanding the Dependence of Performance on the Dielectric-Semiconductor Interface in Pentacene-Based Organic Field-Effect Transistors. *Mater. Lett.* **2017**, *189*, 286–289.

(51) Zhang, X.; Richter, L. J.; DeLongchamp, D. M.; Kline, R. J.; Hammond, M. R.; McCulloch, I.; Heeney, M.; Ashraf, R. S.; Smith, J. N.; Anthopoulos, T. D.; Schroeder, B.; Geerts, Y. H.; Fischer, D. A.; Toney, M. F. Molecular Packing of High-Mobility Diketo Pyrrolo-Pyrrole Polymer Semiconductors with Branched Alkyl Side Chains. *J. Am. Chem. Soc.* **2011**, *133*, 15073–15084.

(52) Kline, R. J.; DeLongchamp, D. M.; Fischer, D. A.; Lin, E. K.; Heeney, M.; McCulloch, I.; Toney, M. F. Significant Dependence of Morphology and Charge Carrier Mobility on Substrate Surface Chemistry in High Performance Polythiophene Semiconductor Films. *Appl. Phys. Lett.* **2007**, *90*, 062117.

(53) Rivnay, J.; Toney, M. F.; Zheng, Y.; Kauvar, I. V.; Chen, Z.; Wagner, V.; Facchetti, A.; Salleo, A. Unconventional Face-On Texture and Exceptional In-Plane Order of a High Mobility n-Type Polymer. *Adv. Mater.* **2010**, *22*, 4359–4363.

(54) Li, J.; Du, J.; Xu, J.; Chan, H. L. W.; Yan, F. The Influence of Gate Dielectrics on a High-Mobility n-Type Conjugated Polymer in Organic Thin-Film Transistors. *Appl. Phys. Lett.* **2012**, *100*, 033301.

(55) Horowitz, G. Organic Field-Effect Transistors. *Adv. Mater.* **1998**, *10*, 365–377.

(56) Horowitz, G. Organic Thin Film Transistors: From Theory to Real Devices. *J. Mater. Res.* **2004**, *19*, 1946–1962.

(57) Dinelli, F.; Murgia, M.; Levy, P.; Cavallini, M.; Biscarini, F.; de Leeuw, D. M. Spatially Correlated Charge Transport in Organic Thin Film Transistors. *Phys. Rev. Lett.* **2004**, *92*, 116802.

(58) Kiguchi, M.; Nakayama, M.; Fujiwara, K.; Ueno, K.; Shimada, T.; Saiki, K. Accumulation and Depletion Layer Thicknesses in Organic Field Effect Transistors. *Jpn. J. Appl. Phys.* **2003**, *42*, L1408.

(59) Zhao, N.; Noh, Y.-Y.; Chang, J.-F.; Heeney, M.; McCulloch, I.; Sirringhaus, H. Polaron Localization at Interfaces in High-Mobility Microcrystalline Conjugated Polymers. *Adv. Mater.* **2009**, *21*, 3759–3763.

(60) Caironi, M.; Bird, M.; Fazzi, D.; Chen, Z.; Pietro, R. D.; Newman, C.; Facchetti, A.; Sirringhaus, H. Very Low Degree of Energetic Disorder as the Origin of High Mobility in an N-Channel Polymer Semiconductor. *Adv. Funct. Mater.* **2011**, *21*, 3371–3381.

(61) Suemori, K.; Uemura, S.; Yoshida, M.; Hoshino, S.; Takada, N.; Kodzasa, T.; Kamata, T. Influence of Fine Roughness of Insulator Surface on Threshold Voltage Stability of Organic Field-Effect Transistors. *Appl. Phys. Lett.* **2008**, *93*, 033308.

(62) Jimison, L. H.; Salleo, A.; Chabinyc, M. L.; Bernstein, D. P.; Toney, M. F. Correlating the Microstructure of Thin Films of Poly[5,5-Bis(3-Dodecyl-2-Thienyl)-2,2-Bithiophene] with Charge Transport: Effect of Dielectric Surface Energy and Thermal Annealing. *Phys. Rev. B* **2008**, *78*, 125319.

(63) Duong, D. T.; Toney, M. F.; Salleo, A. Role of Confinement and Aggregation in Charge Transport in Semicrystalline Polythiophene Thin Films. *Phys. Rev. B* **2012**, *86*, 205205.

(64) Khim, D.; Luzio, A.; Bonacchini, G. E.; Pace, G.; Lee, M.-J.; Noh, Y.-Y.; Caironi, M. Uniaxial Alignment of Conjugated Polymer Films for High-Performance Organic Field-Effect Transistors. *Adv. Mater.* **2018**, *30*, 1705463.

(65) Pisula, W.; Zorn, M.; Chang, J. Y.; Müllen, K.; Zentel, R. Liquid Crystalline Ordering and Charge Transport in Semiconducting Materials. *Macromol. Rapid Commun.* **2009**, *30*, 1179–1202.

(66) Trefz, D.; Gross, Y. M.; Dingler, C.; Tkachov, R.; Hamidi-Sakr, A.; Kiriy, A.; McNeill, C. R.; Brinkmann, M.; Ludwigs, S. Tuning Orientational Order of Highly Aggregating P(NDI2OD-T2) by Solvent Vapor Annealing and Blade Coating. *Macromolecules* **2019**, *52*, 43–54.

(67) Bucella, S. G.; Luzio, A.; Gann, E.; Thomsen, L.; McNeill, C. R.; Pace, G.; Perinot, A.; Chen, Z.; Facchetti, A.; Caironi, M. Macroscopic and High-Throughput Printing of Aligned Nanostructured Polymer Semiconductors for MHz Large-Area Electronics. *Nat. Commun.* **2015**, *6*, 8394.

(68) Kline, R. J.; McGehee, M. D.; Kadnikova, E. N.; Liu, J.; Fréchet, J. M. J. Controlling the Field-Effect Mobility of Regioregular Polythiophene by Changing the Molecular Weight. *Adv. Mater.* **2003**, *15*, 1519–1522.

(69) Nguyen, N. N.; Jo, S. B.; Lee, S. K.; Sin, D. H.; Kang, B.; Kim, H. H.; Lee, H.; Cho, K. Atomically Thin Epitaxial Template for Organic Crystal Growth Using Graphene with Controlled Surface Wettability. *Nano Lett.* **2015**, *15*, 2474–2484.

(70) Yan, H.; Schuettfort, T.; Kronemeijer, A. J.; McNeill, C. R.; Ade, H. W. Influence of Dielectric-Dependent Interfacial Widths on Device Performance in Top-Gate P(NDI2OD-T2) Field-Effect Transistors. *Appl. Phys. Lett.* **2012**, *101*, 093308.

(71) Lee, W. H.; Cho, J. H.; Cho, K. Control of Mesoscale and Nanoscale Ordering of Organic Semiconductors at the Gate Dielectric/Semiconductor Interface for Organic Transistors. *J. Mater. Chem.* **2010**, *20*, 2549–2561.

(72) Wurzbach, I.; Rothe, C.; Bruchlos, K.; Ludwigs, S.; Giesselmann, F. Shear Alignment and 2D Charge Transport of Tilted Smectic Liquid Crystalline Phases – XRD and FET Studies. *J. Mater. Chem. C* **2019**, *7*, 2615–2624.

(73) Sapolsky, M.; McFaddin, J.; Boucher, D. Aggregation Behavior of Poly(3-Hexylthiophene) in Solvent Mixtures: Linear Solvation Energy Relationship (LSER) Modeling and COSMO-RS Calculations. *Macromol. Chem. Phys.* **2018**, *219*, 1700545.

(74) De Gennes, P.; Prost, J., *The Physics of Liquid Crystals*; Oxford University Press: 1995.

(75) Jerome, B. Surface Effects and Anchoring in Liquid Crystals. *Rep. Prog. Phys.* **1991**, *54*, 391–451.

(76) Telo Da Gama, M. M. In *Observation, Prediction and Simulation of Phase Transitions in Complex Fluids*, Baus, M., Rull, L. F., Ryckaert, J.-P., Eds.; Springer Netherlands: Dordrecht, 1995, pp 243–292.

(77) Bates, M. A.; Luckhurst, G. R. In, Mingos, D. M. P., Ed.; Springer Berlin Heidelberg: Berlin, Heidelberg, 1999; Chapter Computer Simulation of Liquid Crystal Phases Formed by Gay-Berne Mesogens, pp 65–137.

(78) Ryu, S. H.; Yoon, D. K. Liquid Crystal Phases in Confined Geometries. *Liq. Cryst.* **2016**, *43*, 1951–1972.

(79) Martín del Río, E.; Telo da Gama, M. M.; de Miguel, E.; Rull, L. F. Surface-Induced Alignment at Model Nematic Interfaces. *Phys. Rev. E* **1995**, *52*, 5028–5039.

(80) Kimura, H.; Nakano, H. Statistical Theory of Surface Tension and Molecular Orientations at the Free Surface in Nematic Liquid Crystals. *J. Phys. Soc. Jpn.* **1985**, *54*, 1730–1736.

(81) Gay, J. G.; Berne, B. J. Modification of the Overlap Potential to Mimic a Linear Site–Site Potential. *J. Chem. Phys.* **1981**, *74*, 3316–3319.

(82) Mills, S. J.; Care, C. M.; Neal, M. P.; Cleaver, D. J. Computer Simulation of an Unconfined Liquid Crystal Film. *Phys. Rev. E* **1998**, *58*, 3284–3294.

(83) Martín del Río, E.; de Miguel, E. Computer Simulation Study of the Free Surfaces of a Liquid Crystal Model. *Phys. Rev. E* **1997**, *55*, 2916–2924.

(84) Rull, L. F.; Romero-Enrique, J. M. Computer Simulation Study of the Nematic–Vapour Interface in the Gay–Berne Model. *Mol. Phys.* **2017**, *115*, 1214–1224.

(85) Okano, K. Anisotropic Excluded Volume Effect and Alignment of Nematic Liquid Crystal in a Sandwich Cell. *Jpn. J. Appl. Phys.* **1983**, *22*, L343–L344.

(86) Egorov, S. A.; Milchev, A.; Binder, K. Semiflexible Polymers in the Bulk and Confined by Planar Walls. *Polymers* **2016**, *8*, 296.

(87) Wall, G. D.; Cleaver, D. J. Computer Simulations of Adsorbed Liquid Crystal Films. *Mol. Phys.* **2003**, *101*, 1105–1112.

(88) Antypov, D.; Cleaver, D. J. The Role of Attractive Interactions in Rod–Sphere Mixtures. *J. Chem. Phys.* **2004**, *120*, 10307–10316.

(89) Brader, J. M.; Esztermann, A.; Schmidt, M. Colloidal Rod-Sphere Mixtures: Fluid-fluid Interfaces and the Onsager Limit. *Phys. Rev. E* **2002**, *66*, 031401.

(90) Kim, B.-G.; Jeong, E. J.; Chung, J. W.; Seo, S.; Koo, B.; Kim, J. A Molecular Design Principle of Lyotropic Liquid-Crystalline Conjugated Polymers with Directed Alignment Capability for Plastic Electronics. *Nat. Mater.* **2013**, *12*, 659–664.

(91) Kim, Y.; Cook, S.; Tuladhar, S. M.; Choulis, S. A.; Nelson, J.; Durrant, J. R.; Bradley, D. D. C.; Giles, M.; McCulloch, I.; Ha, C.-S.; Ree, M. A Strong Regioregularity Effect in Self-Organizing Conjugated Polymer Films and High-Efficiency Polythiophene:Fullerene Solar Cells. *Nat. Mater.* **2006**, *5*, 197.

(92) Kang, H.; Uddin, M. A.; Lee, C.; Kim, K.-H.; Nguyen, T. L.; Lee, W.; Li, Y.; Wang, C.; Woo, H. Y.; Kim, B. J. Determining the Role of Polymer Molecular Weight for High-Performance All-Polymer Solar Cells: Its Effect on Polymer Aggregation and Phase Separation. *J. Am. Chem. Soc.* **2015**, *137*, 2359–2365.

(93) Osaka, I.; Saito, M.; Mori, H.; Koganezawa, T.; Takimiya, K. Drastic Change of Molecular Orientation in a Thiazolothiazole Copolymer by Molecular-Weight Control and Blending with $PC_{61}BM$ Leads to High Efficiencies in Solar Cells. *Adv. Mater.* **2012**, *24*, 425–430.

(94) Zhou, N.; Dudnik, A. S.; Li, T. I. N. G.; Manley, E. F.; Aldrich, T. J.; Guo, P.; Liao, H.-C.; Chen, Z.; Chen, L. X.; Chang, R. P. H.; Facchetti, A.; Olvera de la Cruz, M.; Marks, T. J. All-Polymer Solar Cell Performance Optimized via Systematic Molecular Weight Tuning of Both Donor and Acceptor Polymers. *J. Am. Chem. Soc.* **2016**, *138*, 1240–1251.

(95) Fan, B.; Ying, L.; Wang, Z.; He, B.; Jiang, X.-F.; Huang, F.; Cao, Y. Optimisation of Processing Solvent and Molecular Weight for the Production of Green-Solvent-Processed All-Polymer Solar Cells with a Power Conversion Efficiency over 9%. *Energy Environ. Sci.* **2017**, *10*, 1243–1251.

(96) Zhang, W.; Gomez, E. D.; Milner, S. T. Surface-Induced Chain Alignment of Semiflexible Polymers. *Macromolecules* **2016**, *49*, 963–971.

(97) Antony, L. W.; Jackson, N. E.; Lyubimov, I.; Vishwanath, V.; Ediger, M. D.; de Pablo, J. J. Influence of Vapor Deposition on Structural and Charge Transport Properties of Ethylbenzene Films. *ACS Cent. Sci.* **2017**, *3*, 415–424.

(98) Lyubimov, I.; Antony, L.; Walters, D. M.; Rodney, D.; Ediger, M. D.; de Pablo, J. J. Orientational Anisotropy in Simulated Vapor-Deposited Molecular Glasses. *J. Chem. Phys.* **2015**, *143*, 094502.

(99) Jiang, J.; Walters, D. M.; Zhou, D.; Ediger, M. D. Substrate Temperature Controls Molecular Orientation in Two-Component Vapor-Deposited Glasses. *Soft Matter* **2016**, *12*, 3265–3270.

(100) Gujral, A.; Gómez, J.; Ruan, S.; Toney, M. F.; Bock, H.; Yu, L.; Ediger, M. Vapor-Deposited Glasses with Long-Range Columnar Liquid Crystalline Order. *Chem. Mater.* **2017**, *29*, 9110–9119.

(101) Gómez, J.; Jiang, J.; Gujral, A.; Huang, C.; Yu, L.; Ediger, M. D. Vapor Deposition of a Smectic Liquid Crystal: Highly Anisotropic, Homogeneous Glasses with Tunable Molecular Orientation. *Soft Matter* **2016**, *12*, 2942–2947.

(102) Ediger, M. D.; de Pablo, J.; Yu, L. Anisotropic Vapor-Deposited Glasses: Hybrid Organic Solids. *Acc. Chem. Res.* **2019**, *52*, 407–414.

(103) Rivnay, J.; Steyrleuthner, R.; Jimison, L. H.; Casadei, A.; Chen, Z.; Toney, M. F.; Facchetti, A.; Neher, D.; Salleo, A. Drastic Control of Texture in a High Performance N-Type Polymeric Semiconductor and Implications for Charge Transport. *Macromolecules* **2011**, *44*, 5246–5255.

(104) Bhattacharyya, D.; Montenegro, A.; Dhar, P.; Mammetkuliyev, M.; Pankow, R. M.; Jung, M. C.; Thompson, M. E.; Thompson, B. C.; Benderskii, A. V. Molecular Orientation of Poly-3-hexylthiophene at the Buried Interface with Fullerene. *J. Phys. Chem. Lett.* **2019**, 1757–1762.

(105) Liu, S.; Wang, W. M.; Briseno, A. L.; Mannsfeld, S. C. B.; Bao, Z. Controlled Deposition of Crystalline Organic Semiconductors for Field-Effect-Transistor Applications. *Adv. Mater.* **2009**, *21*, 1217–1232.

(106) Li, Q.-F.; Liu, S.; Chen, H.-Z.; Li, H.-Y. Alignment and Patterning of Organic Single Crystals for Field-Effect Transistors. *Chin. Chem. Lett.* **2016**, *27*, 1421–1428.

(107) Jurow, M. J.; Mayr, C.; Schmidt, T. D.; Lampe, T.; Djurovich, P. I.; Brütting, W.; Thompson, M. E. Understanding and Predicting the Orientation of Heteroleptic Phosphors in Organic Light-Emitting Materials. *Nat. Mater.* **2016**, *15*, 85–91.

(108) Lampe, T.; Schmidt, T. D.; Jurow, M. J.; Djurovich, P. I.; Thompson, M. E.; Brütting, W. Dependence of Phosphorescent Emitter Orientation on Deposition Technique in Doped Organic Films. *Chem. Mater.* **2016**, *28*, 712–715.

(109) Pan, G.; Chen, F.; Hu, L.; Zhang, K.; Dai, J.; Zhang, F. Effective Controlling of Film Texture and Carrier Transport of a High-Performance Polymeric Semiconductor by Magnetic Alignment. *Adv. Funct. Mater.* **2015**, *25*, 5126–5133.

(110) Shklyarevskiy, I. O.; Jonkheijm, P.; Stutzmann, N.; Wasserberg, D.; Wondergem, H. J.; Christianen, P. C. M.; Schenning, A. P. H. J.; de Leeuw, D. M.; Tomović, Ž.; Wu, J.; Müllen, K.; Maan, J. C. High Anisotropy of the Field-Effect Transistor Mobility in Magnetically Aligned Discotic Liquid-Crystalline Semiconductors. *J. Am. Chem. Soc.* **2005**, *127*, 16233–16237.

(111) Mas-Torrent, M.; den Boer, D.; Durkut, M.; Hadley, P.; Schenning, A. P. H. J. Field Effect Transistors Based on Poly(3-Hexylthiophene) at Different Length Scales. *Nanotechnology* **2004**, *15*, S265–S269.

(112) Simoni, F.; Francescangeli, O. Effects of Light on Molecular Orientation of Liquid Crystals. *J. Phys: Condens. Matter* **1999**, *11*, R439–R487.

(113) Zhang, F.; Mohammadi, E.; Luo, X.; Strzalka, J.; Mei, J.; Diao, Y. Critical Role of Surface Energy in Guiding Crystallization of Solution-Coated Conjugated Polymer Thin Films. *Langmuir* **2018**, *34*, 1109–1122.

(114) Meyer, D. L.; Matsidik, R.; Huettner, S.; Sommer, M.; Biskup, T. Solvent-Mediated Aggregate Formation of PNDIT2: Decreasing the Available Conformational Subspace by Introducing Locally Highly Ordered Domains. *Phys. Chem. Chem. Phys.* **2018**, *20*, 2716–2723.

(115) Salleo, A. Charge Transport in Polymeric Transistors. *Mater. Today* **2007**, *10*, 38–45.

(116) Jones, M. L.; Huang, D. M.; Chakrabarti, B.; Groves, C. Relating Molecular Morphology to Charge Mobility in Semicrystalline Conjugated Polymers. *J. Phys. Chem. C* **2016**, *120*, 4240–4250.

(117) Park, K.; Shin, E.-Y.; Jiao, X.; McNeill, C. R.; Kim, Y.-H.; Kwon, S.-K.; Noh, Y.-Y. Effect of Backbone Sequence of a Naphthalene Diimide-Based Copolymer on Performance in n-Type Organic Thin-Film Transistors. *ACS Appl. Mater. Interfaces* **2019**, *11*, 35185–35192.

(118) Wadsworth, A.; Chen, H.; Thorley, K. J.; Cendra, C.; Nikolka, M.; Bristow, H.; Moser, M.; Salleo, A.; Anthopoulos, T. D.; Sirringhaus, H.; McCulloch, I. Modification of Indacenodithiophene-Based Polymers and Its Impact on Charge Carrier Mobility in Organic Thin-Film Transistors. *J. Am. Chem. Soc.* **2020**, *142*, 652–664.

(119) Guo, S.; Wang, W.; Herzig, E. M.; Naumann, A.; Tainter, G.; Perlich, J.; Müller-Buschbaum, P. Solvent-Morphology-Property Relationship of PTB7:PC71BM Polymer Solar Cells. *ACS Appl. Mater. Interfaces* **2017**, *9*, 3740–3748.

(120) Morgan, B.; Dadmun, M. D. The Importance of Solvent Quality on the Modification of Conjugated Polymer Conformation and Thermodynamics with Illumination. *Soft Matter* **2017**, *13*, 2773–2780.

(121) Xiao, Z.; Sun, K.; Subbiah, J.; Qin, T.; Lu, S.; Purushothaman, B.; Jones, D. J.; Holmes, A. B.; Wong, W. W. H. Effect of Molecular Weight on the Properties and Organic Solar Cell Device Performance of a Donor-Acceptor Conjugated Polymer. *Polym. Chem.* **2015**, *6*, 2312–2318.

(122) Babel, A.; Jenekhe, S. A. Alkyl Chain Length Dependence of the Field-Effect Carrier Mobility in Regioregular Poly(3-Alkylthiophene)s. *Synth. Met.* **2005**, *148*, 169–173.

(123) Hu, Y.; Cao, D. X.; Lill, A. T.; Jiang, L.; Di, C.-A.; Gao, X.; Sirringhaus, H.; Nguyen, T.-Q. Effect of Alkyl-Chain Length on Charge Transport Properties of Organic Semiconductors and Organic Field-Effect Transistors. *Adv. Electron. Mater.* **2018**, *0*, 1800175.

(124) Welford, A.; Maniam, S.; Gann, E.; Jiao, X.; Thomsen, L.; Langford, S. J.; McNeill, C. R. Influence of Alkyl Side-Chain Type and Length on the Thin Film Microstructure and OFET Performance of Naphthalene Diimide-Based Organic Semiconductors. *Org. Electron.* **2019**, *75*, 105378.

(125) Ibraikulov, O. A.; Ngov, C.; Chavez, P.; Bulut, I.; Heinrich, B.; Boyron, O.; Gerasimov, K. L.; Ivanov, D. A.; Swaraj, S.; Mery, S.; Leclerc, N.; Leveque, P.; Heiser, T. Face-on Orientation of Fluorinated Polymers Conveyed by Long Alkyl Chains: A Prerequisite for High Photovoltaic Performances. *J. Mater. Chem. A* **2018**, *6*, 12038–12045.

(126) Lei, T.; Wang, J.-Y.; Pei, J. Roles of Flexible Chains in Organic Semiconducting Materials. *Chem. Mater.* **2014**, *26*, 594–603.

(127) Rubinstein, M.; Colby, R. H., *Polymer Physics*; Oxford University Press: 2003; 454 pp.

(128) Caddeo, C.; Mattoni, A. Atomistic Investigation of the Solubility of 3-Alkylthiophene Polymers in Tetrahydrofuran Solvent. *Macromolecules* **2013**, *46*, 8003–8008.

(129) Caddeo, C.; Fazzi, D.; Caironi, M.; Mattoni, A. Atomistic Simulations of P(NDI2OD-T2) Morphologies: From Single Chain to Condensed Phases. *J. Phys. Chem. B* **2014**, *118*, 12556–12565.

(130) Wang, T.; Brédas, J.-L. Organic Photovoltaics: Understanding the Preaggregation of Polymer Donors in Solution and Its Morphological Impact. *J. Am. Chem. Soc.* **2021**, *143*, 1822–1835.

(131) Marenz, M.; Janke, W. Knots as a Topological Order Parameter for Semiflexible Polymers. *Phys. Rev. Lett.* **2016**, *116*, 128301.

(132) Cohen, A. E.; Jackson, N. E.; de Pablo, J. J. Anisotropic Coarse-Grained Model for Conjugated Polymers: Investigations into Solution Morphologies. *Macromolecules* **2021**, *54*, 3780–3789.

(133) Wu, J.; Cheng, C.; Liu, G.; Zhang, P.; Chen, T. The Folding Pathways and Thermodynamics of Semiflexible Polymers. *J. Chem. Phys.* **2018**, *148*, 184901.

(134) Zierenberg, J.; Janke, W. From Amorphous Aggregates to Polymer Bundles: The Role of Stiffness on Structural Phases in Polymer Aggregation. *EPL* **2015**, *109*, 28002.

(135) Lappala, A.; Terentjev, E. M. Maximum Compaction Density of Folded Semiflexible Polymers. *Macromolecules* **2013**, *46*, 7125–7131.

(136) Gordievskaya, Y. D.; Kramarenko, E. Y. Conformational Behavior of a Semiflexible Dipolar Chain with a Variable Relative Size of Charged Groups via Molecular Dynamics Simulations. *Soft Matter* **2019**, *15*, 6073–6085.

(137) Noguchi, H.; Yoshikawa, K. Folding Path in a Semiflexible Homopolymer Chain: A Brownian Dynamics Simulation. *J. Chem. Phys.* **2000**, *113*, 854–862.

(138) Montesi, A.; Pasquali, M.; MacKintosh, F. C. Collapse of a Semiflexible Polymer in Poor Solvent. *Phys. Rev. E* **2004**, *69*, 021916.

(139) Kong, M.; Saha Dalal, I.; Li, G.; Larson, R. G. Systematic Coarse-Graining of the Dynamics of Self-Attractive Semiflexible Polymers. *Macromolecules* **2014**, *47*, 1494–1502.

(140) Huang, W.; Huang, M.; Lei, Q.; Larson, R. G. A Simple Analytical Model for Predicting the Collapsed State of Self-Attractive Semiflexible Polymers. *Polymers* **2016**, *8*, 264.

(141) Kuznetsov, Y. A.; Timoshenko, E. G.; Dawson, K. A. Equilibrium and Kinetic Phenomena in a Stiff Homopolymer and Possible Applications to DNA. *J. Chem. Phys.* **1996**, *105*, 7116–7134.

(142) Yoshinaga, N. Folding and Unfolding Kinetics of a Single Semiflexible Polymer. *Phys. Rev. E* **2008**, *77*, 061805.

(143) Hoang, T. X.; Giacometti, A.; Podgornik, R.; Nguyen, N. T. T.; Banavar, J. R.; Maritan, A. From Toroidal to Rod-like Condensates of Semiflexible Polymers. *J. Chem. Phys.* **2014**, *140*, 064902.

(144) Sakaue, T.; Yoshikawa, K. Folding/Unfolding Kinetics on a Semiflexible Polymer Chain. *J. Chem. Phys.* **2002**, *117*, 6323–6330.

(145) Salleo, A.; Kline, R. J.; DeLongchamp, D. M.; Chabinyc, M. L. Microstructural Characterization and Charge Transport in Thin Films of Conjugated Polymers. *Adv. Mater.* **2010**, *22*, 3812–3838.

(146) Dantanarayana, V.; Huang, D. M.; Staton, J. A.; Moulé, A. J.; Faller, R. In *Third Generation Photovoltaics*, Fthenakis, V., Ed.; IntechOpen: Rijeka, 2012; Chapter 2.

(147) Muccioli, L.; D'Avino, G.; Berardi, R.; Orlandi, S.; Pizzirusso, A.; Ricci, M.; Roscioni, O. M.; Zannoni, C. In *Multiscale Modelling of Organic and Hybrid Photovoltaics*, Beljonne, D., Cornil, J., Eds.; Topics in Current Chemistry; Springer Berlin Heidelberg: Berlin, Heidelberg, 2014, pp 39–101.

(148) Gartner, T. E.; Jayaraman, A. Modeling and Simulations of Polymers: A Roadmap. *Macromolecules* **2019**, *52*, 755–786.

(149) Abeln, S.; Vendruscolo, M.; Dobson, C. M.; Frenkel, D. A Simple Lattice Model That Captures Protein Folding, Aggregation and Amyloid Formation. *PLOS One* **2014**, *9*, e85185.

(150) Bachmann, M.; Janke, W. Multicanonical Chain-Growth Algorithm. *Phys. Rev. Lett.* **2003**, *91*, 208105.

(151) Latshaw, D. C.; Cheon, M.; Hall, C. K. Effects of Macromolecular Crowding on Amyloid Beta (16–22) Aggregation Using Coarse-Grained Simulations. *J. Phys. Chem. B* **2014**, *118*, 13513–13526.

(152) Nguyen, H. D.; Hall, C. K. Molecular Dynamics Simulations of Spontaneous Fibril Formation by Random-Coil Peptides. *Proc. Natl. Acad. Sci. USA* **2004**, *101*, 16180–16185.

(153) Hu, T.; Han, G.; Tu, Z.; Duan, R.; Yi, Y. Origin of High Efficiencies for Thermally Activated Delayed Fluorescence Organic Light-Emitting Diodes: Atomistic Insight into Molecular Orientation and Torsional Disorder. *J. Phys. Chem. C* **2018**, *122*, 27191–27197.

(154) Tonnelé, C.; Stroet, M.; Caron, B.; Clulow, A. J.; Nagiri, R. C. R.; Malde, A. K.; Burn, P. L.; Gentle, I. R.; Mark, A. E.; Powell, B. J. Elucidating the Spatial Arrangement of Emitter Molecules in Organic Light-Emitting Diode Films. *Angew. Chem. Int. Ed.* **2017**, *56*, 8402–8406.

(155) Ratcliff, L. E.; Grisanti, L.; Genovese, L.; Deutsch, T.; Neumann, T.; Danilov, D.; Wenzel, W.; Beljonne, D.; Cornil, J. Toward Fast and Accurate Evaluation of Charge On-Site Energies and Transfer Integrals in Supramolecular Architectures Using Linear Constrained Density Functional Theory (CDFT)-Based Methods. *J. Chem. Theory Comput.* **2015**, *11*, 2077–2086.

(156) Yoo, D.; Song, H.; Youn, Y.; Ho Jeon, S.; Cho, Y.; Han, S. A Molecular Dynamics Study on the Interface Morphology of Vapor-Deposited Amorphous Organic Thin Films. *Phys. Chem. Chem. Phys.* **2019**, *21*, 1484–1490.

(157) Han, G.; Shen, X.; Yi, Y. Deposition Growth and Morphologies of C60 on DTDCTB Surfaces: An Atomistic Insight into the Integrated Impact of Surface Stability, Landscape, and Molecular Orientation. *Adv. Mater. Interfaces* **2015**, *2*, 1500329.

(158) Sener, M.; Strumpfer, J.; Singharoy, A.; Hunter, C. N.; Schulten, K. Overall Energy Conversion Efficiency of a Photosynthetic Vesicle. *eLife* **2016**, *5*, e09541.

(159) Shaw, D. E.; Maragakis, P.; Lindorff-Larsen, K.; Piana, S.; Dror, R. O.; Eastwood, M. P.; Bank, J. A.; Jumper, J. M.; Salmon, J. K.; Shan, Y.; Wriggers, W. Atomic-Level Characterization of the Structural Dynamics of Proteins. *Science* **2010**, *330*, 341–346.

(160) Wang, T.; Ravva, M. K.; Brédas, J.-L. Impact of the Nature of the Side-Chains on the Polymer-Fullerene Packing in the Mixed Regions of Bulk Heterojunction Solar Cells. *Adv. Funct. Mater.* **2016**, *26*, 5913–5921.

(161) Reid, D. R.; Jackson, N. E.; Bourque, A. J.; Snyder, C. R.; Jones, R. L.; de Pablo, J. J. Aggregation and Solubility of a Model Conjugated Donor–Acceptor Polymer. *J. Phys. Chem. Lett.* **2018**, *9*, 4802–4807.

(162) García, E. J.; Hasse, H. Studying Equilibria of Polymers in Solution by Direct Molecular Dynamics Simulations: Poly(N-isopropylacrylamide) in Water as a Test Case. *Eur. Phys. J. Spec. Top.* **2019**, *227*, 1547–1558.

(163) Gertsen, A. S.; Sørensen, M. K.; Andreasen, J. W. Nanostructure of Organic Semiconductor Thin Films: Molecular Dynamics Modeling with Solvent Evaporation. *Phys. Rev. Materials* **2020**, *4*, 075405.

(164) Lee, T.; Sanzogni, A. V.; Burn, P. L.; Mark, A. E. Evolution and Morphology of Thin Films Formed by Solvent Evaporation: An Organic Semiconductor Case Study. *ACS Appl. Mater. Interfaces* **2020**, *12*, 40548–40557.

(165) Kline, R. J.; McGehee, M. D.; Toney, M. F. Highly Oriented Crystals at the Buried Interface in Polythiophene Thin-Film Transistors. *Nat. Mater.* **2006**, *5*, 222–228.

(166) Lyons, B. P.; Clarke, N.; Groves, C. The Relative Importance of Domain Size, Domain Purity and Domain Interfaces to the Performance of Bulk-Heterojunction Organic Photovoltaics. *Energy Environ. Sci.* **2012**, *5*, 7657–7663.

(167) Schwarz, K. N.; Kee, T. W.; Huang, D. M. Coarse-Grained Simulations of the Solution-Phase Self-Assembly of Poly(3-Hexylthiophene) Nanostructures. *Nanoscale* **2013**, *5*, 2017–2027.

(168) Huang, D. M.; Faller, R.; Do, K.; Moulé, A. J. Coarse-Grained Computer Simulations of Polymer/Fullerene Bulk Heterojunctions for Organic Photovoltaic Applications. *J. Chem. Theory Comput.* **2010**, *6*, 526–537.

(169) Alessandri, R.; Uusitalo, J. J.; de Vries, A. H.; Havenith, R. W. A.; Marrink, S. J. Bulk Heterojunction Morphologies with Atomistic Resolution from Coarse-Grain Solvent Evaporation Simulations. *J. Am. Chem. Soc.* **2017**, *139*, 3697–3705.

(170) Noid, W. G. Perspective: Coarse-grained Models for Biomolecular Systems. *J. Chem. Phys.* **2013**, *139*, 090901.

(171) Izvekov, S.; Voth, G. A. Multiscale Coarse Graining of Liquid-State Systems. *J. Chem. Phys.* **2005**, *123*, 134105.

(172) Reith, D.; Pütz, M.; Müller-Plathe, F. Deriving Effective Mesoscale Potentials from Atomistic Simulations. *J. Comput. Chem.* **2003**, *24*, 1624–1636.

(173) Shell, M. S. The Relative Entropy Is Fundamental to Multiscale and Inverse Thermodynamic Problems. *J. Chem. Phys.* **2008**, *129*, 144108.

(174) Lee, C. K.; Hua, C. C.; Chen, S. A. An Ellipsoid-Chain Model for Conjugated Polymer Solutions. *J. Chem. Phys.* **2012**, *136*, 084901.

(175) Lee, C.-K.; Pao, C.-W. Multiscale Molecular Simulation of Solution Processing of SMDPPEH: PCBM Small-Molecule Organic Solar Cells. *ACS Appl. Mater. Interfaces* **2016**, *8*, 20691–20700.

(176) Bowen, A. S.; Jackson, N. E.; Reid, D. R.; de Pablo, J. J. Structural Correlations and Percolation in Twisted Perylene Diimides Using a Simple Anisotropic Coarse-Grained Model. *J. Chem. Theory Comput.* **2018**, DOI: 10.1021/acs.jctc.8b00742.

(177) Berardi, R.; Fava, C.; Zannoni, C. A Generalized Gay-Berne Intermolecular Potential for Biaxial Particles. *Chem. Phys. Lett.* **1995**, *236*, 462–468.

(178) Everaers, R.; Ejtehadi, M. R. Interaction Potentials for Soft and Hard Ellipsoids. *Phys. Rev. E* **2003**, *67*, 041710.

(179) Babadi, M.; Everaers, R.; Ejtehadi, M. R. Coarse-Grained Interaction Potentials for Anisotropic Molecules. *J. Chem. Phys.* **2006**, *124*, 174708.

(180) Babadi, M.; Ejtehadi, M. R.; Everaers, R. Analytical First Derivatives of the RE-squared Interaction Potential. *J. Comput. Phys.* **2006**, *219*, 770–779.

(181) Brown, W. M.; Petersen, M. K.; Plimpton, S. J.; Grest, G. S. Liquid Crystal Nanodroplets in Solution. *J. Chem. Phys.* **2009**, *130*, 044901.

(182) Lee, C.-K.; Pao, C.-W.; Chu, C.-W. Multiscale Molecular Simulations of the Nanoscale Morphologies of P3HT:PCBM Blends for Bulk Heterojunction Organic Photovoltaic Cells. *Energy Environ. Sci.* **2011**, *4*, 4124–4132.

(183) Lee, C.-K.; Pao, C.-W. Solubility of [6,6]-Phenyl-C61-butyric Acid Methyl Ester and Optimal Blending Ratio of Bulk Heterojunction Polymer Solar Cells. *J. Phys. Chem. C* **2012**, *116*, 12455–12461.

(184) Lin, C.-C.; Ho, P.-H.; Huang, C.-L.; Du, C.-H.; Yu, C.-C.; Chen, H.-L.; Yeh, Y.-C.; Li, S.-S.; Lee, C.-K.; Pao, C.-W.; Chang, C.-P.; Chu, M.-W.; Chen, C.-W. Dependence of Nanocrystal Dimensionality on the Polymer Nanomorphology, Anisotropic Optical Absorption, and Carrier Transport in P3HT:TiO2 Bulk Heterojunctions. *J. Phys. Chem. C* **2012**, *116*, 25081–25088.

(185) Jankowski, E.; Marsh, H. S.; Jayaraman, A. Computationally Linking Molecular Features of Conjugated Polymers and Fullerene Derivatives to Bulk Heterojunction Morphology. *Macromolecules* **2013**, *46*, 5775–5785.

(186) To, T. T.; Adams, S. Modelling of P3HT:PCBM Interface Using Coarse-Grained Forcefield Derived from Accurate Atomistic Forcefield. *Phys. Chem. Chem. Phys.* **2014**, *16*, 4653–4663.

(187) Long, G.; Shi, R.; Zhou, Y.; Li, A.; Kan, B.; Wu, W.-R.; Jeng, U.-S.; Xu, T.; Yan, T.; Zhang, M.; Yang, X.; Ke, X.; Sun, L.; Gray-Weale, A.; Wan, X.; Zhang, H.; Li, C.; Wang, Y.; Chen, Y. Molecular Origin of Donor- and Acceptor-Rich Domain Formation in Bulk-Heterojunction Solar Cells with an Enhanced Charge Transport Efficiency. *J. Phys. Chem. C* **2017**, *121*, 5864–5870.

(188) Mansbach, R. A.; Ferguson, A. L. Coarse-Grained Molecular Simulation of the Hierarchical Self-Assembly of π-Conjugated Optoelectronic Peptides. *J. Phys. Chem. B* **2017**, *121*, 1684–1706.

(189) Carbone, P.; Varzaneh, H. A. K.; Chen, X.; Müller-Plathe, F. Transferability of Coarse-Grained Force Fields: The Polymer Case. *J. Chem. Phys.* **2008**, *128*, 064904.

(190) Root, S. E.; Savagatrup, S.; Pais, C. J.; Arya, G.; Lipomi, D. J. Predicting the Mechanical Properties of Organic Semiconductors Using Coarse-Grained Molecular Dynamics Simulations. *Macromolecules* **2016**, *49*, 2886–2894.

(191) Dünweg, B.; Ladd, A. J. C. Lattice Boltzmann Simulations of Soft Matter Systems. *Adv. Polym. Sci.* **2008**, *221*, 89–166.

(192) Schlick, T.; Portillo-Ledesma, S. Biomolecular Modeling Thrives in the Age of Technology. *Nat Comput Sci* **2021**, *1*, 321–331.

(193) Verlet, L. Computer "Experiments" on Classical Fluids. I. Thermodynamical Properties of Lennard-Jones Molecules. *Phys. Rev.* **1967**, *159*, 98–103.

(194) Tuckerman, M. E.; Alejandre, J.; López-Rendón, R.; Jochim, A. L.; Martyna, G. J. A Liouville-operator Derived Measure-Preserving Integrator for Molecular Dynamics Simulations in the Isothermal–Isobaric Ensemble. *J. Phys. A: Math. Gen.* **2006**, *39*, 5629–5651.

(195) Nosé, S. A Unified Formulation of the Constant Temperature Molecular Dynamics Methods. *J. Chem. Phys.* **1984**, *81*, 511–519.

(196) Hoover, W. G. Canonical Dynamics: Equilibrium Phase-Space Distributions. *Phys. Rev. A* **1985**, *31*, 1695–1697.

(197) Schneider, T.; Stoll, E. Molecular-Dynamics Study of a Three-Dimensional One-Component Model for Distortive Phase Transitions. *Phys. Rev. B* **1978**, *17*, 1302–1322.

(198) Martyna, G. J.; Tobias, D. J.; Klein, M. L. Constant Pressure Molecular Dynamics Algorithms. *J. Chem. Phys.* **1994**, *101*, 4177–4189.

(199) Berardi, R.; Fava, C.; Zannoni, C. A Gay–Berne Potential for Dissimilar Biaxial Particles. *Chem. Phys. Lett.* **1998**, *297*, 8–14.

(200) Stone, A. J. The Description of Bimolecular Potentials, Forces and Torques: The S and V Function Expansions. *Mol. Phys.* **1978**, *36*, 241–256.

(201) Hockney, R. W.; Eastwood, J. W., *Computer Simulation Using Particles*; CRC Press: Boca Raton, 1988; 540 pp.

(202) Jorgensen, W. L.; Maxwell, D. S.; Tirado-Rives, J. Development and Testing of the OPLS All-Atom Force Field on Conformational Energetics and Properties of Organic Liquids. *J. Am. Chem. Soc.* **1996**, *118*, 11225–11236.

(203) Jackson, N. E.; Savoie, B. M.; Marks, T. J.; Chen, L. X.; Ratner, M. A. The Next Breakthrough for Organic Photovoltaics? *J. Phys. Chem. Lett.* **2015**, *6*, 77–84.

(204) Huang, D. M. Computational Study of P3HT/C60-Fullerene Miscibility. *Aust. J. Chem.* **2014**, *67*, 585–591.

(205) Noid, W. G.; Chu, J.-W.; Ayton, G. S.; Krishna, V.; Izvekov, S.; Voth, G. A.; Das, A.; Andersen, H. C. The Multiscale Coarse-Graining Method. I. A Rigorous Bridge between Atomistic and Coarse-Grained Models. *J. Chem. Phys.* **2008**, *128*, 244114.

(206) Das, A.; Andersen, H. C. The Multiscale Coarse-Graining Method. V. Isothermal-isobaric Ensemble. *J. Chem. Phys.* **2010**, *132*, 164106.

(207) Izvekov, S.; Chung, P. W.; Rice, B. M. The Multiscale Coarse-Graining Method: Assessing Its Accuracy and Introducing Density Dependent Coarse-Grain Potentials. *J. Chem. Phys.* **2010**, *133*, 064109.

(208) Ollila, S. T. T.; Denniston, C.; Karttunen, M.; Ala-Nissila, T. Fluctuating Lattice-Boltzmann Model for Complex Fluids. *J. Chem. Phys.* **2011**, *134*, 064902.

(209) Invernizzi, M.; Parrinello, M. Rethinking Metadynamics: From Bias Potentials to Probability Distributions. *J. Phys. Chem. Lett.* **2020**, *11*, 2731–2736.

(210) Laio, A.; Parrinello, M. Escaping Free-Energy Minima. *Proc. Natl. Acad. Sci. USA* **2002**, *99*, 12562–12566.

(211) Tribello, G. A.; Bonomi, M.; Branduardi, D.; Camilloni, C.; Bussi, G. PLUMED 2: New Feathers for an Old Bird. *Comput. Phys. Commun.* **2014**, *185*, 604–613.

(212) Bonomi, M.; Bussi, G.; Camilloni, C.; Tribello, G. A.; Banáš, P.; Barducci, A.; Bernetti, M.; Bolhuis, P. G.; Bottaro, S.; Branduardi, D.; Capelli, R.; Carloni, P.; Ceriotti, M.; Cesari, A.; Chen, H.; Chen, W.; Colizzi, F.; De, S.; De La Pierre, M.; Donadio, D.; Drobot, V.; Ensing, B.; Ferguson, A. L.; Filizola, M.; Fraser, J. S.; Fu, H.; Gasparotto, P.; Gervasio, F. L.; Giberti, F.; Gil-Ley, A.; Giorgino, T.; Heller, G. T.; Hocky, G. M.; Iannuzzi, M.; Invernizzi, M.; Jelfs, K. E.; Jussupow, A.; Kirilin, E.; Laio, A.; Limongelli, V.; Lindorff-Larsen, K.; Löhr, T.; Marinelli, F.; Martin-Samos, L.; Masetti, M.; Meyer, R.; Michaelides, A.; Molteni, C.; Morishita, T.; Nava, M.; Paissoni, C.; Papaleo, E.; Parrinello, M.; Pfaendtner, J.; Piaggi, P.; Piccini, G.; Pietropaolo, A.; Pietrucci, F.; Pipolo, S.; Provasi, D.; Quigley, D.; Raiteri, P.; Raniolo, S.; Rydzewski, J.; Salvalaglio, M.; Sosso, G. C.; Spiwok, V.; Šponer, J.; Swenson, D. W. H.; Tiwary, P.; Valsson, O.; Vendruscolo, M.; Voth, G. A.; White, A.; The PLUMED consortium Promoting Transparency and Reproducibility in Enhanced Molecular Simulations. *Nat. Methods* **2019**, *16*, 670–673.

(213) Flory, P. J. Thermodynamics of High Polymer Solutions. *J. Chem. Phys.* **1942**, *10*, 51–61.

(214) Huggins, M. L. Solutions of Long Chain Compounds. *J. Chem. Phys.* **1941**, *9*, 440–440.

(215) Boehm, B. J.; Huang, D. M. A Simple Predictor of Interface Orientation of Fluids of Disk-like Anisotropic Particles and Its Implications for Organic Semiconductors. *Soft Matter* **2022**, *18*, 1843–1857.

(216) DiLisi, G. A., *An Introduction to Liquid Crystals*; IOP Publishing: 2019.

(217) Tang, W.; Huang, Y.; Han, L.; Liu, R.; Su, Y.; Guo, X.; Yan, F. Recent Progress in Printable Organic Field Effect Transistors. *J. Mater. Chem. C* **2019**, *7*, 790–808.

(218) Cheng, P.; Li, G.; Zhan, X.; Yang, Y. Next-Generation Organic Photovoltaics Based on Non-Fullerene Acceptors. *Nat. Photon.* **2018**, *12*, 131–142.

(219) Menke, S. M.; Ran, N. A.; Bazan, G. C.; Friend, R. H. Understanding Energy Loss in Organic Solar Cells: Toward a New Efficiency Regime. *Joule* **2018**, *2*, 25–35.

(220) Poelking, C.; Tietze, M.; Elschner, C.; Olthof, S.; Hertel, D.; Baumeier, B.; Würthner, F.; Meerholz, K.; Leo, K.; Andrienko, D. Impact of Mesoscale Order on Open-Circuit Voltage in Organic Solar Cells. *Nat. Mater.* **2015**, *14*, 434–439.

(221) Ayzner, A. L.; Nordlund, D.; Kim, D.-H.; Bao, Z.; Toney, M. F. Ultrafast Electron Transfer at Organic Semiconductor Interfaces: Importance of Molecular Orientation. *J. Phys. Chem. Lett.* **2015**, *6*, 6–12.

(222) Idé, J.; Méreau, R.; Ducasse, L.; Castet, F.; Bock, H.; Olivier, Y.; Cornil, J.; Beljonne, D.; D'Avino, G.; Roscioni, O. M.; Muccioli, L.; Zannoni, C. Charge Dissociation at Interfaces between Discotic Liquid Crystals: The Surprising Role of Column Mismatch. *J. Am. Chem. Soc.* **2014**, *136*, 2911–2920.

(223) Allen, M. P. Molecular Simulation of Liquid Crystals. *Mol. Phys.* **2019**, *117*, 2391–2417.

(224) Bates, M. A. Phase Behavior and Free Interfaces of a Lattice-Gas Nematic-Liquid-Crystal Model. *Phys. Rev. E* **2002**, *65*, 041706.

(225) Reich, H.; Schmidt, M. Capillary Nematization of Hard Colloidal Platelets Confined between Two Parallel Hard Walls. *J. Phys: Condens. Matter* **2007**, *19*, 326103.

(226) Harnau, L.; Dietrich, S. Fluids of Platelike Particles near a Hard Wall. *Phys. Rev. E* **2002**, *65*, 021505.

(227) Poniewierski, A.; Hołyst, R. Nematic Alignment at a Solid Substrate: The Model of Hard Spherocylinders near a Hard Wall. *Phys. Rev. A* **1988**, *38*, 3721–3727.

(228) Kapanowski, A.; Abram, M. Model of Hard Spheroplatelets near a Hard Wall. *Phys. Rev. E* **2014**, *89*, 062503.

(229) Kimura, H. Statistical Theory of Surface Tension and Molecular Orientations in Nematic Liquid Crystals. III. On Hard Flat Walls. *J. Phys. Soc. Jpn.* **1993**, *62*, 2725–2733.

(230) Breuer, T.; Karthäuser, A.; Witte, G. Effects of Molecular Orientation in Acceptor–Donor Interfaces between Pentacene and C60 and Diels–Alder Adduct Formation at the Molecular Interface. *Adv. Mater. Interfaces* **2016**, *3*, 1500452.

(231) Salgado-Blanco, D.; Mendoza, C. I.; Chávez-Rojo, M. A.; Moreno-Razo, J. A.; Díaz-Herrera, E. Influence of Anchoring in the Phase Behaviour of Discotic Liquid Crystals. *Soft Matter* **2018**, *14*, 2846–2859.

(232) Wang, T.; Kafle, T. R.; Kattel, B.; Liu, Q.; Wu, J.; Chan, W.-L. Growing Ultra-flat Organic Films on Graphene with a Face-on Stacking via Moderate Molecule-Substrate Interaction. *Sci. Rep.* **2016**, *6*, 28895.

(233) Pizzirusso, A.; Berardi, R.; Muccioli, L.; Ricci, M.; Zannoni, C. Predicting Surface Anchoring: Molecular Organization across a Thin Film of 5CB Liquid Crystal on Silicon. *Chem. Sci.* **2012**, *3*, 573–579.

(234) Roscioni, O. M.; Muccioli, L.; Della Valle, R. G.; Pizzirusso, A.; Ricci, M.; Zannoni, C. Predicting the Anchoring of Liquid Crystals at a Solid Surface: 5-Cyanobiphenyl on Cristobalite and Glassy Silica Surfaces of Increasing Roughness. *Langmuir* **2013**, *29*, 8950–8958.

(235) Roscioni, O. M.; Muccioli, L.; Zannoni, C. Predicting the Conditions for Homeotropic Anchoring of Liquid Crystals at a Soft Surface. 4-n-Pentyl-4'-Cyanobiphenyl on Alkylsilane Self-Assembled Monolayers. *ACS Appl. Mater. Interfaces* **2017**, *9*, 11993–12002.

(236) Dolynchuk, O.; Schmode, P.; Fischer, M.; Thelakkat, M.; Thurn-Albrecht, T. Elucidating the Effect of Interfacial Interactions on Crystal Orientations in Thin Films of Polythiophenes. *Macromolecules* **2021**, *54*, 5429–5439.

(237) Boulanger, N.; Yu, V.; Hilke, M.; Toney, M. F.; Barbero, D. R. In Situ Probing of the Crystallization Kinetics of Rr-P3HT on Single Layer Graphene as a Function of Temperature. *Phys. Chem. Chem. Phys.* **2017**, *19*, 8496–8503.

(238) Salzmann, I.; Moser, A.; Oehzelt, M.; Breuer, T.; Feng, X.; Juang, Z.-Y.; Nabok, D.; Della Valle, R. G.; Duhm, S.; Heimel, G.; Brillante, A.; Venuti, E.; Bilotti, I.; Christodoulou, C.; Frisch, J.; Puschnig, P.; Draxl, C.; Witte, G.; Müllen, K.; Koch, N. Epitaxial Growth of π-Stacked Perfluoropentacene on Graphene-Coated Quartz. *ACS Nano* **2012**, *6*, 10874–10883.

(239) Guo, R.; Li, B.; Lu, T.; Lin, T.; Andre, J.; Zhang, C.; Zhi, L.; Chen, Z. Molecular Orientations at Buried Conducting Polymer/Graphene Interfaces. *Macromolecules* **2021**, *54*, 4050–4060.

(240) Shahiduzzaman, M.; Hirayama, T.; Chikamatsu, T.; Koganezawa, T.; Nakano, M.; Miyadera, T.; Karakawa, M.; Takahashi, K.; Taima, T. Substrate-Driven Switchable Molecular Orientation in Bulk Heterojunction Films Identified Using Infrared Reflection Absorption Spectroscopy. *Mol. Syst. Des. Eng.* **2020**, *5*, 559–564.

(241) Beigmohamadi, M.; Niyamakom, P.; Farahzadi, A.; Effertz, C.; Kremers, S.; Brueggemann, D.; Wuttig, M. Structure and Morphology of Perylene Films Grown on Different Substrates. *J. Appl. Phys.* **2008**, *104*, 013505.

(242) Teixeira, P. I. C.; Anquetil-Deck, C.; Cleaver, D. J. Ordering of Oblate Hard Particles between Symmetric Penetrable Walls. *Liq. Cryst.* **2021**, *48*, 75–87.

(243) Anquetil-Deck, C.; Cleaver, D. J.; Teixeira, P. I. C. Ordering of Oblate Hard Particles between Hybrid Penetrable Walls. *J. Phys. Chem. B* **2020**, *124*, 7709–7716.

(244) Plimpton, S. J. Fast Parallel Algorithms for Short-Range Molecular Dynamics. *J. Comput. Phys.* **1995**, *117*, 1–19.

(245) Stukowski, A. Visualization and Analysis of Atomistic Simulation Data with OVITO–the Open Visualization Tool. *Modelling Simul. Mater. Sci. Eng.* **2009**, *18*, 015012.

(246) Lorenz, C.; Webb, E.; Stevens, M.; Chandross, M.; Grest, G. Frictional Dynamics of Perfluorinated Self-Assembled Monolayers on Amorphous SiO_2. *Tribol. Lett.* **2005**, *19*, 93–98.

(247) Becker, P.; Scyfried, P.; Siegert, H. The Lattice Parameter of Highly Pure Silicon Single Crystals. *Z. Phys. B Condens. Matter* **1982**, *48*, 17–21.

(248) Shirts, M. R.; Chodera, J. D. Statistically Optimal Analysis of Samples from Multiple Equilibrium States. *J. Chem. Phys.* **2008**, *129*, 124105.

(249) Chodera, J. D.; Swope, W. C.; Pitera, J. W.; Seok, C.; Dill, K. A. Use of the Weighted Histogram Analysis Method for the Analysis of Simulated and Parallel Tempering Simulations. *J. Chem. Theory Comput.* **2007**, *3*, 26–41.

(250) Chodera, J. D. A Simple Method for Automated Equilibration Detection in Molecular Simulations. *J. Chem. Theory Comput.* **2016**, *12*, 1799–1805.

(251) Rull, L. F. Phase Diagram of a Liquid Crystal Model: A Computer Simulation Study. *Physica A* **1995**, *220*, 113–138.

(252) Weeks, J. D.; Chandler, D.; Andersen, H. C. Role of Repulsive Forces in Determining the Equilibrium Structure of Simple Liquids. *J. Chem. Phys.* **1971**, *54*, 5237–5247.

(253) Cheung, D. L. Monte Carlo Simulations of Liquid Crystals between Microstructured Substrates. *J. Chem. Phys.* **2008**, *128*, 194902.

(254) Maunoury, J. C.; Howse, J. R.; Turner, M. L. Melt-Processing of Conjugated Liquid Crystals: A Simple Route to Fabricate OFETs. *Adv. Mater.* **2007**, *19*, 805–809.

(255) Yang, L.; Tumbleston, J. R.; Zhou, H.; Ade, H.; You, W. Disentangling the Impact of Side Chains and Fluorine Substituents of Conjugated Donor Polymers on the Performance of Photovoltaic Blends. *Energy Environ. Sci.* **2012**, *6*, 316–326.

(256) Nicola, A. D.; Correa, A.; Giunchi, A.; Muccioli, L.; D'Avino, G.; Kido, J.; Milano, G. Bidimensional H-Bond Network Promotes Structural Order and Electron Transport in BPyMPMs Molecular Semiconductor. *Adv. Theory Simul.* **2021**, *4*, 2000302.

(257) Skrypnychuk, V.; Boulanger, N.; Yu, V.; Hilke, M.; Toney, M. F.; Barbero, D. R. Reduced Crystallinity and Enhanced Charge Transport by Melt Annealing of an Organic Semiconductor on Single Layer Graphene. *J. Mater. Chem. C* **2016**, *4*, 4143–4149.

(258) Bagchi, K.; Ediger, M. D. Controlling Structure and Properties of Vapor-Deposited Glasses of Organic Semiconductors: Recent Advances and Challenges. *J. Phys. Chem. Lett.* **2020**, *11*, 6935–6945.

(259) Gujral, A.; Yu, L.; Ediger, M. D. Anisotropic Organic Glasses. *Curr. Opin. Solid State Mater. Sci.* **2018**, *22*, 49–57.

(260) Li, M.; An, C.; Marszalek, T.; Baumgarten, M.; Yan, H.; Müllen, K.; Pisula, W. Controlling the Surface Organization of Conjugated Donor–Acceptor Polymers by Their Aggregation in Solution. *Adv. Mater.* **2016**, *28*, 9430–9438.

(261) Wang, D.; Yuan, Y.; Mardiyati, Y.; Bubeck, C.; Koynov, K. From Single Chains to Aggregates, How Conjugated Polymers Behave in Dilute Solutions. *Macromolecules* **2013**, *46*, 6217–6224.

(262) Zierenberg, J.; Marenz, M.; Janke, W. Dilute Semiflexible Polymers with Attraction: Collapse, Folding and Aggregation. *Polymers* **2016**, *8*, 333.

(263) Thompson, A. P.; Aktulga, H. M.; Berger, R.; Bolintineanu, D. S.; Brown, W. M.; Crozier, P. S.; in 't Veld, P. J.; Kohlmeyer, A.; Moore, S. G.; Nguyen, T. D.; Shan, R.; Stevens, M. J.; Tranchida, J.; Trott, C.; Plimpton, S. J. LAMMPS - a Flexible Simulation Tool for Particle-Based Materials Modeling at the Atomic, Meso, and Continuum Scales. *Comput. Phys. Commun.* **2022**, *271*, 108171.

(264) Brown, W. M.; Wang, P.; Plimpton, S. J.; Tharrington, A. N. Implementing Molecular Dynamics on Hybrid High Performance Computers – Short Range Forces. *Comput. Phys. Commun.* **2011**, *182*, 898–911.

(265) Brown, W. M.; Kohlmeyer, A.; Plimpton, S. J.; Tharrington, A. N. Implementing Molecular Dynamics on Hybrid High Performance Computers – Particle–Particle Particle-Mesh. *Comput. Phys. Commun.* **2012**, *183*, 449–459.

(266) Humphrey, W.; Dalke, A.; Schulten, K. VMD: Visual Molecular Dynamics. *J. Mol. Graph.* **1996**, *14*, 33–38.

(267) DuBay, K. H.; Hall, M. L.; Hughes, T. F.; Wu, C.; Reichman, D. R.; Friesner, R. A. Accurate Force Field Development for Modeling Conjugated Polymers. *J. Chem. Theory Comput.* **2012**, *8*, 4556–4569.

(268) Jorgensen, W. L.; McDonald, N. A. Development of an All-Atom Force Field for Heterocycles. Properties of Liquid Pyridine and Diazenes. *J. Mol. Struct., Theochem* **1998**, *424*, 145–155.

(269) McDonald, N. A.; Jorgensen, W. L. Development of an All-Atom Force Field for Heterocycles. Properties of Liquid Pyrrole, Furan, Diazoles, and Oxazoles. *J. Phys. Chem. B* **1998**, *102*, 8049–8059.

(270) Price, M. L. P.; Ostrovsky, D.; Jorgensen, W. L. Gas-Phase and Liquid-State Properties of Esters, Nitriles, and Nitro Compounds with the OPLS-AA Force Field. *J. Comput. Chem.* **2001**, *22*, 1340–1352.

(271) Rizzo, R. C.; Jorgensen, W. L. OPLS All-Atom Model for Amines: Resolution of the Amine Hydration Problem. *J. Am. Chem. Soc.* **1999**, *121*, 4827–4836.

(272) Watkins, E. K.; Jorgensen, W. L. Perfluoroalkanes: Conformational Analysis and Liquid-State Properties from Ab Initio and Monte Carlo Calculations. *J. Phys. Chem. A* **2001**, *105*, 4118–4125.

(273) Kaminski, G. A.; Friesner, R. A.; Tirado-Rives, J.; Jorgensen, W. L. Evaluation and Reparametrization of the OPLS-AA Force Field for Proteins via Comparison with Accurate Quantum Chemical Calculations on Peptides. *J. Phys. Chem. B* **2001**, *105*, 6474–6487.

(274) Marcon, V.; Raos, G. Free Energies of Molecular Crystal Surfaces by Computer Simulation: Application to Tetrathiophene. *J. Am. Chem. Soc.* **2006**, *128*, 1408–1409.

(275) Pizzirusso, A.; Savini, M.; Muccioli, L.; Zannoni, C. An Atomistic Simulation of the Liquid-Crystalline Phases of Sexithiophene. *J. Mater. Chem.* **2010**, *21*, 125–133.

(276) Ryckaert, J.-P.; Ciccotti, G.; Berendsen, J. Numerical Integration of the Cartesian Equations of Motion of a System with Constraints: Molecular Dynamics of n-Alkanes. *J. Comput. Phys.* **1977**, *23*, 327–341.

(277) Martínez, L.; Andrade, R.; Birgin, E. G.; Martínez, J. M. PACKMOL: A Package for Building Initial Configurations for Molecular Dynamics Simulations. *J. Comput. Chem.* **2009**, *30*, 2157–2164.

(278) Belmares, M.; Blanco, M.; Goddard, W. A.; Ross, R. B.; Caldwell, G.; Chou, S.-H.; Pham, J.; Olofson, P. M.; Thomas, C. Hildebrand and Hansen Solubility Parameters from Molecular Dynamics with Applications to Electronic Nose Polymer Sensors. *J. Comput. Chem.* **2004**, *25*, 1814–1826.

(279) Shinoda, W.; Shiga, M.; Mikami, M. Rapid Estimation of Elastic Constants by Molecular Dynamics Simulation under Constant Stress. *Phys. Rev. B* **2004**, *69*, 134103.

(280) Nguyen, H. T. L.; Huang, D. M. Systematic Bottom-up Molecular Coarse-Graining via Force and Torque Matching Using Anisotropic Particles. *J. Chem. Phys.* **2022**, *156*, 184118.

(281) Faller, R.; Reith, D. Properties of Poly(Isoprene): Model Building in the Melt and in Solution. *Macromolecules* **2003**, *36*, 5406–5414.

(282) Boţan, V.; Ustach, V. D.; Leonhard, K.; Faller, R. Development and Application of a Coarse-Grained Model for PNIPAM by Iterative Boltzmann Inversion and Its Combination with Lattice Boltzmann Hydrodynamics. *J. Phys. Chem. B* **2017**, *121*, 10394–10406.

(283) Majumder, S.; Zierenberg, J.; Janke, W. Kinetics of Polymer Collapse: Effect of Temperature on Cluster Growth and Aging. *Soft Matter* **2017**, *13*, 1276–1290.

(284) Haynes, W. M., *CRC Handbook of Chemistry and Physics, 95th Edition*; CRC Press LLC: Oakville, United Kingdom, 2014.

(285) Karplus, M.; Weaver, D. L. Protein Folding Dynamics: The Diffusion-Collision Model and Experimental Data. *Protein Sci.* **1994**, *3*, 650–668.

(286) Marantan, A.; Mahadevan, L. Mechanics and Statistics of the Worm-like Chain. *Am. J. Phys.* **2018**, *86*, 86–94.

(287) Chandrasekhar, S. Stochastic Problems in Physics and Astronomy. *Rev. Mod. Phys.* **1943**, *15*, 1–89.

(288) Liu, B.; Dünweg, B. Translational Diffusion of Polymer Chains with Excluded Volume and Hydrodynamic Interactions by Brownian Dynamics Simulation. *J. Chem. Phys.* **2003**, *118*, 8061–8072.

(289) Kirkwood, J. G.; Riseman, J. The Intrinsic Viscosities and Diffusion Constants of Flexible Macromolecules in Solution. *J. Chem. Phys.* **1948**, *16*, 565–573.

(290) Doi, M.; Edwards, S. F.; Edwards, S. F., *The Theory of Polymer Dynamics*; Clarendon Press: 1988; 420 pp.

(291) Jackson, N. E.; Chen, L. X.; Ratner, M. A. Charge Transport Network Dynamics in Molecular Aggregates. *Proc. Natl. Acad. Sci. USA* **2016**, *113*, 8595–8600.

(292) Rackers, J. A.; Wang, Z.; Lu, C.; Laury, M. L.; Lagardère, L.; Schnieders, M. J.; Piquemal, J.-P.; Ren, P.; Ponder, J. W. Tinker 8: Software Tools for Molecular Design. *J. Chem. Theory Comput.* **2018**, *14*, 5273–5289.

(293) Spano, F. C.; Silva, C. H- and J-Aggregate Behavior in Polymeric Semiconductors. *Annu. Rev. Phys. Chem.* **2014**, *65*, 477–500.

(294) Brinkmann, M.; Gonthier, E.; Bogen, S.; Tremel, K.; Ludwigs, S.; Hufnagel, M.; Sommer, M. Segregated versus Mixed Interchain Stacking in Highly Oriented Films of Naphthalene Diimide Bithiophene Copolymers. *ACS Nano* **2012**, *6*, 10319–10326.

(295) Shin, Y.-h.; Komber, H.; Caiola, D.; Cassinelli, M.; Sun, H.; Stegerer, D.; Schreiter, M.; Horatz, K.; Lissel, F.; Jiao, X.; McNeill, C. R.; Cimò, S.; Bertarelli, C.; Fabiano, S.; Caironi, M.; Sommer, M. Synthesis and Aggregation Behavior of a Glycolated Naphthalene Diimide Bithiophene Copolymer for Application in Low-Level n-Doped Organic Thermoelectrics. *Macromolecules* **2020**, *53*, 5158–5168.

(296) McNeill, C. R. Personal Communication. Monash University, Melbourne.

(297) Liu, J.-J.; Liu, T.; Xia, S.-B.; He, C.-X.; Cheng, F.-X.; Lin, M.-J.; Huang, C.-C. Cocrystals of Naphthalene Diimide with Naphthalene Derivatives: A Facile Approach to Tune the Luminescent Properties. *Dyes Pigm.* **2018**, *149*, 59–64.

(298) Hestand, N. J.; Spano, F. C. Expanded Theory of H- and J-Molecular Aggregates: The Effects of Vibronic Coupling and Intermolecular Charge Transfer. *Chem. Rev.* **2018**, *118*, 7069–7163.

(299) Wang, H.; Schütte, C.; Delle Site, L. Adaptive Resolution Simulation (AdResS): A Smooth Thermodynamic and Structural Transition from Atomistic to Coarse Grained Resolution and Vice Versa in a Grand Canonical Fashion. *J. Chem. Theory Comput.* **2012**, *8*, 2878–2887.

(300) Cortes-Huerto, R.; Praprotnik, M.; Kremer, K.; Delle Site, L. From Adaptive Resolution to Molecular Dynamics of Open Systems. *Eur. Phys. J. B* **2021**, *94*, 189.

(301) Lemkul, J. A.; Huang, J.; Roux, B.; MacKerell, A. D. An Empirical Polarizable Force Field Based on the Classical Drude Oscillator Model: Development History and Recent Applications. *Chem. Rev.* **2016**, *116*, 4983–5013.

(302) Lamoureux, G.; Roux, B. Modeling Induced Polarization with Classical Drude Oscillators: Theory and Molecular Dynamics Simulation Algorithm. *J. Chem. Phys.* **2003**, *119*, 3025–3039.

(303) Halgren, T. A.; Damm, W. Polarizable Force Fields. *Curr. Opin. Struct. Biol.* **2001**, *11*, 236–242.

(304) Gao, M.; Lee, T.; Burn, P. L.; Mark, A. E.; Pivrikas, A.; Shaw, P. E. Revealing the Interplay between Charge Transport, Luminescence Efficiency, and Morphology in Organic Light-Emitting Diode Blends. *Adv. Funct. Mater.* **2020**, *30*, 1907942.

(305) Lee, C.-K.; Pao, C.-W. Nanomorphology Evolution of P3HT/PCBM Blends during Solution-Processing from Coarse-Grained Molecular Simulations. *J. Phys. Chem. C* **2014**, *118*, 11224–11233.

(306) Mackay, F. E.; Ollila, S. T. T.; Denniston, C. Hydrodynamic Forces Implemented into LAMMPS through a Lattice-Boltzmann Fluid. *Comput. Phys. Commun.* **2013**, *184*, 2021–2031.

(307) Mackay, F. E.; Denniston, C. Coupling MD Particles to a Lattice-Boltzmann Fluid through the Use of Conservative Forces. *J. Comput. Phys.* **2013**, *237*, 289–298.

(308) Adhikari, R.; Stratford, K.; Cates, M. E.; Wagner, A. J. Fluctuating Lattice Boltzmann. *EPL* **2005**, *71*, 473–479.